Double beta decay of ^{48}Ca with NEMO3 and calibration development for SuperNEMO

Benjamin Richards

Thesis submitted for the degree of

Doctor of Philosophy

June 11, 2013

Department of Physics and Astronomy

University College London

Declaration

I, Benjamin J. Richards, confirm that the work presented in this thesis is my own. Where information has been derived from other sources, I confirm that this has been indicated in the thesis.

Benjamin Richards

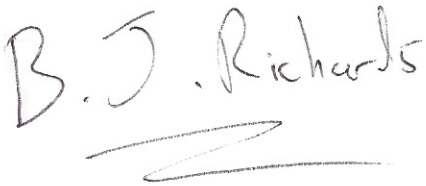

Abstract

The two neutrino double beta ($\beta\beta2\nu$) decay half-life of the ^{48}Ca to ^{48}Ti ground state transition has been measured by analysing 1555 days of NEMO3 data with 6.99g of ^{48}Ca and was found to be $T_{1/2} = 4.11^{+0.23}_{-0.20}(stat.) \pm 0.26(syst.) \times 10^{19}$ years. This is the world's most accurate result for this isotope from which the matrix element for $\beta\beta2\nu$ has been calculated $M_{2\nu} = 0.0247 \pm 0.0015$. A limit on the neutrinoless double beta ($\beta\beta0\nu$) decay half-life for ^{48}Ca has also been obtained at $T_{1/2} > 1.8 \times 10^{22}$ years at 90% CL.. This corresponds to an upper bound on the effective Majorana neutrino mass of $\langle m_\nu \rangle < 19.8$ eV for a $\beta\beta0\nu$ matrix element of $\mathrm{M}_{0\nu} = 0.72$ which is comparable with the best present results for this isotope.

The next incarnation of the NEMO3 technology is SuperNEMO which has its demonstrator module currently under construction and is due to begin operation in 2014. SuperNEMO aims to achieve a half-life sensitivity of $\approx 10^{26}$ years (90% CL) which corresponds to a neutrino mass of 40-100 meV. Calibration of the SuperNEMO detector sub-systems, especially the calorimeter, is important in order to maintain the required sensitivity and determine the detector design. The absolute calibration of SuperNEMO was shown to be achievable with a 6x4 configuration of ^{207}Bi sources inside the detector. The calibration sources strength, position in the detector and the length and periodicity of the calibration runs have been optimised.

Explanation of Data Loss

During the writing of my Ph.D. thesis and before I had begun to write my results sections, a computer support technician accidentally deleted the data disk for the SuperNEMO group whilst attempting a disk server migration. This data loss, which totalled 5TB, included files and backups for all group members. Unfortunately this data was not recoverable. My files which were lost from the disk server included all of my analysis data and plots, as well as all of my software work and data backups over the entire length of my Ph.D.

This thesis was therefore written using my notes and any data and plots that could be used from my internal talks and presentations, which were stored on a different server. Due to this, the plots used are not of as high a standard and quality as I would have liked and are not able to show the full extent of my work. I would have liked to present further plots from my work to illustrate areas such as my analysis cut efficiencies (to demonstrate background contributions), my exploration of the analysis cut's effect on the deficit seen, comparisons of the electron energies for two electron events before and after the 1MeV cut and a more in-depth representation of the exploration of background contaminations.

Acknowledgements

Firstly I would like to thank my supervisor Ruben Saakyan for his support, advice and guidance throughout my Ph.D. Secondly, all the members of my collaboration that I have interacted with over the years during discussion and debate, especially all those within UCL. I would also like to thank the Science and Technology Facilities Council (STFC) for their funding of my Ph.D. studies.

Thanks to Robert Flack and Justin Evans for their help and advice during my studies and collaboration meetings and to my office mates Hilal Kucuk and Jim Grozier for their solidarity and companionship during my time at UCL.

Finally I would like to thank my brother for his endless technical help, my father for his extensive proof reading and all of my family, loved ones and girlfriend for their support and encouragement that made this possible.

"For my family

and those lost along the way."

Contents

1 Introduction **19**

1.1 Why is the Neutrino Important? . . . 19

1.2 History of Discovery . . . 20

1.3 Theory of Neutrinos . . . 23

1.3.1 General Nature . . . 23

1.3.2 Flavours . . . 23

1.3.3 Neutrino Mixing . . . 24

1.3.4 Neutrino Oscillations . . . 25

1.3.4.1 Solar Neutrinos . . . 27

1.3.4.2 Atmospheric Neutrinos . . . 29

1.3.4.3 Artificial Neutrinos . . . 29

1.3.5 Mass Differences and Hierarchies . . . 31

1.3.6 Mass Mechanisms . . . 31

1.3.6.1 Dirac . . . 31

1.3.6.2 Majorana . . . 32

1.3.6.3 The See-Saw Mechanism . . . 33

1.3.7 Direct Mass Measurements . . . 35

1.3.7.1 Tritium Decay . . . 35

1.3.7.2 Cosmology . . . 36

1.3.7.3 Summary . . . 37

2 Double Beta Decay Theory **39**

2.1 Single β Decay . . . 39

2.2 The Semi Empirical Mass Formula . . . 40

2.3 Double Beta Decay . . . 41

2.3.1 Two Neutrino Double Beta Decay . . . 41

2.3.2 Neutrinoless Double Beta Decay and Neutrino Mass . . . 43

2.3.3 Exotic $\beta\beta0\nu$ Mechanisms . . . 49

2.3.3.1 Right Handed Current . . . 49

2.3.3.2 Majoron Emission . . . 50
2.3.3.3 Heavy Neutrino Exchange . . . 51
2.3.3.4 R-Parity Breaking SUSY Mechanism . . . 51
2.3.3.5 Squark Mixing Mechanism . . . 52
2.3.3.6 Resonant Neutrinoless Double Electron Capture . . . 52
2.3.3.7 Distinguishing the $\beta\beta0\nu$ Decay Mechanisms . . . 53
2.4 Nuclear Matrix Elements . . . 54
2.4.1 The Nuclear Shell Model . . . 55
2.4.2 The Quasiparticle Random Phase Approximation . . . 55
2.4.3 Other NME Models . . . 57

3 Current Experimental Techniques and Status **59**
3.1 Detector Construction Criteria . . . 59
3.1.1 $0\nu\beta\beta$ Decay Sensitivity in the Zero Background Case . . . 59
3.1.2 $0\nu\beta\beta$ Decay Sensitivity Including Backgrounds . . . 60
3.2 Double Beta Decay Detection Technologies . . . 61
3.2.1 Bolometers . . . 62
3.2.2 Germanium Detectors . . . 63
3.2.3 Scintillator Experiments . . . 66
3.2.4 Tracking Detectors and TPCs . . . 68
3.2.5 Indirect Detection . . . 69
3.2.5.1 Geochemical Experiments . . . 69
3.2.5.2 Radiochemical Experiments . . . 69
3.3 ^{48}Ca Experiments . . . 70
3.3.1 Mateosian and Goldhaber Experiment . . . 70
3.3.2 The Beijing Experiment . . . 70
3.3.3 Hoover Dam Experiment . . . 70
3.3.4 TGV Experiment . . . 71
3.3.5 ELEGANT VI . . . 71
3.3.6 CANDLES . . . 71
3.4 Current Double Beta Decay Results . . . 72

4 NEMO3 Detector **74**
4.1 How NEMO3 is Different from other Double Beta Experiments . . . 74
4.2 Detector Description . . . 75
4.2.1 Overview . . . 75
4.2.2 Isotopes and Foils . . . 78
4.2.2.1 Isotope Selection . . . 78
4.2.2.2 Enrichment and Purification . . . 79

4.2.2.3 Production . . . 81
4.2.2.4 Radio Purity . . . 82
4.2.3 Tracking . . . 85
4.2.3.1 Design . . . 85
4.2.3.2 Operation and Theory . . . 87
4.2.4 Calorimetry . . . 91
4.2.4.1 Calorimeter Design . . . 91
4.2.5 Calibration . . . 93
4.2.6 Shielding . . . 96
4.2.6.1 Radon Tent . . . 98
4.2.7 Ancillaries and Electronics and Trigger . . . 100
4.2.7.1 Gas System . . . 100
4.2.7.2 Electronics and Trigger . . . 100
4.3 Backgrounds . . . 102
4.4 BiPo . . . 105
4.5 Phases . . . 107

5 ^{48}Ca Double Beta Decay Studies with NEMO3 **108**
5.1 NEMO3 Simulation and Analysis Software . . . 109
5.1.1 Event Generation and Simulation . . . 109
5.1.2 Event Reconstruction . . . 109
5.1.3 Analysis . . . 110
5.2 Analysis Techniques and Description . . . 110
5.2.1 Data Phases and Status . . . 110
5.2.2 Particle ID . . . 111
5.2.3 Time of Flight . . . 112
5.2.3.1 Internal Two Electrons Hypothesis . . . 113
5.2.3.2 External Two Electron Crossing Hypothesis . . . 114
5.2.4 Fitting of Data Components using Log Likelihood . . . 114
5.2.5 Determination of Half-Life . . . 115
5.2.6 Limit Setting and Confidence Limits . . . 116
5.2.7 Data Set . . . 118
5.3 ^{48}Ca Background Measurements . . . 119
5.3.1 External Background . . . 119
5.3.2 Internal Background Contamination Measurements . . . 121
5.3.2.1 HPGe Internal Background Measurements . . . 121
5.3.2.2 The 1e Channel and Measurement of the ^{90}Y Background . . . 122
5.3.2.3 The 1e1γ Channel . . . 129

5.3.2.4 The 1e2γ Channel . . . 133
5.4 The 2e Signal Channel . . . 135
5.5 Investigation of Deficit . . . 137
5.5.1 Multichannel Background Search . . . 139
5.5.2 Detector Effects . . . 142
5.6 $\beta\beta2\nu$ Decay Analysis and Results . . . 144
5.7 Systematic Errors . . . 152
5.8 $\beta\beta0\nu$ Analysis and Results . . . 152
5.9 Concluding Remarks . . . 153

6 SuperNEMO **156**
6.1 Case for SuperNEMO . . . 156
6.2 SuperNEMO Detector Description . . . 156
6.2.1 SuperNEMO Detector Design . . . 157
6.2.2 Alternative Detector Designs . . . 158
6.2.3 SuperNEMO Research and Development . . . 161
6.2.4 SuperNEMO and NEMO3 Detector Technical Differences . . . 162
6.3 SuperNEMO Demonstrator . . . 162
6.4 SuperNEMO Sensitivity . . . 163

7 SuperNEMO Software **166**
7.1 SuperNEMO Software Description . . . 166
7.1.1 SuperNEMO Software Operation and Executables . . . 167
7.1.1.1 Simulation . . . 167
7.1.1.2 Digitisation and Software Trigger . . . 168
7.1.1.3 Tracking and Reconstruction . . . 168
7.1.1.4 Analysis . . . 169
7.2 SuperNEMO Software Development . . . 169
7.2.1 SuperNEMO Analysis Software . . . 169
7.2.2 SuperNEMO Event Display . . . 170
7.2.3 SuperNEMO Automated Nightly Build and Validation . . . 172
7.2.4 SuperNEMO Framework Design . . . 175

8 SuperNEMO Calibration **177**
8.1 Calibration Systems . . . 177
8.1.1 Light Injection Calibration System . . . 177
8.1.2 Radioactive Source Calibration System . . . 177
8.1.3 ^{207}Bi . . . 178
8.2 Absolute Calibration Design . . . 182

8.2.1 Calibration Source Delivery Systems 183
8.2.1.1 Vacuum Tube System 183
8.2.1.2 Tubeless Weighted Wire System 183
8.2.2 Calibration Source Distribution 187
8.3 Simulation Studies 187
8.3.1 Determination of the Maximum Geiger Hit Rate 190
8.3.2 Optimisation of the Relative Source to Geiger Cell Alignment 193
8.3.3 Number of Events Needed for Peak Reconstruction Calibration 197
8.4 Simulation and Study of Calibration Source Placement within the Detector 200
8.4.1 Calibration Distribution Simulation with Tubeless Weighted Line Delivery . . 201

9 Conclusion **206**

10 Appendix **208**
10.1 My Contributions to the NEMO Collaboration 208
10.2 ^{48}Ca Source Issues 209

List of figures

1.1 The total cross section of the e^+e^- collisions as a function of the centre-of-mass energy in the neighbourhood of the Z^0 rest mass . . . 25
1.2 The $\nu_e(\bar{\nu}_e)$ survival probability $\mathrm{P}(\nu_e \to \nu_e) = \mathrm{P}(\bar{\nu}_e \to \bar{\nu}_e)$, as a function of the neutrino energy for L = 180 km, Δm^2 =7.0 $10^{-5} eV^2$ and $\sin^2 2\theta = 0.84$. [28] . . . 26
1.3 Graphical representation of contibution of flavour states to the mass states and their relative mass differences squared. . . . 27
1.4 pp fission chain and branches. [34] . . . 28
1.5 CNO fission cycle. [35] . . . 28
1.6 Solar neutrino energies and fluxes. [36] . . . 29
1.7 Fission neutrinos energy versus flux normalised to one fission event. [38] . . . 30
1.8 Diagram of possible neutrino hierarchies. . . . 31
1.9 Distortion in the tail of a tritium beta decay electron energy distribution. [42] . . . 36
1.10 Demonstration of the effect of Δ on the matter power spectrum for a given Σ. [43] . 37
1.11 Limits of hierarchy and lightest mass predictions on Σ and Δ. [43] . . . 38

2.1 Deficit from the SEMF showing the effect of even and odd A and the splitting of the pairing term. [49] . . . 41
2.2 Two neutrino double beta decay Feynman diagram. [50] . . . 42
2.3 Double beta decay isotope mass curves[51] and transition energy levels. [50] . . . 42
2.4 $\beta\beta 2\nu$ summed 2 electron energy distribution. [52] . . . 43
2.5 Neutrinoless double beta decay Feynman diagram. [50] . . . 44
2.6 $\beta\beta 0\nu$ 2 electron energy distribution. [52] . . . 45
2.7 The effective Majorana neutrino mass $m_{\beta\beta}$ as a function of the lightest neutrino mass m_1 for the normal hierarchy of neutrino masses. [62] . . . 47
2.8 The effective Majorana neutrino mass $m_{\beta\beta}$ as a function of the lightest neutrino mass m_3 for the inverted hierarchy of neutrino masses. [62] . . . 48
2.9 Example of summed 2 electron energy distributions for varied Majoron spectral indices. [75] . . . 51

2.10 The calculated $\beta\beta0\nu$ half-lives by assuming $m_{\beta\beta} = 50$ meV and NMEs of different approaches. [62] 57

3.1 Sum of all 5 spectra giving $0\nu\beta\beta$ discovery plot. [54] 64
3.2 Sum spectra giving $0\nu\beta\beta$ discovery plot. [65] 64
3.3 Sensitivity of the GERDA detector. [103] 65
3.4 Schematic of the Kamland-Zen detector. [108] 66
3.5 Spectra from Kamland-Zen double beta decay search. [108] 67
3.6 SNO+ example double beta decay search. [109] 67
3.7 Results from the EXO-200 on neutrinoless double beta decay search. [114] 69
3.8 The design of the CANDLES III system. [129] 71

4.1 Pictorial representation of the NEMO3 detector layers (not geometrically accurate). 76
4.2 Frejus location. 77
4.3 The Location of LSM in the Frejus road tunnel. 77
4.4 The distribution of sources inside the NEMO3 detector. [147] 79
4.5 Preparation of sector 5 source which contains Ca discs. [147] 80
4.6 Sector 5 strip 7 configuration. 83
4.7 Schematic of an HPGe detector. [147] 83
4.8 Sector wire positions. [147] 86
4.9 Theoretical anode and cathode signals for Geiger mode operation. [148] 89
4.10 Top down representation of track segment and possible connections. 90
4.11 Example of calorimeter sector design and use of different blocks. [147] 92
4.12 Example of a complete optical module of the calorimeter. [147] 94
4.13 Image of calibration tubes at the end of a sector with visible window. [147] 95
4.14 Laser calibration system and configuration. [147] 97
4.15 Schematic diagram of radon tent. [147] 99
4.16 Simplified principle of active charcoal trapping. [147] 99
4.17 Radon system schematic. [147] 100
4.18 Gas regulation system schematic. [147] 101
4.19 Chronogram for the trigger in the PMT + GG mode. [147] 102
4.20 The main decay chains of natural radioactivity with the grey indicating major backgrounds for NEMO3. [147] 103
4.21 Internal background production. [148] 104
4.22 External background production. [147] 105
4.23 NEMO3 event display of a BiPo event originating from the source foil seen from above 106
4.24 Temporal ^{222}Rn activity variations inside tracker volume from the start of data taking till 2007 measured on an hourly basis. [135] 107

5.1 Sector 5 strip 7 CaF_2 disk locations. 119
5.2 Background model prediction compared to the data for $2e^-$ events from the copper foils. [135] 121
5.3 Example of ^{90}Y (red) fit to the 1e energy spectra, with apparent low energy background deficit (The 10 largest contributing backgrounds shown along with their activities and their type (internal (intbg) or external (extbg)) and their position in the detector (surface of the foil, surface of the wires or in the PMT glass (sfoil, swires, PMT))). 123
5.4 Example of 1e events reconstructed vertices distributed over calcium foil surface. . . 125
5.5 ^{90}Y activity variation plotted for 3 month time slices. 126
5.6 Example of 1e distribution with fitted ^{90}Y and ^{210}Bi on the surface of the wires. . . 126
5.7 Example of 1e distribution with fitted ^{90}Y and ^{210}Bi on the surface of the foil. . . . 127
5.8 ^{90}Y activity for 3 month time slices with low energy ^{210}Bi background 128
5.9 Example of 1e1γ distributions. 130
5.10 Example of 1e1γ residuals. 131
5.11 Spatial distribution of event vertices across the foil surface. 132
5.12 Example of the 1e2γ distribution. 133
5.13 Example of the 1e2γ residuals. 134
5.14 Example of 2e distributions. 136
5.15 Example 2e residuals. 137
5.16 Distribution of reconstructed 2e event vertices over the surface of the foil for large angles ($\cos(\theta) \leq 0$). 138
5.17 1e1γ residuals fitted with internal ^{212}Bi contamination. 140
5.18 Thorium decay chain. [158] 141
5.19 Example 1e spectrum with ^{212}Bi (sfoil) the ^{90}Y component (red) has been reduced to account for the addition of the ^{212}Bi component (light green). 142
5.20 Schematic of the 3 types of 2 electron events for inside and outside wall interactions. 143
5.21 Energy distributions for the 1 electron events on either side of the foil (left:inside calorimiter wall, right:outside calorimiter wall). 144
5.22 Energy and angular distributions for the 2e events where both electrons go to the calorimiter wall on the inner side of foil. 145
5.23 Energy and angular distributions for the 2e events where both electrons go to the calorimiter wall on the outer side of foil. 146
5.24 Energy and angular distributions for the 2e events where one electron goes to either side of the foil. 147
5.25 Energy and angular distributions for the 1e1γ events where both particles go to the calorimiter wall on the inner side of foil. 148

5.26 Energy and angular distributions for the 1e1γ events where both particles go to the calorimiter wall on the outer side of foil. 149
5.27 Energy and angular distributions for the 1e1γ events where one particle goes to either side of the ^{48}Ca foil. 150
5.28 2e distributions of events with applied energy cut (E_{sum} >1.5MeV) and angle cut ($\cos(\theta)$< 0). 151
5.29 Spatial distribution of 1e events in the azimuthal position (X) and the height (Z). [156]153
5.30 Example of tail of the 2e summed energy distribution. 154

6.1 Simple schematic of SuperNEMO detector. [163] 157
6.2 Diagram of a single SuperNEMO module. [164] 159
6.3 SuperNEMO bar design showing complete sandwiched module construction and exploded view. 159
6.4 SuperNEMO two neutrino double beta decay half-life sensitivity for the basic block and bar design versus calorimeter energy resolution FWHM at 1MeV. Sensitivity data shown comes from effect of 3 different backgrounds (no background (2n2b) , NEMO3 background levels (N3_bgr) and SuperNEMO background level (SN_bgr)) for each of the detector designs. [165] 164
6.5 SuperNEMO two neutrino double beta decay half-life sensitivity verses the exposure in kg years for the bar and basic block design with varying foil thicknesses for the bar design and 2 different background models (SuperNEMO background levels (SN_bgr) and SuperNEMO foil backgrounds with NEMO3 gass backgrounds (SN_foil_N3_gas_bgr)). [165] 165

7.1 SNSW code diagram. 167
7.2 Example of old GEANT based event display. 171
7.3 Example of new event display top down projection. 172
7.4 Example of side 3D view of event display showing colour coded energy deposits with particle impacts on bars. 173
7.5 Example of close up 3D view of 2 single electrons emanating from green bounded source foil propagating through yellow tracking volume and impacting on scintillator bars. 174
7.6 Example of automated web status page. 175
7.7 Example of automated plot generation from test run. 176

8.1 ^{207}Bi decay scheme. 179
8.2 ^{60}Co decay scheme. 180
8.3 Example of energy spectrum from ^{207}Bi showing conversion electrons. [168] 181

8.4 Example of energy spectrum from ^{207}Bi showing conversion electrons peaks with 7.4% energy resolution. [163] . . . 182
8.5 NEMO3 manual source delivery system and holder. . . . 183
8.6 Schematic of copper tube vacuum delivery system. . . . 184
8.7 Schematic of opening angle acceptances for copper tube design. . . . 185
8.8 Schematic of tubeless wire delivery system. . . . 186
8.9 Schematic of tubeless source holder's opening angles. . . . 187
8.10 Schematic of source distribution compared to source foil position. . . . 188
8.11 Schematic of source illumination. . . . 189
8.12 Distribution of second pulse amplitude with trigger time separation. [169] . . . 190
8.13 Distribution of second pulse plasma propagation times with trigger time separation. [169] . . . 191
8.14 Example plot of special Geiger runs to test cell rate using NEMO3. . . . 192
8.15 NEMO3 source cell alignment geometry schematic. . . . 192
8.16 Simulation of Geiger triggering during calibration. . . . 193
8.17 Schematic of source alignment with respect to Geiger cells. . . . 194
8.18 Example of cell trigger amounts for fixed number of events whilst the source position is varied in X and Y. . . . 196
8.19 Schematic of angular acceptance of the closest cell where D is the distance from the cell boundary. . . . 196
8.20 Effect of cell boundary source displacement on subtended angle. . . . 197
8.21 Effect of cell boundary source displacement on cell rates. . . . 197
8.22 Effect of number of electrons on fitted peak position error for SuperNEMO. . . . 199
8.23 Main-wall scint block occupancies (0.7 < E < 1.2 MeV) for 6 x 4 grid (X = 836 mm) (no tubes). . . . 202
8.24 Main-wall scint block occupancies (0.7 < E < 1.2 MeV) for 6 x 4 grid (X = 836 mm) (no tubes). . . . 203
8.25 X-wall scint block occupancies (0.7 < E < 1.2 MeV) for 6 x 4 grid (X = 836 mm) (no tubes). . . . 203
8.26 Simulation of tracking hits distribution. . . . 204
8.27 6 x 4 grid: 836 mm horizontal source spacing and 200 mm foil strips (total width 4984 mm). . . . 204
8.28 6 x 4 grid: 924 mm horizontal source spacing and 180 mm foil strips (total width 4996 mm). . . . 205

10.1 Photograph of the CaF_2 dicks after disassembly from Mylar foil. Picture shows correct geometric dimensions. [171] . . . 209
10.2 Photograph taken during detector disassembly showing two foil defects. . . . 210

List of tables

1.1 Sensitivity of different oscillation experiments. [29] 27
1.2 Latest mixing parameter measurements. [29] 27
1.3 Neutrino properties addressed by different experimental approaches. 38
1.4 Existing constraints on absolute neutrino mass. 38

2.1 Double Beta Decay Isotopes and $\beta\beta2\nu$ results. 44
2.2 Table of spectral index relations to Majoron emissions. [70, 71, 72, 73, 74] 50
2.3 Comparison of LSSM and QRPA. [88] 56

3.1 Summary table of double beta decay results by isotope. 73

4.1 Enrichment and purification summary table. 80
4.2 NEMO3 sector source distribution. 82
4.3 Summary of major source contamination levels for HPGe. [147] 84
4.4 Summary of major detector backgrounds from HPGe. [147] 84

5.1 Main component contamination contributions as measured by HPGe detectors. . . . 120
5.2 Results of external background activity studies (where iframe = in the iron frame, swire = on the surface of the geiger wires and sfoil = on the surface of the foil. [135] 120
5.3 Copper foil internal contaminations. [135] 121
5.4 ^{48}Ca internal contamination activity levels measured using HPGe detectors on the original potion of the source that was not made into disks and post dismantling of the actual CaF_2 disks. [157] 122
5.5 Example of some internal contamination fits for multiple channels, listing the activity of the source and the associated χ^2. 139
5.6 ^{212}Bi activities from fits to ^{48}Ca channels. 142

6.1 Comparison between major design and performance parameters of NEMO3 and SuperNEMO. 162

8.1 Betas from ^{207}Bi. [167] 178

8.2 Gammas from ^{207}Bi. [167] 179
8.3 X-rays from ^{207}Bi. [167] 180
8.4 Effect of boundary offset on trigger rate. 198
8.5 Relative conversion electron intensities. [170] 198
8.6 Calibration source distribution results showing minimum block occupancy (C_{min}) highest tracker cell firing (T_{max}) and the calibration time (T_C) and source activity (A_S). 202

Chapter 1

Introduction

A list of my personal contributions to the NEMO collaboration can be seen in sec.10.1

1.1 Why is the Neutrino Important?

The neutrino has some fundamental properties that make it unique among all other particles. It is the only non-electrically charged fundamental fermion and it also has the least mass (or weakest Higgs coupling) that is far below all other particles and thus hard to explain. These properties alone make it an interesting and strange prospect that could reveal new processes and underlying physics. But also these properties allow for the possibility of the particle being Majorana in nature (being its own anti-particle), a mechanism that is not present in any other fundamental particles (which have distinct anti-matter partners). These properties also have wider implications for areas like cosmology and leptogenesis, grand unified theories (GUTs) and super symmetry mechanisms, in terms of impacting the possible causes of the matter anti-matter asymmetry in the early universe and the proposed groups for which Majorana neutrinos must inhabit. So the importance and effect of the neutrino's exact nature has far-reaching implications in wider physics.

Currently it has been discovered that neutrinos have mass and can mix and oscillate between 3 distinct flavours. However there are still a plethora of unknown attributes that make them interesting for study as well as the further measurement of mixing and oscillations to tie down mixing parameters and the mass differences between neutrino flavours, as well as the comparison of these attributes with their anti-particle equivalents. The four biggest unknowns for neutrinos at the moment are their fundamental nature (i.e. Dirac or Majorana), their absolute mass, their hierarchy (which neutrino mass eigenstate is the heaviest and which the lightest) and the size of their CP violating phases. Current experiments haven't managed to answer these questions as yet, but hopefully the next range of experiments, and specifically double beta decay experiments with help from oscillation measurments, will be sensitive to all four unknown properties.

1.2 History of Discovery

The continuous nature of the electron energy spectra in beta decay shown by Lise Meitner, Otto Hahn, Wilson and von Baeyer and James Chadwick in 1914 provided the first indications that electrons were not the only particles emitted in beta decay. However it wasn't until Wolfgang Pauli attempted to reconcile this with "the energy conservation principle" in 1930, that the idea of a second particle being emitted was considered. The name neutrino however was not coined by Fermi until 1933 [1]. In October of that year Pauli stated:

"... their mass can not be very much more than the electron mass. In order to distinguish them from heavy neutrons, mister Fermi has proposed to name them "neutrinos". It is possible that the proper mass of neutrinos be zero... It seems to me plausible that neutrinos have a spin 1/2... We know nothing about the interaction of neutrinos with the other particles of matter and with photons: the hypothesis that they have a magnetic moment seems to me not funded at all."

In 1934, the very next year, great efforts began to discover more about this theorised particle. Hans Bethe and Rudolf Peierls showed that the neutrino's cross section with matter should be extremely small, in the order of 1 billion times smaller than an electron and as such they could pass all the way through the earth without interaction [2]. The neutrino would prove difficult to detect.

Over the next 10 or more years physicists tried to learn as much information as they could about neutrinos from atoms that were known to undergo beta decay. Measurements of the kinematic recoil of atomic nuclei undergoing this process of emitting an electron and a neutrino were undertaken. These measurements were compatible with the hypothesis that only one neutrino is created in a beta decay reaction. But direct detection was still out of reach owing to the low probability of interaction due to the neutrino's weak nature and low cross section. It is clear what is needed is an extremely large source of neutrinos with a big flux and a large detector.

With the first atomic bomb in 1945 scientists realised this could be the good source of neutrinos they were looking for. Meanwhile a year later Shoichi Sakata and Takesi Inoue straightened out our understanding of the spins of π and μ particles and suggested that a separate neutrino might exist for muons.

In 1951 Frederick Reines, (whilst working at Los Alamos) talked to Fermi about the possibility of using an atomic bomb as this neutrino source. However, along with Clyde Cowan in 1952, he used the nuclear plant of Hanford, Washington instead. The detector was quickly built and results published by the end of 1953, but were inconclusive. [3]

However they repeated the experiment in 1956 near the nuclear plant of Savannah River, South Carolina, with greater care spent to decrease backgrounds and an anti-electron neutrino signal was

clearly seen over the cosmic backgrounds. [4, 5]

Reines and Cowan's experiment consisted of a fixed liquid target of about 400 litres of a water-cadmium chloride mixture. Anti-electron neutrinos from the reactor interacted with protons. The anti-electron neutrinos impact a proton creating a positron and a neutron. The positrons emitted from the target proton would then annihilate with an electron within the mixture, producing 2 simultaneous photons with the combined energy of the electron and positron. The neutron produced slows gradually until it is captured by a cadmium nucleus which then emits some photons 15 microseconds later. Measurement of all of these photons and identification of the 15 microsecond interval provides the neutrino event identification method.

That was the first discovery of a neutrino of any type and 1957 led to Goldhaber, Grodzins and Sunyar finding that it was left handed [6]. However it wasn't till a few years later in 1959 the search for other neutrino types began. In 1960 Lee and Yang became more and more convinced that if muon decay to an electron and gamma is not observed then a second type of neutrino must exist.

Meanwhile in 1962 an experiment started with a 10 ton spark chamber filled with neon gas. The neutrinos this time came from an accelerator at Brookhaven which would produce hundreds of millions of neutrinos per hour [7]. The experiment saw 40 clear events, of which in 6 the particle coming from the interaction point was determined to be an electron, which was consistent with expected background rates. However for 34 of the emanating particles it was a muon. This led to the conclusion that these were distinct and different neutrinos (a muon neutrino) as, if they were analogous, then the observed electron and muon rate would be the same.

Initially in the 1960s Bruno Pontecorvo postualted that neutrinos might change state from neutrino to anti neutrinos [8] and further work by Ziro Maki, Masami Nakagawa and Sakata at this time introduced the idea that maybe neutrino's flavours could be mixed and even oscillate between states if they had mass. Other sources of neutrinos were sought and 1969 heralded the first detection of solar neutrinos by Ray Davis in Homestake mine [9]. His detector consisted of 600 tons of industrial solvent based on chlorine, under 3000 meters of earth and it only managed to catch a few neutrinos a year. But his results led to a surprise, a huge deficit of neutrinos was seen with only a third the expected level. This was to be called the solar neutrino problem and other experiments were built to confirm his findings. Could this be neutrino oscillations? More evidence was needed.

At the end of 1974 a 2nd quark generation was found and a nice symmetry was observed between quarks and leptons [10, 11]. Neutrinos started to prove useful helping in the discovery of neutral currents, electrons and neutrinos were being used in scattering experiments to probe quark structure and better understanding was reached about the weak force and neutrino interactions.

1977 led to two big discoveries by a team led by Leon Lederman at the Stanford accelerator and the second by Martin Perl at the same time led to discovery of a 3rd generation of quarks and leptons [12, 13]. The B quark, and more importantly to neutrinos the tau particle, had been discovered. The race was on to find a tau neutrino to partner it.

However for definitive confirmation of it physicists would have to wait. But whilst waiting the W boson at UA1 was found in 1983 as it decays into an electron and anti-neutrino [14]. This was followed by the Z boson giving the neutrino's charged and neutral current interactions a mediator. On the oscillations front, work by S.P. Mikheyev and A.Y. Smirnov in 1985 developed the work of L. Wolfenstein about neutrino oscillation as they travelled through matter. The MSW effect as it was to be known could explain the solar neutrino problem but experiment was needed to confirm it.

Towards the end of the 1980s the first observations of neutrinos from outside our solar system were seen when a supernova in 1987 increased the neutrino flux at Kamiokande [15] and IMB experiments, giving birth to new ideas of neutrino astronomy, but more importantly for the neutrino, 1989 saw a measurement of the Z boson width at LEP [16]. We now had a measure of the number of neutrino generations up to 45GeV and the answer was only 3. A partner to the tau seemed inevitable.

The 1990s saw a lot of effort in neutrino physics from 2 experiments at CERN to detect neutrino oscillations in a neutrino beam (1992), as well as confirmation of the solar neutrino deficit by Gallax as well as other experiments like Sage, Kamiokande, Homestake and LSND seeing deficits too in solar, reactor and atmospheric neutrinos from cosmic rays. All these deficits could be explained by the MSW effect but trying to fit them all together into one interpretation is hard.

1998 led to the moment when oscillation evidence was seen conclusively with Super-Kamiokande seeing a deficit of muon neutrinos from atmospheric sources and electron neutrinos from the sun. Preliminary oscillation evidence had been found, the neutrino appears to have mass. [17]

The DONUT experiment in the year 2000 finally provided the piece that everyone had been waiting for as it announced it had seen the tau neutrino [18] and SuperK determined that the oscillation partner of the muon neutrino is not sterile, but the tau neutrino.

The final evidence to secure the theory of neutrino oscillations was found in 2002 when SNO announced that observation of charged and neutral currents as well as elastic scattering showed that oscillation is the cause of the solar neutrino problem [19] and 2004 saw SuperKamiokande and KamLAND present evidence of experiments into neutrino disappearance and reappearance [20]. Oscillations were here to stay.

The next 6 years have seen experiments like K2K, MINOS and T2K among others dutifully measuring the exact mixing parameters by oscillations of neutrino and anti-neutrino beams. As of

yet however no strong evidence for differences between neutrino and anti-neutrinos has been observed. At the same time other groups like the NEMO collaboration build and work to measure double beta decay processes to try and answer the remaining unknowns of this elusive particle. Measurements of the time of flight by OPERA in 2011 led to an announcement of the possibility of superluminal neutrinos [21] with others moving to confirm and 2012 brought to light possible errors in this initial result by OPERA. For now we are still waiting to see if double beta decay can be observed and what the cross checks of OPERA show and bigger experiments are being built with new techniques to measure neutrinos and all their aspects, ranging from acoustic and Cherenkov detection of stellar high energy neutrinos, neutrino factories and oscillation experiments, and bigger and more sensitive double beta decay experiments.

Material written with reference to [22, 23, 24, 21, 25]

1.3 Theory of Neutrinos

1.3.1 General Nature

The neutrino is a weakly interacting particle that has no charge, very small mass and a spin of $\frac{1}{2}$. There are three known flavours (e, μ, τ) but also many unknown properties related to them (hierarchy, mass, nature). The current understanding of these particles is summarised in the following section.

1.3.2 Flavours

Currently the most precise measurement of the number of light neutrino generations comes from Z boson decays produced at the Large Electron Positron Collider (LEP) for e^+e^- collisions. The Z boson decays into many types of quarks, charged leptons etc. These make up the visible portion of the decay's total width. Therefore if they are subtracted from the measured total width of Z decay then we obtain the partial width for the invisible undetected particles, i.e. the neutrinos. Each generation's partial width contribution is assumed to be equal from the standard model (SM) and, to reduce model dependence, we take the ratio of the neutrino partial to charged lepton partial width $(\Gamma_\nu/\Gamma_l)_{SM} = 1.991 \pm 0.001$ instead of $(\Gamma_\nu)_{SM}$ in the calculation of light neutrinos. Therefore the invisible contribution is equivalent to the number of neutrino generations N_ν multiplied by $(\Gamma_\nu/\Gamma_l)_{SM}$.

i.e.

$$\Gamma_{total} = \Gamma_{visible} + \Gamma_{invisible} \tag{1.1}$$

$$\Gamma_{total} - \Gamma_{visible} = \Gamma_{invisible} \tag{1.2}$$

and

$$\Gamma_{invisible} = N_\nu(\Gamma\nu)_{SM}. \tag{1.3}$$

Using reduced model dependence

$$\frac{\Gamma_{invisible}}{\Gamma_l} = N_\nu \left(\frac{\Gamma\nu}{\Gamma l}\right)_{SM} \tag{1.4}$$

Therefore

$$N_\nu = \frac{\Gamma_{invisible}}{\Gamma_l} \left(\frac{\Gamma_l}{\Gamma_\nu}\right)_{SM} \tag{1.5}$$

The combined result from the 4 LEP experiments ALEPH, DELPHI, L3, and OPAL experiments is $N_\nu = 2.984 \pm 0.008$ [26]

However this is only a measure of light neutrino generations for neutrino masses ≤ 45.6 GeV (the mass of the Z boson), so there is the possibility of more massive and sterile (only interacting with gravity) neutrinos to exist.

Although this is the most precise measurement to date, there have been many other measurements of the number of generations from other sources and methods, such as:

- $e^+ + e^- \rightarrow \nu\bar{\nu}\gamma$. With lower $e^+ + e^-$ energies at the ASP, CELLO, MAC, MARK J and VENUS experiments giving 95% CL limit of $N_\nu < 4.8$ and at LEP giving $N_\nu = 3.00 \pm 0.08$ [26]
- Also when combined with LEP's higher energy new physics searches at between 130 and 208 GeV, the result is $N_\nu = 2.92 \pm 0.05$ [26]
- Proton anti proton collisions were also used to place limits on the number of generations in the past from finding the Z leptonic partial widths [26]

1.3.3 Neutrino Mixing

Neutrino oscillations were first proposed by Pontecorvo in 1957. He postulated that neutrinos might oscillate to anti neutrinos and later that if the neutrino had mass then a process might occur where the neutrino flavour would not be conserved and one neutrino could become another. This work was then furthered in 1962 by Maki, Nakagawa and Sakata. Like that of Cabibbo-Kobyashi-Maskawa (CKM) mixing in the quark sector, it is used to represent the observed three generation flavour eigenstates of neutrinos $(\nu_e, \nu_\mu, \nu_\tau)$ in terms of three mass eigenstates (ν_1, ν_2, ν_3) via a unitary Pontecorvo-Maki-Nakagawa-Sakata (PMNS) matrix denoted as U.

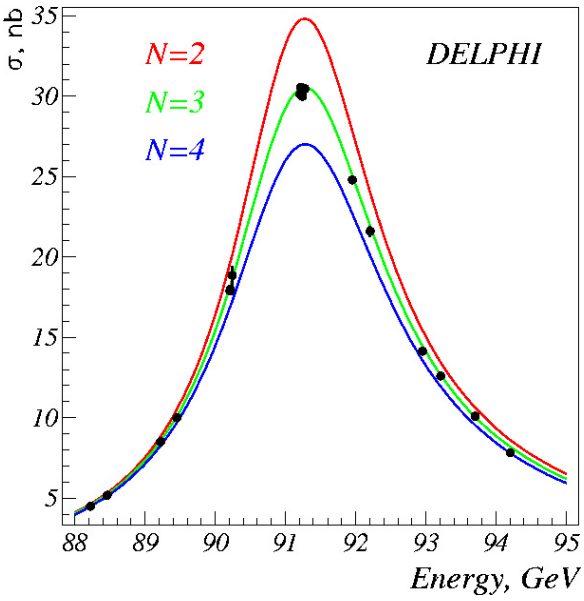

Figure 1.1: The total cross section of the e^+e^- collisions as a function of the centre-of-mass energy in the neighbourhood of the Z^0 rest mass. The total decay width of Z^0 is determined from the shape of the curve describing the cross section. Coloured lines correspond to theoretical calculations of the Standard Model of electroweak interactions with different numbers of particle generations. The dark circles indicate the measured values. [27]

$$|\nu_a\rangle = \sum_i U_{ai} |\nu_i\rangle \tag{1.6}$$

where ν_a are the flavour eigenstates and ν_i are the mass eigenstates.

The PMNS matrix U can be represented as:

$$U = \begin{pmatrix} c_{12}c_{13} & s_{12}c_{13} & s_{13}e^{-i\delta} \\ -s_{12}c_{23} - c_{12}s_{23}s_{13}e^{i\delta} & c_{12}c_{23} - s_{12}s_{23}s_{13}e^{i\delta} & s_{23}c_{13} \\ s_{12}c_{23} - c_{12}c_{23}s_{13}e^{i\delta} & -c_{12}s_{23} - s_{12}c_{23}s_{13}e^{i\delta} & c_{23}c_{13} \end{pmatrix} \begin{pmatrix} 1 & 0 & 0 \\ 0 & e^{i\phi_2} & 0 \\ 0 & 0 & e^{i\phi_3} \end{pmatrix} \tag{1.7}$$

where s_{ij} and c_{ij} are sine and cosine of θ_{ij}, the three mixing angles, and δ is the Dirac CP violating phase. In second diagonal Majorana matrix, ϕ_1 and ϕ_2 are the Majorana phases, that only apply to Majorana particles.

1.3.4 Neutrino Oscillations

A neutrino oscillation is the process in which a neutrino of one flavour state can change into another flavour state. The first possible neutrino oscillation proclamation was made in 1998 by the Super-Kamiokande experiment.

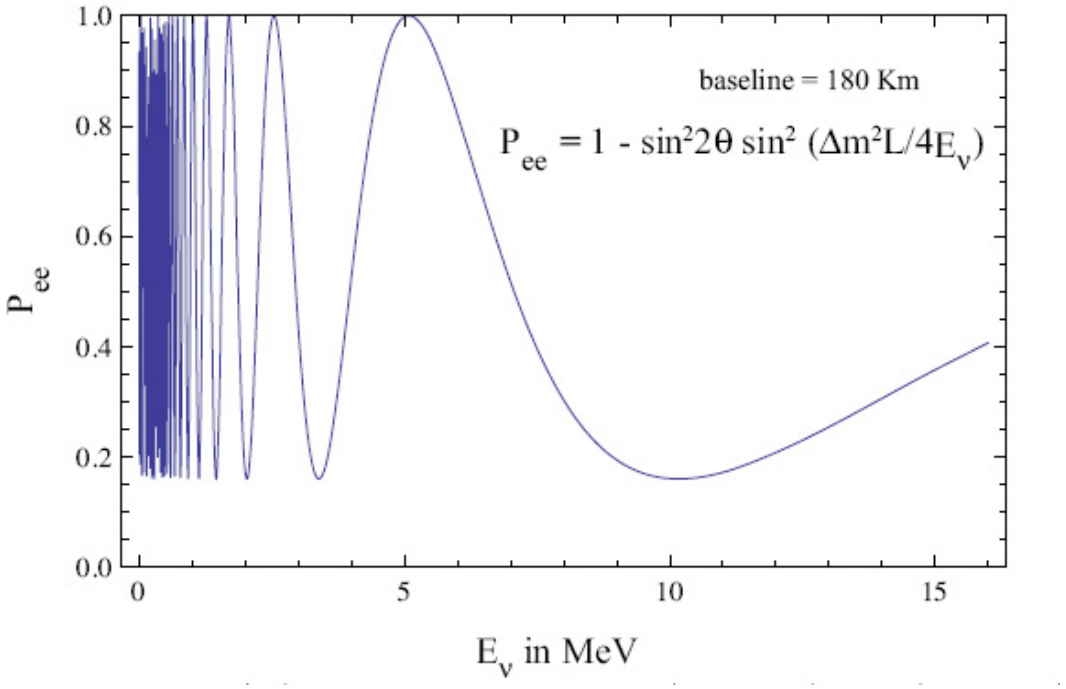

Figure 1.2: The $\nu_e(\bar{\nu}_e)$ survival probability $P(\nu_e \to \nu_e) = P(\bar{\nu}_e \to \bar{\nu}_e)$, as a function of the neutrino energy for L = 180 km, Δm^2 =7.0 $10^{-5} eV^2$ and $\sin^2 2\theta = 0.84$. [28]

The probability of a neutrino undergoing an oscillation from flavour α to another flavour β in a vacuum is given by:

$$P(\nu_\alpha \to \nu_\beta) = \left| \sum_i U^*_{\alpha i} U_{\beta i} e^{-i \frac{m_i^2 L}{2E}} \right|^2 \tag{1.8}$$

where m_i is the neutrino mass, L is the propagation length, and E is the neutrino energy. For a simplified case of two neutrino flavours, the neutrino appearance and disappearance probabilities are expressed as the following.

$$P(\nu_\alpha \to \nu_\beta) = \sin^2 2\theta \sin^2 \left[1.27 \frac{\Delta m^2 L}{E} \right] \tag{1.9}$$

$$P(\nu_\alpha \to \nu_\alpha) = 1 - \sin^2 2\theta \sin^2 \left[1.27 \frac{\Delta m^2 L}{E} \right] \tag{1.10}$$

where $\Delta m^2 = m_i^2 - m_j^2$ in eV^2, L is in km and E is in GeV. A graphical example of the survival probability of electron neutrinos as they oscillate can be seen in Fig.1.2

The oscillation probabilities are altered by transmission through matter instead of vacuum, but the dependence of these probabilities on mixing angles and mass differences between the mass and flavour eigenstates respectively gives us the opportunity to measure these properties of neutrinos.

Therefore the values of θ_{ij} and m_{ij} are both experimentally determined from the appearance and disappearance of neutrino flavours from solar, reactor, accelerator and atmospheric sources. Each of these are sensitive to different transitions based on their initial neutrino emanations and the length of their baseline as that determines the probability of oscillation to a new flavour. The relative sensitivities of these types of experiments are summarised in Table.1.1

Source	Type of ν	E[MeV]	L[km]	min(Δm^2)[eV^2]
Reactor	$\bar{\nu}_e$	~1	1	$\sim 10^{-3}$
Reactor	$\bar{\nu}_e$	~ 1	100	$\sim 10^{-5}$
Accelerator	$\nu_\mu, \bar{\nu}_\mu$	$\sim 10^3$	1	~ 1
Accelerator	$\nu_\mu, \bar{\nu}_\mu$	$\sim 10^3$	1000	$\sim 10^{-3}$
Atmospheric	$\nu_{\mu,e}, \bar{\nu}_{\mu,e}$	$\sim 10^3$	10^4	$\sim 10^{-4}$
Sun	ν_e	~1	1.5 x 10^8	$\sim 10^{-11}$

Table 1.1: Sensitivity of different oscillation experiments. [29]

Parameter	Value
$\sin^2(2\theta_{12})$	$0.861^{+0.026}_{-0.022}$ [30]
Δm^2_{21}	(7.59 ± 0.21)x$10^{-5} eV^2$ [30]
$\sin^2(2\theta_{23})$	> 0.92 [31]
Δm^2_{32}	$(0.00243 \pm 0.00013) eV^2$ [32]
$\sin^2(2\theta_{13})$	$0.092 \pm 0.016(stat.) \pm 0.005(syst.)$ [33]

Table 1.2: Latest mixing parameter measurements. [29]

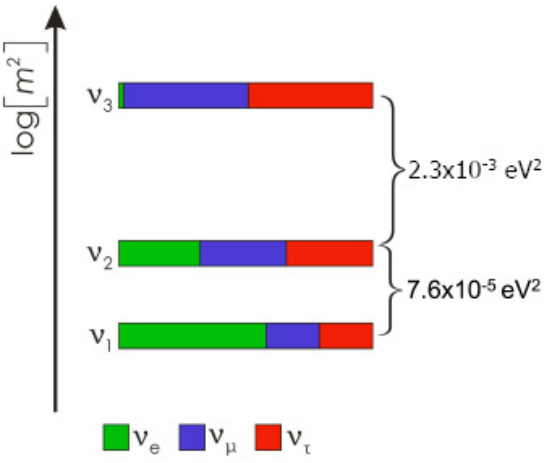

Figure 1.3: Graphical representation of contibution of flavour states to the mass states and their relative mass differences squared.

1.3.4.1 Solar Neutrinos

Solar neutrinos originate from fusion reactions inside the sun. Various fusion products are made in the sun depending on temperature but the processes which produce the greatest abundance of neutrinos are those of the pp chain fission products (Fig.1.4) and the CNO cycle (Fig.1.5).

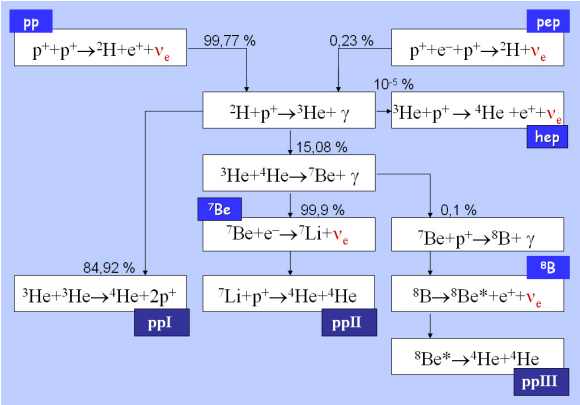

Figure 1.4: pp fission chain and branches. [34]

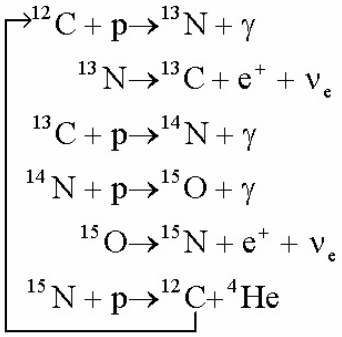

Figure 1.5: CNO fission cycle. [35]

Both of these processes produce electron neutrinos (ν_e) at various fluxes and energies shown in Fig.1.6.

These then travel the 149.60x10^9 m between the sun and the earth where a small proportion interact with large detector volumes of materials like chlorine or germanium or water. Interactions with these volumes usually produce neutrino-stimulated beta- events (Eqn.1.11), where either the emitted electron or the new element are used for event determination. This of course led to the previously mentioned solar neutrino problem where later neutral current, charged current and elastic scattering interactions in deuterium (D_2O) were used to measure not only electron neutrinos from the sun but neutrinos of other flavours at the same time to prove oscillation of solar electron neutrinos (Eqn.1.12).

$$ {}^{Z}_{A}X + \nu_e \rightarrow {}^{Z+1}_{A} X + e^- \tag{1.11} $$

$$ \begin{aligned} ChargedCurrent &= d + \nu_e \rightarrow p + p + e^- \\ NeutralCurrent &= d + \nu_x \rightarrow n + p + \nu_x \\ ElasticScattering &= \nu_x + e^- \rightarrow \nu_x + e^- \end{aligned} \tag{1.12} $$

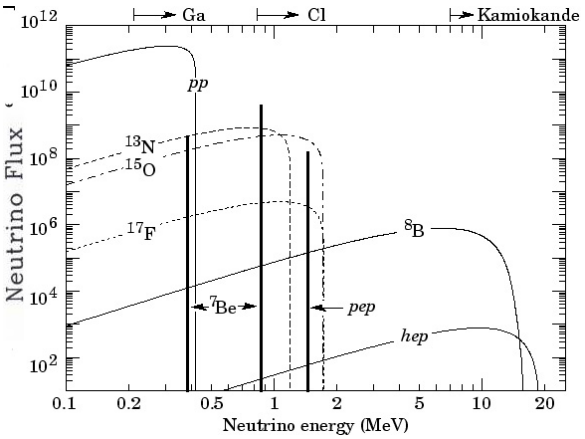

Figure 1.6: Solar neutrino energies and fluxes. [36]

1.3.4.2 Atmospheric Neutrinos

Atmospheric neutrinos originate from charged particles like cosmic rays interacting with our upper atmosphere at high energies. These mainly contain particles like protons which collide with oxygen and nitrogen molecules of our atmosphere. The interaction causes an air shower where the original proton collision will usually produce mesons of the form of positive and negative pions and kaons, that then decay to muons and muon neutrinos and then possibly electrons and electron neutrinos. These particles then reach the planet's surface where we can detect them.

The majority of neutrinos produced in the atmosphere are muon neutrinos and anti-neutrinos (ν_μ,$\overline{\nu}_\mu$) but there are also electron neutrinos and anti-neutrinos (ν_e,$\overline{\nu}_e$). The relative proportions of these are about 2 to 1 respectively due to the processes by which they are formed (Eqn.1.13) [37].

$$\pi^\pm \rightarrow \mu^\pm + \nu_\mu(\overline{\nu}_\mu) \rightarrow e^\pm + \nu_e(\overline{\nu}_e) + \nu_\mu(\overline{\nu}_\mu) \tag{1.13}$$

Detectors usually deep underground in mines can detect the abundance of neutrinos and their oscillation in the form of deficits. These deficits are due to their oscillation over the vertical distance between the atmosphere where the neutrinos are made and the earth's surface (roughly 15km). Also any neutrinos on the other side of the planet that are produced in the atmosphere will also be detected as they transverse not only the atmosphere's thickness whilst oscillating but also the thickness of the earth (roughly 13,000km). Unlike fixed baseline experiments of L and E are not fixed but inferred from measurements of neutrino rate as a function of angle. Detection of these neutrinos can be done, as with most neutrinos, with water Cherenkov techniques or liquid scintillator or iron calorimeter etc.

1.3.4.3 Artificial Neutrinos

There are two major sources of artificial neutrinos, nuclear reactors and particle accelerators. Nuclear fission reactors work by breaking ^{235}U atoms (by neutron impact) into smaller atoms and in the

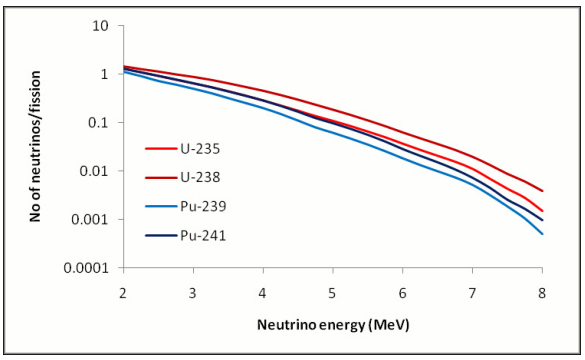

Figure 1.7: Fission neutrinos energy versus flux normalised to one fission event. [38]

process releasing more neutrons and lots of energy. However these smaller fragment atoms are generally unstable as they carry excess neutrons, as are the initial uranium atoms. Because of this atomic instability they undergo radioactive decays including that of beta minus decay which produces anti-electron neutrinos. The main isotopes responsible for these anti-neutrino emissions are the decay products of ^{235}U, ^{238}U, ^{239}Pu and ^{241}Pu. The number of neutrinos produced per fission reaction averages out to a very stable 6 which means fluxes are very reliable. An average sized reactor therefore would produce about 10^{20} neutrinos a second. The energy range of these neutrinos is somewhat dependent on the depletion of the fuel inside but generally peaks around the 2 - 4 MeV range with some emissions up to 8 MeV (see Fig.1.7) [38].

Due to the lower energy of the emitted neutrino momenta, base lines for neutrino oscillations are relatively shorter and near detectors are needed to monitor the initial reactor output of neutrinos.

Particle accelerators can be made to produce neutrino beams too. Usually this is done by first accelerating protons and then firing them at a fixed target. Interaction with the fixed target produces secondary pions and kaons and a magnetic field is used to select the preferred charge pions (negative for anti-neutrinos, positive for neutrinos). The applied field is also used to focus the output into a beam which is then sent into a decay volume. Pions have a lifetime of 0.026 μs before they decay to muons and muon neutrinos, whilst muons have a life time of 2.2 μs. Therefore the decay volume is constructed such that most of the pions can decay without the muons decaying as well. Once this has occurred the beam then hits a beam dump that stops all of the particles other than the neutrinos or anti neutrinos and thus a muon neutrino beam is created. Muon detectors can also be used to monitor the beam but usually for oscillation experiments a near and far detector are used again to determine the appearance and disappearance between them. Base lines can be very long through the earth.

The next step for neutrino beam experiments is to build a neutrino factory with a muon storage ring that allows the muons to decay into electrons and electron neutrinos. This will give a much cleaner production with electron neutrinos produced with very well understood energies and a mixed beam of electrons neutrinos and muon antineutrinos or vice versa depending on muon charge [38].

1.3.5 Mass Differences and Hierarchies

The experimentally found mass differences of the mass eigenstates and the mixing angles in the table above give us a picture of the levels of mixing and the relative masses of the mass eigenstates. However these measurements still leave us with two big unknowns as no information as to the absolute mass scale or the hierarchical size of the masses is obtained by looking at flavour oscillations. This leads to two possible scenarios, the "normal hierarchy" where ν_1 is the lightest and ν_3 is the heaviest or the "inverted hierarchy" where ν_3 is the lightest and ν_1 the heaviest.

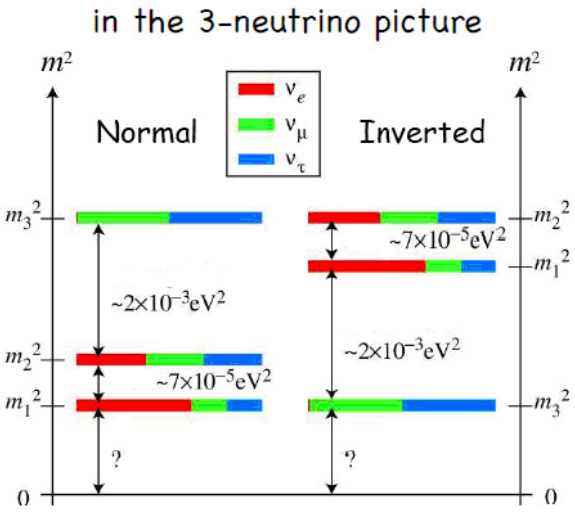

Figure 1.8: Diagram of possible neutrino hierarchies.

1.3.6 Mass Mechanisms

Two forms of mass Lagrangian can be constructed to define neutrino masses. One is the Dirac form which uses the standard model Higgs-lepton Yukawa coupling. This couples the left and right handed chiral flavour fields together and allows for sterile neutrinos. The other, the Majorana form, uses only one chiral field (left or right) and can construct and show that the charge conjugate is equivalent to a projection of opposite chirality. This gives rise to a massive Majorana neutrino. The combination of these two forms can provide an explanation for the small masses seen using the see-saw mechanism, which predicts that a massive neutrino must exist.

1.3.6.1 Dirac

The Dirac mass Lagrangian is constructed of 4 independent fields (ν_L, ν_R, $\overline{\nu_L}$, $\overline{\nu_R}$) and can be written as:

$$-m_D(\overline{\nu}_L\nu_R + \overline{\nu}_R\nu_L) \tag{1.14}$$

$$\mathcal{L}^{D}_{mass} = -\overline{\nu_R} m_D \nu_L + H.c \tag{1.15}$$

where m_D is the complex non diagonal mass matrix, H.c stands for the hermitian conjugate and ν_R and ν_L are the chirally left-handed and right-handed neutrino flavour fields expressed as

$$\nu_R = \begin{pmatrix} \nu_{eR} \\ \nu_{\mu R} \\ \nu_{\tau R} \end{pmatrix} \quad , \quad \nu_L = \begin{pmatrix} \nu_{eL} \\ \nu_{\mu L} \\ \nu_{\tau L} \end{pmatrix} \tag{1.16}$$

The mass term m_D allows for conservation of lepton number whilst coupling the fields and can be easily expanded to greater than 3 flavours if required. For the ordinary SM the doublet state ν_L is only present and the neutrino has no mass, so the sterile singlet was included ν_R (because no weak interactions, only interactions with gravity, except due to mixing) The transition is $\Delta \mathrm{I} = \frac{1}{2}$, where I is the weak isospin. The mass requires SU(2) breaking and is generated by a Yukawa coupling.[39, 40]

1.3.6.2 Majorana

The Majorana Lagrangian mass term is written as:

$$-\frac{1}{2} m^{L}_{M} (\overline{\nu}_L \nu^{c}_{L} + \overline{\nu}^{c}_{L} \nu_L) - \frac{1}{2} m^{R}_{M} (\overline{\nu}_R \nu^{c}_{R} + \overline{\nu}^{c}_{R} \nu_R) \tag{1.17}$$

$$\mathcal{L}^{m}_{mass} = -\frac{1}{2} \left(\overline{\nu_L}\right)^{c} M_M \nu_L + H.c \tag{1.18}$$

where M_M is the Majorana mass matrix, ν_R and ν_L are the right and left handed fields which are not independent in this case and are linked via the following equation

$$\nu_R = C \overline{\nu_L}^{T} = \nu^{c}_{L}. \tag{1.19}$$

Mathematically, charge conjugation of the field, where C is the charge conjugation operator, can be expressed as:

$$\nu^{c} = C\nu = i\gamma^2 \nu^{*} \quad , \quad \overline{\nu}^{c} = \nu^{T} i\gamma^2 \tag{1.20}$$

where T denotes the transpose and C obeys

$$C^{T} \gamma_\alpha C^{-1} = -\gamma_\alpha C^{T} \tag{1.21}$$

As can be seen, the Lagrangian can be constructed out of only one chirality neutrino field (left or right). Very importantly however Eqn.1.19 shows that the Majorana mass Lagrangian is built out of only 2 independent fields (ν_L, $\overline{\nu^{c}_{L}}$) as the charge conjugate (antiparticle) leaves the field unchanged.

This of course only works if the particle itself is neutral in charge as the neutrino is. It also allows for breaking of lepton number by $\Delta L = \pm 2$

1.3.6.3 The See-Saw Mechanism

The following is written with reference to [41] where a more in-depth description can be seen.

The see-saw mechanism tries to explain the relatively small mass (small Higgs coupling) observed with neutrino flavours by combining both the Dirac and Majorana mass mechanisms into a single Lagrangian

$$\mathcal{L}_{see-saw} = \mathcal{L}_D + \mathcal{L}_M \tag{1.22}$$

which using the Eqn.1.14 and Eqn.1.17 looks like this

$$\mathcal{L}_{see-saw} = -\frac{1}{2} m_M^L (\overline{\nu}_L \nu_L^c + \overline{\nu}_L^c \nu_L) - \frac{1}{2} m_M^R (\overline{\nu}_R \nu_R^c + \overline{\nu}_R^c \nu_R) - m_D (\overline{\nu}_L \nu_R + \overline{\nu}_R \nu_L) \tag{1.23}$$

which can be simplified and expressed in terms of a mass matrix $\mathcal{M}$

$$\mathcal{L}_{see-saw} = -\frac{1}{2} (\overline{\nu}_L \overline{\nu}_R^c)(m_M^L \nu_L^c + m_D \nu_R + m_D \nu_L^c + m_M^R \nu_R) + H.c \tag{1.24}$$

$$\mathcal{L}_{see-saw} = -\frac{1}{2} (\overline{\nu}_L \overline{\nu}_R^c) \begin{bmatrix} m_M^L & m_D \\ m_D & m_M^R \end{bmatrix} \begin{pmatrix} \nu_L^c \\ \nu_R \end{pmatrix} + H.c \tag{1.25}$$

$$\mathcal{L}_{see-saw} = -\frac{1}{2} (\overline{\nu}_L \overline{\nu}_R^c) \mathcal{M} \begin{pmatrix} \nu_L^c \\ \nu_R \end{pmatrix} + H.c \tag{1.26}$$

$$\mathcal{M} = \begin{bmatrix} m_M^L & m_D \\ m_D & m_M^R \end{bmatrix} \tag{1.27}$$

where m_D are the Dirac mass components and m_M^L, m_M^R are the right handed and left handed chiral Majorana mass components.

If we assume that the weak eigenstates ν_L and ν_R which stem from a mixing of Majorana and Dirac mass terms are in fact linear combinations of mass eigenstates ν and N that couple directly to the Higgs field via a purely Majorana mass term with no Dirac mass term, then this would give the following Lagrangian for the neutrino mass.

$$\mathcal{L}_{\substack{mass \\ terms}} = -\frac{1}{2} (\overline{\nu} \overline{N}) \tilde{\mathcal{M}} \begin{pmatrix} m_\nu \\ M \end{pmatrix} + H.c \tag{1.28}$$

where

$$\tilde{\mathcal{M}} = \begin{bmatrix} m_\nu & 0 \\ 0 & M \end{bmatrix}. \tag{1.29}$$

Essentially in this scenario we have 2 new fields for which we can say one of them ν has no Higgs coupling (therefore $m_\nu = 0$) whilst the other N does. This helps as it's easier to explain no coupling than an extremely weak coupling. From here we can say that a mixing of these mass eigenstates to form the weak eigenstates we observe is just a rotation of basis vectors and diagonalising, for which we can use eigenvalue equations to find the relation of the weak masses to the mass states. If this mixing is small of course it will lead to one small mass state and one large as can be seen in the following. The eigenvalue equation is the following

$$(m_M^L - \lambda)(m_M^R - \lambda) - (M_D)^2 = 0 \tag{1.30}$$

which gives us the eigen values of

$$\lambda_{1,2} = \frac{1}{2}(m_M^R +, m_M^L) \pm \sqrt{(m_M^R + m_M^L)^2 - 4(m_M^R m_M^L - m_D^2)} \tag{1.31}$$

$$\lambda_1 = m_\nu = 0 \quad , \quad \lambda_2 = M = m_M^R + m_M^L \tag{1.32}$$

Then, using these back in Eqn.1.30 we get.

$$m_M^R m_M^L = m_D^2 \tag{1.33}$$

This is where the see-saw mechanism gets its name as it can be seen that for a fixed value of the Dirac mass m_D that as the right-handed or left-handed Majorana mass is increased the other will be decreased and vice versa. The mass eigen vector fields become

$$\begin{aligned} N &= (\nu_R + \nu_R^c) + \tfrac{m_D}{m_M^R}(\nu_L + \nu_L^c) \\ \nu &= (\nu_L + \nu_L^c) - \tfrac{m_D}{m_M^R}(\nu_R + \nu_R^c) \end{aligned} \tag{1.34}$$

therefore (using Eqn.1.34 and Eqn.1.33)if m_M^R is very big then N is almost entirely ν_R and vice versa and so is very heavy and effectively sterile. Conversely m_M^L is very small and ν is almost entirely ν_L or ν_L is almost entirely the weightless ν giving rise to the sought property of a very weak Higgs coupling (mass) neutrino state. It is therefore obvious from Eqn.1.33 that

$$\mathcal{M} \approx m_M^R >> m_D >> m_M^L \approx 0 \tag{1.35}$$

1.3.7 Direct Mass Measurements

As seen in in Sec.1.3.4, oscillation measurements can only produce information of the mass squared differences between neutrino mass states and not the neutrino's absolute mass directly. There are however some experimental techniques that could measure the absolute mass scale of the neutrino and they are summarised below.

1.3.7.1 Tritium Decay

One method of determining the mass of the neutrino is to use the kinematics of beta decay (see sec.2.1). The difference in energy of the final state and initial state of an atom is made up of the rest mass of both the electron and neutrino and their momenta, which give rise to a distribution of electron total energies. However the maximum energy the electron can obtain depends on the mass of the neutrino as the most energetic electron possible from a beta decay will be given by Eqn.1.36

$$E_e = (M_i - M_f) - m_0^\nu \tag{1.36}$$

where E_e is the electron's total energy, M_i and M_f are the initial and final energy of the decaying atom respectively and m_0^ν is the rest mass of the neutrino.

So therefore the mass of the neutrino will distort the end of the electron energy spectrum as its deficit from the (Q_β) value will be the mass of the neutrino. Of course these high electron energy events are rare and so specific beta decay isotopes are chosen for experimentation, like tritium.

Tritium is an isotope of hydrogen ($^3_1$H) with 2 neutrons and can undergo a beta- decay to the following

$$^3_1H \rightarrow ^3_2 He^{+1} + e^- + \overline{\nu}_e \tag{1.37}$$

The half-life of this decay is roughly 12.32 years and it has a very small Q_β value of 18.6 keV. These properties make it an ideal source for neutrino mass measurements as a relatively short life time means lots of events so high statistics, and a small Q_β means that the decay spectrum has less phase space and so more decays fall in the higher energy region. Also its molecular structure is simple enough for theoretical calculations to be able to determine the energy spectrum with a high level of confidence.

However even with tritium only one out of every 10 million decays emits an electron in the last 100 eV of the beta decay spectrum where the divergence of the spectra caused by neutrino masses is starting to become visible for a neutrino mass of 30 eV or higher. Therefore for a neutrino mass of 1 eV or less the high enough energy event rate is even less than 1 in a trillion (Fig.1.9).

This is because the most probable beta decay events are when the electron and neutrino have roughly equal energy. Therefore in order to select these high energy events and filter out the lower ones we are not interested in, the detectors are built with an electric potential that emanating

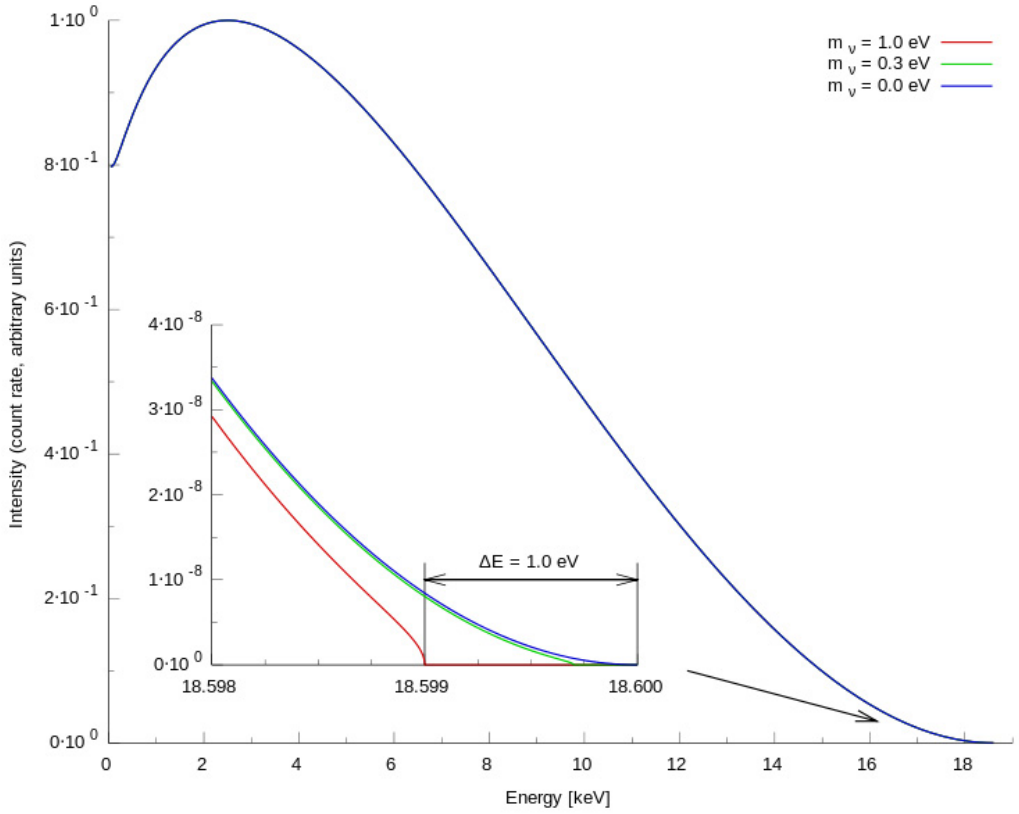

Figure 1.9: Distortion in the tail of a tritium beta decay electron energy distribution. [42]

electrons must overcome so only the highest energy ones proceed. This is in the form of a spectrometer that bends the electron's path where ones only a few eV lower than the Q_β above can navigate through.

1.3.7.2 Cosmology

For more information about Cosmology's contributions to neutrino physics and the material for which this section was derived please refer to [43].

Within cosmology there may be ways of gathering useful information to help determine which hierarchy neutrinos follow and also the absolute mass scale of these neutrinos,

For instance one way cosmology can help is by looking at the free streaming effect of neutrinos, the results of the Cosmic Microwave Background (CMB) and large-scale structure experiments and by using theoretical models they can provide bounds for the sum of neutrino mass eigenstate masses i.e. $\Sigma = m_1 + m_2 + m_3$. The current bounds for this quantity are $0.05eV \geq \Sigma \leq 2eV$, but are very model dependant.

Once Σ is better constrained then it could be used to measure the mass splitting $\Delta = m_3 - m_1$ by substituting it into the matter power spectrum of large scale structure. This, as can be seen below

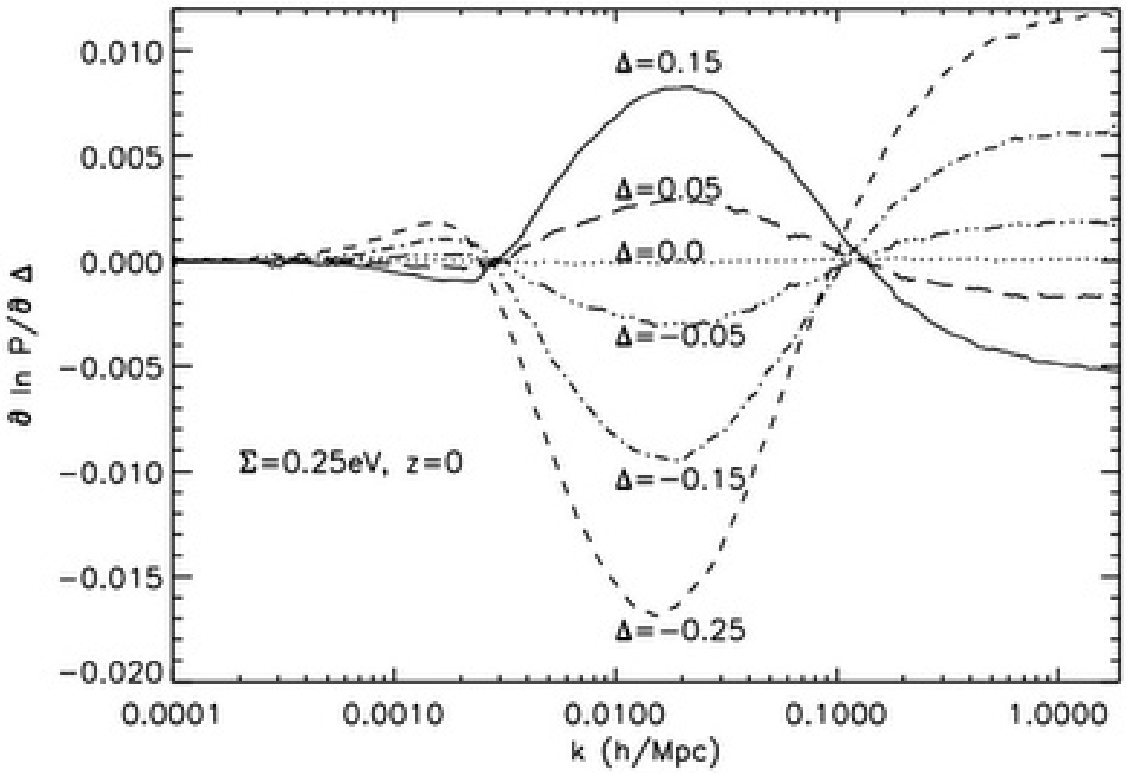

Figure 1.10: Demonstration of the effect of Δ on the matter power spectrum for a given Σ. [43]

(Fig.1.10), greatly affects the distribution, which could hopefully be verified by observation, thus determining both the magnitude and sign of Δ. By knowing Δ, we can obtain both the absolute mass and direction of hierarchy (Fig.1.11).

The matter power spectrum P(k) describes the difference in density between the local space and the mean universe as a function of scale. It is the Fourier transform of the matter correlation function. At large scales cosmic expansion is linear where gravity and cosmic expansion compete. At small scales gravitational collapse is non-linear. However the determinations of any quantities are heavily model dependant.

1.3.7.3 Summary

Whilst both beta decay kinematic experiments and cosmology can make measurements / limits of the absolute neutrino mass, they cannot probe the fundamental nature of the neutrino or make direct measurements of the hierarchy of neutrino states. Oscillation experiments can probe mass mixing parameters of the mixing matrix and soon the hierarchy, but not fundamental nature and absolute mass scale only the mass differences. However a further direct mass measurement technique exists called double beta decay that is sensitive to all 3 of the fundamental questions of the neutrino, its absolute mass, its hierarchy and importantly its fundamental nature. This is the technique used in this thesis and is explored in depth in Section 2. Double beta decay as a process cannot exist unless

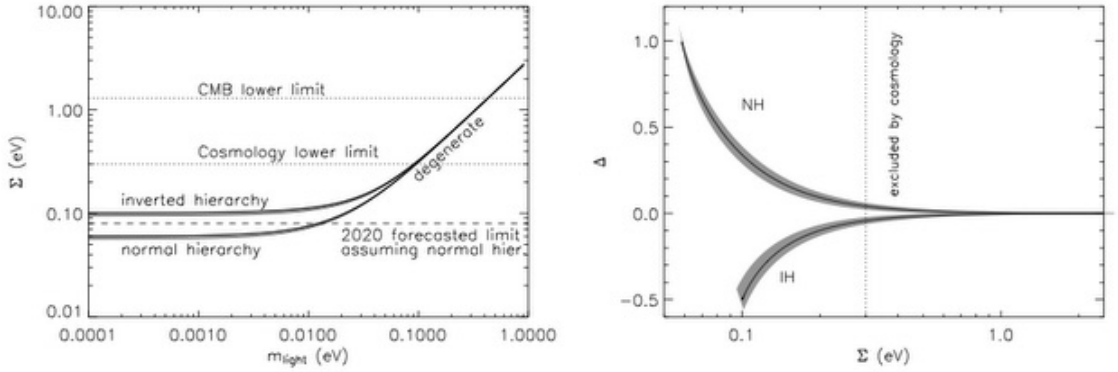

Figure 1.11: Limits of hierarchy and lightest mass predictions on Σ and Δ. [43]

the neutrino is Majorana, therefore any events observed will determine this property, If hierarchy is inverted and no events are seen in the allowed range, it will also give a strong indication that the neutrino is Dirac in nature. The half-life of double beta decay is intimately associated with the neutrino mass and so measurement of this if the process exists gives us a direct mass measurement. Also the effective mass measured from the half-life has 2 distinct ranges of possible values for inverted and normal hierarchies so a determination of the mass in a divergent region will give evidence for the neutrino's hierarchy. Therefore the combined ability to answer all of the three unanswered neutrino questions makes double beta decay a very interesting and important prospect for study.

A comparison of the sensitivity to neutrino fundamental properties for each type of neutrino experiment is summarised in Table.1.3 and the current best limits for the associated neutrino masses for each are given in Table.1.4.

Experiment type	Absolute mass	Fundamental nature	Mass hierarchy	Mixing parameters	Dirac cp	Majorana cp
Oscillations			✔	✔	✔	
Beta decay	✔					
Double beta decay	✔	✔	✔			✔
Cosmology	✔		✔			

Table 1.3: Neutrino properties addressed by different experimental approaches.

Experiment type	Measured parameter	value	confidence limit
Beta decay	$\langle m_{\nu_e} \rangle$	< 2.0 eV	95% [44, 45]
Double beta decay	$\langle m_{\beta\beta} \rangle$	< 0.3 eV	90% [46]
Cosmology	$\sum m_i$	< 2 eV	95% [47, 48]

Table 1.4: Existing constraints on absolute neutrino mass.

Chapter 2

Double Beta Decay Theory

2.1 Single β Decay

Standard beta decay can occur in three different forms when a nucleon decays to another type along with the emission of a neutrino. They are classified by either the emission of an electron (β^-), emission of a positron (β^+) or an electron capture (EC) that occurs with this process.

β^- decay is the process by which a neutron decays to a proton whilst emitting an electron and an anti-electron neutrino.

$$n \rightarrow p + e^- + \overline{\nu_e} \tag{2.1}$$

β^+ decay is the process by which a proton decays to a neutron whilst emitting a positron and an electron neutrino.

$$p \rightarrow n + e^+ + \nu_e \tag{2.2}$$

Electron capture (EC) occurs when a nucleus does not possess enough energy to create and emit a positron and therefore instead captures an electron from a low orbital (usually K shell) this leaves a hole which is filled by a higher orbital electron. This cascade transition causes an accompanying emission of an X-ray and/or Auger electrons (liberated higher shell electrons).

$$e^- + p \rightarrow n + \nu_e \tag{2.3}$$

As all three processes are accompanied by emission of particles and loss of energy, beta decay is therefore only possible if the parent nucleus has a greater atomic mass than the final nucleus.

ie.

$$M(A, Z) > M(A, Z + 1) \tag{2.4}$$

where M is the atomic mass and A and Z represent the proton number and mass number

respectively.

2.2 The Semi Empirical Mass Formula

The semi empirical mass formula (SEMF) is:

$$m = Zm_p + (A - Z)m_n - E_B \tag{2.5}$$

where m is the semi empirical mass and E_B is the binding energy determined by the formula

$$E_B = a_V A - a_S A^{2/3} - a_C \frac{Z(Z-1)}{A^{1/3}} - a_A \frac{(A-2Z)^2}{A} + \delta(A, Z) \tag{2.6}$$

where:

a_V - Is the volume term for the nucleus of the atom. It's related to the inter-nucleon strong force binding so is proportional to A.

a_S - Is the surface term which concerns correcting the strong force of the nucleons on the nucleus's surface due to a reduced number of nearest neighbours so is proportional to $A^{2/3}$.

a_C - Is the Coulomb or electrostatic term, which concerns the electrostatic repulsion between protons in the nucleus

a_A - Is the asymmetry term that is proportional to the relative number of protons and neutrons in the nucleus and is based in the Pauli exclusion principle, as, being fermions, the more neutrons and protons present increases the energy level at which they exist

$\delta(A, Z)$ - Is the pairing term which concerns the effect of spin-coupling. The Pauli exclusion principle dictates that if one has an even number of protons (or neutrons) then equal number of spin up and down protons (or neutrons) exist. The largest binding energy therefore exists when an even number of both protons and neutrons are present.

$$\delta(A, Z) = \begin{cases} +\delta_0 & Z, N \text{even } (A \text{ even}) \\ 0 & \text{A odd} \\ -\delta_0 & Z, N \text{ odd } (A \text{ even}) \end{cases} \tag{2.7}$$

where $\delta_0 = \frac{a_P}{A^{3/4}}$

This formula gives rise to parabolic curves for a fixed mass number (A) and different proton number (Z). For an odd A one curve exists whereas for even nuclei the pairing term gives rise to a splitting which produces two curves which can be transitioned between by a beta decay process.

From the curves we can see that transitions from Z to $Z + 1$ are caused by β^- decay but only when the initial state is of higher energy than the final state. Transitions from Z to $Z - 1$ are caused by either β^+ or EC depending on whether the energy difference from the initial to final state is big enough to produce a positron or not, but as with β^- the initial state must be of higher energy than the final state.

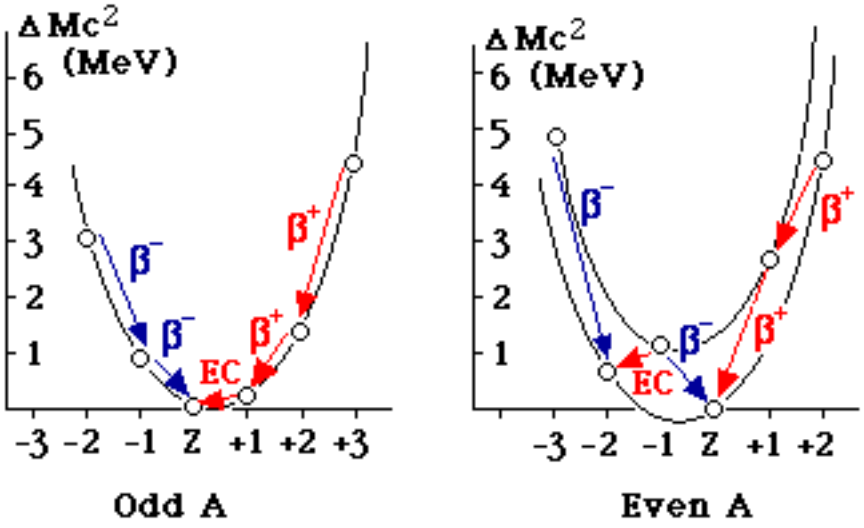

Figure 2.1: Deficit from the SEMF showing the effect of even and odd A and the splitting of the pairing term. [49]

2.3 Double Beta Decay

2.3.1 Two Neutrino Double Beta Decay

Double beta decay is a second-order weak semi-leptonic process. There are actually four different types of double beta decay process, where 2 single beta decay processes occur simultaneously. They are; double electron capture, double beta plus decays, a simultaneous electron capture and a beta plus decay and double beta minus decay. Double beta minus is the sole focus of this thesis and is referred to as double beta decay henceforth. In two neutrino double beta (minus) decay ($\beta\beta2\nu$) there is a spontaneous decay of two neutrons to 2 protons accompanied by the emission of 2 electrons and 2 anti-electron neutrinos (ie. equivalent to 2 β^- decays, fig.2.2). Two-neutrino double beta decay is a standard model allowed electroweak process that conserves both electric charge and lepton number.

$$(A, Z) \rightarrow (A, Z+2) + 2e^- + 2\overline{\nu_e} \tag{2.8}$$

where Z is the proton number and A is atomic mass number.

$\beta\beta2\nu$ can only occur in even even nuclei. The pairing term splitting in certain nuclei causes a situation in which a single beta decay is energetically unfavourable as the final state would be of higher energy than the initial state. However a double beta decay is possible.

In Fig.2.3 a β^- transition from $(a) \rightarrow (b)$ is not allowed due to the energy of $(b) > (a)$. However a double beta decay ($\beta\beta2\nu$) can occur from $(a) \rightarrow (c)$. On the right an example of energy levels involved in a $\beta\beta2\nu$ is shown where the intermediate single beta decay is not allowed as the $Z+1$ state is higher in energy than the initial state. $Q_{\beta\beta}$ is defined as the energy difference between the initial and final states.

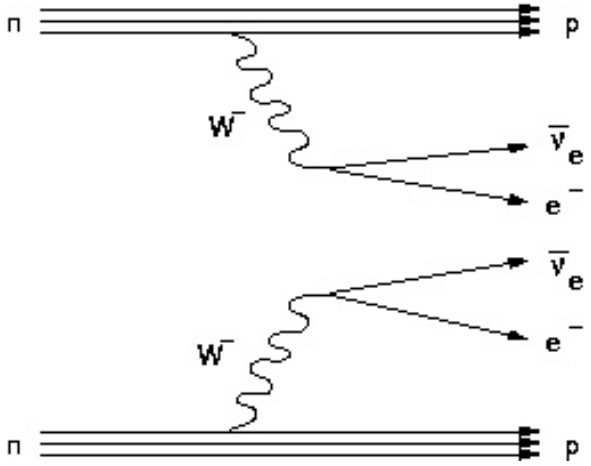

Figure 2.2: Two neutrino double beta decay Feynman diagram. [50]

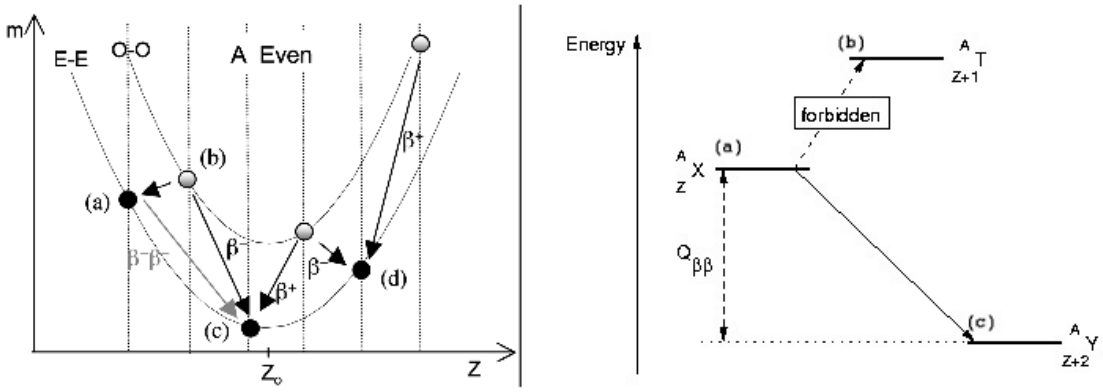

Figure 2.3: Double beta decay isotope mass curves[51] and transition energy levels. [50]

$$Q_{\beta\beta} = M(A, Z) - M(A, Z + 2) \tag{2.9}$$

where $M(A, Z)$ and $M(A, Z+2)$ are respectively the atomic masses of the initial and final nucleus.

This energy would be shared between the kinetic energy of the 2 electron products and the 2 anti-electron neutrinos produced. This gives rise to a continuous distribution of electron energies like that of single beta decay. The sum of the 2 electrons' energies gives the following distribution Fig.2.4.

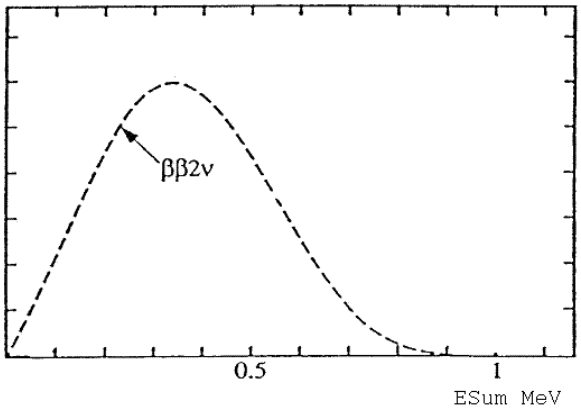

Figure 2.4: $\beta\beta2\nu$ summed 2 electron energy distribution. [52]

The rate of $\beta\beta2\nu$ is given by the following half-life equation

$$(T^{2\nu}_{1/2})^{-1} = G^{2\nu} \left|M_{2\nu}\right|^2 \tag{2.10}$$

where $G^{2\nu}$ is the phase space factor which can be calculated analytically and $M_{2\nu}$ is the nuclear matrix element (NME) which is theoretically determined but depends on the theoretical model used. Due to the NME being model dependant, direct measurement of the $\beta\beta2\nu$ half-life is important to tie down the model variables.

35 naturally occurring isotopes are capable of undergoing $\beta\beta2\nu$ decay, however 12 have been experimentally observed and measured due to $\beta\beta2\nu$ decay being a rare second order process. A list of them, their natural abundances, their $Q_{\beta\beta}$ values and measured half-lives is given below in Table.2.1.

2.3.2 Neutrinoless Double Beta Decay and Neutrino Mass

Neutrinoless double beta decay ($\beta\beta0\nu$) is a theoretical process that violates lepton number conservation. In the electroweak interactions of standard model (SM) all lepton flavours as well as total lepton numbers are conserved. However lepton number conservation is only an empirical assumption and has no implicit symmetry behind its existence, therefore it is possible for lepton conservation to be broken and pertinent to explore (sec.1.3.6). Oscillation experiments have already shown that

Isotope	Natural abundance (%)	$Q_{\beta\beta}(keV)$	Half-life (yr)
^{48}Ca	0.187	4271	$(4.2^{+1.3}_{-3.3})$x10^{19} [53]
^{76}Ge	7.61	2039	$(1.55^{+0.19}_{-0.15})$x10^{21} [54]
^{82}Se	8.73	2995	(9.6 ± 0.4)x10^{19} [55]
^{96}Zr	2.80	3350	(2.35 ± 0.30)x10^{19} [56]
^{100}Mo	9.63	3034	(7.11 ± 0.56)x10^{18} [55]
^{116}Cd	7.49	2802	$(2.9^{+0.4}_{-0.3})$x10^{19} [57]
^{128}Te	31.74	868	(2.5 ± 0.3)x10^{24}[58]
^{130}Te	34.08	2533	$(0.61^{+0.43}_{-0.49})$x10^{21} [59]
^{136}Xe	8.87	2459	(2.1 ± 0.2)x10^{21} [60]
^{150}Nd	5.6	3367	$(9.11^{+0.88}_{-0.85})$x10^{18} [61]
^{238}U	99.2745	1145	(2.0 ± 0.6)x10^{21} [58]

Table 2.1: Double Beta Decay Isotopes and $\beta\beta2\nu$ results.

mass differences exist between neutrino mass eigenstates and so it is not unreasonable to expect the possibility of lepton number breaking existing in some extension to the SM. This lepton number breaking would remove any restrictions to the neutrino non-zero Majorana masses after electroweak symmetry breaking. A possible theory is that at some high-energy scale the neutrino masses are generated. Motivation for this theory includes the properties of the light neutrinos including tiny masses, large mixings, and that neutrinos are both electrically neutral and fundamental unlike any other particle.[62]

In the process two neutrons decay to protons simultaneously and two electrons are released from the nucleus.

$$(A, Z) \rightarrow (A, Z + 2) + e_1^- + e_2^- \tag{2.11}$$

This process could occur if the 2 neutrinos that would normally be produced along with the electrons annihilate inside the nucleus and for that to happen the electron neutrino needs to be its own anti-particle $\nu_e = \overline{\nu_e}$ ie. a Majorana particle.

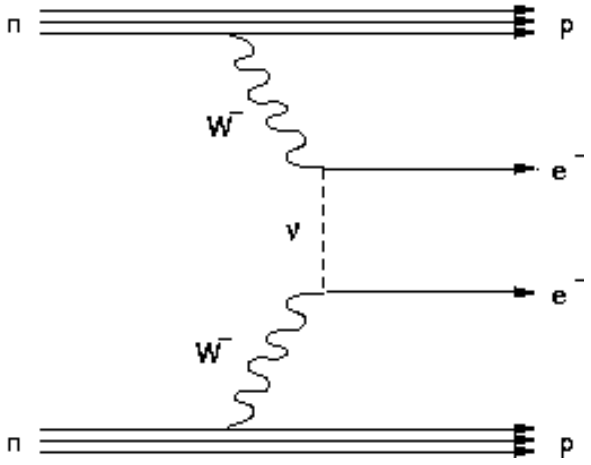

Figure 2.5: Neutrinoless double beta decay Feynman diagram. [50]

Neutrinoless double beta decay can be described by a virtual Majorana neutrino exchange via the interactions at the two vertices (fig.2.12). In this, at the first vertex a neutron decays to a proton and produces a left-handed electron and a virtual right-handed Majorana neutrino. This neutrino can then undergo a helicity flip which is rare.

This can only occur if the neutrino has mass as therefore its wave function is not solely made of a left handed neutrino state, but a mixture of left and right handed states given by the equation Eqn.2.12. This allows it to change from a right-handed neutrino at the first vertex to virtual left-handed neutrino. This virtual left-handed Majorana neutrino is absorbed by a neutron at the second vertex which decays to a proton and another left-handed electron.

$$|\nu_L\rangle + \frac{m_o}{m_e}|\nu_R\rangle\,. \tag{2.12}$$

The lack of neutrinos in the final state of $\beta\beta0\nu$ means that all the mass difference in the initial and final atoms must go into the rest mass of the electrons and their momentum. As these are fixed quantities then the electron kinetic energy sums will be constant at $Q_{\beta\beta}$ eq.2.9.

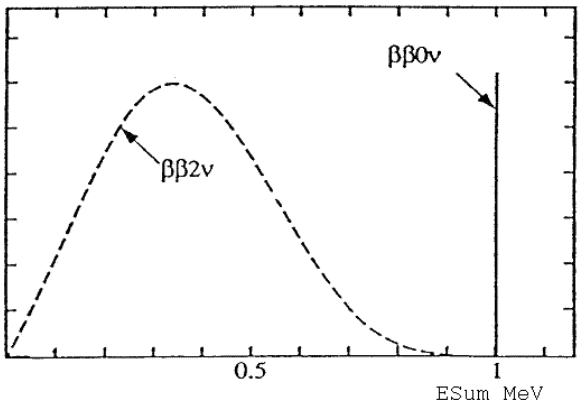

Figure 2.6: $\beta\beta0\nu$ 2 electron energy distribution. [52]

In Fig.2.6 as seen experimentally, the $\beta\beta0\nu$ signal will appear as a mono-energetic excess at the maximum of the $\beta\beta2\nu$ distribution (the $Q_{\beta\beta}$ value). Of course experimental uncertainties will broaden this peak and the relative rates of the two processes will cause the $\beta\beta0\nu$ to become hard to distinguish and determine.

The amplitude of the decay in this mode is proportional to the helicity flip, which is in itself proportional to the Majorana neutrino's mass. Therefore the probability is proportional to the helicity change squared and Majorana neutrino's mass squared. The rate and half-life are proportional to the mass squared of the neutrino.

There are many different mechanisms that exist to explain $\beta\beta0\nu$ but the most popular is that of light neutrino mass due to its connections with oscillation experiments and being the minimal scenario for Majorana nature. Some others are talked about and summarised later in Sec.2.3.3

The neutrinoless half-life equation for light neutrino mass is given in Eqn.2.13.

$$(T^{0\nu}_{1/2})^{-1} = G^{0\nu} \left|M_{0\nu}\right|^2 \langle m_{\beta\beta}\rangle^2 \tag{2.13}$$

where $\langle m_{\beta\beta}\rangle$ is the effective electron neutrino mass (a linear combination of the mass Eigen states whose coefficients are elements of the neutrino mixing matrix) and the nuclear matrix element

$$\langle m_{\beta\beta}\rangle = \textstyle\sum_i^N \left|U_{ei}\right|^2 e^{i\alpha_i} m_i \quad (\text{all } m_i \geq 0) \tag{2.14}$$

where U_{ei} is the 1st row of the neutrino mixing matrix and the α_i are unknown Majorana phases. This contains the usual 3-neutrino mixing angles plus a CP-violating phase, which appears in oscillations, and two additional Majorana phases, ϕ_1, ϕ_2. If tritium experiments can set limits on m_i and oscillation experiments provide U_{ei} data, then double beta decay results of $\langle m_{\beta\beta}\rangle$ can give access to measuring the Majorana phases ϕ_1 and ϕ_2.

The effective Majorana neutrino mass $m_{\beta\beta}$ as can be seen above depends on several phases and masses. Depending on the hierarchy of the neutrino mass eigenstates the value of the effective mass when plotted against the lightest neutrino mass eigenstate produces two distinct distributions for its value. In the normal (Fig.2.7) case, when m_1 is the lightest neutrino, a large range of effective mass values are allowed including zero in the most extreme and unfortunate case [63, 62]. Although even in this case $\beta\beta0\nu$ will still be allowed due to a contribution to the mass from the neutrino propagators mass term [64, 62]. However this would have a decay rate that is effectively impossible to measure. In Fig.2.7 we can see the limits on the lightest mass neutrino from cosmology's induced limit from the sum of neutrino flavour states and the claim for evidence on the effective neutrino mass from the Hidelberg-Moscow Experiment [65]. Also present are the proposed sensitivities of effective neutrino mass ($m_{\beta\beta}$) limits for both the latest 100kg active source experiments and the future 1 tonne endeavours. If the hierarchy is inverted with m_3 being the lightest neutrino eigenstate then the distribution is greatly affected below an effective neutrino mass of around 10^{-1} eV (Fig.2.8). The region above this is degenerate between both normal and inverted hierarchies and so if a signal was seen in this area the two could not be distinguished. However in the inverted case the effective neutrino mass cannot be zero and cannot be lower than approximately 10^{-2} eV. This divergence from the normal hierarchy for low mass Eigen state, gives us an opportunity to be able to determine the hierarchical nature of the neutrino if we can observe an effective neutrino mass low enough with an experiment of high enough sensitivity. As can be seen from Fig.2.8 SuperNEMO is one of the current generation of 100kg experiments in construction that could sample this possibly divergent region. Also if oscillation experiments are able to show that the hierarchy is definitely inverted and we see no signal with an effective mass of greater than 10^{-2} eV then it is a strong indication assuming this model of the neutrino being Dirac in nature not Majorana.

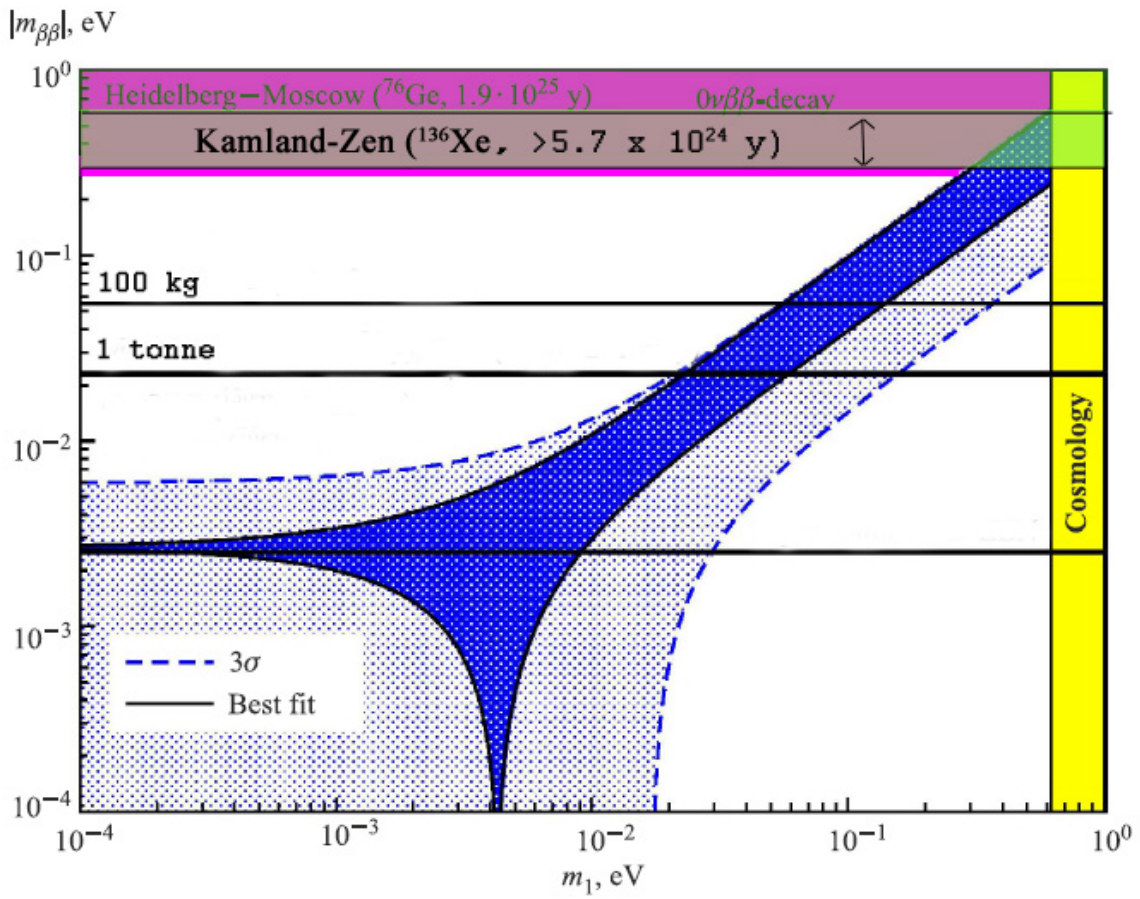

Figure 2.7: The effective Majorana neutrino mass $m_{\beta\beta}$ as a function of the lightest neutrino mass m_1 for the normal hierarchy of neutrino masses. [62]

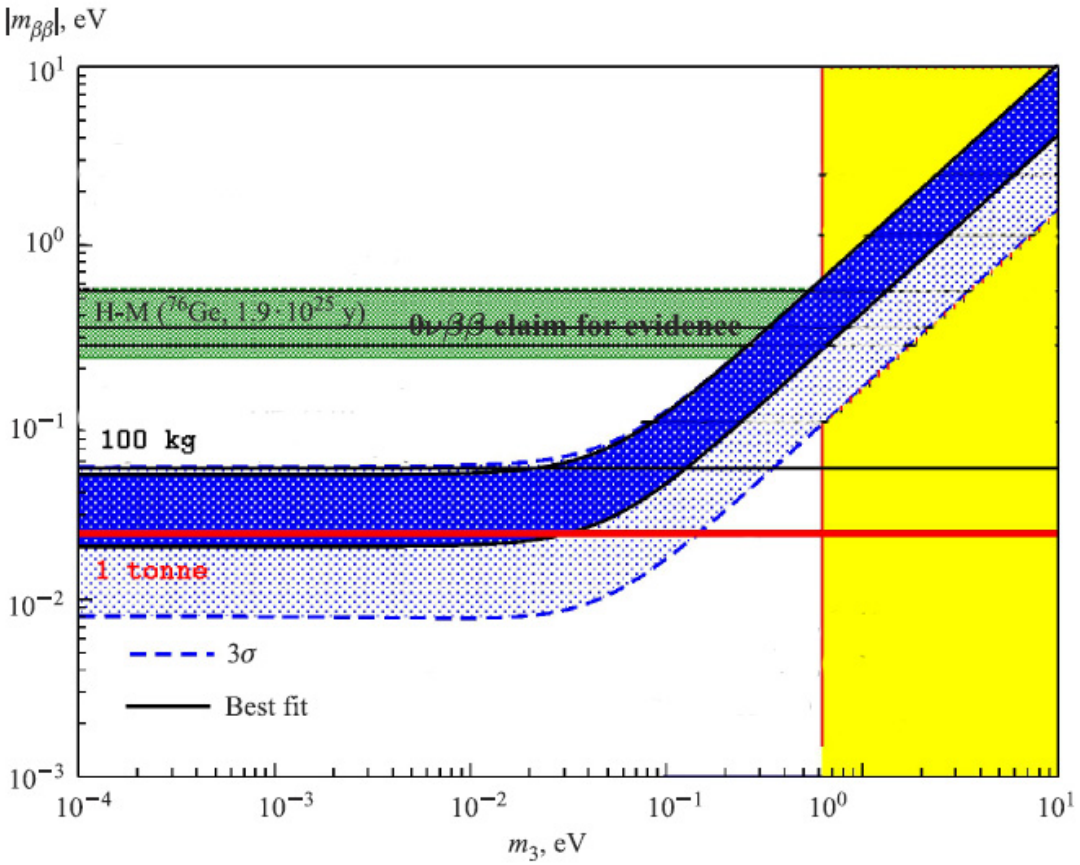

Figure 2.8: The effective Majorana neutrino mass $m_{\beta\beta}$ as a function of the lightest neutrino mass m_3 for the inverted hierarchy of neutrino masses. [62]

2.3.3 Exotic $\beta\beta0\nu$ Mechanisms

As mentioned above, the light neutrino mass mechanism for $\beta\beta0\nu$ is the most popular at the moment, due to it being the minimal scenario and it also gaining attention from its connection with neutrino oscillations. But even if $\beta\beta0\nu$ decay is observed, it will not mean that it is the dominant mechanism for the process. Lots of other mechanisms have been theorised and constructed to extend the SM and include Majorana neutrino masses, such as exchange of SUSY super partners with R-parity violating, leptoquarks, right-handed W-bosons or Kaluza-Klein excitations, but they will not be discussed in detail here. Some of the searches for these processes in neutrinoless double beta decay overlap with lepton number violating searches in the large hadron collider (LHC), namely the right-handed current mechanism and a heavy particle exchange mechanism. For the right handed current mechanism, the LHC will be looking for the right-handed W boson with a mass sensitivity of ≈2 TeV, whilst neutrinoless double beta decay experiments will look to measure η and λ. The relationship of these parameters is somewhat model-dependent and complementary in tying down the process, and upcoming generations of double beta decay experiments should be able to achieve similar sensitivities to the mechanisms giving half-life measurements of the order 10^{26} - 10^{27} years [66, 67].

Some neutrinoless double beta decay mechanisms cannot be separated from those of light neutrino exchange kinematically, these include heavy neutrino exchange and trilinear R-parity breaking mechanisms. There is a generic half-life equation to cover all of these Eqn.2.15.

$$(T^{0\nu}_{1/2})^{-1} = G^{0\nu} \left|M_{0\nu}\right|^2 \eta^2 \tag{2.15}$$

where $G^{0\nu}$ is the phase space term for $\beta\beta0\nu$ which is analytically calculable and which includes the fourth power of axial-coupling constant g_A and the inverse square of the nuclear radius R^{-2}. $M_{0\nu}$ is the neutrinoless NME for this transition which is model dependant and η represents the lepton violation parameter. η is a generalised term whose form varies for the mass mechanism used in the $\beta\beta0\nu$ calculation.

The most popular mechanism of light Majorana exchange (eqn.2.12) η becomes the effective neutrino mass $\langle m_{\beta\beta}\rangle$ and has already been covered 2.3.2. For right handed currents mechanism $\eta = \langle\lambda, (\eta)\rangle$ and for Majoron emission mechanism $\eta = \left\langle g_{\chi^0}\right\rangle$. For the most part my work will focus on these but some more are summarised below.

2.3.3.1 Right Handed Current

Right-handed electro weak currents mediated by a right-handed W boson go beyond the standard model's normal left-handed chiral states Lagrangian, but addition of a right handed or mixed state W boson into the Lagrangian allows for Majorana neutrinos to exist. As with the previous mechanism 2 electrons are still seen in the final state and the virtual neutrino can interact at the second vertex without needing a helicity flip. [68]

In this case η from the general half-life equation 2.15 becomes

$$\eta = \langle \lambda \rangle \tag{2.16}$$

where $\langle \lambda \rangle$ is a new physics parameter which represents the right chiral state coupling of the right-handed quarks to the right-handed lepton. This is the most often considered version however there is a similar coupling of the right-handed quarks to the left-handed leptons which is represented as $\langle \eta \rangle$.

Importantly for NEMO3 the angular distributions of the electrons emitted from a right-handed current double beta events are different from that of the above mass mechanism and so can be distinguished with appropriate angular studies if observed.

2.3.3.2 Majoron Emission

A Majoron is a light or massless singlet particle that has a coupling to the neutrino that is weak in nature. Originally the term "Majoron" was defined for a Goldstone boson, which was predicted from the breaking of global Baryon-Lepton symmetry [69], but is now not limited to that.

Many Majoron models have been proposed and are differentiated by their spectral index (n) which denotes the phase space dependence on the decaying particle's energy (see Eqn.2.17).

$$G^{0_\nu} \propto (Q_{\beta\beta} - E_{sum})^n \tag{2.17}$$

where E_{sum} is the emitted electron's kinetic energy sum and n is the spectral index. A table of spectral index values and their associated Majoron emissions can be seen in Table. 2.2

Spectral index number (n=)	Emission
1	Models with one Majoron emission
2	Models with "bulk" Majoron
3	Models with one or two massless lepton number carrying Majorons emissions
7	Models with two light Majorons emissions

Table 2.2: Table of spectral index relations to Majoron emissions. [70, 71, 72, 73, 74]

Each of these spectral indexes has their own unique 2 electron energy distribution due to the varied decay products. An example of these distributions can be seen in Fig.2.9

The η from generalised neutrinoless double beta decay half-life equation (eqn.2.15) for Majoron emission becomes the following.

$$\eta = \langle g_{x^0} \rangle \tag{2.18}$$

where $\langle g_{x^0} \rangle$ is the Majoron to neutrino coupling, which is of the order of the light neutrino mass over the symmetry breaking energy scale.

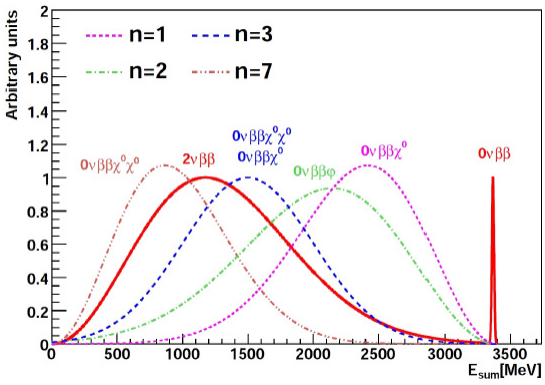

Figure 2.9: Example of summed 2 electron energy distributions for varied Majoron spectral indices. [75]

2.3.3.3 Heavy Neutrino Exchange

Heavy neutrino exchange is a similar mechanism to that of light neutrino exchange except that the assertion of a heavy mass Majoran state N_K exists much above that of the energy scale of $\beta\beta0\nu$ and that this is the mediator of the $\beta\beta0\nu$ process. In this case η from Eqn.2.15 has the form

$$\eta_N = \sum_{k}^{Heavy} |U_{ek}U_{ek}|\,\epsilon_k \frac{m_p}{M_k}[62] \tag{2.19}$$

where U_{ek} are left-handed neutrino mixing matrix elements, ϵ_k are CP-violating phases and m_p is the mass a proton. M_k is the heavy neutrino's mass (large when compared to average momentum eg. Mk >> 1 GeV).

The mediating particle is not the only difference from the light neutrino exchange mechanism, the effective transition operators are also local unlike the long ranged ones of light neutrino exchange. This is due to the neutrino propagators being contracted to points

2.3.3.4 R-Parity Breaking SUSY Mechanism

R parity is a quantum number that is defined as $R = (-1)^{2S+3B+L}$ where S, B, L are spin, baryon, and lepton numbers respectively. Normal non super symmetric particles have an R-parity of R = +1, their super symmetric partners R = -1. Some super symmetry (SUSY) models have a super potential that breaks R parity and it is from this that couplings which could form a mechanism for $\beta\beta0\nu$ arise.

Two types of $\not{R}_p$ SUSY mechanisms can give rise to this, an exchange of a heavy super symmetric particle (eg. gluino, neutralinos, selectron, and squarks) that is a short ranged mechanism [76, 77] or a longer ranged one that has an exchange of heavy squarks and light neutrinos [78] called squark-neutrino mechanism.

Assuming that gluino exchange dominates then η in Eqn.2.15

$$\eta_{\lambda'} = \frac{\pi\alpha_s}{6}\frac{\lambda'^2_{211}}{G_F^2 m^4_{\tilde{d}_R}}\frac{m_p}{m_{\tilde{g}}}\left[1+\left(\frac{m_{\tilde{d_R}}}{m_{\tilde{u_L}}}\right)^2\right]^2 \text{[62]} \tag{2.20}$$

where G_F is the Fermi constant,α_s is the gauge coupling constant and $m_{\tilde{u_L}}, m_{\tilde{d_R}}$ and $m_{\tilde{g}}$ are masses of the u-squark, d-squark, and gluino, respectively

2.3.3.5 Squark Mixing Mechanism

Unlike light neutrino exchange the $\beta\beta0\nu$ amplitude in the squark-neutrino mechanism does not vanish if the neutrino is of zero mass. This is due to the chiral structure of $\not{R}_p$ SUSY interactions. Instead exchange of a Majorana neutrino is proportional to the momentum of the exchanged virtual neutrino, of the same order as the Fermi momentum of the nucleus $p_F \approx 100$ MeV. This lack of a neutrino zero mass suppression is due to its derivation from $\not{R}_p$ SUSY interactions and not proportional to the Majorana mass term. In this situation η becomes.[78]

$$\eta_{\tilde{q}} = \sum_k \frac{\lambda'_{11k}\lambda'_{1k1}}{2\sqrt{2}G_F} sin2\theta^d_{(k)}\left(\frac{1}{m^2_{\tilde{d}_1(k)}} - \frac{1}{m^2_{\tilde{d}_2(k)}}\right) \text{[62]} \tag{2.21}$$

Where $d_{(k)}$ = d, s, b.

2.3.3.6 Resonant Neutrinoless Double Electron Capture

A recent theoretical mechanism for neutrinoless double electron capture ($0\nu\epsilon\epsilon$) has been proposed [79]. $0\nu\epsilon\epsilon$ is the process by which the nucleus of an atom theoretically undergoes simultaneous capture of two electrons mediated by a virtual neutrino similar to $\beta\beta0\nu$. If the final state is at an excited level and close in energy to that of the initial state oscillations and de-excitations might occur between the two states

$$(A, Z) \rightleftharpoons (A, Z \pm 2) \tag{2.22}$$

where A is the mass number and Z is the number of protons

So in this process back to back neutrinoless double beta decays followed by neutrinoless electron captures occur. However in this form of $\beta\beta0\nu$ the electrons never leave the atom instead they are kept as bound state electrons ie.

$$p + p + e^-_\beta + e^-_\beta \rightleftharpoons n + n \tag{2.23}$$

where p are protons, n are neutrons and e^-_β are electrons from the beta decay.

The signature of this process can be electromagnetic de-excitation of the unstable nuclei and the atomic shell with electron holes. There is also a possibility of resonance enhancement of the $0\nu\epsilon\epsilon$ decay. Near resonance then transition rate is described by the Breit-Wigner formula. This resonance enhancement is apparent when the initial and final states are very close in mass and so oscillation

evidence, if seen would give direction to uncover a process in which total lepton number violation can occur. The degeneracy is controlled by a parameter Δ which is given by the following formula.

$$\Delta = Q_{\epsilon\epsilon} - B_{2h} - E_{\gamma} \tag{2.24}$$

where $Q_{\epsilon\epsilon}$ is the Q-value (ie. the difference in mass between initial and final states), B_{2h} is the energy of excitation of the daughter atom and E_{γ} is the nuclear excitation energy.

The rate of this process is proportional to this degeneracy parameter due to it defining the energy difference of the initial and final states. This is given by

$$\Gamma^{\epsilon\epsilon} = |V_{\epsilon\epsilon}|^2 \frac{\Gamma}{\Delta^2 + \Gamma^2/4} = m_e \left|\frac{m_{\beta\beta}}{1eV}\right|^2 \left|\frac{V_{\epsilon\epsilon}}{m_{\beta\beta}}\right|^2 R \tag{2.25}$$

where Γ is the sum of partial widths from excited states of the $0\nu\epsilon\epsilon$ daughter nucleus, R is the resonance enhancement factor and $V_{\epsilon\epsilon}$ is the transition amplitude between the initial and final states through non conservative lepton number process. $V_{\epsilon\epsilon}$ is proportional to both $m_{\beta\beta}$ and the matrix element $M^{0\nu}$.

2.3.3.7 Distinguishing the $\beta\beta0\nu$ Decay Mechanisms

Determining which of the many possible mechanisms triggers the decay is a very difficult task even with a direct and definite determination of a $\beta\beta0\nu$ event. Also there may not be just a single mechanism but more than one at play. Regardless of which mechanism is observed it will provide solid evidence for lepton number non conservation and the Majorana nature of neutrinos [80], but more evidence is needed for mechanism determination. Generally it is agreed that observation of $\beta\beta0\nu$ decay in a single isotope would not be enough to determine the physics mechanism of its origin, so it is important to study many isotopes. Further disentanglement could be achieved if greater knowledge of the event is known. For instance in most detectors there is no information on the kinematics, angular distributions etc., as no tracking is performed. Use of tracking information could determine the presence of the right handed current mechanism, due to its unique kinematics, and experiments like SuperNEMO could provide this. Also use of branching ratios of decays to different excited states can be used to help determination as well as other quantities. However without tracking and more complicated detectors it is hard to observe the X-rays or transitions to excited states [81, 82, 83, 84, 85, 86].Therefore it is important to experiment with as many isotopes and scenarios as possible and it is important to have as accurate and reliable nuclear matrix elements for these processes as well, especially if interference between mechanisms is present.

However thanks to the Schechter-Valle theorem [87] if $\beta\beta0\nu$ decay is observed then whatever the dominant mechanism we can always add a higher order Majorana mass mechanism, so will have proof of its Majorana nature [80].

2.4 Nuclear Matrix Elements

By direct measurement of the half-life of $\beta\beta0\nu$ from experiments and knowledge of the associated NME, the effective neutrino mass can be either determined or new limits on its value/existence be found using Eqn.2.13. A single measurement of course cannot constrain both, but any advances in one can be used to help better constrain the other. However the accuracy of determination of the effective neutrino mass from the half-life is influenced by the degree of accuracy to which the nuclear matrix element (NME) $M_{0\nu}$ is known. Without a good level of accuracy it is impossible to reach qualitative conclusions about neutrino masses, the type of neutrino mass spectrum and CP violation.

The nuclear matrix element must be determined using nuclear structure theory due to the fact that no observables can give us direct measurements of this value in a model-independent way. Its calculation is not an easy task due to inclusion of ground and excited states of open shell nuclei considered in its determination. An accuracy of determination with an uncertainty of less than 30% is required to make assertions of neutrino mass spectrum and CP-violating phases of the neutrino mixing matrix. However observation of a $\beta\beta0\nu$ signal will in itself provide evidence that the neutrino is a Majorana particle.

In $\beta\beta2\nu$ the NME $M_{2\nu}$ (Eqn.2.10) is less easily calculable, owing to the many possible intermediate state contributions. It can be expressed as [88]

$$M_{GT}^{2\nu} = \sum_i \frac{\langle D \left|\vec{\sigma}.\vec{\tau}\right| i\rangle \langle i \left|\vec{\sigma}.\vec{\tau}\right| F\rangle}{E_i} \tag{2.26}$$

where F is the father nucleus and D is the daughter. The summation over i represents all the possible intermediate states and GT stands for Gamow-Teller.

For this calculation we need the wave function of the ground state of the father nucleus and the ground state and occasionally a few excited states of the daughter.

For $\beta\beta0\nu$, in this case the transition is mediated by terms that go beyond the standard model and the NME is a less complicated object than the $\beta\beta2\nu$ NME due to intermediate states and can be re-expressed as the following in the half-life equation. [88]

$$(T_{1/2}^{0\nu})^{-1} = G^{0\nu}\left(-\frac{M_F}{g_A^2} + M_{GT} + M_T\right)^2 \left(\frac{\langle m_\nu\rangle}{m_e}\right)^2 \tag{2.27}$$

Where M_{GT},M_F and M_T are the Gamow-Teller, Fermi and tensor contributions respectively and g_A is the axial coupling.

In the closure approximation (good to better than 90%) due to the high neutrino momentum($\approx$ 100 MeV) the matrix elements have no knowledge of the intermediate nucleus and so in this approximation have the following form. [88]

$$M_{0\nu} = \frac{\langle D \left|h(|\vec{r_1}.\vec{r_2}|)(\vec{\sigma_1}.\vec{\tau_1})(\vec{\sigma_2}.\vec{\tau_2})\right| F\rangle}{\langle E_\nu + E_i\rangle} \tag{2.28}$$

where $h(|\vec{r_1}.\vec{r_2}|)$ are the neutrino potentials ($\approx 1/r$).

There are two major successful methods of evaluation of the NME for $\beta\beta0\nu$ and $\beta\beta2\nu$ which are the Quasiparticle Random Phase Approximation (QRPA) and the Large Scale Shell Model (LSSM)/nuclear shell model (NSM). Both methods start from the same basis of Slater determinant of independent particles but employ different approaches to their calculation. However the correlations actually lead to them being complimentary in nature.

QRPA focuses on a large single-particle model space truncating heavily the included configurations

LSSM/NSM however allows for arbitrary nucleon correlations but has a smaller fraction of the possible valence space modelled.

2.4.1 The Nuclear Shell Model

The nuclear shell model (NSM) models the nucleus of an atom as a large inert core with a few single-particle orbitals around it. However it also makes use of more complicated corrections within the single particle space which adds complexity, as it neglects nothing and treats all configurations on the same footing. With such a model it can handle most isotopes but does run into difficulties when nuclei are deformed, as in ^{150}Nd, or when doing larger scale models for medium or heavy nuclei where inherent calculations become much more complicated and time consuming with more corrections. Isotopes with more stable magic number nuclei or doubly magic nuclei however are more easy to calculate with this method which is relevant for ^{48}Ca and other double beta isotopes NMEs have also been calculated using this method including ^{76}Ge, ^{82}Se and ^{136}Xe. In 2007 short-range correlations were added to the NSM to obtain better agreement and consistency between NSM and the QRPA model.

2.4.2 The Quasiparticle Random Phase Approximation

The random phase approximation (RPA) is a method by which nuclear collective excitations can be described in magic number nuclei as oscillations of small amplitude in the ground state density. This process has been expanded for non-magic number nuclei and open shells by use of the Bogoliubov transformation to move from single particle to quasi particle basis and the canonical basis with diagonalised density matrix. This then becomes the quasiparticle random phase approximation (QRPA), which not only includes mean field contributions but also effects of pairing terms. The QRPA equations can be obtained from the linearization of the Schrodinger equation. [89, 90]

One of the models that goes into the formulation of QPRA is the Skyrme-HFB approximation in which a nucleus' total energy is given as:

$$\begin{gathered} E = K_\tau + E_{Skyrme} + E_{pair} + E_{Coul} \\ E = \int d^3r \left[K_\tau(r) + \epsilon_{Skyrme}(r) + \epsilon_{pair}(r) + \epsilon_{Coul}(r)\right] [89] \end{gathered} \tag{2.29}$$

where $K_\tau, E_{Skyrme}, E_{pair}$ and E_{Coul} are the kinetic, Skyrme, pairing and Coulomb terms respectively. The HFB equations are then obtained by minimizing this total energy.

The pairing force used is a density-dependent zero-range effective interaction with 4 parameters

$$V_{epp}^{eff} = V_0 \left[1 - x \left(\frac{\rho(r)}{\rho_0}\right)^\gamma\right] \delta(r - r') \tag{2.30}$$

where γ= 1, ρ_0 is the saturation density of nuclear matter, and V_0 is an effective pairing strength parameter which fits the pairing gap (Sn 1.32 MeV). x = 0, 0.5, 1 is volume (V.P.), mixed (M.P.) and surface (S.P.) pairing force, respectively [89].

QRPA aims to simplify the calculation of matrix elements for nuclei by modelling lots of single-particle orbitals surrounding a small inert core but is unable to express more complex states.
A relativistic form of the method also exists called the relativistic quasiparticle random phase approximation (RQRPA) formulated in the canonical basis of the relativistic Hartee-Bogoliubov (RHB) model.
These theories of collective excitations for closed and open shell nuclei provide information on nuclear vibrations including [90]

- isoscalar and isovector giant resonances
- low-lying excitations
- exotic modes of excitations in neutron rich nuclei

A comparison of properties of QRPA and LSSM can be seen in table.2.3

	LSSM	**QRPA**
Interaction	Monopole corrected G-matrices	Realistic or schematic interactions tuned with the g_{ph} and g_{pp} strengths
Valence space	"Small", but all the possible ways of distributing the valence particles among the valence orbits are taken into account.	"Large", but only 1p-1h and 2p-2h excitations from the normal filling are considered (and not all of them).
Pairing	It is treated exactly in the valence space. Proton and neutron numbers are exactly conserved. Proton-proton, neutron-neutron, and proton-neutron (isovector and isoscalar) pairing is included.	Only proton-proton, and neutron-neutron pairing is considered. It is treated in the BCS approximation. Proton and neutron numbers are not exactly conserved.
Deformation	Described properly in the laboratory frame. Angular momentum conservation preserved.	Recently incorporated but in progress.

Table 2.3: Comparison of LSSM and QRPA. [88]

2.4.3 Other NME Models

There exist some other methods for calculating the matrix elements for neutrinoless double beta decay. They include angular momentum projected (with real quasiparticle transformation) Hartree-Fock-Bogoliubov (P-HFB) wave functions [91], the Interacting Boson Model (IBM) [92] and by Energy Density Functional Method (EDF) [93].

In P-HFB there is large suppression of the non-ground state nucleon pairs, unlike that of LSSM and QRPA. Both LSSM and QRPA have shown that pairs other than the ground state have major contributions to the overall matrix elements and these contributions are therefore not present in P-HFB calculations.

IBM also has some restrictions over LSSM and QRPA pertaining to the 0+ and 2+ neutron pairs, which are only allowed to be proton pairs.

Comparisons of the NMEs calculated via different methods tells us about the relative strengths and weaknesses of each analytical model. However measurement of the neutrino effective mass is the actual experimental quantity that we need to determine and so we can use these different methods to represent how for a neutrino mass of $m_{\beta\beta} = 50$ meV the half-life is altered by using each method in turn Fig.2.10.

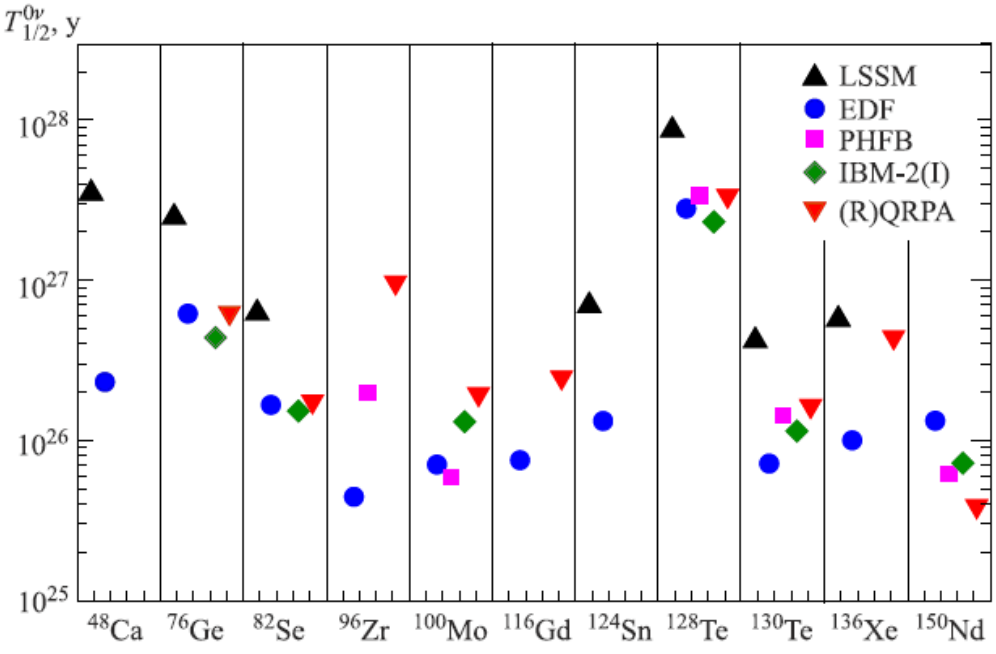

Figure 2.10: The calculated $\beta\beta0\nu$ half-lives by assuming $m_{\beta\beta} = 50$ meV and NMEs of different approaches. [62]

As can be seen in Fig.2.10 the relative effect of the different NME models is a factor of 4-5 difference in half-life value. There are however ways to improve these values using related processes as experimental probes to help constrain models giving more accurate results. These include such things as charge exchange reactions, muon capture and charged current (anti)neutrino-nucleus re-

actions. In this vein it is prudent therefore to have accurate measurement of the $\beta\beta2\nu$ half-life in order to help constrain and tighten NME models [94, 95].

There has been a lot of progress in this direction recently, however no consensus about which NME method or value gives the least uncertainty and therefore best to use in determining the neutrino's effective mass for $\beta\beta0\nu$ processes.

Chapter 3

Current Experimental Techniques and Status

In double beta decay experiments emphasis is not on detection of neutrinos but on the electrons produced in a double beta decay reaction. Because of this some detection technology and methods differ from those of neutrino detection. Different problems are faced in designing a double beta decay detector and different aspects have more significance.

3.1 Detector Construction Criteria

When designing and building a detector to measure either $2\nu\beta\beta$ or $0\nu\beta\beta$ decay processes of a source it is important to maximise the sensitivity to these processes. This is very important as double beta decay is a very rare process and even more important when searching for $0\nu\beta\beta$ decay as its mono energetic peak is even rarer than $2\nu\beta\beta$ and can be both lost in the tail of the $2\nu\beta\beta$ energy distribution and also broadened by experimental uncertainties (see Sec.2). Therefore low backgrounds and high efficiency to the double beta decay are of paramount importance in detector design and construction.

3.1.1 $0\nu\beta\beta$ Decay Sensitivity in the Zero Background Case

For the ideal case of no backgrounds the sensitivity of a detector to $0\nu\beta\beta$ decay is given by Eqn.3.1.

$$T^{0\nu}_{1/2} > \frac{\ln 2 \,.\, Na}{k_{CL}} \frac{M \,.\, \alpha}{W} (\eta \,.\, t) \tag{3.1}$$

The Eqn.3.1 shows that in order to constrain the $0\nu\beta\beta$ half-life limit (maximise the sensitivity) measured by an experiment, then design decisions must optimise the given parameters. The right hand side of the equation has been grouped into three parts which will be described below along with their relevance to maximising the sensitivity when designing a detector.

- The first part $\frac{ln2 \,.\, Na}{k_{CL}}$ is a collection of constants where Na is Avogadro's number and k_{CL} is

the number of excluded events at a certain CL level and so confidence limit at which the half-life sensitivity is required (2.3 for a 90% CL in the current form of eqn.3.1 with no backgrounds). As these terms are all constant they cannot be altered or optimised to affect the sensitivity.

- The second term $\frac{M \,.\, \alpha}{W}$ pertains to the choice and quantity of double beta decay source. $M$is the total mass of the double beta decay source, α is the isotopic abundance to which the source is enriched and W is the molar mass of the source.

  Therefore sensitivity can be maximised by making an experiment with a large amount of source isotope (M) which is enriched to as high a level as possible (α). This will increase the amount of active double beta decay source and thus the number of decays that can occur. The second term also shows that isotopes with a smaller molar mass will give greater sensitivity, however when choosing a source it's always a balancing act between the properties of $Q_{\beta\beta}$, price, ease of enrichment and these factors.

- The third term ($\eta \,.\, t$) refers to the experiment, with η representing the detection efficiency of $0\nu\beta\beta$ events from the source and t is the length of time for which the experiment will run.

  Obviously the greater the detection efficiency and exposure time the greater the probability of observing candidate events. However the life span of most experiments is less than 10 yrs. and components will need replacing, wear out or drift in that time which may lower the detection efficiency with time.

Eqn. 3.1 shows that in the specific case of a zero background experiment the sensitivity is linearly correlated to the amount of active source present and the time for which the source is exposed in the detector.

3.1.2 $0\nu\beta\beta$ Decay Sensitivity Including Backgrounds

However the previous is for the ideal case of a zero background experiment. If we were to include the inherent backgrounds from radioactive contaminations of U and Th in the detector materials, local radon emanation, cosmic ray interactions and the irreducible $\beta\beta2\nu$ signal component (Sec.4.3), then Eqn.3.1 would become Eqn.3.2.

$$T^{0\nu}_{1/2} > \frac{ln2 \,.\, Na}{n_\sigma} \frac{\alpha}{W} \eta \sqrt{\frac{Mt}{N_{bkg} \Delta E}} \tag{3.2}$$

- The first term $\frac{ln2 \,.\, Na}{n_\sigma}$ as before contains the same constants. However now with the inclusion of backgrounds we have n_σ which is the number of sigma for the limit assuming a Gaussian distribution of background events (1.64σ for a 90% CL for the case of a non-zero background experiment).

- The second term $\frac{\alpha}{W}$ still contains both the source enrichment level (α) and the molar mass (W), so the optimisation of these values is the same as before (more atoms/kg). However with

the inclusion of backgrounds it is now also important to optimise the prevalence of signal over background. The sensitivity limit is also no longer linear with the total mass of the source (M)

- The third term now contains only the detector efficiency η as the sensitivity limit is no longer linear in the exposure time as well

- There is now a 4th term $\sqrt{\frac{Mt}{N_{bkg}\Delta E}}$ which contains both the total source mass (M) and exposure time (t), as well as N_{bkg} which is the normalised background index ($kg^{-1}keV^{-1}yr^{-1}$) and ΔE which is the energy window for the $0\nu\beta\beta$ decay which can be approximated by the energy resolution in keV of the detector (FWHM).

  As before, increasing the total mass (M) and the exposure time (t) will increase the sensitivity, however this time not linearly anymore but by square root. Reducing the backgrounds (N_{bkg}) is one of the most important ways to increase sensitivities in double beta decay experiments as natural radioactivity contaminations and cosmic sources can all easily swamp the signal region. To this end experiments usually make use of very pure materials, heavily shielded and housed in subterranean laboratories. Also topological tracking information from tracking detectors can be used to reduce backgrounds. Another method of background reduction is to choose a double beta decay source with its $Q_{\beta\beta}$ value higher than the background level. ^{208}Tl has the highest energy gamma of the natural background chains at 2.6 MeV so a double beta decay source with a $Q_{\beta\beta}$ higher than this (like ^{48}Ca $Q_{\beta\beta}$ = 4.3 MeV) will have a significant background reduction in the energy window. The other major method that sensitivity can be increased is by reducing the energy window ΔE /improving the energy resolution, this will allow for greater determination and separation of the $0\nu\beta\beta$ signal from that of backgrounds and the irreducible background of $2\nu\beta\beta$ decay.

3.2 Double Beta Decay Detection Technologies

As seen in the previous section (Sec.3) there are four main considerations when building a detector, they are, isotope choice and source strength, energy resolution, background reduction and efficiency of the detector. In terms of physical design of detectors these translate to the following considerations.

- Source availability and procurement, price, ease and level of enrichment, ability to meet design needs in terms of working with and forming detectors or foils and its $Q_{\beta\beta}$. Having a large amount of the highest $Q_{\beta\beta}$ with high enrichment is the ideal as it takes it out of the region of common backgrounds and increases the exposure to active isotope which can undergo $\beta\beta$ decay. However this is not always practical or possible for example the highest $Q_{\beta\beta}$ isotope ^{48}Ca is very expensive, is hard to enrich and acquire.

- Energy resolution is one of the most important measurement factors in double beta decay due to its importance in resolving the 0ν and 2ν decay modes. So the type of energy detection

(ionisation, scintillation, thermal excitation) and whether it's homogeneous (where the source and detector are combined) or heterogeneous (where source and detector are distinct) will affect the energy resolution. Homogeneous detectors normally have better energy resolution but less topological information.

- Detector, source and all components are required to have a low radioactivity contamination (e.g currently planned experiments as low as roughly 1μBq/kg for the fiducial volume). Due to the rarity of the process all backgrounds need to be suppressed if any chance of observing a signal is possible, therefore pure component materials are needed with low U and Th contaminations to limit backgrounds from their decay chains.

- Geometrically smaller detectors are favourable or ones that use less support material, unlike neutrino detection where bigger is better. Small detectors reduce materials and so contamination levels,

- Sited in a low background location with external shielding to reduce backgrounds even more.

- Reconstruction of event topology although difficult is very useful in background suppression and providing information about the underlying physics of decay modes but means that separation between source and energy detection is required which can cause a worse energy resolution.

Below is a list of detection methods including descriptions and instances of deployment.

3.2.1 Bolometers

Bolometers are detectors that use small thermal changes in a material and a thermistor attached to them to measure the temperature rise via resistance. In double beta decay crystals are used as the thermal material which also contains double beta decay isotopes. The crystals are kept at very low temperatures and have small specific heat capacity so small energy depositions inside the crystal are enough to raise the temperature by measurable levels. This gives these detectors a very good energy resolution and current research and development is focused on using the signal shape to distinguish multiple gamma interactions from single electron energy depositions giving some particle id information, which could help background suppression. However they cannot distinguish a single gamma interaction from an electron deposition and they give no directional reconstruction to particle events within a crystal. The devices also require external shielding and complicated dilution refrigerators for liquid cooling to maintain 10mK for suppression of thermal noise backgrounds.

Some examples of bolometers include

- **CUORICINO** which consists of 62 TeO_2 crystals arranged in a 13 plane tower structure measuring between 5cm and 3cm in width, height and length, with mass 790g. Most crystals used natural Te but 4 crystals were enriched with ^{130}Te to 82%. Operated between 2003 and 2008, with a total exposure of 19.75 kg yr, it gave a result of $T^{1/2}_{0\nu} > 2.8 \times 10^{24}$ years at 90% C.L [96]

- **CUORE** A future 200kg scale ^{130}Te bolometric detector using 988 TeO_2 crystals in 19 towers. CUORE should obtain a sensitivity of $T^{0\nu}_{1/2} > 5.7 \times 10^{25}$ at 90%CL [97]

3.2.2 Germanium Detectors

Semiconductor detectors work by situating a semiconductor material usually silicon or germanium between two electrodes creating a diode with the semiconductor. Incident ionising radiation interacts with the semiconductor producing a number of electron-hole pairs within it. The number of these pairs produced is proportional to the energy deposited in the semiconductor during interaction. A number of the electrons produced are transferred from the valence band to the conduction band where with use of electric fields they can be driven towards the electrodes producing a current.

Germanium detectors (also called high-purity germanium detectors (HPGe)) can have a depleted sensitive thickness of centimetres and so can be used as a total absorption detector for gamma rays up to roughly 4 or 5 MeV. Therefore their major use is as spectroscopic detectors. However they have the drawback of needing constant liquid nitrogen cooling, at higher temperature electrical noise occurs, where thermally excited electrons can cross the band gap. They have a very good energy resolution.

Some examples of germanium detectors are

- **Heidelberg-Moscow Experiment** consists of 5 high purity Ge semiconductor detectors placed next to Ge crystals enriched to 86-87% in ^{76}Ge. The set up was flushed with nitrogen to reduce radon and has a muon veto detector. The results were as follows, 47.7 kg yr resulting in a half-life of $T^{2\nu}_{1/2} = (1.55 \pm 0.01\ (\text{stat})\ ^{+0.19}_{-0.15}\ (\text{syst})) \times 10^{21}$ years. The lower limit on the half-life of the $0\nu\beta\beta$ decay obtained with pulse shape analysis (see fig.3.1) is $T^{0\nu}_{1/2} > 1.9 \times 10^{25}$ years with 90% CL (with 35.5 kg y). [54, 98]

  A sub set of the collaboration believed that a $\beta\beta0\nu$ decay signal was observed (fig.3.2). This led to the Klapdor claim with a half-life of $T^{0\nu}_{1/2} = (0.88 - 22.38) \times 10^{25}$ yr [65].

- **IGEX** 6 germanium detectors, 3 x 2.2kg detectors and 3 smaller detectors, giving an active mass of 2.0kg enriched to 86% in ^{76}Ge. Nitrogen gas surrounds the detector and it has plastic cosmic vetos situated externally. Its current results for $0\nu\beta\beta$ are $T^{0\nu}_{1/2} > 1.57 \times 10^{25}$ yr (90% CL). [99, 100]

- **GERDA** uses bare Ge diodes which are of high purity and enriched in ^{76}Ge. In phase 1 these were the same detectors used in the Heidelberg-Moscow experiment. The diodes are housed inside a 70m^3 cryostat tank, containing liquid argon. A second tank of water surrounds this as a Cherenkov detector to detect cosmic muon backgrounds with scintillating planes at the top and bottom of the detector. They intend to probe the neutrinoless double beta decay half-life of Ge up to 2×10^{26} years (at 90% CL) as a demonstration of the technique for a tonne scale

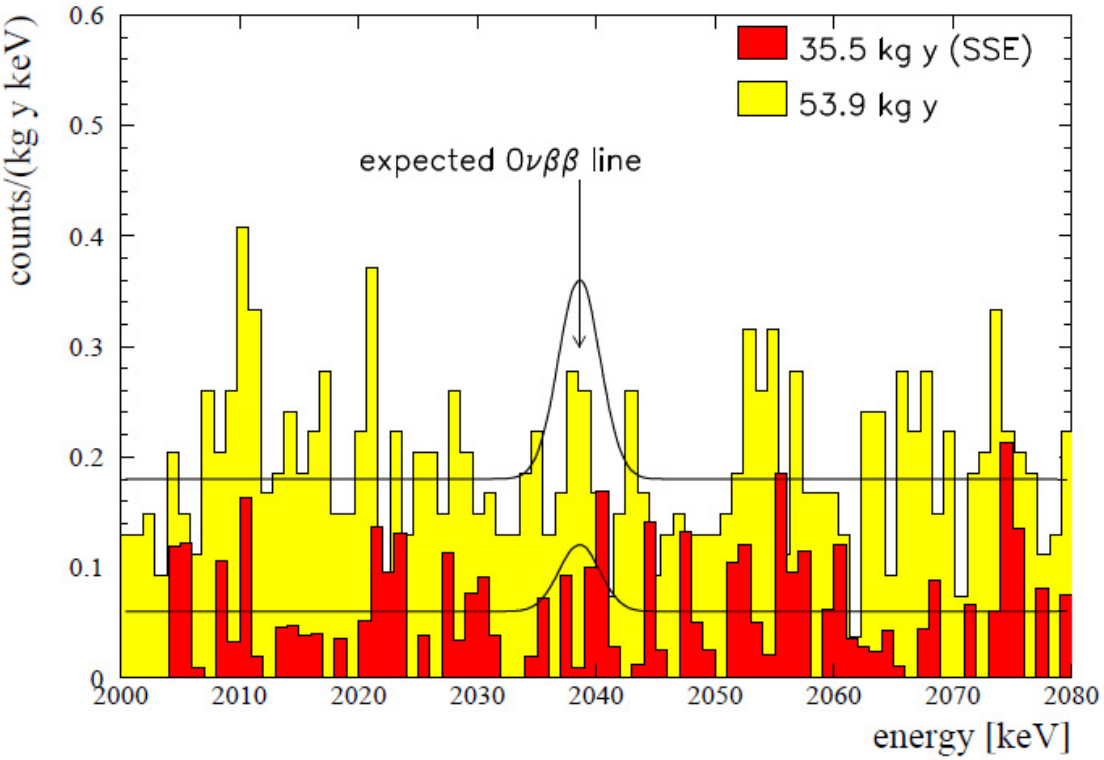

Figure 3.1: Sum of all 5 spectra giving $0\nu\beta\beta$ discovery plot. [54]

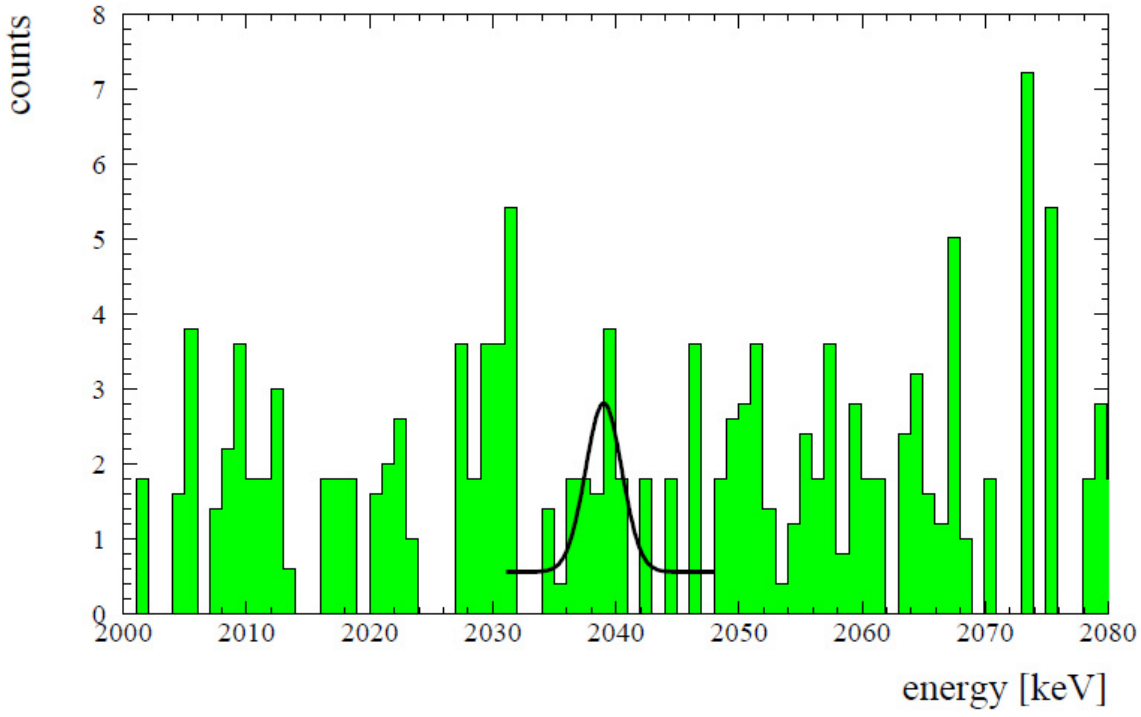

Figure 3.2: Sum spectra giving $0\nu\beta\beta$ discovery plot. [65]

experiment. This corresponding to a range of the effective neutrino mass of $< 0.09 - 0.29$ eV. [101, 102]

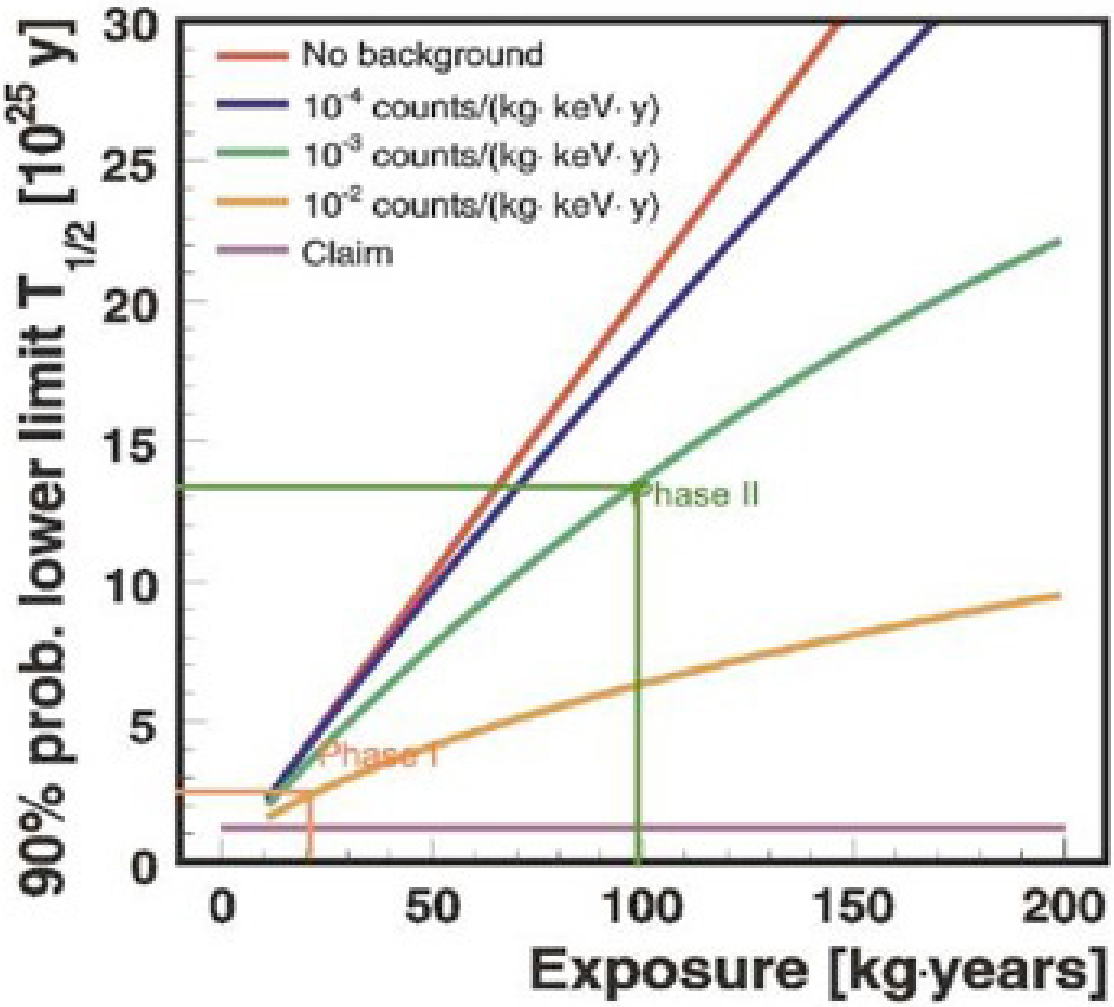

Figure 3.3: Sensitivity of the GERDA detector. [103]

- **MAJORANA** Is a project that will partner with GERDA for a tonne scale project in the future, but currently is using an alternative method for its demonstrator. MAJORANA uses 40 kg of Ge enriched to 86% ^{76}Ge with a more traditional an ultra-low background electroformed Cu cryostat. Each cryostat contains 7 strings of 5 contact detectors [104, 105]

- **COBRA** makes use of 4 CdZnTe (CZT) semiconductor detectors measuring 1cm x 1cm x 1cm. There are nine sources inside the detectors, 5 of which undergo double beta (minus) decay and the other 4 can decay via either double beta (plus) decay, double electron capture or a mixture of the two. Positron emission and electron capture can be used for lepton number violation search processes, but are less sensitive than standard searches. [106]

  The most recent results of the COBRA detector can be found in [106, 107].

3.2.3 Scintillator Experiments

Scintillation experiments either have the double beta decay source inside the scintillating medium or separated from it. Either way they work by the lepton emission from double beta decay ionising the medium and causing scintillation light to be produced proportional to the energy deposited in the medium. These scintillating media can be both liquid and solid and are instrumented by PMTs. They have the favourable properties of being very radioactivity clean, inexpensive and have good timing resolution

Some examples of scintillation experiments include:

- **Kamland-Zen** is a new experiment using the old Kamland detector in which 13 tonnes of liquid scintillator is used. There is an inner spherical balloon (radius 1.54m) of liquid scintillator loaded with (300kg) ^{136}Xe as a double beta decay source. This is housed in a 13m diameter spherical vessel containing more liquid scintillator. Outside the vessel is a buffer oil Cherenkov muon veto detector surrounded by PMTs to detect both Cherenkov and scintillation light from the source (Fig.3.4). This allows it to measure double beta decay events from ^{136}Xe whilst removing backgrounds. A recent measurement from Kamland-Zen has been published for the $\beta\beta2\nu$ half-life of ^{136}Xe of $T^{2\nu}_{1/2} = 2.38 \pm 0.02(stat) \pm 0.14(syst) \times 10^{21}$ years and also importantly a new limit on $\beta\beta0\nu$ dacay of $T^{0\nu}_{1/2} > 5.7 \times 10^{24}$ years that almost closes the Klapdor claim (Fig.3.5). This is equivalent to an effective mass limit of $\langle m_{\beta\beta} \rangle < (0.3 - 0.6)$ eV

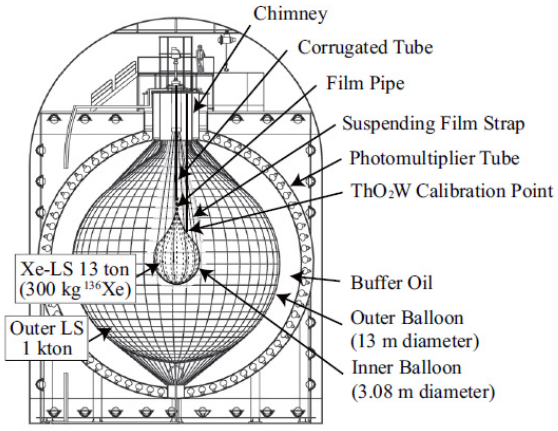

Figure 3.4: Schematic of the Kamland-Zen detector. [108]

- **SNO+** is an upgrade to the SNO detector. It houses 800 tonnes of liquid scintillator (linear alkyl benzene) in a 12m diameter acrylic sphere. The sphere will float in a water bath in which 10,000 PMTs are used for scintillation measurements. The liquid scintillator will be loaded with natural Nd (56kg of ^{150}Nd) as a double beta source and possibly enriched Nd later if possible. The detector is housed 2km underground in Sudbury Canada and can also detect low energy solar neutrinos. The sensitivity to $0\nu\beta\beta$ decay achievable by the detector is $T^{0\nu}_{1/2} > 9.4 \times 10^{24}$ yr (90% C.L.) in 4 years [109, 110]

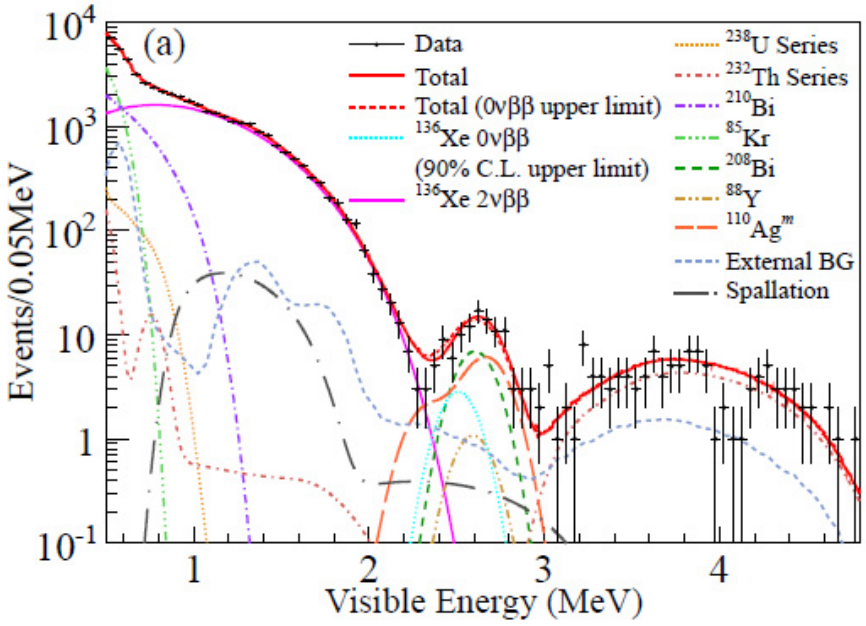

Figure 3.5: Spectra from Kamland-Zen double beta decay search. [108]

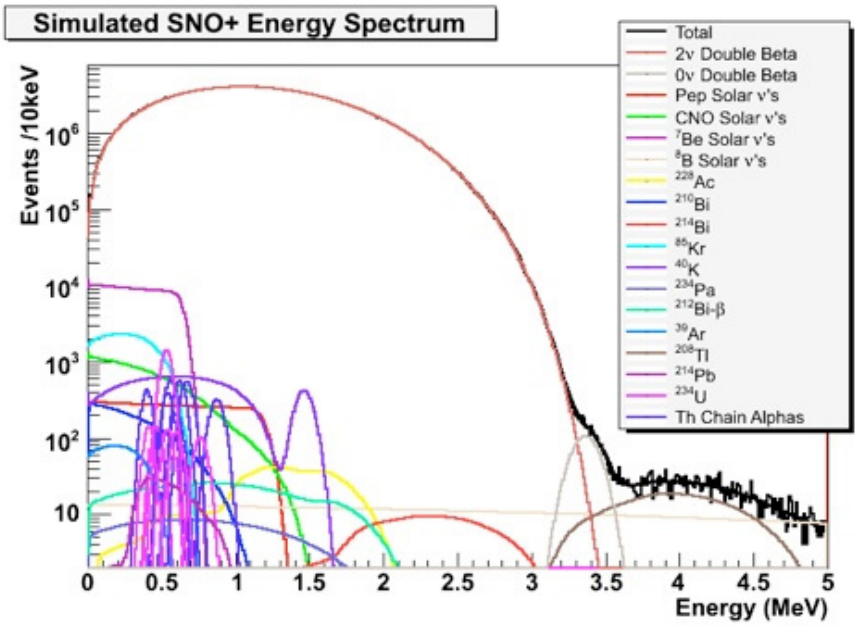

Figure 3.6: SNO+ example double beta decay search. [109]

3.2.4 Tracking Detectors and TPCs

Tracking detectors work by measuring the position of electrons as they pass through a medium. The detection of the electrons is achieved by either the electron ionising or depositing energy through the detector and the measurement of these effects. This sort of detector can be gaseous like a TPC or Geiger detector or solid like calorimeter planes. However the behaviour of the electron moving through each medium is different depending on the energy of the electron and the density of the medium. Tracking detectors can also have a magnetic field present to bend the path of charged particles as they move through it. This gives the ability to differentiate between particle's charges and measure their momentum allowing for determination of the type of lepton present. Therefore tracking detectors have good time and possibly energy resolution and maintain directional reconstruction ability information of the incident neutrino.

- **GothardTPC** was a copper vessel TPC filled with xenon gas enriched to 68% in ^{136}Xe and 5% CH_4 which acted as a quencher. It had a volume of 180 litres and contained 5.3kg of xenon. The entire vessel was surrounded by lead shielding.

  It resulted in a limit on the $0\nu\beta\beta$ half-life of $T^{1/2}_{0\nu} > 4.4 \times 10^{23}$ [111]

- **EXO-200** is a 200kg device that is both a preliminary step for development and measurement techniques for the intended tonne scale experiment EXO and capable of physics measurement. It consists of a liquid Xe TPC, where the Xe is enriched to 80% in ^{130}Xe. It is housed inside a cryostat where an electric field is applied to drift electrons to the charge collection wires. Initial ionisation of the liquid Xe produces scintillation light which is detected by the avalanche photodiodes, the electrons produced then drift to the collection wires giving a signal. The difference between the two gives the drift time and thus event location.[112, 113]

  EXO-200 has recently produced limits on the half-life of neutrinoless double beta decay for Xe of $T^{0\nu}_{1/2} > 1.6 \times 10^{25}$ years (90%CL) which corresponds to a mass of a Majorana mass less than 140-380 meV [114].

- **NEXT** is a high pressure gas xenon TPC enriched in ^{136}Xe, it has a concept of separated tracking and calorimetry . Tracking is performed by electric field induced drift to a surface covered in SiPM and PMTs provide the energy measurement. The initial primary scintillation is detected by PMTs as the start of an event and then a secondary scintillation occurs when it passes through 2 grids with an electric field which is very close to the tracking plane. The experiment is currently under construction [115, 116].

NEMO3 and SUPERNEMO combine both scintillation and tracking detectors, but uniquely they are separate with Geiger drift cells providing tracking information and organic calorimeter blocks providing energy measurements. The main distinguishing features are that the source is separate from the detector and so not only interchangeable but gives event vertex reconstruction and the use

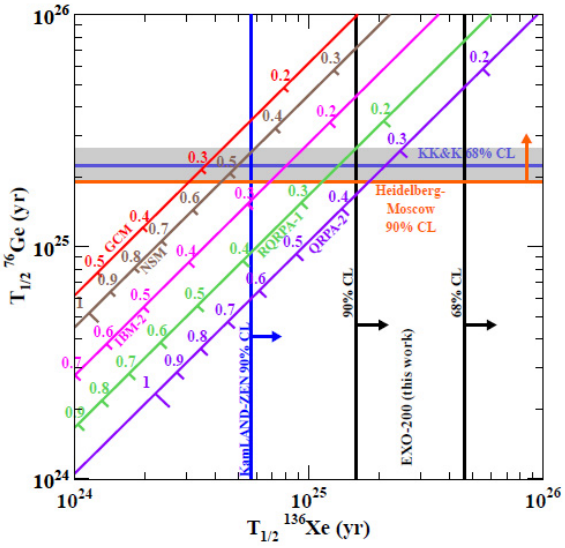

Figure 3.7: Results from the EXO-200 on neutrinoless double beta decay search. [114]

of low density He gas for tracking makes analysis of the angular distribution possible. A much more in depth detector description of these experiments can be found in Sec.4 and Sec.6 respectively.

3.2.5 Indirect Detection

There are also some indirect detection methods that can be used for double beta decay detection. They include geochemical and radiochemical techniques. A basic description of their techniques is presented below.

3.2.5.1 Geochemical Experiments

Geochemical experiments involve studying mineral ores of double beta isotopes that have existed for many hundreds of millions up to billions of years. The quantity of daughter isotopes of the double beta decays can then be measured using chemical techniques to prepare and then a mass spectrometer to analyse and a rate derived. This is very sensitive due to the very long time that the decays can have occurred, however the mode of decay cannot be distinguished. However ore selection requires that the daughter isotope is not naturally present in the ore so that the rate can be accurately determined. This limits selection to currently ^{82}Se, ^{128}Te, ^{130}Te, ^{96}Zr and ^{130}Ba. Results so far have been mixed with some showing large deviations from direct measurements [117, 118, 119, 120, 121] and others like Se agreeing closely [122].

3.2.5.2 Radiochemical Experiments

Radiochemical experiments are based on detecting radioactive daughters of the double beta decay transition. The daughter isotope's rarity and short lifetime mean that contamination can be effectively zero, giving good sensitivity. The daughter isotopes must be radioactive to be viable, as the

process involves extraction of the daughter isotopes and then allowing them to subsequently decay and counting these decays to determine the number of daughter atoms and hence derive the double beta decay rate. This method was successfully applied to detect the $^{238}U \rightarrow {}^{238}Pu$ transition. Pu has been isolated from an uranyl nitrate sample, purified and put into low background alpha counters to observe 5.51 MeV alpha particles from ^{238}Pu and thus count the number of ^{238}Pu. This can give a clear discovery signal, but no mechanism or topological information can be obtained.

3.3 ^{48}Ca Experiments

^{48}Ca is a the double beta decay isotope with the biggest $Q_{\beta\beta}$ value and also is a doubly magic nucleus. This makes it an important isotope and is the one in which this thesis focuses on. Below is a list of experiments and associated results of the double beta decay experiments using ^{48}Ca as their source isotope.

3.3.1 Mateosian and Goldhaber Experiment

CaF_2 scintillating crystals were used enriched to 96.59%, giving a total active ^{48}Ca double beta source of 11.4g. The experiment was housed in a naval gun and aimed to study lepton number conservation.

Data was taken over 28.7 days in 1966 and that gave the following limits on double beta decay $T^{1/2}_{2nu} > 5$ x 10^{18} years & $T^{1/2}_{0nu} > 2$ x 10^{20} years. [123]

3.3.2 The Beijing Experiment

The Beijing experiment used un-enriched CaF_2 scintillating crystals as they gave a better energy resolution than enriched ones. The crystals were of varying density and 15.8 cm long and 17.8 cm wide. 2 crystals were used originally with another 2 added later giving a total ^{48}Ca mass of 43g. The crystals were housed underground in a mine in a sealed oxygen free copper container filled with pure argon. Each crystal was coupled to a quartz PMT.

The $0\nu\beta\beta$ half-life result of this experiment after 7588.5 hrs (0.87 yrs) of data taking was $T^{1/2}_{0nu} >$ 9.5 x 10^{21} years (at 78% C.L.). [124]

3.3.3 Hoover Dam Experiment

A TPC was mounted in the Hoover dam with sources of two different thicknesses totalling 42.2g of powdered $CaCO_3$ source enriched to 76% in ^{48}Ca. The exposure of the source led to a measurement of the $2\nu\beta\beta$ half-life of $T^{1/2}_{2nu} = (4.3^{+2.6}_{-1.1}(stat.) \pm 1.4(syst.))\ 10^{19}$ years. [125]

3.3.4 TGV Experiment

The TGV (Telescope Germanium Vertical) experiment was housed in Modan and uses HPGe multi-detector spectrometers and 16 $CaCO_3$ sources made of 80% $CaCO_3$ and 20% polyvinyl with mylar as support. 8 of the sources were enriched to 78% in ^{48}Ca whilst the other 8 were using natural Ca. This gave a total mass of 3.5g and 1g of active double beta decay source ^{48}Ca.

The results after 8700 hours of data taking gave the following [53]

$T^{1/2}_{2nu} = (4.2^{+3.3}_{-1.3})$ x 10^{19} years & $T^{1/2}_{0nu} > 1.5$ x 10^{21} years (at 90% C.L.).

3.3.5 ELEGANT VI

ELEGANT uses 25 CaF_3 crystal detectors surrounded by 38 CsI(TI) scintillators which work as veto counters. The detectors consist of a central cubic crystal of CaF_2(Eu) and two pure CaF_2 crystals as wave guides to PMTs. The whole apparatus is contained in an air tight box filled with N_2 to prevent radon and an external paraffin and lead shielding. The total active double beta source is roughly $\approx 9.61 \times 10^{22}$ atoms of ^{48}Ca. [126]

The result after 5567 hours of data taking was $T^{0\nu}_{1/2} > 5.8$ x 10^{22} years (at 90% C.L.) [127].

3.3.6 CANDLES

CANDLES is a Japanese experiment to measure double beta decay from ^{48}Ca. The CANDLES III detector consists of 60 CaF_2 scintillator cubes 10cm thick (191kg) (Fig.3.8). The cubes are immersed in liquid scintillator which acts as both a passive shield and a veto for backgrounds. Scintillation light from both types of scintillator can be detected from 40 large PMTs which surround the detector. The aim is to reach a sensitivity of 10^{26} years for the $\beta\beta0\nu$ decay of ^{48}Ca, corresponding to a neutrino mass of ≈30 meV.[128].

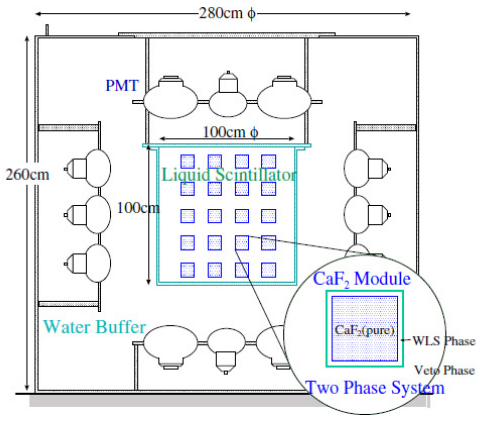

Figure 3.8: The design of the CANDLES III system. [129]

3.4 Current Double Beta Decay Results

The double beta decay of many isotopes has now been observed by a wide collection of experimental methods. Below is a summary of some of these measurements for isotopes transitioning to ground states for both $\beta\beta 2\nu$ decay and limits obtained for $\beta\beta 0\nu$ decay.

Isotope	Mode	Result (years) (all limits at 90% CL)	Type	Citation
^{48}Ca	$\beta\beta2\nu$	$(4.4^{+0.5}_{-0.4} \pm 0.4) \times 10^{19}$ NEMO3	Track-Calo	[130]
	$\beta\beta2\nu$	$(4.2^{+3.3}_{-1.3}) \times 10^{19}$	Ge spectrometer	[131]
	$\beta\beta2\nu$	$(4.3^{+2.4}_{-1.1} \pm 1.4) \times 10^{19}$	TPC	[125]
	$\beta\beta0\nu$	$> 13 \times 10^{21}$ NEMO3	Track-Calo	[130]
	$\beta\beta0\nu$	$> 58 \times 10^{21}$	CaF_2 scint.	[127]
^{76}Ge	$\beta\beta2\nu$	$(1.74 \pm 0.01^{+0.18}_{-0.16}) \times 10^{21}$	Enriched HPGe	[132]
	$\beta\beta2\nu$	$(1.45 \pm 0.15) \times 10^{21}$	Enriched HPGe	[99]
	$\beta\beta2\nu$	$(1.84^{+0.14}_{-0.10}) \times 10^{21}$	Enriched HPGe	[54]
	$\beta\beta0\nu$	$(2.23^{+0.44}_{-0.31}) \times 10^{25}$	Enriched HPGe	[133]
	$\beta\beta0\nu$	$> 1.57 \times 10^{25}$	Enriched HPGe	[99]
	$\beta\beta0\nu$	$> 1.9 \times 10^{25}$	Enriched HPGe	[54]
^{82}Se	$\beta\beta2\nu$	$(9.6 \pm 0.3 \pm 1.0) \times 10^{19}$ NEMO3	Track-Calo	[55]
	$\beta\beta2\nu$	$(1.08^{+0.26}_{-0.06}) \times 10^{20}$	TPC	[134]
	$\beta\beta(2+0)\nu$	$(1.2 \pm 0.1 \pm 0.4) \times 10^{20}$	Geochem.	[122]
	$\beta\beta0\nu$	$> 3.6 \times 10^{23}$ NEMO3	Track-Calo	[130]
^{96}Zr	$\beta\beta2\nu$	$(2.35 \pm 0.14 \pm 0.16) \times 10^{19}$ NEMO3	Track-Calo	[135]
	$\beta\beta(2+0)\nu$	0.0390.009	Geochem	[118]
	$\beta\beta(2+0)\nu$	$(9.4 \pm 3.2) \times 10^{18}$	Geochem	[117]
	$\beta\beta0\nu$	$> 9.2 \times 10^{21}$ NEMO3	Track-Calo	[135]
^{100}Mo	$\beta\beta2\nu$	$(7.17 \pm 0.01 \pm 0.54) \times 10^{18}$ NEMO3	Track-Calo	[55]
	$\beta\beta2\nu$	$(7.6^{+2.2}_{-1.4}) \times 10^{18}$	Si(Li)	[136]
	$\beta\beta2\nu$	$(6.82^{+0.38}_{-0.53} \pm 0.68) \times 10^{18}$	TPC	[137]
	$\beta\beta2\nu$	$(7.2 \pm 1.1(stat) \pm 1.8(syst)) \times 10^{18}$	TPC	[138]
	$\beta\beta(2+0)\nu$	$(2.1 \pm 0.3) \times 10^{18}$	Geochem	[119]
	$\beta\beta0\nu$	$> 1.1 \times 10^{24}$ NEMO3	Track-Calo	[130]
	$\beta\beta0\nu$	$> 4.9 \times 10^{21}$	Liq. Ar ioniz.	[138]
^{116}Cd	$\beta\beta2\nu$	$(2.8 \pm 0.1 \pm 0.3) \times 10^{19}$ NEMO3	Track-Calo	[130]
	$\beta\beta2\nu$	$(2.9^{+0.4}_{-0.3}) \times 10^{21}$	$^{116}CdWO_4$ scint.	[57]
	$\beta\beta0\nu$	$> 16 \times 10^{21}$ NEMO3	Track-Calo	[130]
	$\beta\beta0\nu$	$> 170 \times 10^{21}$	$^{116}CdWO_4$ scint.	[57]
^{128}Te	$\beta\beta(2+0)\nu$	$(7.2 \pm 0.4) \times 10^{24}$	Geochem	[121]
	$\beta\beta(2+0)\nu$	$(1.80.7) \times 10^{24}$	Geochem.	[139]
	$\beta\beta0\nu$	$> 110 \times 10^{21}$	Cryog. det.	[59]
^{130}Te	$\beta\beta2\nu$	$(0.7 \pm 0.09 \pm 0.11) \times 10^{21}$ NEMO3	Track-Calo	[140]
	$\beta\beta2\nu$	$(0.61 \pm 0.14^{+0.29}_{-0.35}) \times 10^{21}$	Cryog. det.	[59]
	$\beta\beta(2+0)\nu$	$(0.79 \pm 0.10) \times 10^{21}$	Geochem	[141]
	$\beta\beta(2+0)\nu$	$(2.7 \pm 0.1) \times 10^{21}$	Geochem	[121]
	$\beta\beta(2+0)\nu$	$(0.75 \pm 0.03 \pm 0.23) \times 10^{21}$	Geochem.	[122]
	$\beta\beta(2+0)\nu$	$(2.60 \pm 0.28) \times 10^{21}$	Geochem.	[120]
	$\beta\beta0\nu$	$> 1.3 \times 10^{23}$ NEMO3	Track-Calo	[140]
	$\beta\beta0\nu$	$> 30 \times 10^{23}$	TeO_2 bolometer	[142]
	$\beta\beta0\nu$	$> 18 \times 10^{23}$	Cryog. det.	[143]
^{136}Xe	$\beta\beta2\nu$	$(2.11 \pm 0.04 \pm 0.21) \times 10^{21}$	Liquid Xe TPC	[60]
	$\beta\beta2\nu$	$(2.38 \pm 0.02(stat) \pm 0.14(syst)) \times 10^{21})$	Liquid Xe	[108]
	$\beta\beta0\nu$	$> 1.2 \times 10^{24}$	Liquid Xe Scint.	[144]
^{150}Nd	$\beta\beta2\nu$	$(9.11^{+0.25}_{-0.22} \pm 0.63) \times 10^{18}$ NEMO3	Track-Calo	[61]
	$\beta\beta2\nu$	$(6.75^{+0.37}_{-0.42} \pm 0.68) \times 10^{18}$	TPC	[137]
	$\beta\beta0\nu$	$> 18.0 \times 10^{21}$ NEMO3	Track-Calo	[61]
^{238}U	$\beta\beta(2+0)\nu$	$(2.0 \pm 0.6) \times 10^{21}$	Radiochem	[145]
^{130}Ba	$\beta\beta2\nu$	$(2.2 \pm 0.5) \times 10^{21}$	Geochem	[146]

Table 3.1: Summary table of double beta decay results by isotope.

Chapter 4

NEMO3 Detector

For full in depth technical details refer to the NEMO3 technical design report [147], on which the following technical description is based

4.1 How NEMO3 is Different from other Double Beta Experiments

The primary objective of the NEMO3 experiment is to study and measure 2ν double beta decay for several isotopes and to search for neutrinoless double beta decay. Where NEMO3 is different from most other double beta decay experiments is that it doesn't focus solely on energy detection to find the double beta process (e.g. unlike the Ge type of experiments). NEMO3 has the ability to add topological information to observed events due to the inclusion of a tracking detector. This gives the ability to reduce background events and lower their influence on measurements and to do targeted searches for known channels and examine decays to excited states. It also gives the ability to perform much more detailed studies on backgrounds, systematic effects present and, thanks to tracking information, angular dependencies of observed events can be studied. These angular dependencies provide some of the only experimental distinguishing characteristics of competing theoretical mechanisms and are possible due to the low density He gas used inside the tracker. Importantly NEMO3 was designed from the start with the idea that the detector and source should be independent. This also allows for many isotopes to be studied with the same apparatus simultaneously giving the capabilities of confirmation between isotopes and thus reduced dependence on nuclear matrix elements. All these differences add up to a real ability to advance the field of understanding of neutrinoless double beta decay over simple energy measurements.

4.2 Detector Description

4.2.1 Overview

NEMO3 is the third incarnation in the group of Neutrino Ettore Majorana Observatories (NEMO). It follows on from its 2 predecessors NEMO2 and NEMO1. NEMO3 however is the first full scale experiment designed and run for 8 years to actually make measurements of double beta decay processes. whereas NEMO1 was merely a small prototype to prove the principles of tracking, detection efficiencies and radio purity and NEMO2 then developed on these ideas to make small scale measurements of ^{100}Mo, ^{116}Cd, ^{82}Se and ^{96}Zr double beta decay processes.

NEMO3 is toroidal in design and is separated into 20 equal sectors for ease of construction and access. It measures 4m in height and has a radius of 3m. Contained within the detector at a radius of 1.55m is a central cylindrical source foil of between 20 - 50 mg/cm^2 thick and 2.5 m in height, which houses 10kg of various double beta decay sources (see sec.4.2.2). Either side of this central source lie the tracking volumes. They consist of two concentric volumes which sandwich the source foil, with a total of 6180 vertically mounted open octagonal drift cells. The cells are 270 cm long and operate in a 7mbar environment of helium alcohol mix (see sec.4.2.3). This arrangement enables 3D volumetric tracking to be achieved on particles emanating from the foil or entering the tracking volume. Surrounding the tracking volumes are cylindrical calorimeters both comprising of 10 cm thick polystyrene scintillator blocks coupled to PMTs to provide energy measurements at a resolution of about 14% FWHM at 1 MeV (see sec.4.2.4). In between Geiger layers on the top and bottom endcaps there are also scintillator blocks to tag particles leaving the volume via the extremities. Surrounding the calorimeter cylinders is a solenoid which provides a 25 Gauss field parallel to the foil axis. The major reason for its inclusion is to deflect the path of charged particles allowing for charge identification within the tracking volume by measuring their curvature. External to this magnetic field are 18 cm thick iron panels to reduce gamma rays. Outside these are 30cm borated water tanks and in awkward places like the top and bottom of the detector 40cm of wood to thermalise fast neutrons. Placed over this is a wooden cover surrounded by a radon tent, connected to an activated carbon filter system to reduce the atmospheric radon gas contamination (Note: radon tent was only installed post phase 1 of data taking). The detector is able to achieve a minimum neutrino mass measurement exclusion sensitivity of roughly 0.3 eV.

The NEMO3 detector was installed in the Frejus Underground Laboratory (LSM) in France. The laboratory is situated 2932 m under the Frejus mountain on the border of France and Italy. A road tunnel connects the two countries under the mountain and half way along is the site of the laboratory. The large amount of rock above it (equivalent to 4800 m of water) provides excellent background shielding from cosmic rays.

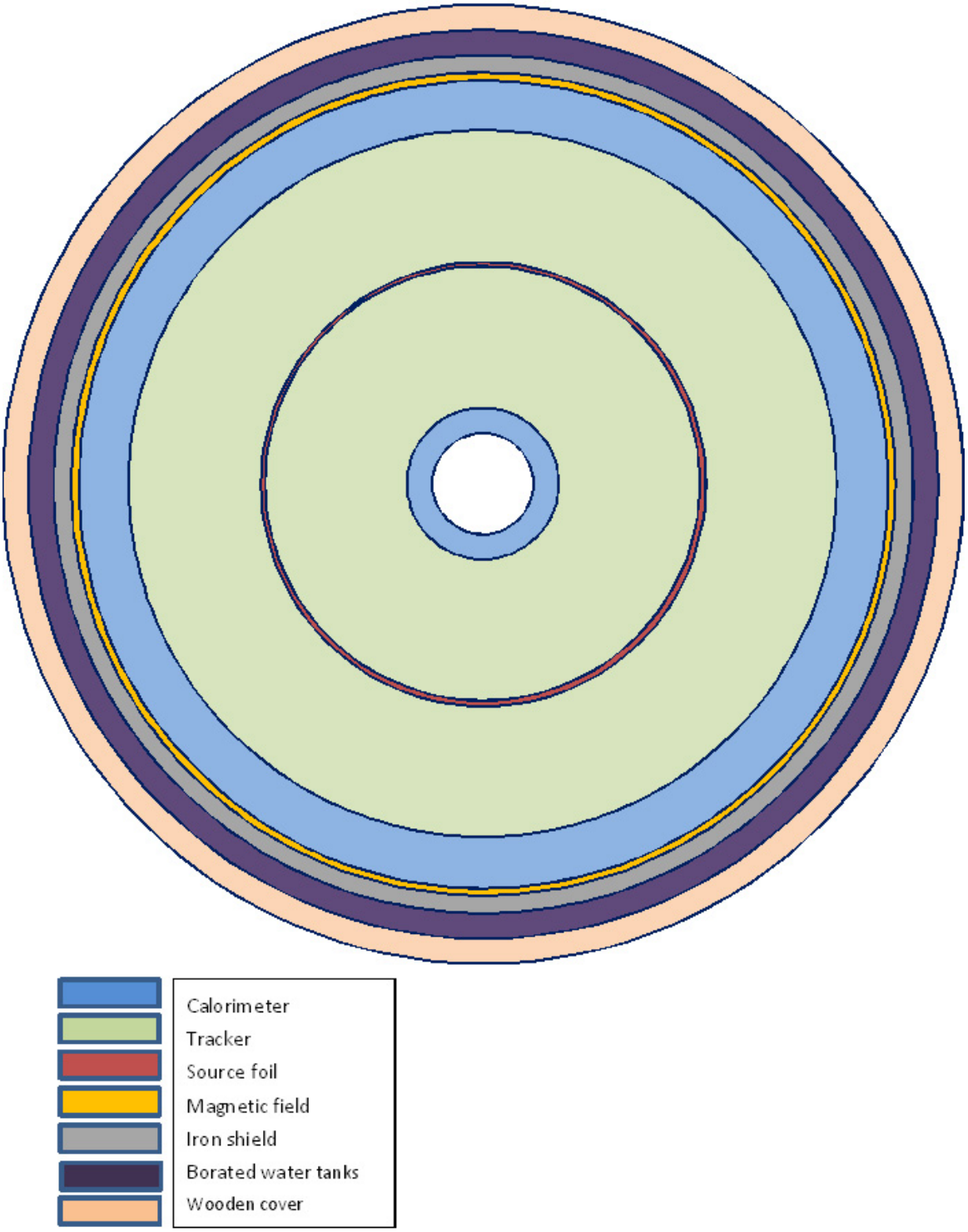

Figure 4.1: Pictorial representation of the NEMO3 detector layers (not geometrically accurate).

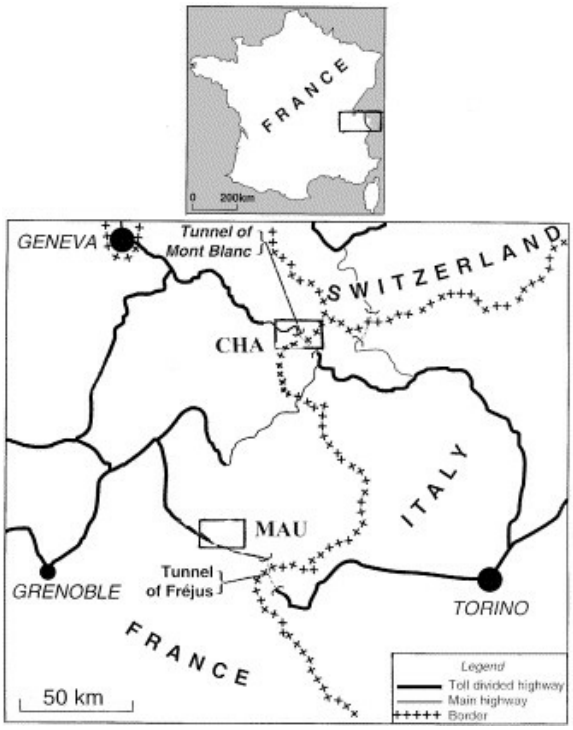

Figure 4.2: Frejus location.

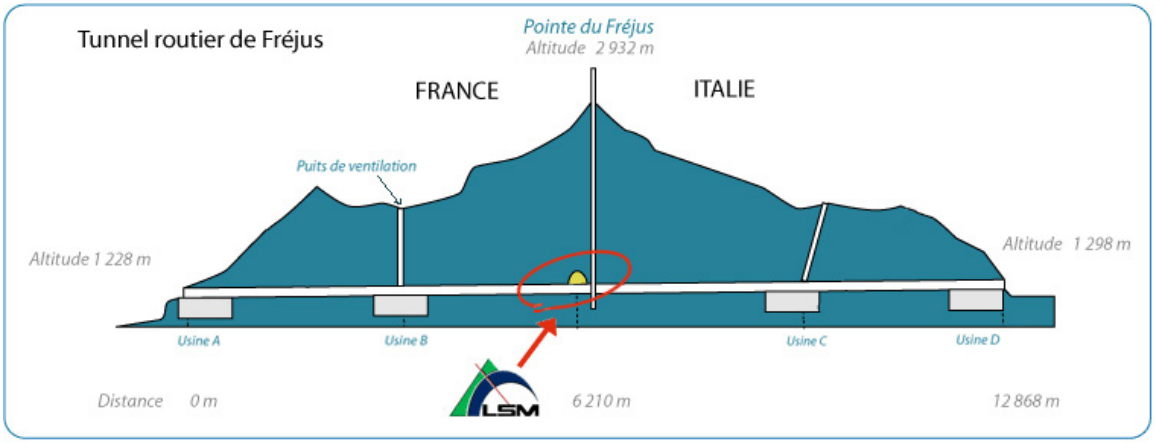

Figure 4.3: The Location of LSM in the Frejus road tunnel.

4.2.2 Isotopes and Foils

The primary design feature in this experiment was to have the detector and source independent. This permits one to study several double beta decay isotopes as the isotope is not integral to detection. It also reduces the dependence of the results on the nuclear matrix element calculations. Furthermore, the use of multiple sources within the same detector and test conditions, allows for a more detailed study of the backgrounds and systematic effects. The source foils were 30-60 mg/cm^2 thick and 2.5 m in height and are fixed vertically at a radius of 1.55 m, between concentric cylinder volumes.

4.2.2.1 Isotope Selection

Due to the unique nature of NEMO3 to allow multiple double beta decay isotopes to be measured simultaneously, a choice or selection criterion was needed to determine which sources were the best candidates for measurement within it.

In deciding, the NEMO collaboration used many factors and not solely the NME of $\beta\beta0\nu$ for each isotope, as this by itself is a bad idea due to the inherent uncertainty of this value as stipulated in sec.2.4. The criteria of selection also included the transition energy ($Q_{\beta\beta}$) as it represents the energy given to the decay products and so the region in which detection of these product's energy would be made. This is especially important with respect to backgrounds of the detector as both Bi and Tl have major background contributions which would hamper detection in specific regions (ie. ^{208}Tl has a γ ray emission at 2.615 MeV which is at the top cut off energy for gammas from natural radioactivity. So double beta decay candidates are desirable if their $Q_{\beta\beta}$ value is above this) see sec.4.3. The phase space of each element is also important as it plays a role in determination of the half-life we are attempting to be measured for both $\beta\beta0\nu$ and $\beta\beta2\nu$ (Eqn.2.10 and Eqn.2.13). The larger the phase space value the smaller the expected half-life for each process, as is also the case with the NMEs for both processes as well. Selecting criteria based on $\beta\beta2\nu$ decays as well as $\beta\beta0\nu$ is important as mentioned before as the measurement of its half-life and NME are in themselves important quantities. $\beta\beta2\nu$ is the major background for $\beta\beta0\nu$ signal discovery and determination of the $\beta\beta2\nu$ NME helps to tie down the theoretical NME for $\beta\beta0\nu$.

Another important selection criterion is the natural isotopic abundance for which the criterion chosen was that isotopes had to have a natural abundance of $> 2\%$. This is also linked to the ease and quality of enrichment and of course cost. The reason behind these factors of course is the importance of obtaining large mass highly pure samples of isotopes. The larger the quantity the greater sensitivity can be achieved due to the greater exposure to possible decays and the quality and level of enrichment for radio purity issues as well as the previous increased exposure.

These criteria selected 5 nuclei ^{116}Cd, ^{82}Se, ^{100}Mo, ^{96}Zr and ^{150}Nd. Of these five two were chosen to concentrate on for $\beta\beta0\nu$ studies due to cost implications as well as availability and experience. These were 6.914 kg of ^{100}Mo (some recycled form NEMO2) and 0.932 kg of ^{82}Se. Using these quantities of enriched isotope it is possible to make measurements with sensitivity of 0.3 eV of the

effective neutrino mass, via $\beta\beta0\nu$

The other 3 isotopes were added in much smaller quantities to make detailed studies of $\beta\beta2\nu$ decay half-lives (0.4kg of ^{116}Cd, 9.43g of ^{96}Zr and 36.5g ^{150}Nd). ^{48}Ca was also added despite it not reaching the required abundance level of 2% (^{48}Ca abundance =0.187%). ^{48}Ca is a very interesting prospect which is why it was added as it has the largest $Q_{\beta\beta}$ = 4.272 MeV which takes it entirely out of the range of most backgrounds, however its difficulty to enrich and obtain meant only 6.99g was added to the detector.

Three other materials were added to NEMO3, 0.62kg of very radio pure copper to allow for external background studies as it has effectively zero internal contaminations in our energy range, 0.61kg of very pure oxide of natural tellurium and 0.45kg of enriched ^{130}Te for studies of backgrounds around 3 MeV and also to verify 2 opposing measurements of ^{130}Te $\beta\beta2\nu$ decay half-life. The natural tellurium has a 33.8% abundance of ^{130}Te which gives us 166g of this isotope in the natural sample. The Te samples were added as no direct measurment of the double beta decay process for the isotope had ever been made. Geochemical measurements had observed the process but with large descrepancies between samples. Tellurium itself is also very important due to its very high natural abundance (33.8%) of ^{130}Te.

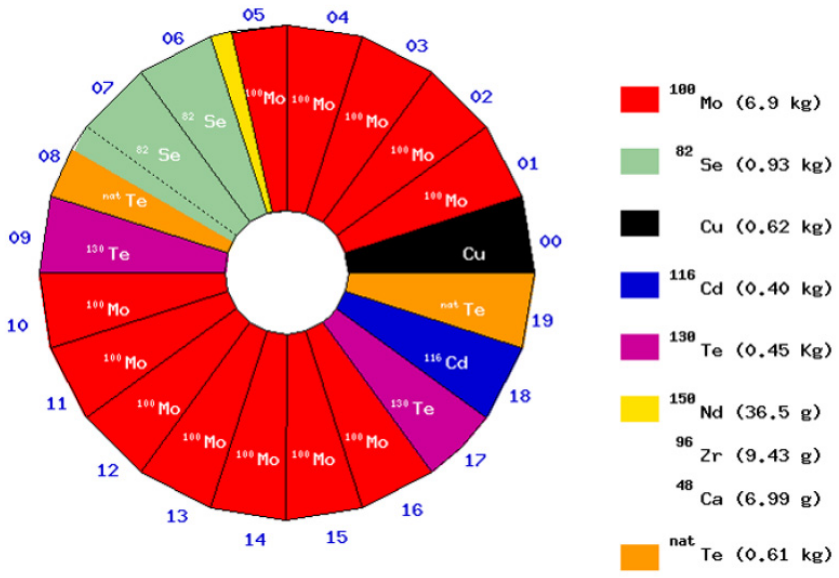

Figure 4.4: The distribution of sources inside the NEMO3 detector. [147]

4.2.2.2 Enrichment and Purification

Due to the natural abundances of these isotopes being modest (< 10%), enrichment was needed to increase the amounts of active double beta isotope and subsequent purification needed to remove impurities added during enrichment. These steps of purification and enrichment were slightly different for each isotope and some involved first making a fluoride gas before starting the processes. The

Figure 4.5: Preparation of sector 5 source which contains Ca discs. [147]

techniques used for each sample are listed below in table.4.1.

Source	Enrichment	Purification	Percentage Abundance
^{100}Mo	Centrifugal separation	Physical & Chemical	$95.14 \pm 0.05\% \rightarrow 98.95 \pm 0.05\%$
^{82}Se	Centrifugal separation	None	$97.02 \pm 0.05\% \rightarrow 96.82 \pm 0.05\%$
^{130}Te	Centrifugal separation	None	$89.4 \pm 0.5\%$
^{116}Cd	Centrifugal separation	Distillation	$93.2 \pm 0.2\%$
^{150}Nd	Electromagnetic separation	Chemical	$91.0 \pm 0.5\%$
^{86}Zr	Electromagnetic separation	Chemical	$57.3 \pm 1.4\%$
^{48}Ca	Electromagnetic separation	Chemical	$73.2 \pm 1.6\%$

Table 4.1: Enrichment and purification summary table.

After enrichment various purification techniques were used if required. The 2 major methods were either chemical or physical, both with the same aim to remove long lived troublesome background isotopes like ^{238}U or ^{232}Th. Chemical purification uses chemical reactions to replace these isotopes with atoms like Ba whilst physical involved growing mono-crystals to isolate the impurities.

Other purification processes were used such as distillation and a specially developed purification method at ITEP and the Kurchatov institute for ^{48}Ca, it removed ^{226}Ra, ^{228}Ra, ^{60}Co and ^{152}Eu, as well as elements from the uranium and thorium decay chains. This process converts the 64g of enriched $CaCO_3$ to 42.1g of enriched CaF_2. A portion of this powder (24.6g) of the enriched CaF_2 was sent to LSM for radioactivity measurements with an HPGE detector. The rest (17.5g) was used to make the 9 composite 45mm disks.

A summary of all the sources, their enrichment and purification and final percentage abundances of active isotope can be seen in Table.4.1.

4.2.2.3 Production

The source foils in each of the 20 sectors were subdivided into 7 strips of mean size 2480mm long and about 63mm wide if the strips were on the edge of a sector (strip 1 or strip 7) and 65mm wide if one of the middle ones (strips 2-6). Each strip was attached vertically to a copper support frame by use of two Perspex clips in a clean room in LSM.

The powdered or sheet metal isotope sources obtained after enrichment and purification were turned into foils for mounting inside the NEMO3 detector. The foils were categorised as either metallic or composite. Metallic foils included cadmium, copper and a fraction of the Molybdenum sample (which was purified by physical process) and were essentially thin sheets of the metallic sources that were cut and glued to create the strips for inserting. The other type of foil known as composite foils were constructed from a sandwich of 2 layers of Mylar backing film with a mixture of source powder and PVA glue between them. The source was first sieved to ensure no grains larger than 45μm in diameter were obtained, any excess powder was reground and re-sieved. This ensured a good bond to the backing film. The glue used was a mixture of water and PVA (polyvinyl acetate), to which the powdered source was added. The end result was foil strips of the correct length and a surface density lower than 60mg/cm^2. The remainder of the foils created were composite in nature. They include the remaining 64% of ^{100}Mo, ^{82}Se, $^{(nat+130)}$Te, ^{96}Zr, ^{150}Nd and ^{48}Ca. The Mylar used to create these foils has two uses, it forms an impermeable gas barrier and it adds mechanical strength.

^{48}Ca actually had a slightly different construction to that of the other composite foils. The second portion of CaF_2 powder (17.5g which was not measured with a HPGe detector) was used to make 9 disks which were composite sandwiches using Mylar backing film as described above. These disks were then attached to a strip of Mylar creating the calcium section of the foil (Fig.4.5). The size of these disks is the cause of an issue with my analysis. It was recorded at creation of NEMO3 that these ^{48}Ca disks were 40mm in diameter. Subsequently on decommissioning and dismantling 8 years later the disks were measured to be 45mm. This oversight was later confirmed that no 40mm disks were created. However the timing of this discovery was during my writing and concluding my studies and so some of the work presented will include models based on these earlier 40mm models. It is presently unclear what the exact effects of these differences will be on the end result, but studies are being undertaken to re-examine the data.

The exact positioning of sources with respect to sector and strip in NEMO3 as well as the composite (C.) or metallic (M.) nature are summarised in Table 4.2.

Sector 5 foil strip 7 is actually quite complicated in its construction and does not include a single source. In fact it is made up of 2 sub-strips of ^{96}Zr, one of ^{48}Ca and one of six layers of type 2 Mylar backing film to study backgrounds coming from this backing film. Each of the source sub-strips

	Strip 1	Strip 2	Strip 3	Strip 4	Strip 5	Strip 6	Strip 7
Sector 0	M. Cu	M. Cu	M. Cu	M. Cu	M. Cu	M. Cu	M. Cu
Sector 1	M. ^{100}Mo	M. ^{100}Mo	M. ^{100}Mo	M. ^{100}Mo	M. ^{100}Mo	C. ^{100}Mo	C. ^{100}Mo
Sector 2	M. ^{100}Mo	M. ^{100}Mo	M. ^{100}Mo	M. ^{100}Mo	M. ^{100}Mo	M. ^{100}Mo	M. ^{100}Mo
Sector 3	M. ^{100}Mo	M. ^{100}Mo	M. ^{100}Mo	M. ^{100}Mo	M. ^{100}Mo	M. ^{100}Mo	M. ^{100}Mo
Sector 4	M. ^{100}Mo	M. ^{100}Mo	M. ^{100}Mo	M. ^{100}Mo	M. ^{100}Mo	M. ^{100}Mo	M. ^{100}Mo
Sector 5	M. ^{100}Mo	M. ^{100}Mo	C. ^{100}Mo	C. ^{100}Mo	C. ^{100}Mo	C. $^{150}Nd_2O_3$	C. $^{96}ZrO_2$ & C. $^{48}CaF_2$
Sector 6	C. ^{82}Se	C. ^{82}Se	C. ^{82}Se	C. ^{82}Se	C. ^{82}Se	C. ^{82}Se	C. ^{82}Se
Sector 7	C. ^{82}Se	C. ^{82}Se	C. ^{82}Se	C. ^{82}Se	C. ^{82}Se	C. ^{82}Se	C. ^{82}Se
Sector 8	C. ^{82}Se	C. ^{82}Se	C. $^{nat}TeO_2$	C. $^{nat}TeO_2$	C. $^{nat}TeO_2$	C. $^{nat}TeO_2$	C. $^{nat}TeO_2$
Sector 9	C. $^{130}TeO_2$	C. $^{130}TeO_2$	C. $^{130}TeO_2$	C. $^{130}TeO_2$	C. $^{130}TeO_2$	C. $^{130}TeO_2$	C. $^{130}TeO_2$
Sector 10	C. ^{100}Mo	C. ^{100}Mo	C. ^{100}Mo	C. ^{100}Mo	C. ^{100}Mo	C. ^{100}Mo	C. ^{100}Mo
Sector 11	C. ^{100}Mo	C. ^{100}Mo	C. ^{100}Mo	C. ^{100}Mo	C. ^{100}Mo	C. ^{100}Mo	C. ^{100}Mo
Sector 12	C. ^{100}Mo	C. ^{100}Mo	C. ^{100}Mo	C. ^{100}Mo	C. ^{100}Mo	C. ^{100}Mo	C. ^{100}Mo
Sector 13	C. ^{100}Mo	C. ^{100}Mo	C. ^{100}Mo	C. ^{100}Mo	C. ^{100}Mo	C. ^{100}Mo	C. ^{100}Mo
Sector 14	C. ^{100}Mo	C. ^{100}Mo	C. ^{100}Mo	C. ^{100}Mo	C. ^{100}Mo	C. ^{100}Mo	C. ^{100}Mo
Sector 15	C. ^{100}Mo	C. ^{100}Mo	C. ^{100}Mo	C. ^{100}Mo	C. ^{100}Mo	C. ^{100}Mo	C. ^{100}Mo
Sector 16	C. ^{100}Mo	C. ^{100}Mo	C. ^{100}Mo	C. ^{100}Mo	C. ^{100}Mo	C. ^{100}Mo	C. ^{100}Mo
Sector 17	C. $^{130}TeO_2$	C. $^{130}TeO_2$	C. $^{130}TeO_2$	C. $^{130}TeO_2$	C. $^{130}TeO_2$	C. $^{130}TeO_2$	C. $^{130}TeO_2$
Sector 18	M. ^{116}Cd	M. ^{116}Cd	M. ^{116}Cd	M. ^{116}Cd	M. ^{116}Cd	M. ^{116}Cd	M. ^{116}Cd
Sector 19	C. $^{nat}TeO_2$	C. $^{nat}TeO_2$	C. $^{nat}TeO_2$	C. $^{nat}TeO_2$	C. $^{nat}TeO_2$	C. $^{nat}TeO_2$	C. $^{nat}TeO_2$

Table 4.2: NEMO3 sector source distribution.

was also separated from each other by a small blank foil region as well for isolation to stop cross contamination of events. Fig4.6 shows a breakdown of this strip's configuration.

All the foil's thicknesses were made to ensure that the density does not exceed 60 mg/cm^2 to ensure that the energy resolution is not compromised by energy losses in the foils. The actual densities of the foils fall between 30 and 60 mg/cm^2. This gives an actual thickness of lower than 60 μm for metallic foils and lower than 300μm for composite foils.

4.2.2.4 Radio Purity

Radio purity is of very high importance in all of NEMO3's materials for suppression of backgrounds (see sec.4.3). To this end all sources were measured for radio purity in germanium detectors to ensure they met the stringent levels needed (see Table.4.3). Also all the backing Mylar film and glues used were tested in this way. Radio purity was not just a consideration to source foils as can be seen in Sec.4.3, all materials were extensively checked and selected both internally and externally from the Geiger component's support structure, the PMTs, calorimeter components even the gas (see Table.4.4). On a practical basis this means use of very pure copper, steel, iron as well as no plastic components other than uncoloured delrin. The sources were all purified to ensure reductions in ^{214}Bi, ^{208}Tl, ^{40}K, ^{238}U and ^{232}Th in order to decrease backgrounds and increase the sensitivity to $\beta\beta0\nu$ decays.

The purity measurements were all done with HPGe detectors (4 in total) which look at the gamma ray spectra of sample materials in the energy region of 30 - 3000 keV. From these we can work out the levels of common radioactive elements from their characteristic gamma ray spectra. A schematic of an HPGe detector is shown in Fig.4.7.

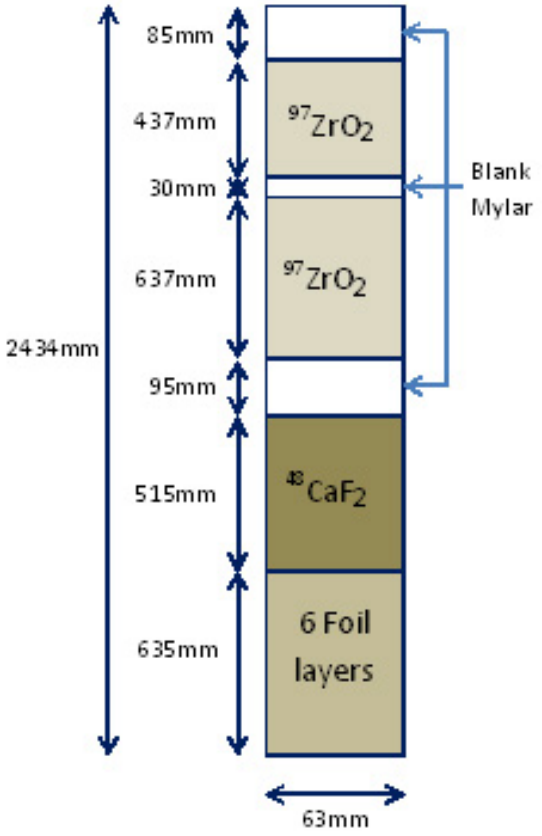

Figure 4.6: Sector 5 strip 7 configuration.

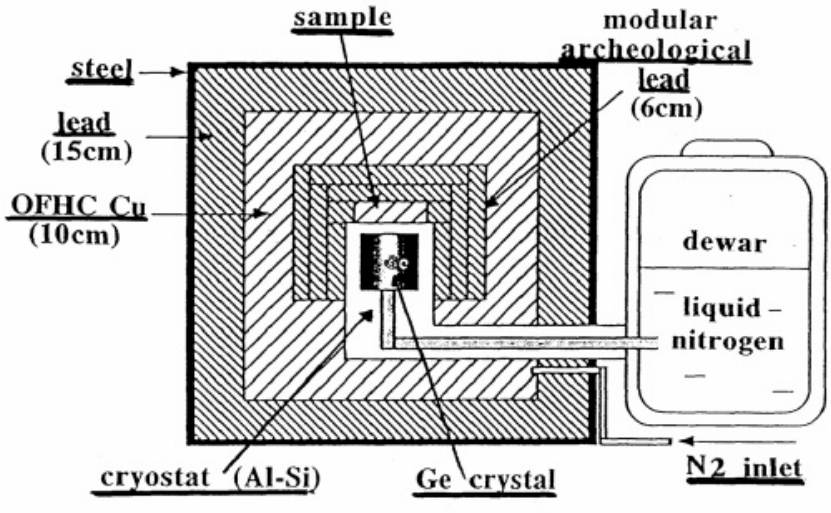

Figure 4.7: Schematic of an HPGe detector. [147]

Source sample Activity (mBq/kg)	Meas. mass (g)	Exp. (h)	^{40}K	^{235}U	^{238}U		^{232}Th	
					^{234}Th	^{214}Pb ^{214}Bi	^{228}Ac	^{208}Tl
^{100}Mo (M) 2479g	733	840	<5	1.5 ± 0.3	<15	<0.39	<0.5	<0.11
^{100}Mo (C) 4435g	735	648	<6	<0.3	<15	<0.34	<0.3	<0.10
^{82}Se (C) 932g	800	628	55±5	20.0±0.7	<18	1.2±0.5	<1	0.4±0.1
$^{130}TeO_2$ (C) 454g of ^{130}Te	633	666	<8	0.5	<20	<0.67	1.7±0.7	<0.46
^{116}Cd (M) + Mylar Cd(I)	299	368	<20	<1	<56	<1.7	<4	<0.83
405g of ^{116}Cd Cd(II)	257	778	<13	<0.5	<12	<1.5	<2	<0.51
$^{150}Nd_20_3$ (C) 37.0g of ^{150}Nd	58.2	458	<70	<1	<66	<3.0	20±7	10±2
$^{96}ZrO_2$ ITEP (C) 4.1g of ^{96}Zr	13.7	624	<217	<7	222	<16	<23	<10
$^{96}ZrO_2$ INR (C) 5.3g of ^{96}Zr	16.6	456	583±167	<10	<211	<14	<27	<5.5
$^{48}CaF_2$ (C) 6.99g of ^{48}Ca	24.56	1590	<50	<2	<15	<4	<6	<2
$^{Nat}TeO_2$ (C) 166g of ^{130}Te	620	700	8±3	<0.3	<17	<0.17	<0.9	<0.090
Cu (M) 621g	1656	853	<8	<0.2	<5	<0.12	<0.4	<0.040

Table 4.3: Summary of major source contamination levels for HPGe. [147]

Components of NEMO 3	Weight in kg	Total radioactivity (Bq)			
		^{40}K	^{214}Bi	^{208}Tl	^{60}Co
Photomultiplier tubes	600	831	302	17.8	not measured
Scintillator blocks	6400	<102	<1.2	<0.6	<3
Copper	25000	<125	<25	<10	<6
Iron petals	10000	<50	<6	<8	17±4
μ-metal PMT shield	2000	<40	<4	<4	<4
Tracking detector wires	1.7	$<8\times10^{-3}$	$< 10^{-3}$	$<6\times10^{-4}$	$< 10^{-2}$
Iron shield	180000	<3000	<400	<300	<600

Table 4.4: Summary of major detector backgrounds from HPGe. [147]

4.2.3 Tracking

4.2.3.1 Design

The tracking and identifying of particles inside the NEMO3 detector is the combined purpose of the Geiger tracking volume and the magnetic field. This system allows for full 3D tracking with charge identification. Inside the tracking volume are vertically suspended wire drift cells working in Geiger mode (sec. 4.2.3.2). There are a total of 6180 cells which each consist of 8 vertically mounted cathode wires in an octagonal configuration with a central anode wire. Each octagonal cell is 3cm in diameter and 2.3m long. The 8 cathode wires are shared with their four nearest neighbours to reduce the number of wires used (and increase the transparency of the tracking volume). These cells are assembled into 18 layers (9 either side of the foil) with extra cathode wires present between layers to reduce electrostatic cross talk between layers Fig.4.8. The wires are all stainless steel (due to the presence of a magnetic field) and 2.3m long with 50μm diameter and are attached to the top and bottom iron plates that cover the segments known as petals. At the very top and bottom of each cell is a copper tube that is 2.3cm in diameter (so fits inside the cathode wires) and is 3cm long with the anode wire running through it, these are is known as the cathode rings.

Lots of research and development went into the design of the tracking detector especially in optimising the gas mixture used as well as the wire thicknesses and operating voltages. These quantities require balance in order to obtain maximum efficiency, longevity, accuracy and minimisation of the ageing effect. 9 layers were chosen between source foil and calorimeter as the optimum balance between tracker volume transparency (the reduction of material in the tracker causing possible scattering) and giving enough vertices to provide accurate and efficient track reconstruction.

The gas mixture used in the detector was helium and ethyl alcohol at 14^{o}C (at this temperature the alcohol has a 39 mbar partial pressure). The helium provides a very low Z medium (important in minimising energy losses and scattering in the tracking volume) and the alcohol acts as a quencher. 1% Argon and 1500ppm of water were added to the He alcohol mixture to increase stability of the cell operation. A gas overpressure of roughly 10mbar was maintained to flush contaminants from the surrounding volume. These operating conditions allow for a maximal operating voltage of the cell of 1900V.

The 18 tracker cell layers are divided into 2, 9 either side of the central foil. These 9 layers are sub grouped into 3 groups. The first 4 consecutive layers lie next to the foil to provide good event vertex reconstruction then there is a gap for a top and bottom mounted γ veto calorimeter block and then 2 layers and another gap for a second veto block. After that there are the final 3 layers which give accurate vertices for calorimeter hits.

Electrostatic simulations with Garfield were used to create a voltage map to try and keep the cells operating at the same electric field strength throughout the tracker. This is important as it affects the propagation times and triggering of cells. Because of this during detector operation cells were grouped and connected to voltage supplies that maintained the voltage differences set out by

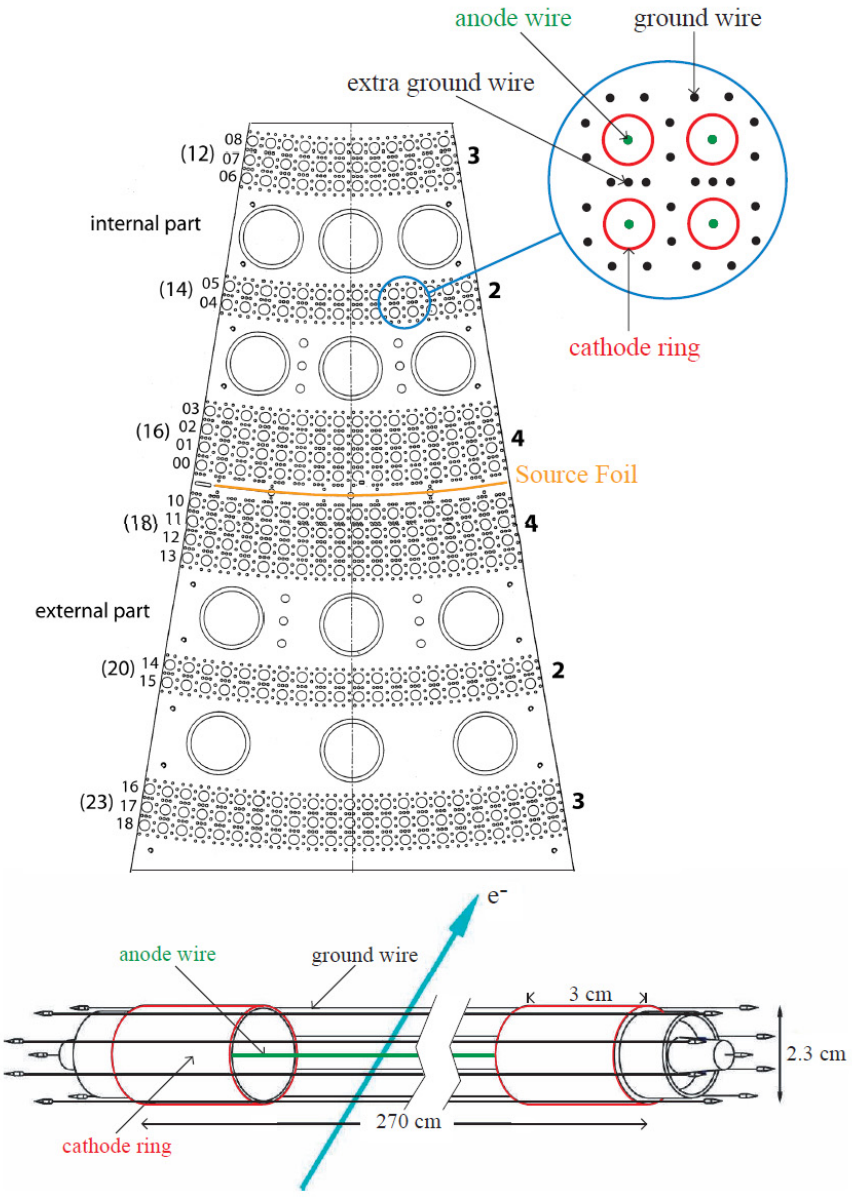

Figure 4.8: Sector wire positions. [147]

the voltage maps.

The magnetic copper coil outside of the calorimeter creates a constant field of 25 Gauss in the vertical direction (parallel to the tracking wires), which gives charged tracks a curvature through the tracking volume as they follow a helical path.

The wiring and construction of the tracking detector was done by hand in a clean room environment class 10,000. Stainless steel wires were used due to the presence of the magnetic field. A special machine was also used to check the consistency of wires prior to construction and after construction quality tests were undertaken. These tests consisted of a determination of the ability of the cell to obtain consistent Geiger plasma that propagates to both end of the cell and free from extraneous secondary triggers of plasma production. A full test rig for completed sections was made for use with cosmic rays. The cathode rings were connected to grounds and the anode pulse was read with an oscilloscope to see the 2 negative peaks when the plasma reached the 2 ends. Tests were done at ground level and so a cosmic ray rate of 60Hz was apparent for the tests, which is a factor of 30 greater than the operating conditions so equivalent to several years of running. If any anode or cathode wires were found to be faulty in these and other tests they were replaced.

4.2.3.2 Operation and Theory

The drift cells in NEMO3 work in Geiger mode. The more common operation of cells of this type is proportional mode. Both modes make use of the ionisation of tracking gas by the incident ionising particles (usually electrons in this case) to produce a signal in the anode wire but the mechanism differs depending on the voltage on the anode wire.

When ionising radiation (for example electrons) moves through the tracking volume it ionises some of the He atoms present in the tracking gas (initial ionisation yields roughly 6 electrons per cm). The incident particles then proceed to propagate with minimal energy loss, whilst the electrons liberated from the He will then drift towards the nearest positively charged anode due to the potential difference between it and the grounded cathode wires. The positive He^+ will move towards the cathode much more slowly until it reaches it and recovers its missing electron and returns to He. However it is the electron that produces the signal and the speed of its drift is proportional to the level of voltage applied to the anode. Depending on the size of this voltage an avalanche effect can occur. An avalanche of helium occurs when acceleration due to the potential difference speeds up the liberated electrons enough to ionise further helium atoms on their path to the anode this causes an exponential multiplication of the initial electrons produced, known as an avalanche. Also excited helium atoms on returning to the ground state will emit short range UV photons (mean free path is about 1mm) that will also ionise further He atoms adding to this process.

In Geiger mode a large voltage is applied on the anode, this is how NEMO3 operates at roughly +1620V. In this mode large avalanche effects occur over a time period of about 10^{-8}s and drift velocities far from the wire are about 1cm/μs and increase to 2.3cm/μs close to the wire where the field is high, at about 100 μm away. During this small time scale period close to the wire large

numbers of electrons accumulate separated from their positive ions forming a plasma. These electrons act to screen subsequent electrons from the field in the region close to the wire. Further away the field remains constant as the electron's field is cancelled by the positive He^+ ions. This reduction in field seen by the electrons close to the wire reduces the electron's momentum and consequently the rate of new ions and liberated electrons created. The same is true with the number of UV photons produced. Therefore the avalanche drops off for this small region of the wire this is known as a burnt out region as the plasma reduces the effect that causes it and so destabilises and stops. However before this happens the UV photons produced in this region travel far enough (mean free path of about 1mm) to neighbouring regions of the wire and cause ionisation of He atoms there, where no electrons are shielding the wire charge and so initiate plasma in the neighbouring regions. This process causes a propagation of the plasma from the initial point of incident particle interaction, along the anode wire to its two ends. The speed of this plasma propagation is of the order of 5cm/μs taking a total of 50μs to traverse the entire wire. The size of the signal produced by the cell in this mode is of the order of 100mV and therefore able to be read out directly without complicated amplification. Also this mode of use provides 3D tracking information from the signal on the anode wire. This is achieved by measuring the time difference between the arrival time of the pulses at either end of the anode wire see Eqn.4.9. This can be converted into a vertical position due to the fact that the plasma propagates with the same speed in either direction, whilst maintaining good detector transparency. The downside of this operation mode is that the down/dead time for a cell after firing is quite large, in the order of 10ms. However NEMO3's expected event rate is 0.2Hz and therefore this is adequate for our uses.

In NEMO3 both the anode wire and the two cathode rings at each end of every cell are read out by the DAQ electronics. It is from these that the track hit is reconstructed. The cell's anode voltage varies as follows. Initially the anode voltage is at its high operating level roughly 1620V as the avalanche occurs and electrons drift toward the anode and cause a voltage drop in the anode. The voltage continues to drop as the number of electrons reaching the anode increase until the continuous level of a stable plasma (the rise time is very fast taking about 10ns). Next the level remains roughly constant as the plasma propagates towards the ends of the anode wire. When the plasma reaches the closest end a positive signal spike is created in the cathode ring. At the same time the plasma destabilises as the area burns out and the anode voltage rises as now only half the plasma exists. This is known as the "'one plasma"' amplitude which is roughly 50mV on a 270Ω readout. When this last remaining plasma reaches the end of the wire a similar positive cathode pulse is seen in the cathode ring at that end and the voltage on the anode voltage rises to its normal operational value. A theoretical example of these traces is seen in Fig. 4.9.

From these traces 6 times can be determined using analysis using thresholds. They are

- ta_1 - start of a signal, which is the time the electrons ionised from the gas reach the anode wire.

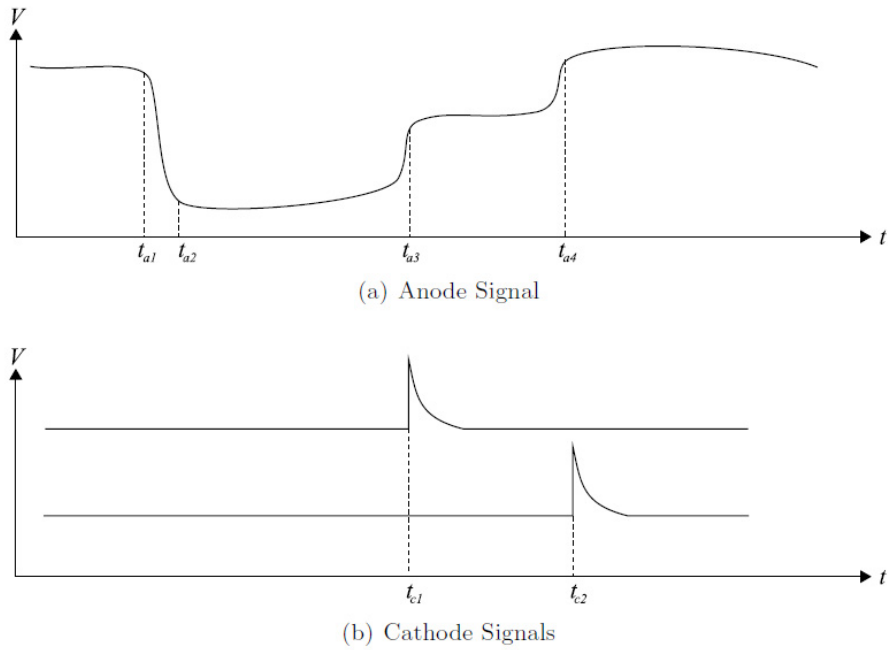

Figure 4.9: Theoretical anode and cathode signals for Geiger mode operation. [148]

- ta_2 - beginning of the lowest part of the anode signal
- ta_3 - the time at which the plasma has arrived at one end of the cell
- ta_4 - the time at which the plasma has arrived at the other end of the cell
- tc_1 and tc_2 - time at which the plasma arrives at cathode one and two

in practice $ta_3 \approx tc_1$ and $ta_4 \approx tc_2$

This gives us 4 times and from these 4 plus the calorimeter hit time (Ct) which starts the TDC we can calculate a ring in which the track must intersect at a tangent this is done as follows.

The centre of the ring is the exact position of the tracking wire that is fired therefore has a fixed location in X and Y. The Z coordinate comes from the cathode signal arrival times tc_1 and tc_2. if the event happened in the exact centre of the wire the arrival time at each cathode ring would be identical. If it was closer to one end than another then arrival at the closer end would be sooner than the far end. Knowing this and the average plasma propagation velocity V_p we can work out the distance from one end of the wire using Eqn.4.1

$$D_z = tc_1 V_p \tag{4.1}$$

where D_Z is the distance from the centre of the wire.

The time of the cell firing is taken as half way up the leading edge of the anode distribution in this case $ta = (ta_1 + ta_2)/2$. From this we then calculate the degenerate ring from which the initial ionisation point could have been before drifting to the anode wire using V_d the known average drift velocity using Eqn.4.2.

$$r = (Ct - ta)V_d \tag{4.2}$$

where r is the radius of the ring of possible degenerate initial ionisation positions and Ct is the calorimeter trigger time. It is impossible to tie down the location of the initial ionisation in a single cell any more precisely. So to determine the actual position, tracking information for more cells must be included. Track segments are generated from 3 consecutive fired cells these can be joined via possible track paths between each cell see Fig.4.10. From this we can see that each cell can be joined to its neighbour by 4 possible paths and by comparing paths between 2 sets of 2 connections (ie.3 consecutive cells) we can use algorithms to determine the most likely path of a particle (i.e. one that conforms to a theoretical shape or path or has the least deflection between cells) shown in red.

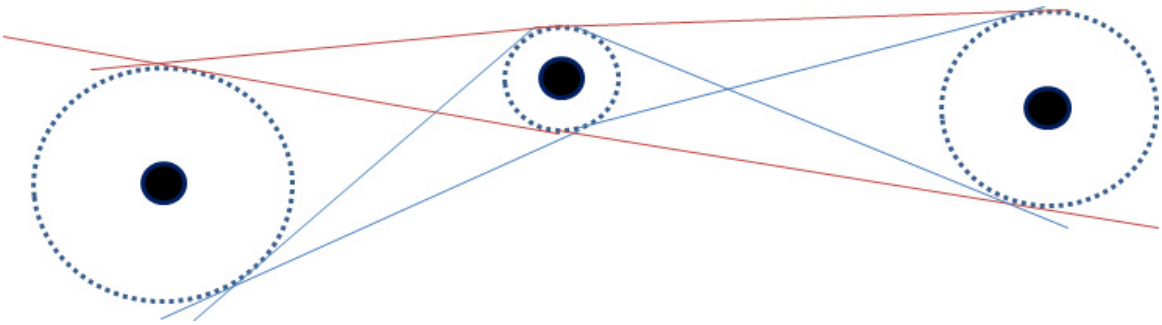

Figure 4.10: Top down representation of track segment and possible connections.

In Fig.4.10 the black points are the cell anodes and the dotted circles are the degenerate locations on the radius. The possible paths are shown in blue and the most likely paths with least deflection are shown in red

These track segments can then be combined with algorithms devised from helical track paths using chi squared likelihood fits to create a complete track of an ionising particle through the tracking volume

The ethyl alcohol acts to quench the photo-ionisation process. Alcohol has many vibrational and rotational energy levels that can be excited on absorption of a UV photon with no subsequent photon emission. This will stop subsequent ionisations and avalanches as well as reducing the mean free path of UV photons in the detector. This is important to stop cells from constant triggering as well as stopping neighbouring cells being triggered. Also the alcohol acts to mop up/neutralise the He^+ ions. Because of this alcohol molecules become the charge carriers back to the cathode wires. Therefore no UV photons are produced by helium ions when neutralised, which halts creation of secondary avalanches at cathode wires. The alcohol ions are instead neutralised at the cathode wires and the excess energy gained will only break apart the molecule into simpler ones and not emit photons. However it is a balancing act between suppression of unwanted effects and not too high a concentration to stop the creation of a stable propagating plasma. The argon and water added later was only to stabilise the cell's behaviour, the end product was a stable plasma generation with a

propagation time of around 52μs.

4.2.4 Calorimetry

4.2.4.1 Calorimeter Design

The calorimeter is designed to surround the tracking volumes with 2 circular vertical walls at either end of the tracking volume either side of the foil and some strategically placed blocks on the top and bottom end caps between gaps in the tracking volume. The calorimeter has 3 major uses in NEMO3; measurement of the incident particle energy, providing fast timing information of incident particles (allowing time of flight measurements to be made) and providing a fast triggering signal for DAQ and event reconstruction.

The calorimeter comprises 1940 optical modules. These consist of many components which can be seen below in fig.4.12. But the three major components are a scintillating plastic block for energy deposition, a PMT for measurement of scintillation light and a number of light guides for interfacing the previous two.

The blocks used in the calorimeter are plastic scintillators and were chosen to minimize backscattering and for their radio purity. The blocks were constructed of a regular polystyrene ($C_6H_5CH{=}CH_2$) and were produced with conventional polymerization methods with the addition of small percentage of p-terphenyl (PTP) and 1.4bis (5-phenyl-2-oxazoly) benzene (POPOP). All the scintillator blocks have a mean Z value of 3.7 per atom and a thickness of 10cm which stems from a trade-off between transparency of the block for scintillator light propagation and efficiency at tagging gammas passing through it, which is important for distinguishing and measuring background events. Only 3cm is actually needed to stop electrons with an energy of 4 MeV but at 10cm thicknesses 50% of gamma ray energy at 500 keV is absorbed.

Due to the toroidal nature of NEMO3 there are 7 different shapes of polystyrene blocks used. Each of the 20 sectors has 97 blocks in total. For the top and bottom petals 12 blocks are used for each and are arranged into 4 rows of 3 blocks. Each row is progressively further from the centre of the detector so has a different shape labelled L1-L4. The inside wall has a unique shaped block labelled IN for which there are 2 rows of 17 blocks for each sector and the outside wall has two types of block known as EE and EC for edge and centre blocks respectively. These are arranged in 3 columns of 13 rows. The position of these 7 block types in a sector can bee see in Fig.4.11.

All the blocks are mounted on a rigid frame inside of the He gas volume, this maximises the efficiency and minimises the energy losses. The PMTs however are mounted outside and isolated from the He gas volume. This isolation of the PMTs greatly reduces ageing effects caused by He gas permeating into the evacuated tubes.

The photon multiplier tubes (PMTs) used in NEMO3 were constructed by Hamamatsu and were chosen for 2 reasons. The first reason was their very low background activity. From work on NEMO2 it was found that the greatest source of activity in the detector was the glass used in the PMTs.

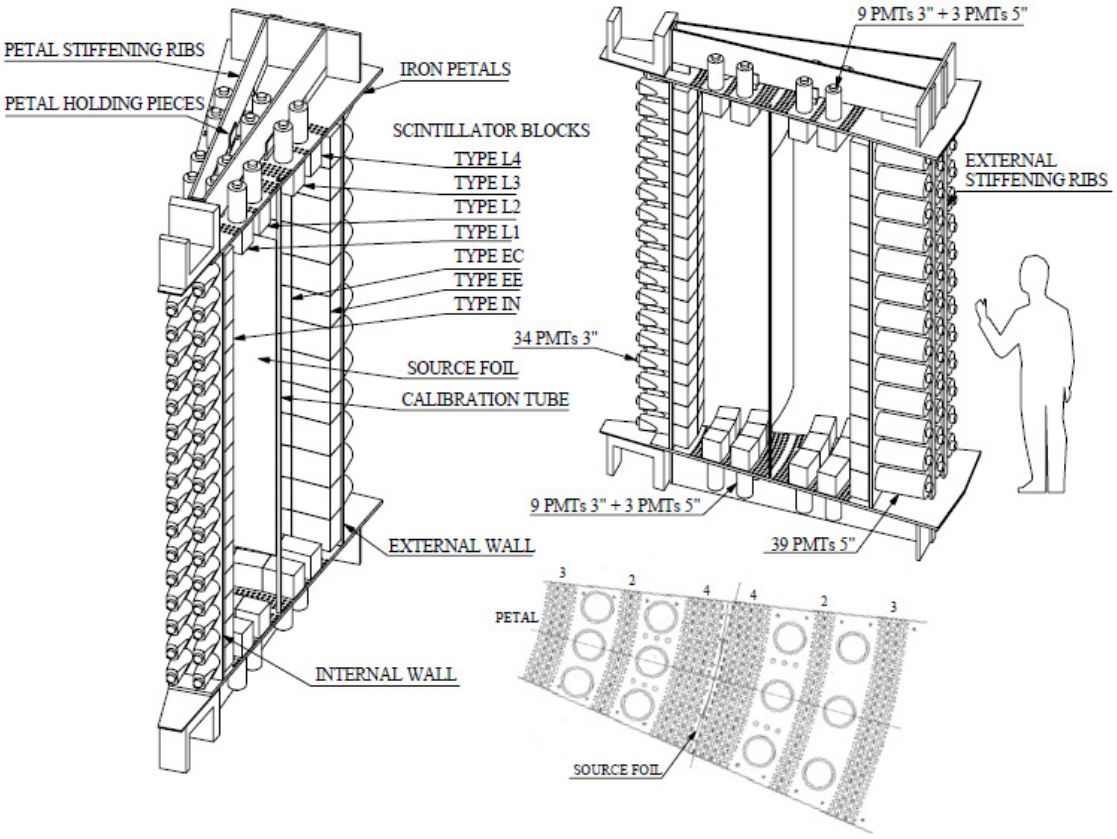

Figure 4.11: Example of calorimeter sector design and use of different blocks. [147]

The major contaminants were ^{40}K, ^{214}Bi and ^{208}Tl and Hamamatsu were able to produce PMTs with radio purity 10 to 100 times better than standard glass, which was able to meet our criteria of less than 0.83 and 0.17 Bq/kg for ^{214}Bi and ^{208}Tl respectively. The other reason Hamamatsu was chosen was the performance of their PMTs. The experiment required energy measurements up to 12 MeV and their tubes had excellent linearity of voltage response with energy up to 4 MeV and good performance right up to 12 MeV, all with low electronic noise (around 10Hz) at minimal threshold. Also they had a superior combination of quantum efficiency and gain of the photocathode which gave excellent energy resolution performance.

Two different PMT sizes were required for use in NEMO3 due to its geometry they were the R6091 3" PMT with 12 dynodes and a flat photocathode and the R6594 5" PMT with 10 dynodes and a hemispherical photocathode.

Due to the differing size and shape of the front fascia of the 3" and 5" PMT compared to the polystyrene blocks, a configuration of light guides was needed to couple the two types to blocks. For the 3"' PMTs a single light guide was used to couple the flat front face to the blocks, but for the 5" PMTs the same light guide was used with an addition of a second light guide between the PMT and it to accommodate the hemispherical front face.

The light guides themselves were made of an optical PMMA (poly(methyl methacrylate)) plexiglass of 60 mm thickness for the initial guide. Its role was not just in channelling scintillation light but also to protect the front surface of the PMT from helium gas. The light guides had a 98% transmission of wavelengths between 380-420nm, 420nm being the wavelength of the shifted scintillation light. The light guides were secured with an iron ring which proved useful in making things gas tight and securing magnetic shielding to the PMT.

Many other components went into a complete optical module as can be seen in Fig.4.12. They include a light-tight sleeve cover for the PMT, a magnetic mu metal shield around the PMT to protect it from the magnetic fields which would hamper its operation. There is an electronic base attached to the PMTs for distribution of voltages to the dynodes and an optical fibre inserted into the block for calibration measurements (see sec.4.2.5). Also the scintillator blocks and light guides were wrapped in layers of Teflon for light diffusion and aluminised Mylar for specular light reflection, all of these measures were to isolate and contain both scintillation light and ambient light from Geiger propagation and enhance the light collection of the device whilst minimising energy losses by incident ionising particles.

A schematic of a complete 5" optical module can be seen in Fig.4.12

4.2.5 Calibration

It is very important with a long running experiment like NEMO3 to maintain accuracy of time and energy measurements inside the detector. Despite initial calibrations on installation, components like PMTs tend to drift and alter with time. For that reason a multitude of calibration mechanisms and slow controls for PMT and Geiger voltages were designed to track and correct changes in the

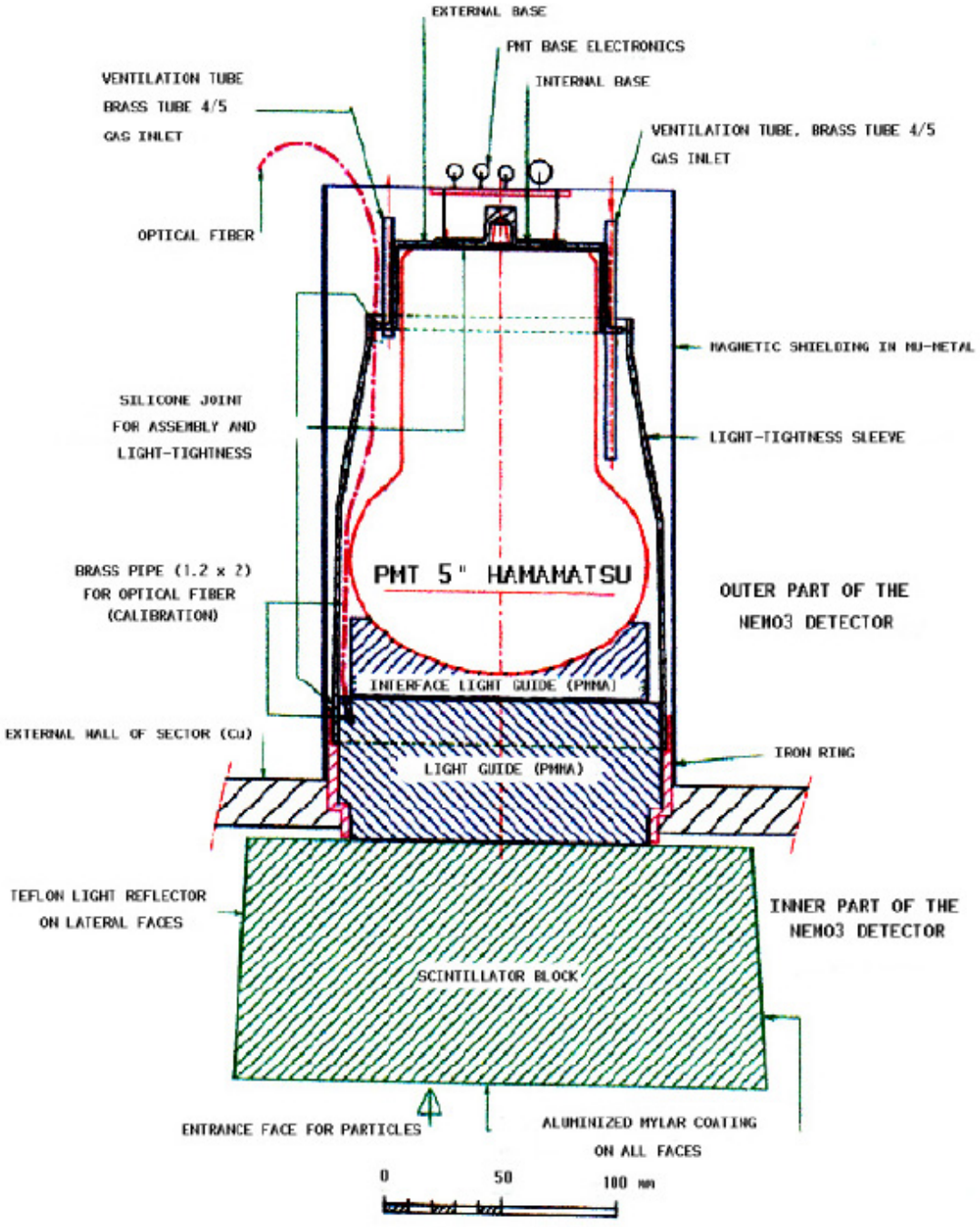

Figure 4.12: Example of a complete optical module of the calorimeter. [147]

machine on a post processing and immediate basis.

There were two types of calibration procedures. Absolute calibrations of energy and timing were done with special runs 6 times a year for about 3 consecutive days where data taking was stopped. During these times radioactive sources were lowered down special high purity copper tubes filled with the same He tracking gas as the rest of the track volume. This was done manually by technicians on site removing some of the top covers and lowering source holders attached to delrin rods down these normally sealed holes. These copper calibration tubes were placed at the edges of each sector during construction, they were mounted vertically next to the source foils and spanned the entire height of the detector. The tubes contained 6 small window Kapton aperture windows measuring 26 x 20 mm and 25μm thick (fig.4.13). The windows were placed back to back facing the inner and outer walls and were situated at the pipe centre, +90 cm and -90cm. This was chosen to provide approximately uniform illumination of the scintillator blocks on the walls. A single source was used for each pair of windows giving 60 calibration sources.

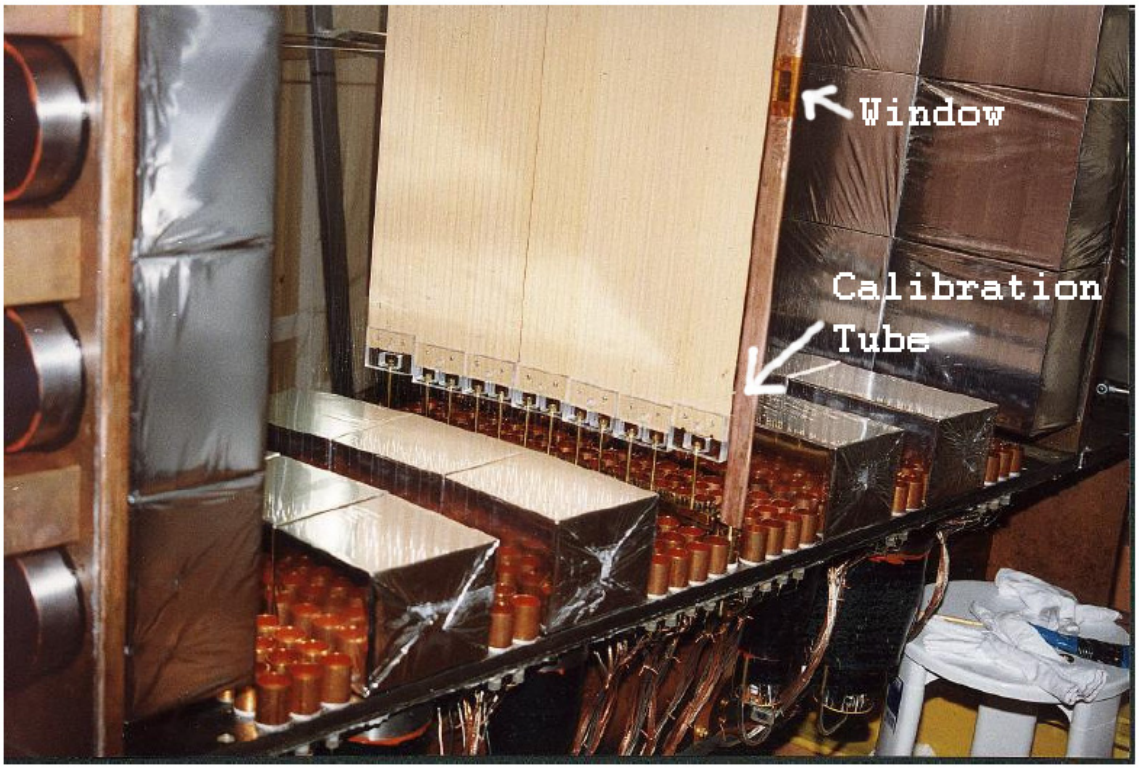

Figure 4.13: Image of calibration tubes at the end of a sector with visible window. [147]

Because most of the energy measurements being made by the calorimeter and certainly the most important ones are from electrons, they were chosen to be the particle of choice for calibration. To this end 2 electron sources were used to provide an absolute standard energy calibration of all the PMTs inside the NEMO detector, they were a ^{207}Bi source and ^{90}Sr. The ^{207}Bi was the main source used and has 2 mono-energetic conversion electron emissions at 482 and 975 keV which can provide energy calibration up to 1 MeV. However decays of ^{207}Bi also produce similar energy gammas and

so tracking needs to be switched on for these calibration runs in order to distinguish the calorimeter hits. As a consequence a compromise must be made between the greater statistics from a more active source and not overloading the tracker cells. The activity of the source was chosen to be 222Bq to achieve this. To measure higher energies up to 3 MeV an additional calibration point is required this comes from the upper tail of beta emissions from ^{90}Y a daughter of ^{90}Sr. For timing calibrations a third source was used ^{60}Co during construction to make relative offset corrections to PMT channels. ^{60}Co decays giving 2 simultaneous gamma rays of energy 1332 and 1172 keV these can be used to measure the relative corrections.

Between absolute calibrations there are daily corrections made of the energy (ADC), timing (TDC) and more infrequently linearity between 0 and 12 MeV. This is done prior to every data taking run using a laser system. A N_2 laser was used emitting wavelengths of 337.1nm. The laser light was passed to a scintillator and that light transmitted to each of the scintillating blocks via an optical fibre attached during construction. The scintillator was used so that the pulse shape and wavelength emitted mimicked the light deposition of an electron in the scintillator.

The light from the laser was first split and half sent to a reference system to monitor the laser output. The reference part was split again sending half to a photo diode and half to a small reference PMT via optical fibre. The other half was directed to a carousel of optical filters that could be automatically changed. The filters attenuate the light, simulating energies from 0 to 12 MeV, and then the bowl-shaped scintillators wavelength-shift it to the 420nm needed to mimic the wavelength of light from an electron absorption in the scintillators. This half was then split again and sent via arrays of optical fibres to all the 5" and 3" PMTs as well as some more reference PMTs to monitor output after filtering. Using these combinations of energies and reference systems linearity over the energy range and gain and timing of each PMT could be monitored and corrected for. Figure 4.14 shows a schematic view of the laser calibration system configuration and housing.

4.2.6 Shielding

Due to the rarity of neutrinoless and 2 neutrino double beta decay not only do all materials inside the detector need to be as radio-pure as possible but also external backgrounds need to be reduced as well. This was done by using shielding and the presence of the magnetic field. One of the most significant shieldings that NEMO3 has is its location in LSM. The rock of the mountain above it reduces cosmic muons flux to $5 \times 10^{-5} m^{-2} s^{-1}$ a reduction of more than a million over sea level and the flux of fast and thermal neutrons is 10^{-6}neutrons.cm^{-2}s^{-1} (the flux of neutrons greater than 1 MeV is 1.6×10^{-6}cm^{-2}s^{-1}). The rock accounts for a for a water equivalent of 4800m depth and because of this the major backgrounds are externally entering gammas from radioactive decays or neutron capture. The neutron component comes from (α,n) reactions, spontaneous fission of uranium and interactions of cosmic ray muons in the rocks. The gamma ray flux inside LSM that comes from natural radioactivity, radiative neutron capture and bremsstrahlung of muons, has been studied extensivly by both the NEMO collaboration and others [149, 150]. The dominant

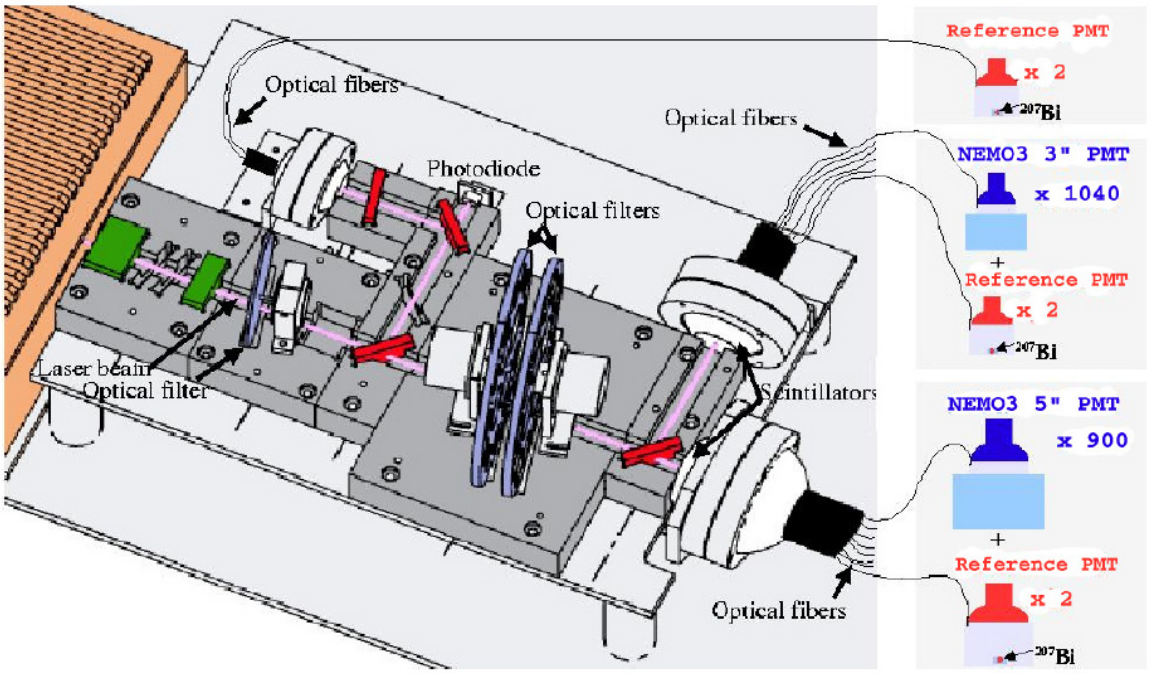

Figure 4.14: Laser calibration system and configuration. [147]

component is the radioactivity of the surrounding rocks. A background gamma ray component can cause extraneous events from interactions leading to $e^- + e^+$ pairs or a pair of e^-. These can occur in the outer structure leading to transiting external electrons from one side of the detector to the other or inside the foil leading to extra events or even just gamma interactions casing scintillator hits with no associated electrons in the tracking volume. Therefore methods are required to reduce their effect. There are two major ways these backgrounds are reduced or rejected.

The first is due to the magnetic coil that lies just outside the PMTs of the calorimeter layer. This coil is made of 203 copper rings 10 mm in height and 10 mm thick. The exterior is covered with 90mm thick panels of iron for backfield plates. In total it weighs 5 tonnes. This provides a field of 25 Gauss which is used to make any electrons inside the tracking volume curve. The helical path of these electrons can be used to determine their charge so e^+ particles can be determined. This alone rejects 95% of the e^+ e^- events. Time of flight measurements can also be used to reject crossing electrons as well as charge reconstruction.

Exterior to the magnetic field are 2 layers of shielding the first is a big iron plate to reduce gamma ray flux. This iron plate is in sections so easily removable and covers the sides and the top and bottom of the petals as well. On the sides behind the magnetic coil it is 20 cm thick whereas on the top and bottom of the petals it's 18cm thick to allow for the necessary structural supports.

The remaining backgrounds can only be reduced by decreasing the neutron capture flux into the detector volume. To this end NEMO3's neutron shielding was designed and optimised to stop fast neutrons of a few MeV as well as reduce the number of thermal and epithermal neutrons. The neutron shield has three separate parts for each surface (sides, top and bottom). For the major

walls of the side behind the iron shielding and magnetic coil 10 large water tanks were placed. The tanks were 35cm thick and contained borated water separated by 28cm of wood. The water in the tanks kinetically slows the fast neutrons via collisions and then the boron atoms capture these slowed neutrons and emit gammas. On the tops and bottom of the detector were 28 cm of wood and below the central tower were tanks containing 20cm thickness of paraffin.

4.2.6.1 Radon Tent

It was found that during initial running of NEMO3 that the radon gas contamination inside the detector was higher than expected (1.2Bq in the 28m^3 gas volume of the tracker) and was hampering the sensitivity of the double beta process. It was hypothesised that radon gas was diffusing through the RTV seals between sectors and getting into the tracking volume. Therefore it was decided that in order to reduce the radon concentration inside the detector a tent would be constructed to fully enclose and isolate the detector from the laboratory air. To construct the tent first a low radioactivity epoxy paint was painted onto the ground to hamper emanation then an iron frame was used to support the 10 sided tent. Two chambers were created one that covered the electronics under NEMO3 and the second that contained the detector. Extra cooling was needed for the electronics so they did not over heat. The lower tented chamber's walls were made of aluminium and plexiglass whereas the chamber housing the detector was made of 200μm of polyethylene walls. The top of the tent was made of iron with 8 outlet vents with filters and active charcoal (Fig.4.15).

The reduced-radon air entering the tent was produced onsite from the laboratory air by use of pumps, filters and active charcoal trapping. The active carbon has microscopic holes that trap and slow the diffusion of the cold slow moving radon atoms due to Van der Waals forces, but allow quick diffusion of the He and other molecules(Fig.4.16). Radon has a half-life of 3.8 days so whilst caught in the carbon it can decay away to its products. The result of this was a reduction of radon contamination to 0.2Bq for the 28m^3 volume.

The system used to do this can be seen in Fig.4.17. First the lab air (15Bq/m^3) is compressed and stored in a tank before filtering with a 0.3μm filter to remove particulates. Next the air is passed into a cooler to reduce the temperature to -50^{o}C this acts to slow the movement of the atoms in the gas before their introduction to the active carbon traps. This increases the capture and therefore reduction of radon in the final gas. The reduced radon gas is then passed through another filter (0.01μm) in order to capture any carbon dust before being introduced to the tented area at a concentration of 0.015Bq/m^3 and rate of 153m^3/h. This is a reduction factor of 1000.

Radon levels were measured and monitored in both the laboratory air and the gas in the tracking detector during certain periods to examine radon level fluctuations. The radon levels we see inside the detector volume after the tent was installed to reduce the concentration in 2003, were 0.2Bq for the entire detector volume which reduces significantly radon's impact on sensitivity. The reduction of the radon gas filtering system of 1000 from that of the lab air but only a reduction of a factor of 6 inside the detector led to the hypothesis that radon must be emanating from detector components.

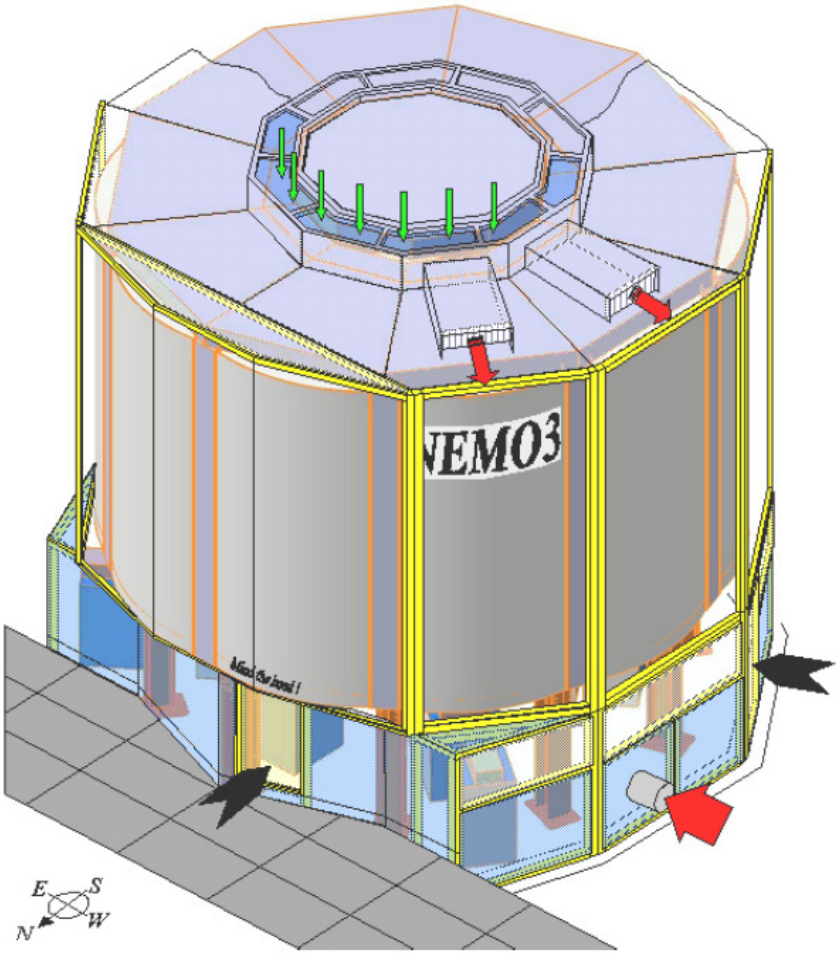

Figure 4.15: Schematic diagram of radon tent. [147]

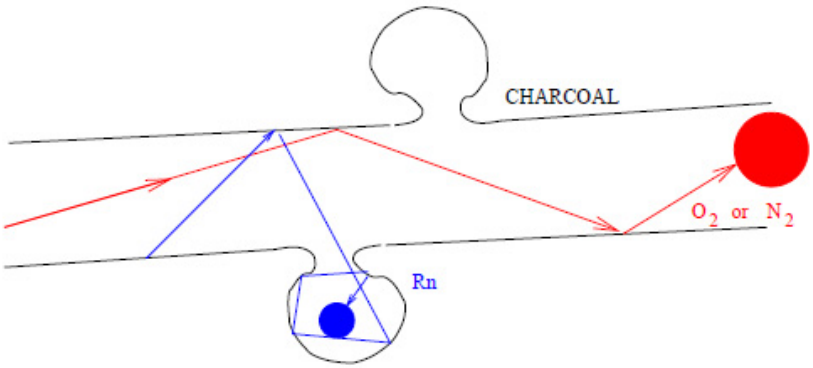

Figure 4.16: Simplified principle of active charcoal trapping. [147]

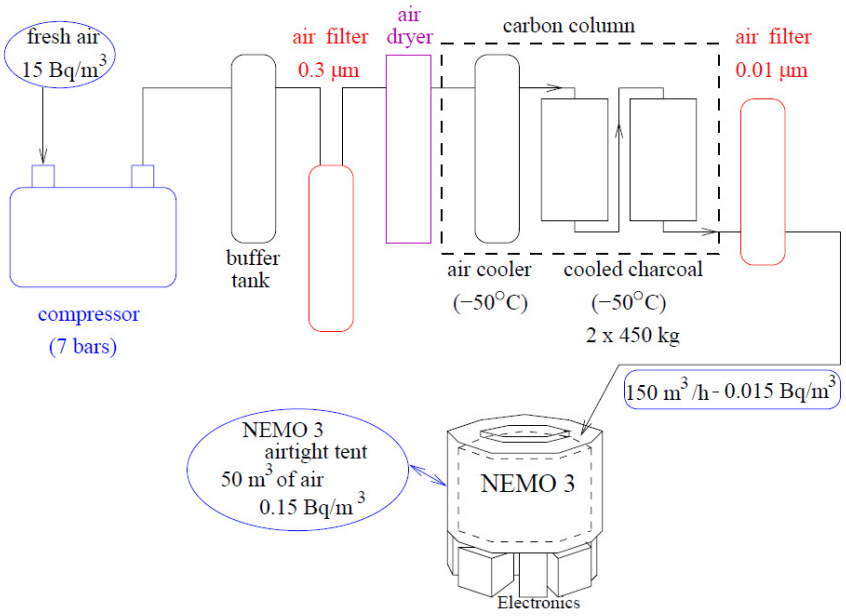

Figure 4.17: Radon system schematic. [147]

4.2.7 Ancillaries and Electronics and Trigger

4.2.7.1 Gas System

As mentioned above the Geiger tracking detector requires constant gas renewal and replacement, this is done by a purpose built gas system (Fig.4.18). The gas mixture is mixed on site by first bottled helium gas being passed through a flow and pressure meter to monitor the gas exchange rate. The He gas is then passed through the primary bubbler in which it is bubbled through ethyl alcohol. It then passes to the cooler (FRIDGEBAC) and secondary bubbler which bubbles the gas mixture through ethyl alcohol again at a constant temperature of 14 ± 0.1^{o}C to obtain the required concentration of 4% alcohol in the gas mixture. There are in fact 2 coolers that do this and either can be used and switched between for fidelity purposes. After chilling the extra argon and water vapour is added to the mixture to achieve the final gas mixture needed for NEMO3 of 1% argon, 0.1% water, 4% alcohol and 94.9% helium. The gas then enters the top of the NEMO3 detector via 2 inlets at the top petal of each sector. At the bottom of each sector there are also 2 outlets for the gas as well. Attached to the gas system is a brass inlet pipe to an external Geiger cell for testing of the gas mixture. This can be filled with gas using valves from either the NEMO3 inlet feed or the NEMO3 outlet after exiting the detector.

4.2.7.2 Electronics and Trigger

NEMO3 has an interdependent electronic readout, data acquisition and trigger system that all share a VME bus. The design allows for normal data taking double beta runs as well as calibration and laser runs.

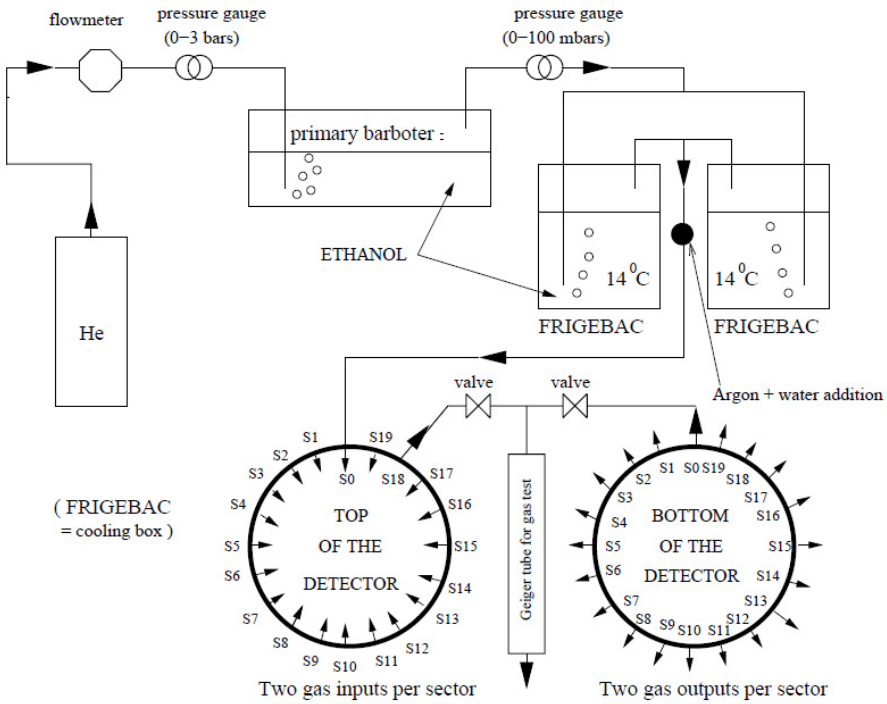

Figure 4.18: Gas regulation system schematic. [147]

NEMO3 has 3 trigger levels. In normal data taking operation only 2 levels are used, with the third reserved for use in calibration runs

The level 1 trigger (T1) comprises a PMT check. For each of the 20 sectors all the PMTs on each side of the foil are separately considered and the number that have exceeded a threshold (activated) are counted. If the number exceeding this threshold is more than a variable limit then the T1 trigger is activated. Its activation produces a 20ns window for which the activated (above threshold) PMTs are sampled.

For the level 2 trigger (T2) hits in the Geiger layers are counted. For each of the 40 half sectors, first, it is determined if they contain possible long tracks from large numbers of spread out Geiger hits (>3 hits), small collections of hits near the foil and scintillators, or no hits at all. Then adjacent half sectors are compared as tracks are attempted to be joined across sectors.

These two levels are used in normal data taking such that only events with at least one scintillator hit and one track candidate in a similar region are needed to trigger acquisition.

The level 3 trigger (T3) is only used in calibration runs. It is a hardwired check for coincidence between tracks in T2 and PMT hits in T1 as it's intended to trigger on electrons coming from the calibration tubes to the calorimeter.

The trigger chronogram for normal PMT+GG (T1 + T2) operation can be seen in Fig.4.19. After the event is started the system waits for activation of the level 1 PMT trigger (T1). The arrival of T1 initiates the "STOP PMT" signal 20ns later that stops PMT sampling. The "STOP PMT" signal triggers a stop via 2 delays the "STOP A" and "STOP-α" signals after 6.14μs and 710μs

respectively. The "STOP A" signal starts a timer for 102μs at the end of which will automatically reset the PMTs taking measurement and start waiting for a new event. The T1 and T2 signals are also sent with a delay of 6.14μs after the "STOP PMT" and if they arrive before the "STOP A" automatic reset timer has counted down two things occur. Firstly the "STOP A" automatic reset timer is cancelled and secondly the PMT electronics are told to start digitising their read out. The "STOP-α" does much the same for the Geiger electronics but there is no delay to the reset, its instantaneous. If no T2 activation has occurred within the delay time then the Geiger electronics are reset but if it has the Geiger electronics are told to digitize the Geiger readouts

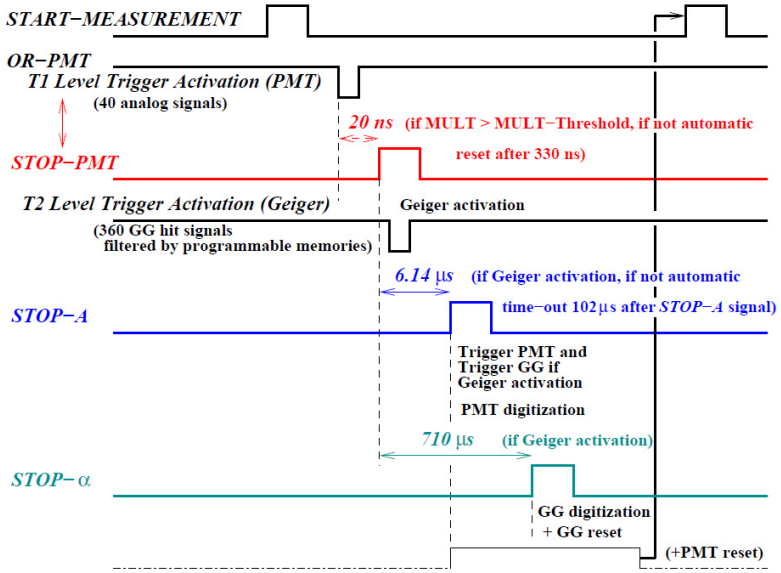

Figure 4.19: Chronogram for the trigger in the PMT + GG mode. [147]

Other electronics for NEMO3 include the slow control and remote Labview access for the HV distribution boards to the Geiger wires and PMT tubes.

4.3 Backgrounds

Due to the nature of NEMO3 looking for rare low activity events, it is of paramount importance to reduce and understand any sources of background that exist in the energy window ($\approx$ 1-3 MeV). Unfortunately this energy level is shared with some sources of natural radioactivity which can mimic a double beta signal both internally and externally. This is why great effort was taken to ensure all materials used in its construction were as radio pure as possible (see sec.4.2.2.4) and that shielding and distinguishing methods were used to exclude as many as possible (see sec.4.2.6).

The long lived natural contaminations of ^{238}U and ^{232}Th that are present inside all material and thus inside the NEMO3 detector, as well as radon deposition give rise to two of the biggest sources of background contamination in the required energy range, they are ^{214}Bi and ^{208}Tl (see Fig.4.20). These isotopes are problematic because their Q_β values are 3.270 and 4.992 MeV respec-

tively and both produce gamma with high enough branching ratio and energy to simulate double beta decay events in the foil and cause problems. ^{214}Bi and ^{208}Tl have half-lives of 19.9 and 3.05 mins respectively.

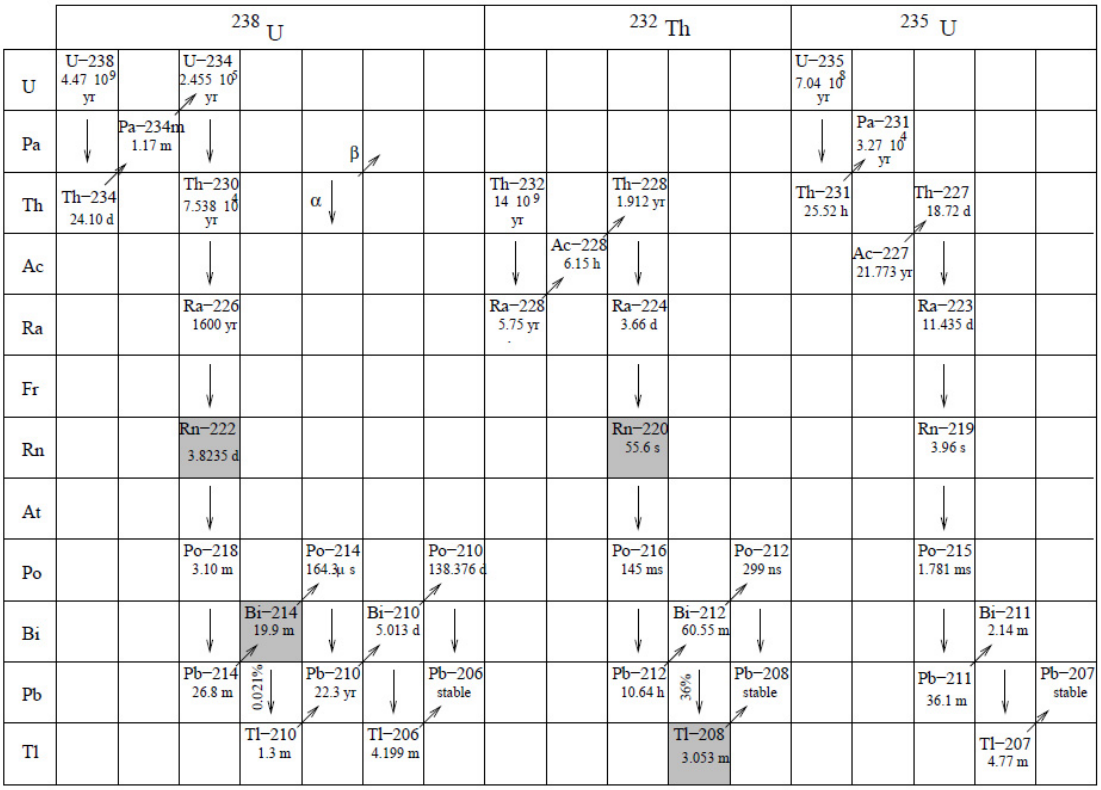

Figure 4.20: The main decay chains of natural radioactivity with the grey indicating major backgrounds for NEMO3. [147]

Backgrounds in NEMO3 are usually separated into internal or external which refers to the location of the background source. Unlike other double beta decay experiments NEMO3's use of topology and tracking means that not all particle interactions inside the detector in the energy window are considered backgrounds as only those which produce two electrons from the same vertex are problematic. This helps limit background contributions to the internal and external processes listed below.

Internal backgrounds are those which occur inside the source foil and occur in two forms. One of those is from natural radioactivity as mentioned before such as ^{214}Bi and ^{208}Tl which can mimic a double beta event by one of three processes (see Fig.4.21)

1. β decay + Internal conversion = A standard single beta decay from beta decay isotope plus the emission of an internal conversion electron to de-excite the nucleus.

2. β decay + Möller scattering = A standard beta decay which produces an electron which on collision with another electron bound to an atom scatters and liberates the incident electron (this is the most prominent).

3. β decay + Compton scattering = A standard beta decay followed by a high energy gamma that scatters off a very close bound electron liberating the electron (the short possible distance between the beta decay and the Compton makes it less likely)

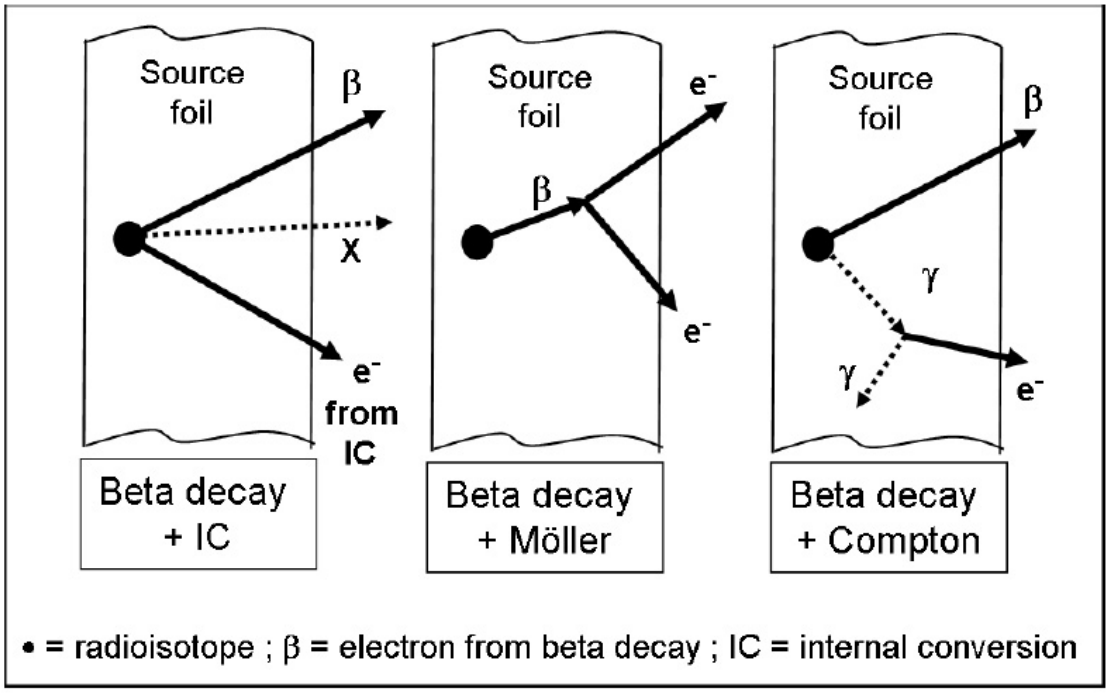

Figure 4.21: Internal background production. [148]

The other form of internal background only affects $\beta\beta0\nu$ decay searches and is the $\beta\beta2\nu$ decay signal from the active double beta decay isotope. Commonly known as the irreducible background due to the having the same topology as $\beta\beta0\nu$. Ultimately the ability to observe the $\beta\beta0\nu$ over $\beta\beta2\nu$ is down to the energy resolution of the detector and the overlap between the two distributions is for NEMO3 an important factor. In NEMO3's ^{100}Mo sample the natural background contribution is roughly equal to that of $\beta\beta2\nu$.

The external backgrounds of the experiment are gamma rays that have many sources such as from external natural contamination of ^{214}Bi and ^{208}Tl from support structures and PMTs but also from cosmic rays neutrons and radon gas. Radon gas, ^{222}Rn and ^{220}Rn, which have half-lives of 3.8 days and 55 seconds respectively, come from radium isotopes. Radon itself is an alpha emitter but decays to ^{208}Tl and ^{214}Bi. It exists naturally in the rocks everywhere and has the troublesome property of being a very diffuse gas so can permeate into the detector depositing positively charged radioactive progenies on the charged wires and surfaces. The gamma rays produced by these external backgrounds can mimic double beta events via one of three processes (see Fig.4.22). Some of these progeny are deposited on the surface of the foil or first Geiger wire layer which make them much more troublesome as they are indistinguishable from internal backgrounds within the foil.

1. Pair Production = Interaction of an incoming gamma ray with the field of an atomic nucleus can produce the momentum transfer needed to create an electron positron pair

2. Double Compton scattering = The incident gamma ray scatters off a bound state electron liberating it and then moving off with reduced momentum. if this photon still carries on with enough energy this process can happen a second time within a very short distance producing the two electrons needed to mimic a double beta event.

3. Compton and Moller scattering = The incident gamma ray scatters of an electron liberating it with enough energy to then scatter off a second electron liberating that.

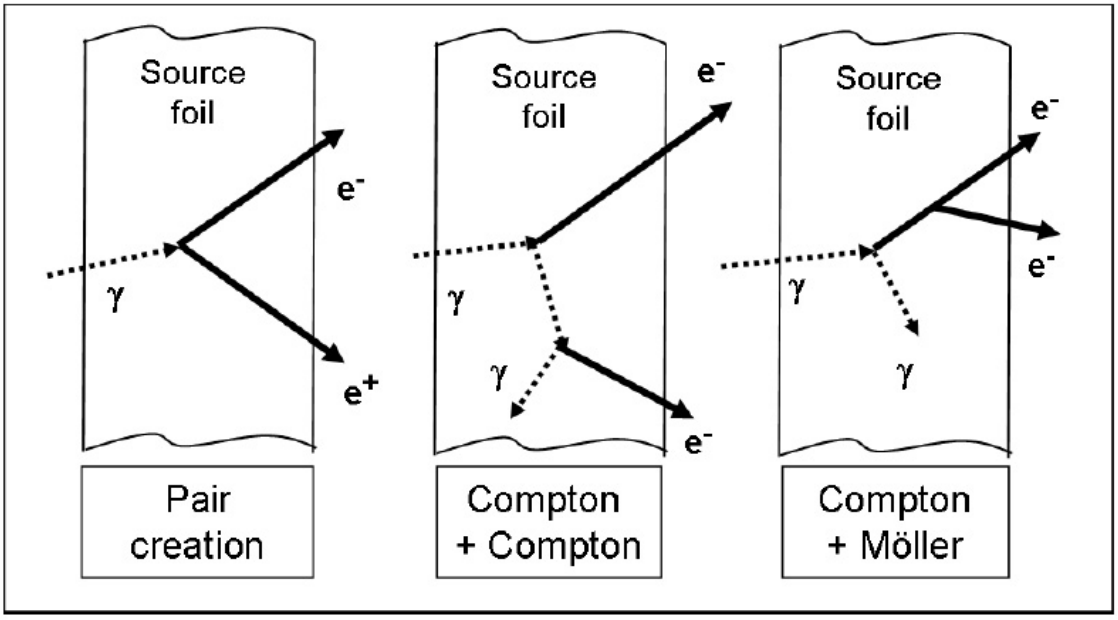

Figure 4.22: External background production. [147]

Both radon with its α decays and the BiPo effect of ^{214}Bi decaying to ^{214}Po, means that it is important to carry out tracking of alpha particles. For this purpose the window of acquisition was expanded to 710μs to try and capture these delayed alphas with short tracks so as to provide a means to reduce their background effect via exclusion.

For ^{48}Ca due to the $Q_{\beta\beta}$ value of 4272keV being very high, it actually takes the critical $\beta\beta0\nu$ region out of the reach of the majority of backgrounds that dominate other samples.

4.4 BiPo

BiPo events are a troublesome background for $\beta\beta2\nu$ and $\beta\beta0\nu$ decays in the NEMO3 detector. BiPo refers to the decay of ^{214}Bi atoms to ^{214}Po with a Q_β value of 3.27 MeV. The ^{214}Bi atoms that are the source of these events come from ^{222}Rn decays, which in turn are part of the natural ^{238}U chain that can exist both inside and outside the detector. The identification and subsequent removal of these

events from double beta decay data can be achieved by examining the delayed decay of the daughter ^{214}Po atoms. ^{214}Po decays to produce an α particle with a half-life of 164μs. Therefore BiPo events can be identified by an electron followed by a delayed α particle within a 710μs time window, that reconstruct to a common vertex within the detector. Alpha particles within the detector would have short straight tracks of no greater than 36cm length. The alpha particles may appear as single delayed Geiger hit or multiple grouped hits and as such the following temporal and spatial conditions are imposed to maximise the likelihood of α event determination over random cross talk and cell coincidences.

- For events with a single delayed hit the hits delay exceed 90μs.
- For groups of hits (where hits must fall within 2.1μs of each other) the delay must exceed 30μs.
- Delayed hits must be within 35cm of each other (the maximum transition length within the gas volume).
- The reconstructed vertex of the electron and α particle must spatially be separated by ΔXY $<$ 10cm (where XY $= \sqrt{X^2 + Y^2}$) and ΔZ $<$ 15cm to be considered from a common vertex.

Below in fig.4.23 is an example of a BiPo type event.

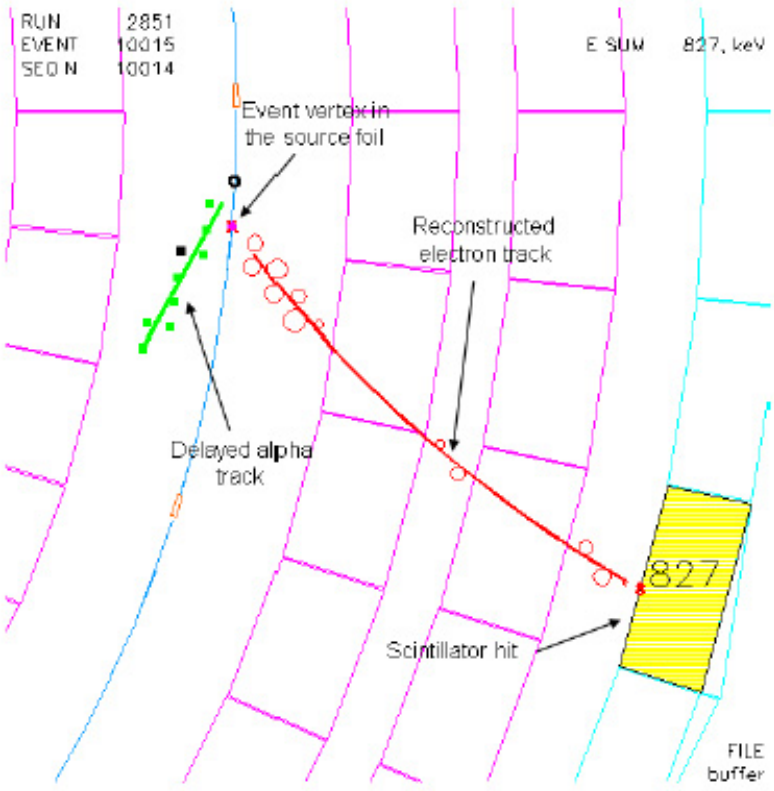

Figure 4.23: NEMO3 event display of a BiPo event originating from the source foil seen from above. Alpha particle track shown in green, electron track shown in red and calorimeter hit in yellow. The source foil is shown in blue.

4.5 Phases

The backgrounds during data taking were not constant especially the level of radon gas. Two phases of data taking exist, phase 1 (February 2003 to September 2004) where the radon levels were relatively high and phase 2 where the radon tent was introduced and so radon levels were much reduced (October 2004 onwards) as demonstrated in radon measurements seen in Fig.4.24.

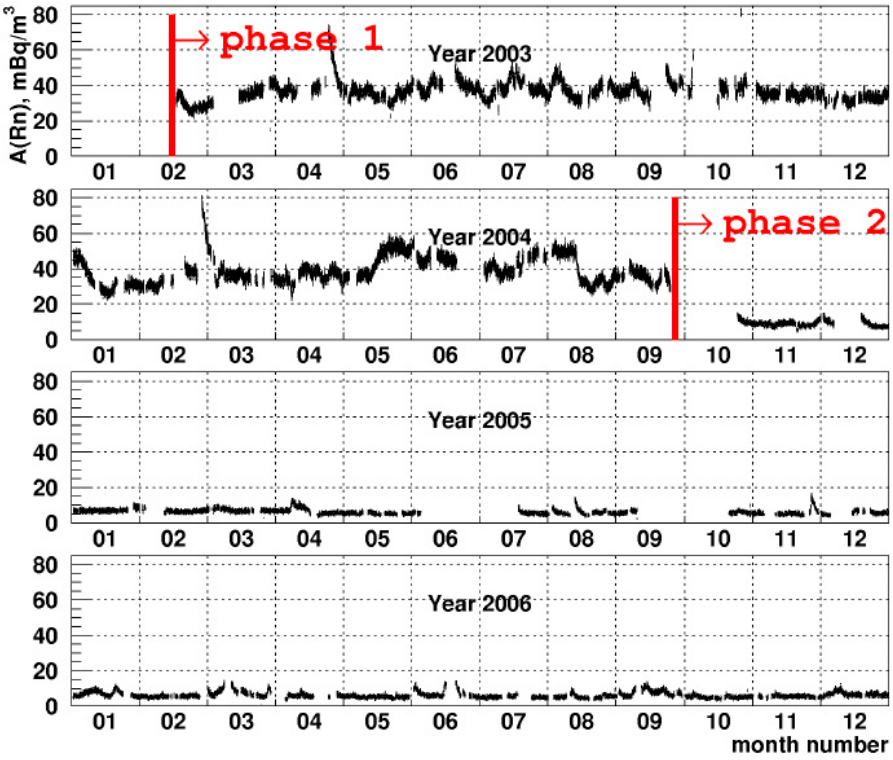

Figure 4.24: Temporal ^{222}Rn activity variations inside tracker volume from the start of data taking till 2007 measured on an hourly basis. [135]

^{48}Ca is a very small source inside NEMO3 and the contribution of external backgrounds are proportional to the source size. This means the effect of the differing radon levels accounts for a negligible less than 1% effect on backgrounds contributions to the discovery channels. This allows both phase 1 and phase 2 data to be analysed together despite the relative change in radon backgrounds levels.

Chapter 5

^{48}Ca Double Beta Decay Studies with NEMO3

As mentioned previously, ^{48}Ca is a very important double beta decay candidate. It has many favourable properties, like the highest $Q_{\beta\beta}$ of any isotope which takes it clear of most lower energy backgrounds like those from the natural U and Th chains, and a large phase space factor, which would make it an ideal choice if it weren't for its low natural abundance and the difficulties with its enrichment. However one more important property that adds to the motivation for studying this particular isotope, is that it is the only double beta decay candidate that is also a doubly magic nucleus. This property makes it the best benchmark isotope for the shell model calculations as it has completed shells with no extra valence interactions to calculate.

The study of ^{48}Ca in this chapter will follow the following structure

- Analysis technique
  - Main software
  - Definitions of main quantities
- Measurement of backgrounds
  - External backgrounds
  - Internal background measurements
- Investigation of background model deficit
- Signal measurement results
  - $\beta\beta2\nu$ decay
  - $\beta\beta0\nu$ decay
- Concluding remarks

5.1 NEMO3 Simulation and Analysis Software

The NEMO3 software is made up of 3 distinct parts, Monte Carlo (MC) event generation and simulation (Sec.5.1.1), data and MC reconstruction (Sec.5.1.2) and analysis (Sec.5.1.3). The analysis strategy is to generate both signal and background Monte Carlo (MC) events for the detector and then simulate the detector's response to these events. The MC and the real detector data can then be reconstructed identically and cuts applied to select different final state channel topologies. Different channels can then be used to adjust the normalisation of the MC background components to fit the real data and then the two electron discovery channel can be selected and the MC signal component's normalisation fitted to the excess over the background. From this the activity and the half-life of the process can be found.

5.1.1 Event Generation and Simulation

The NEMO3 event generation and detector simulation is carried out by an all-encompassing package known as NEMOS within which most of the code is predominantly written in FORTRAN.

The MC events are initially generated inside NEMOS using the DECAY0 package [151]. This package is used widely in dark matter, low background and nuclear decay experiments as it contains the decay schemes, branching ratios and kinematics of all the α, β and γ particles released by the decays of many radioactive nuclei including double beta decays to the ground and excited states of all the required isotopes. This therefore provides all the necessary generation of all internal and external backgrounds of the detector as well as the signal events from $\beta\beta0\nu$, $\beta\beta2\nu$ and Majoron emissions for analysis studies.

These events are then propagated through the detector using GEANT3.21 to simulate the interactions of each emitted particle with the full detector geometry and its effects on particle kinematics, energy deposits and further decays according to their known cross-sections, as well as the detector responses.

The NEMOS software then passes the results through a digitisation process where simulated events are converted into the same data format as the output from the data acquisition software and electronics (DAQ). This is done by converting the energy and time values into ADC and TDC units and applying smearing to account for resolutions and detector effects.

5.1.2 Event Reconstruction

The next stage in the software is reconstruction of both data and MC events. This is done by a package known as NEMOR. Reconstruction involves conversion of ADC and TDC output into energies and times from both calorimeter and Geiger channels, as well as the processes of track finding, fitting, curvature determination used for charge reconstruction and the extrapolation and association of tracks to source foils and scintillator hits for electrons and positrons. Essential calibration data from calibration runs needed for these conversions are provided by a MYSQL database and read into

the program when needed. The processes for reconstructing events are identical for both raw data and MC, however the MC undergoes an initial step whereby the MC data is distributed throughout a given data acquisition period and the status of the detector's calorimeter channels, Geiger cell characteristics and other specific quantities are applied to the MC data such that they reflect the detector output at this time. These quantities are all also stored in the NEMO3 database and the result is MC data that represents the raw output of that time period with all intrinsic smearing resolutions and detector effects.

The reconstruction program is actually run twice over data sets and on each of these runs a different event topology is selected and events that match this are saved to a root file. One of these files contains all events that have just one reconstructed track that is associated with a scintillator hit and the other where there is one track and anything else.

5.1.3 Analysis

The analysis of the events was achieved in two steps by programs known as Slim and Rootana written in C/C++. Slim is initially used to reduce the data set to focus greater processing time and resources on the specific topology being analysed. A series of cuts to the data are implemented and then a ROOT file is produced of the greatly reduced selected events.

This reduced data set is then used by Rootana firstly to cut on run status and time period and then to apply more specific cuts, plots, statistical calculations, fitting and renormalisation. The package itself contains a large number of statistical algorithms for processing and determining quantities of interest about a given distribution. Ultimately these statistical tools yield a measurement of the signal strength.

Rootana itself, whilst powerful, is written in a very obscure style requiring data to be processed twice, once into user defined plots, which are then fitted and renormalized on a second pass. Some of these fitting functions and the multi pass process as well as the requirement of the program to read events from the NEMO3 database on each execution created unwanted bottlenecks and inefficiencies.

These problems were addressed by myself and collaborators by developing replacement code and redesigning and optimising the Rootana code. However large scale validation was needed before its use for results. To that end the analysis from NEMO3 in this thesis uses the old Rootana application.

5.2 Analysis Techniques and Description

5.2.1 Data Phases and Status

As mentioned previously, the time for which data taking occurred was split into two phases. Phase 1 where the radon contamination was relatively high, running from February 2003 to September 2004 and Phase 2 October 2004 onwards, where the radon tent was added and radon trapping occurred to reduce the concentration (sec.4.2.6.1). Data taking sessions are known as runs and each has its

own sequential run number and a status applied. The status applied to each run number denotes how the detector was operating and any faults such as high Geiger trigger rate or noisy PMTs or Geiger cells. For the study of ^{48}Ca only run status 1 was selected, in which only the times when the detector was running at its most stable conditions with no known problems (such as e.g. radon activity spikes) were used. The number of events classed as status 1 account for $\approx 80\%$ of all events recorded during active running.

5.2.2 Particle ID

The NEMO3 detector is able to distinguish 5 particle types, electrons, positrons, gamma rays, muons and alpha particles from their distinct topology signatures.

Electrons (and positrons) ionise the tracking gas giving Geiger hits which can be reconstructed and fit with a helix of negative (positive) curvature due to the deflection in the magnetic field. Within an event electrons (and positrons) will only be identified as such if these tracks extend to a calorimeter block and have an associated energy deposit. The exact selection criteria for electrons coming from the source foil are presented below.

- A reconstructed track present for the event which means that an ionising particle must be present in the event.
- The track must have curvature consistent with a negatively charged particle for electrons (positive for positrons).
- The track must be associated to a calorimeter hit of energy > 200 keV. This is used to remove the large and poorly modelled (by simulation) low energy background that is present below this energy.
- The scintillator hit must be isolated (have no neighbouring hits). This acts to eliminate electrons scattering from one calorimeter block to its neighbour or entering the region between two blocks where the whole energy would not be measured or false hits seen.
- The track must originate in the source foil (allowing for resolution errors). This is to ensure that the electron events selected are from the foil not external sources.
- The track must have a Geiger hit in one of the first 2 layers closest to the foil. This ensures that the initial event vertex on the foil is reconstructed with the required level of accuracy to determine the source position.
- The track must have a Geiger hit in one of the last 2 layers closest to the scintillator hit. This ensures that the calorimeter vertex is reconstructed accurately for precise track calorimeter hit association.

- The track length has to be > 30 cm. 30cm is the minimum distance between the source foil and the calorimeter wall and therefore ensures that the track is reconstructed for the entire length of the particle's transit.

Unfortunatly optimisation and validation plots for these selection criteria were lost, so cannot be presented.

Gamma-rays are identified in the detector by calorimeter hits that are not associated with any tracks, as gamma rays will not ionise the tracking gas. This definition is used for their identification however only 60% of the gammas at 0.5MeV will interact with calorimeter blocks of the thickness used in NEMO3. Also un-associated calorimeter hits can be caused by other effects in the detector as well, such as electron back scattering from scintillators detected by another scintillator and where an electron hits the boundary between two scintillators or crosses into an adjacent scintillator during its absorption by the scintillating blocks. These effects can be reduced by looking for Geiger hits directly in front of un-associated scintillator hits and the proximity of scintillating hits ensure that all are isolated from their nearest neighbour respectively. The exact selection criteria for a gamma-ray are presented below

- An un-associated scintillator hit
- The scintillator hit must be > 200 keV
- The scintillator hit must be isolated (have no neighbouring hits)
- The scintillator hit should have no localised Geiger hits in the closest 2 layers

Muons can also be observed in the detector although their occurrence is both rare and not of interest in the study of double beta decay. Their presence in the detector is characterised by very long tracks with large energy deposits of roughly 20 MeV in the calorimeter.

Alpha particles appear in the detector as short straight tracks close to their source. They do not have any associated scintillation hits as, due to their highly ionising nature they don't penetrate very far though the gas volume. The tagging of alpha particles is used mainly in the suppression of backgrounds from Bi-Po type events within the foil. These events are characterised by electrons emitted from the foil surface with a delayed alpha particle within 30-700 μs of the electron arriving at the scintillator. The Geiger hits from the alpha particle are seen as either single spatially close Geiger hits or groups close to the foil.

5.2.3 Time of Flight

Another important tool and selection criterion when determining which events are caused by internal decays or by external backgrounds is the calculation of the probabilities associated with the time of flight (TOF) of the particles in the event, by using the calorimeter trigger times. As in sec.4.3, internal backgrounds are defined as radioactive contaminants inside the source foil and external

backgrounds are any other radioactive impurities that can exist, e.g. from the surface of the foil, to radioactive isotopes present in the gas, detector materials and laboratory environment. The TOF is important when determining if an observed γe event is an internal foil decay or an external γ ray Compton scattering off the foil surface (see Sec.4.3), or in the two electron double beta searches, if the two electrons originate from the foil surface or are due to Compton electrons from the calorimeter walls crossing the foil surface and interacting on the opposite side of the detector calorimeter wall. To help distinguish these events we can calculate the probability of each case.

5.2.3.1 Internal Two Electrons Hypothesis

The probability of 2 electrons coming from the internal source foil can be calculated using the triggering time from the TDC of each of the two calorimeter hits (t_i^{tdc}) the length of their reconstructed tracks (l_i) and their energies deposited in each of the calorimeter blocks including corrections for the energy calibration and energy loss caused by transition through the tracking gas volume (E_i), where i denotes the electron (i = 1,2).

From these quantities the time of flight of the electron can be determined using Eqn.5.1 (in natural units)

$$t_i^{tof} = \frac{l_i}{\beta_i} \tag{5.1}$$

where β_i is the speed calculated by

$$\beta_i = \frac{\sqrt{E_i(E_i + 2m_e)}}{E_i + m_e} \tag{5.2}$$

From this the initial time of emission from the foil can be calculated for each particle using Eqn.5.3

$$t_i^{int} = t_i^{tdc} - t_i^{tof} = t_i^{tdc} - \frac{l_i}{\beta_i} \tag{5.3}$$

The χ^2 variable for this internal time of flight hypothesis can be constructed as

$$\chi^2_{int} = \frac{\left(\left(t_2^{tdc} - \frac{l_2}{\beta_2}\right) - \left(t_1^{tdc} - \frac{l_1}{\beta_1}\right)\right)^2}{\sigma^2_{t^{int}}} \tag{5.4}$$

where $\sigma^2_{t^{int}}$ is the summation of all the errors from the quantities of length σ_l, energy σ_E and time σ_t, which can be expressed as

$$\sigma^2_{t^{int}} = \sum_{i=1}^{2} \left(\frac{\delta t^{int}}{\delta t_i^{tdc}}\right)^2 \sigma^2_{t_i^{tdc}} + \left(\frac{\delta t^{int}}{\delta \beta_i}\right)^2 \sigma^2_{\beta_i} + \left(\frac{\delta t^{int}}{\delta l_i}\right)^2 \sigma^2_{l_i} \tag{5.5}$$

which when substituting for β_i and evaluating the partial derivatives becomes

$$\sigma^2_{t^{int}} = \sum_{i=1}^{2}\left[\sigma^2_{t_i^{tdc}} + \left(\frac{t^{tof}m_e^2}{E_i(E_i+m_e)(E_i+2m_e)}\right)^2\sigma^2_{e_i} + \left(\frac{1}{\beta_i}\right)^2\sigma^2_{l_i}\right] \tag{5.6}$$

where the probability of the event being of internal origin $P(\chi^2_{int})$ is given by

$$P(\chi^2_{int}) = 1 - \frac{2}{\pi}\int_0^{x^2} e^{x^2}dx \tag{5.7}$$

where

$$x = \frac{1}{1+\sqrt{2\chi^2_{int}}} \tag{5.8}$$

This same formulation of the internal hypothesis can be used to create similar expressions when looking at other topologies like eγ , the difference being that for γ-rays $\beta \to c$ the speed of light in Eqn.5.1.

5.2.3.2 External Two Electron Crossing Hypothesis

For the hypothesis of an electron crossing from one calorimeter module on one side of the detector through the foil to a calorimeter module on the other side, the time of flight is once again given by (in natural units).

$$t^{tof} = \frac{l_1}{\beta_1} + \frac{l_2}{\beta_2} \tag{5.9}$$

However in this case β_2 is not independent of β_1 but is instead the equivalent to β_1 with some applied energy losses to account for its passage first through the gas volume and foil.

This affects also the formulation of the χ^2 variable which becomes

$$\chi^2_{ext} = \frac{\left(\left(t_2^{tdc} - t_1^{tdc}\right) - t^{tof}\right)^2}{\sigma^2_{t^{ext}}} \tag{5.10}$$

where $\sigma^2_{t^{ext}}$ and $P(\chi^2_{ext})$ are equivalent to the internal hypothesis given in Eqn.5.6 and Eqn.5.7 respectively.

As with the internal probability this formalism can be used to construct TOF hypotheses for other event topologies (eg. eγ) in the same way with gamma speeds equal to the speed of light.

5.2.4 Fitting of Data Components using Log Likelihood

The raw data from the detector when plotted forms distributions which are the summation of all collective background components and the desired signal components (Eqn.5.11)

$$D = B + S \tag{5.11}$$

where D is the data, B the collection of backgrounds and S the signal component.

When disentangling these contributions we use a maximised binned log-likelihood function to fit the simulated MC to this data. This method treats every bin in the distribution independently which allows the overall distribution shape to be taken into account during the fitting process, unlike methods which sum up all the bins and only concintrait on total numbers of events within an energy window. The probability (P) for each bin to observe a number of events (n) can therefore be calculated using the Poisson distribution (Eqn.5.12)

$$P_i = \frac{e^{-D_i} D_i^{n_i}}{n_i!} = \frac{e^{-(B_i+S_i)}(B_i+S_i)^{n_i}}{n_i!} \tag{5.12}$$

where i denotes a specific bin.

using this approach the likelihood (L) can be constructed by the product of the probabilities of all the bins' Poissonian probabilities (Eqn.5.13)

$$L = \prod_{i=0}^{N} P_i = \prod_{i=0}^{N} \frac{e^{-(B_i+S_i)}(B_i+S_i)^{n_i}}{n_i!} \tag{5.13}$$

where N is the total number of bins in the distribution.

As the likelihood function is monotonic then its maximum would be the same for the logarithm of the likelihood function and it would simplify the variable dependence. The log-likelihood is therefore given by eqn.5.14.

$$ln(L) = \sum_{i=0}^{N} -(B_i+S_i) + n_i ln(B_i+S_i) - ln(n_i!) \tag{5.14}$$

the derivative with respect to the signal (S) can then be undertaken and set to zero to find the maximum of the log-likelihood function (Eqn.5.15)

$$\frac{\delta ln(L)}{\delta S} = -1 + \sum_{i=0}^{N} \left(\frac{n_i}{B_i+S_i} \frac{\delta S_i}{\delta S} \right) \tag{5.15}$$

where S is the total number of signal events and can be solved for numerically. The total number of signal events for $\beta\beta2\nu$ decay can be found using this method and then the half-life determined by following the prescription in sec.5.2.5.

The error on S can be found at the one σ level by determining the value of S where the log-likelihood is a half of its maximum value (Eqn.5.16). This can be done as eqn.5.14 follows a χ^2 distribution.

$$ln(L(S)) - ln(L(S \pm \Delta S)) = \frac{1}{2} \tag{5.16}$$

5.2.5 Determination of Half-Life

To determine the half-life of an observed signal once selection and backgrounds have been identified we can use Eqn.5.22, which is derived from the standard exponential radioactive decay formula

Eqn.5.17.

$$N = N_0 e^{-\lambda t} \tag{5.17}$$

where N is the number of atoms left that haven't decayed after time t and N_0 is the initial number of atoms at t=0. λ here denotes the decay constant which is defined as $\lambda = \frac{ln2}{T_{1/2}}$, where $T_{1/2}$ is the half-life.

using Eqn.5.17 the number of decays N_{dec} can be determined for a given time t.

$$N_{dec} = N_0 - N \tag{5.18}$$

$$N_{dec} = N_0(1 - e^{-\lambda t}) \tag{5.19}$$

Taking the first term in the Taylor expansion of Eqn.5.19 we get

$$N_{dec} = N_0 t \frac{ln(2)}{T_{1/2}} \tag{5.20}$$

This can be done due to the very long lifetimes of the nuclei we are studying. We can then substitute N_0 for $\frac{m_i N_A}{A_r}$, where m_i is the mass of the isotope, N_A is Avogadro's number and A_r is the atomic weight, and rearrange to express the half-life as

$$T_{1/2} = \frac{m_i N_A}{A_r N_{dec}} ln(2) t \tag{5.21}$$

As the half-life will be experimentally found and some of the events will be lost due to the detector efficiency (ϵ), then it needs to be included into the half-life calculations to account for this.

$$T_{1/2} = \epsilon \frac{m_i N_A}{A_r N_{dec}} ln(2) t \tag{5.22}$$

When using Eqn.5.22 experimentally we apply the topology cuts to the data and then looking at the energy and angular distributions, perform likelihood fits using the previously measured background components and the floated signal component as described in sec.5.2.4. This will give us the total number of signal events which equates to the number of events decayed (N_{dec}) in the equation.

5.2.6 Limit Setting and Confidence Limits

When no signal events are observed above the background then we can set limits on the $\beta\beta0\nu$ process using both the Poissonian statistics of the associated errors and Eq.5.22.

As radioactive events are independent of each other and have an average rate, their frequency follows the Poissonian distribution, which therefore governs the errors of any frequency based measurements.

The normalised Poissonian distribution is given by Eq.5.23

$$P(n) = e^{-\bar{n}} \frac{\bar{n}^n}{n!} \tag{5.23}$$

where P(n) is the normalised probability that in a given time interval n events will be observed. $\bar{n}$ is the average number of events or the expected number of events determined from large samples over long time periods, in our case MC simulations.

Due to its normalised nature the summation of this function over all n (Eq.5.24) will give a probability of 1 and summation to an arbitrary value (n_0) will give the probability that during the specified time period less than n_0 events will be observed given an expected value of $\bar{n}$.

$$CL = e^{-\bar{n}} \sum_{n=0}^{n_0} \frac{\bar{n}^n}{n!} \tag{5.24}$$

where CL is this cumulative summation and stands for confidence limit and n_0 is the value of the number of events observed.

Using this we can construct a confidence limit for the desired signal (CL_S) from the confidence limits of the background component (CL_B) and the combined signal and background component (CL_{S+B}) using Eq.5.25.

$$CL_S = \frac{CL_{S+B}}{CL_B} \tag{5.25}$$

where CL_{S+B} and CL_B are given by Eq.5.26 and Eq.5.27 respectively.

$$CL_{S+B} = e^{-(\mu_B+\eta)} \sum_{0}^{n_0} \frac{(\mu_B+\eta)^n}{n!} \tag{5.26}$$

$$CL_B = e^{-\mu_B} \sum_{0}^{n_0} \frac{\mu_B^n}{n!} \tag{5.27}$$

μ_B is the expected background component from MC simulations after normalisation to the backgrounds observed and η is the number of expected signal events.

In the particular case where no events are observed over the data taking time period $n_0 = 0$ and if no background is expected $\mu_B = 0$ then

$$CL_{S+B} = e^{-\eta} \qquad CL_B = 1 \tag{5.28}$$

and the confidence limit for the signal will be given by Eq.5.29

$$CL_S = e^{-\eta} \tag{5.29}$$

The number of excluded events at the 90% CL can be found from (Eq.5.30)

$$CL_{90\%} = 1 - CL_S \tag{5.30}$$

and η found by doing the following.

$$CL_{90\%} = 1 - e^{-\eta} \tag{5.31}$$

$$0.9 = 1 - e^{-\eta} \tag{5.32}$$

$$0.1 = e^{-\eta} \tag{5.33}$$

$$\eta \approx 2.3 \tag{5.34}$$

Therefore the upper bound of signal events would be 2.3 and can be used as N_{dec} to produce an upper limit on the half-life, given by Eq.5.22. Determination of these confidence limits for $\beta\beta0\nu$ decay in NEMO3 are achieved by two implementations known as the Helene method and MCLimit [152, 153]. The Helene method uses an optimised energy window, where the contents of all the bins in the window are summed and considered as a single bin. However MCLimit uses a binned log-likelihood approach over the entire distribution which takes into account the shape of the distribution by considering each bin as an independent measurement and then taking the product of each. MCLimit should provide a more robust and reliable confidence limit [154, 155].

5.2.7 Data Set

As mentioned before due to negligible effects of radon background, data from both phase one and two were combined to form 4.26 years of active data taking stretching from Feb 2003 to Dec 2009 (all 0.93 years of phase 1 and 3.34 years of phase 2). The active data taking time takes into account the dead time for each event recorded which works out to be $\approx 0.8\%$ of the total time or around 1.5 ms/event for a double beta event with two triggered PMTs and an average of 16 triggered Geiger cells. This time comes from 710 μs due to the search for delayed alpha particles, plus the addition of a minimum of 586.5 μs for the Geiger dead time for 3 cells, 2.5 μs from the Geiger read out of the acquisition cards and finally the interrupt handling and Cascade overhead take around 150 μs [147]. To this data laser corrections and cuts were applied to examine particular channels presented below. Whilst only the 2 electron channel was used for the final $\beta\beta2\nu$ and $\beta\beta0\nu$ results the other channels were used to help determine and measure the associated backgrounds present. 2010 data was not included in the studies performed as the relevant calibration and correction factors had not been determined at the time of the analysis.

5.3 ^{48}Ca Background Measurements

The ^{48}Ca used by NEMO3 was split into two samples. One was sent to be measured in a germanium detector to establish its contamination levels and the other was made into 9 CaF_2 disks which were placed into the detector (Sec.4.2.2). The disks are located just below the ^{96}Zr source of strip 7 of sector 5, which is the last strip in the sector (See Fig.5.1).

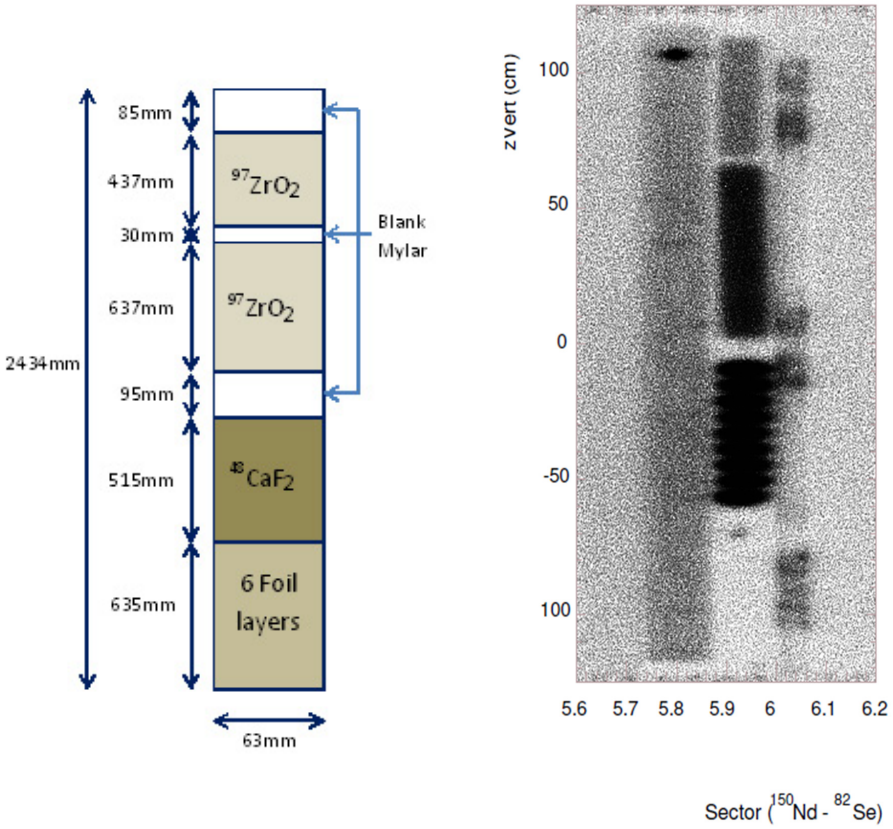

Figure 5.1: Sector 5 strip 7 CaF_2 disk locations (note: strip 7 is the central strip of the right diagram of the distribution of single electron events whose event vertex are on the foil). [156]

As mentioned previously in Sec.4.3, backgrounds are classified as internal and external and stem from 2 main sources, the external photon interactions and the natural radioactivity and contaminations of the lab and materials of the detector. Also for the case of $\beta\beta0\nu$ decay the irreducible signal tail of the $\beta\beta2\nu$ distribution is a background component. Each of these background contributions must be determined and simulated to produce an analysis of ^{48}Ca.

5.3.1 External Background

Before construction each component and material used for the detector was measured using HPGe detectors and as far as possible low activity alternatives were sought as their contamination with U and Th cannot be avoided and their decay chains Fig.4.20 produce ^{214}Bi and ^{208}Tl which have

energies and half-lives of Q_β = 3.27 MeV, $T_{1/2}$ = 19.9 mins and Q_β = 4.992 MeV $T_{1/2}$ = 3.05 mins respectively. These Q_β values take them right into the energy range of the ^{48}Ca $\beta\beta2\nu$ decay and so are problematic. The HPGe measurements of the main component's contributions can be seen below in table.5.1.

Detector Element	Weight (kg)	214Bi (Bq)	208Tl (Bq)
PMTs	600	300	18
Scintillators	5000	<0.7	<0.3
Copper Frame	25000	<25	<10
Steel Frame	10000	<6	<8
μ-metal	2000	<2	<2.7
Wires	1.7	$< 10^{-3}$	$< 6 \times 10^{-4}$
Iron Shield	180000	<300	<300

Table 5.1: Main component contamination contributions as measured by HPGe detectors.

The HPGe detector also determined that iron in the frame was contaminated with ^{60}Co which undergoes a beta decay with two associated photons of 1.17 MeV and 1.33MeV. Further contamination of the detector components would be caused by the presence of radon gas in the detection volume. The levels of radon emanation into the tracker varied over time and between phase 1 and 2 as can be seen in fig4.24. The radon would coat the surface of the wires (swire) and surface of the foil (sfoil) with the decay products of its decay chain especially ^{214}Bi and ^{208}Tl which could mimic internal backgrounds. However any extra external contaminations can only be measured post construction by the detector itself.

There were two main topologies that were used to obtain the external background model, crossing electrons (that propagate from one calorimeter wall to the opposite through the foil) and 1e1g events (with external hypothesis) measured throughout the detector. The radon contribution was assessed by separate channels containing e-alpha and e-gamma events. The results of these studies can be seen in table.5.2, where two background models can be seen for each of the two phases of data taking [135].

Background Component	Phase 1 (Bq)	Phase 2 (Bq)
^{228}Ac PMT	515	515
^{208}Tl PMT	67	41.6
^{214}Bi PMT	374	374
^{40}K PMT	954	954
Rn	702	/
^{60}Co iframe	50.7	50.7
^{214}Bi swire	$(598 \pm 6) \times 10^{-3}$	$(84 \pm 6) \times 10^{-3}$
^{214}Pb swire	$(598 \pm 6) \times 10^{-3}$	$(84 \pm 6) \times 10^{-3}$
^{208}Tl swire	2.8×10^{-3}	2.8×10^{-3}
^{210}Bi swire	5.05 ± 1	5.05 ± 1
^{214}Bi sfoil	$(19.5 \pm 3.5) \times 10^{-3}$	$(8.5 \pm 1.9) \times 10^{-3}$
^{214}Pb sfoil	$(19.5 \pm 3.5) \times 10^{-3}$	$(8.5 \pm 1.9) \times 10^{-3}$
^{210}Bi sfoil	$(17.4 \pm 5) \times 10^{-3}$	$(17.4 \pm 5) \times 10^{-3}$

Table 5.2: Results of external background activity studies (where iframe = in the iron frame, swire = on the surface of the geiger wires and sfoil = on the surface of the foil. [135]

As can be seen when comparing table.5.1 and table.5.2 the activity levels do not necessarily agree, this is because table.5.2 is an effective background model. These external background activities can be cross checked and verified for the model by using an analysis of both the 1e1γ and 2e channels for the regions of the detector holding the copper foils. The copper foils were installed for this reason as they are very pure and have minimal and well understood internal contaminations. An example of the 2e channels predicted model against background for the copper foils can be seen in fig.5.2. The internal copper contaminations can be seen in table.5.3.

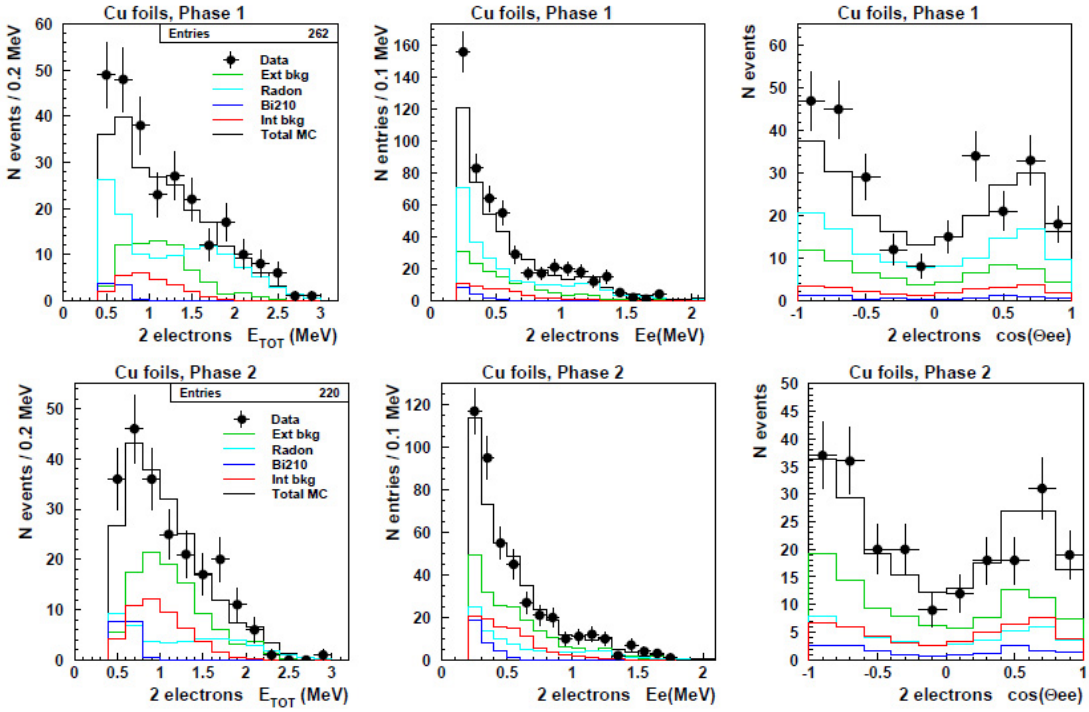

Figure 5.2: Background model prediction compared to the data for 2e$^-$ events from the copper foils. [135]

Contaminant	Activity (Bq)
^{228}Ac	9×10^{-5}
^{212}Bi	6×10^{-5}
^{234m}Pa	1.22×10^{-3}
^{208}Tl	3×10^{-5}

Table 5.3: Copper foil internal contaminations. [135]

5.3.2 Internal Background Contamination Measurements

5.3.2.1 HPGe Internal Background Measurements

As with the external contaminations the internal contaminations were initially determined with an HPGe detector. This was first produced in 2001 on about half (24.558g) of the ^{48}Ca sample using a

400cm^3 HPGe for 1589.83 hours, however this was not the half that was used for making the disks in the detector. Because of this a priority on decommissioning of the detector was measurement of the actual ^{48}Ca disks used (17.506g). This was done with a 600cm^3 HPGe detector over a period of 1244.8 hours. The results for both are shown below in table.5.4.

Isotope	Half-life	Original measurement (mBq/kg)	Measurement of actual source (mBq/kg)
^{226}Ra (^{214}Pb + ^{214}Bi)	1600 yr (26.8 min + 19.9 min)	<4	<4.6
^{228}Ac	6.13 hr	<6	<8.4
^{228}Th	1.91 yr	<6	<8.4
^{235}U	7.04×10^8 yr	<2	<6.0 or 7.8 ±3.4
^{40}K	1.25×10^9 yr	<50	<56.7
^{60}Co	5.27 yr	<2	<2.3
^{152}Eu	13.52 yr	30±5	17.3±5.4
^{22}Na	2.60 yr	-	<4.3
^{26}Al	7.17×10^5 yr	-	<4.0
^{46}Sc	83.79 d	-	<2.4

Table 5.4: ^{48}Ca internal contamination activity levels measured using HPGe detectors on the original potion of the source that was not made into disks and post dismantling of the actual CaF_2 disks. [157]

It is also known that the CaF_2 disk samples were contaminated with ^{90}Sr during production. ^{90}Sr and its daughter ^{90}Y are both beta emitters decaying with single electrons and no gammas making them difficult to detect in a HPGe detector other than using Bremsstrahlung. ^{90}Sr has a low Q_β of 0.546 MeV and a half-life of 28.79 years and so is not as major a background as ^{90}Y which has a Q_β of 2.282 MeV and a half-life of 64 hours. The electron emissions from these isotopes can mimic $\beta\beta$ events through Moller scattering so they are an important internal background that needs determining.

To measure the background contributions of these isotopes the HPGe backgrounds already determined formed an initial fixed background model and the ^{90}Sr/^{90}Y contribution was determined by looking at the one electron channel (1e) from NEMO3 data taking.

5.3.2.2 The 1e Channel and Measurement of the ^{90}Y Background

To select single electron events from the ^{48}Ca region of the detector the basic electron cuts were made as laid out in sec.5.2.2 plus a cut to ensure only 1 electron was present and no other scintillator hits. Also that the reconstructed vertex of the electron should come from the CaF_2 disks region and that no delayed alphas were observed.

Using these cuts on both data and MC we can fit the ^{90}Y and ^{90}Sr to the data with all of the fixed known external and internal backgrounds mentioned previously (see Fig.5.3). Due to the half-lives of ^{90}Y and ^{90}Sr and that ^{90}Y is the daughter of ^{90}Sr decay the two should be in equilibrium so their activities can be fitted as one variable.

As can be seen in Fig.5.3 ^{90}Y is the largest contribution to the distribution, but there is discrepancy between data and the background model below 1MeV. Part of the problem may be due to difficulties in describing the interaction of low energy gammas in plastic scintillator.

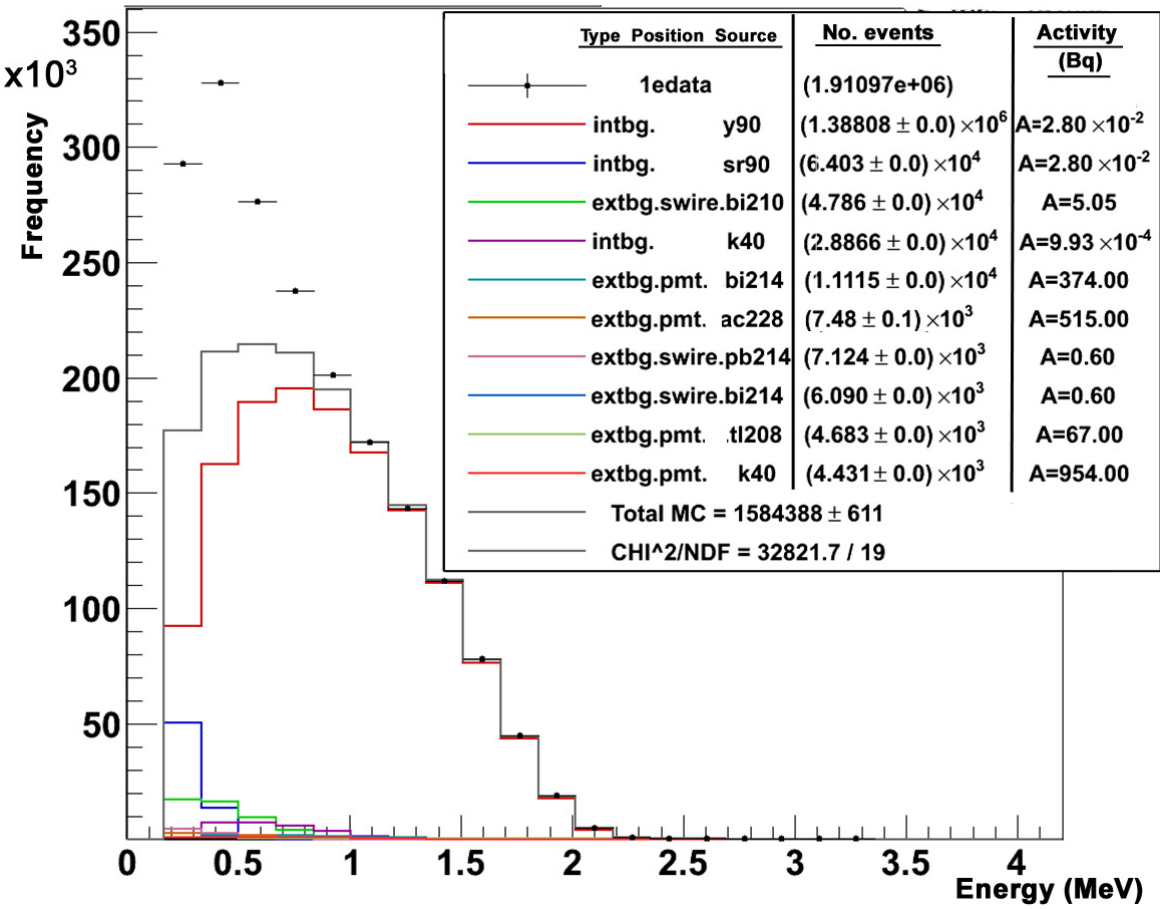

Figure 5.3: Example of ^{90}Y (red) fit to the 1e energy spectra, with apparent low energy background deficit (The 10 largest contributing backgrounds shown along with their activities and their type (internal (intbg) or external (extbg)) and their position in the detector (surface of the foil, surface of the wires or in the PMT glass (sfoil, swires, PMT))).

In order to check if local hotspots exist which would account for this low energy contribution, the distribution of the reconstructed event vertices over the surface of the foil was plotted (Fig.5.4)

Fig.5.4 clearly shows the 9 CaF_2 disks with the bottom one that was known to be slightly misaligned. No hotspots were visible on the disk's surface and the likelihood is that even if any were there they would be overwhelmed by the strength of the ^{90}Y background. So the one electron channel was divided into 3 month blocks of data to see if this background had any temporal dependence or dependence on the large radon contribution from Phase 1. For each of these three month chunks of data the energy distribution was examined and it was found that the low energy background was apparent throughout. For each of these temporal energy distributions the activity level of ^{90}Y and ^{90}Sr were fitted to the data and then the activity for each time slice plotted to determine the half-life (Fig.5.5). The half-life should be equal to 28.8 years (that of ^{90}Sr), however the result obtained was calculated to be 23.1 $\pm$ 0.7 years.

It was therefore decided to examine causes that could account for this discrepancy in the low energy. It was found by looking at the energy spectrum of the discrepancy that if the ^{210}Bi background component from either the surface of the wires or the surface of the foil were increased they could account for this low energy excess (Fig.5.6 and Fig.5.7) and would also have minimal effect on the 2e, 1e1g channels. To test this hypothesis the one electron energy spectrum was refitted whilst floating the ^{210}Bi components.

As can be seen from the fig.5.6 and fig.5.7, an increase of ^{210}Bi on the surface of the wire (swire) requires an activity an order of magnitude higher than on the surface of the foil (sfoil) and both provide a good fit to the data. If the surface of the wires were contaminated as strongly as the fit suggests other local sources would also be affected and see similar results. However an inflated activity level of ^{210}Bi as suggested locally on the surface of the foil could be a possibility, despite it being out of equilibrium with ^{214}Bi on the foil surface and them being in the same decay chain. This non-equilibrium state could occur due to the very long life-time of its parent atom ^{210}Pb ($T_{1/2}$ = 22.20 years). With a half-life of this magnitude any extra contamination from radon deposited in a more dirty construction environment will not have had time to decay away to equilibrium.

Using this premise of inflated ^{210}Bi on the surface of the foil the ^{90}Y and ^{90}Sr contributions were refitted whilst floating both these internal contaminations and the external ^{210}Bi sfoil at the same time. This was done for both the 3 month time slices giving a ^{90}Y half-life of 23.8 $\pm$ 0.2 years (Fig.5.8) and for the entire data set as a whole giving an activity of $(2.8\pm.02)\times10^{-2}$ Bq for the combined period.

Fig.5.8 Shows results of two fits of the independant 3 montly time slices. As can be seen the ROOT's standard fit failed to converge from many of the time slices which is why the Mathematica implimentation was used to try and recover data points for them. Comparison of the points shows aclose agreement between the methods with error bars for the Mathematica fits of a similar magnitude to that of ROOT's fit (error bars not shown due to loss of source data). Fits of the time varying activity using both sets of points were made and found to be consistent with better half-life error

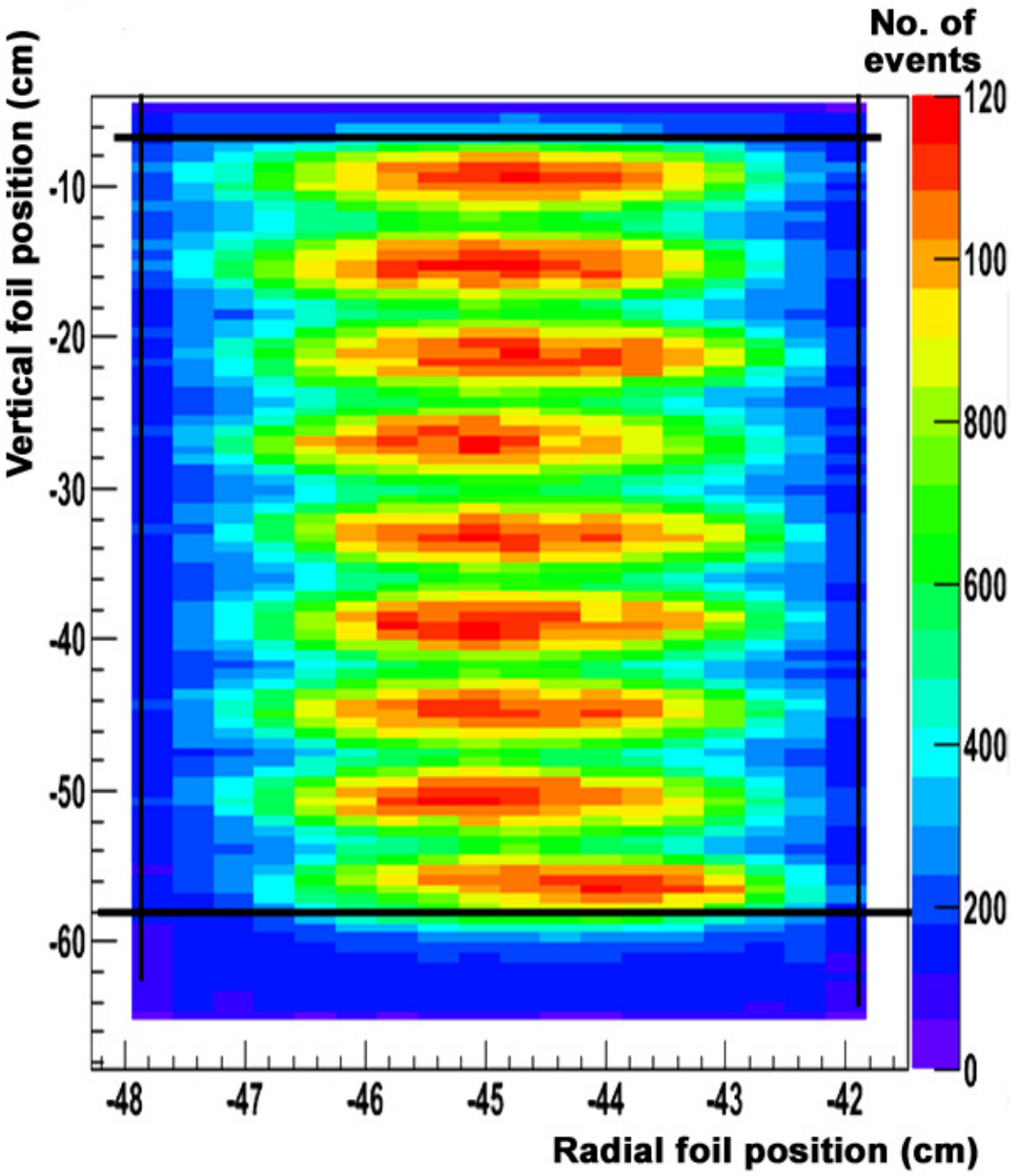

Figure 5.4: Example of 1e events reconstructed vertices distributed over calcium foil surface.

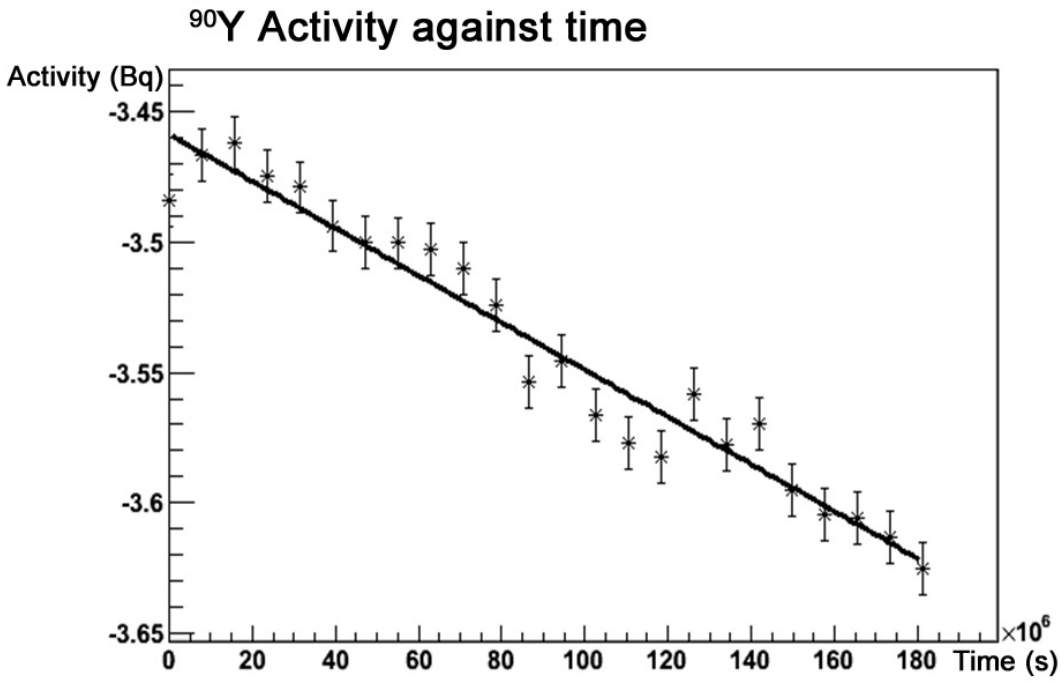

Figure 5.5: ^{90}Y activity variation plotted for 3 month time slices.

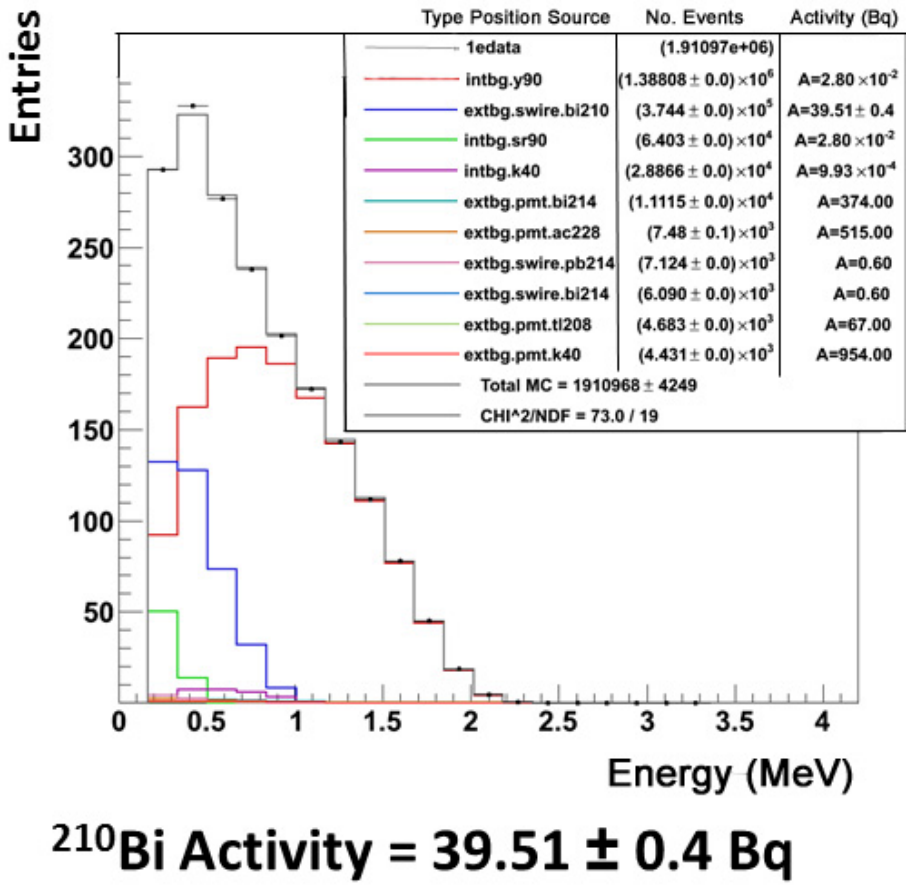

Figure 5.6: Example of 1e distribution with fitted ^{90}Y and ^{210}Bi on the surface of the wires.

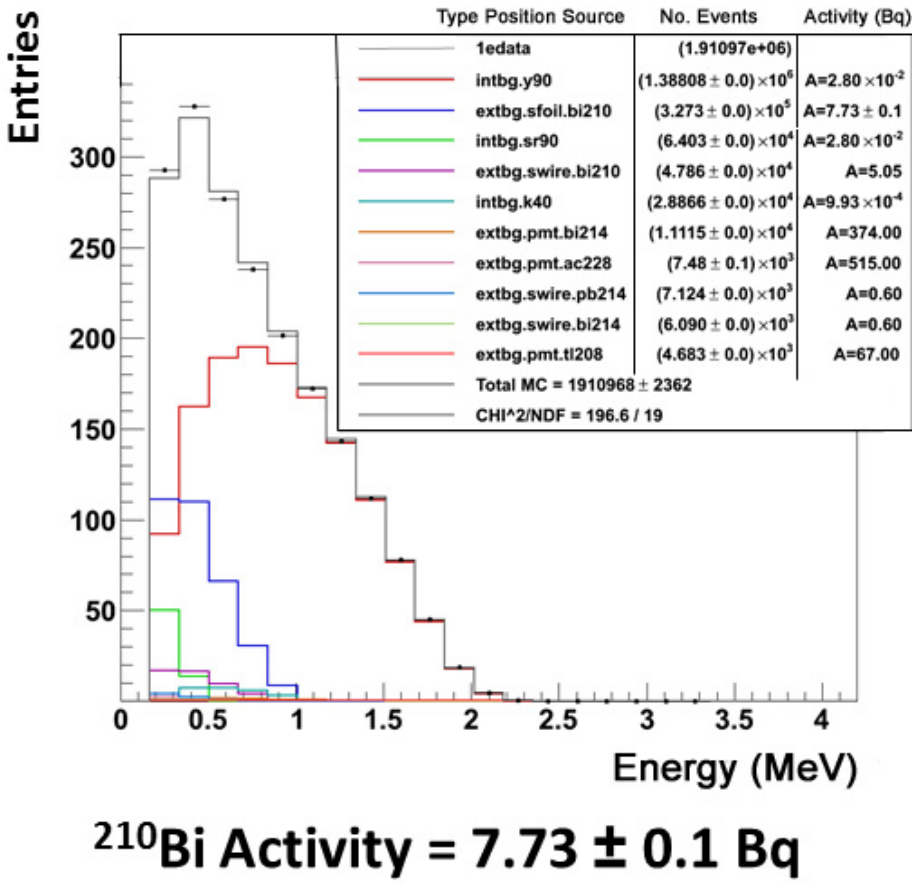

Figure 5.7: Example of 1e distribution with fitted ^{90}Y and ^{210}Bi on the surface of the foil.

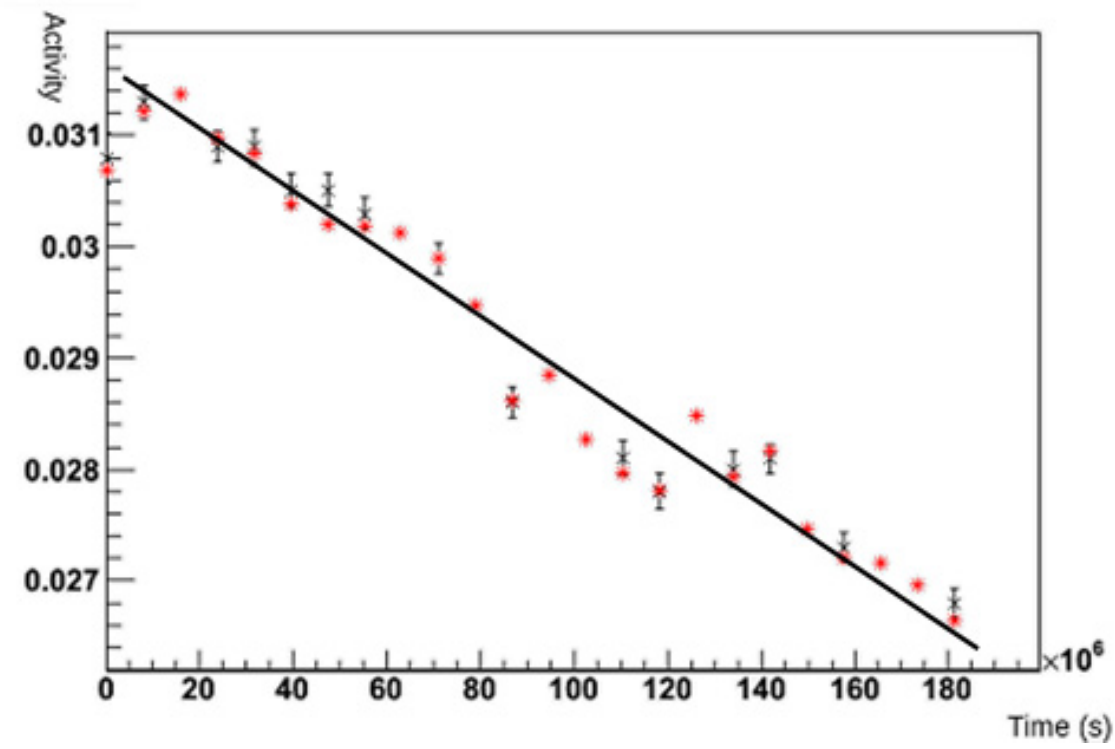

Figure 5.8: ^{90}Y activity for 3 month time slices with low energy ^{210}Bi background added (colours represent two different fitting algorithms, Black: ROOT standard fit data and Red: Mathematica implementation of binned least squares fit data) (errors bars missing due to data loss but of same magnitude as that of the ROOT's standard fit). The trend line shown is based on Mathematica fit data points.

acheved using the Mathmatica data points which is shown in the figure.

This result is close but 20% less than the expected value of the half-life of ^{90}Sr. Therefore to explore the discrepancy further the 1e1γ channel was measured to cross check the background model established from germanium measurements. For these measurements the activities of ^{90}Y and ^{210}Bi backgrounds were fixed to the levels determined from the 1e distribution.

5.3.2.3 The 1e1γ Channel

As the HPGe detectors detect gamma rays, the 1e1γ channel should allow us to probe the same measurement region for isotopes like ^{40}K, ^{214}Bi and ^{210}Bi. This will allow us to cross check our internal background model to see if it accurately describes the energy and angular distributions of the experimental 1e1γ channel data. To achieve this we need to first apply the correct selection criteria.

To select 1 electron and 1 gamma particles the basic cuts for each particle were made as seen in sec.5.2.2 ensuring only 2 scintillator hits were seen, one associated with a track which was the only track detected for that event and had a reconstructed event vertex in the CaF_2 disk region of the foil. Each scintillator hit was isolated and no delayed alpha particles were observed. A TOF hypothesis was also introduced as 2 particles are apparent in this channel and cuts were made on the probabilities. For the internal TOF probability (Pint) the data was cut such that $0.01 \leq \text{Pint} \leq 1.0$ and for the external probability (Pext) $0.0 \leq \text{Pext} \leq 0.04$.

Using these cuts on both the data and MC distributions of the electron energy, gamma energy, electron and gamma energy and the cosine of the angle between the electron and gamma were plotted (Fig.5.9) with all the internal and external background levels mentioned in sec.5.3 and the ^{90}Y and ^{210}Bi levels determined from the 1e channel.

As can be seen from Fig.5.9 the dominant background is ^{90}Y followed by external sources of ^{214}Bi and predominantly from ^{90}Y at small angles due to Bremsstrahlung. However there is a disparity between data and MC below roughly 1.5MeV which exists for all angles. In order to study this discrepancy further the total MC was subtracted from the data to find the residuals (Fig.5.10).

One explanation for this might be a missing background component, one that would not have any preferential angular dependence. A reason for this could perhaps be that as only half the ^{48}Ca sample was measured in the HPGe detector (and not the half used in the detector), the other half may have a contamination from the procedure of creating and handling the sample to make and install the disks. As with the one electron channel the region of the foil was studied to see if there were any hot spots for this channel (fig.5.11).

As can be seen from fig.5.11, the low statistics prevent detailed hotspot analysis but no hugely predominant areas are seen. Therefore any extra backgrounds would be evenly distributed. It might also be some form of detector effect that seems to only cause problems with the ^{48}Ca events as others in that region are not subject to discrepancies of this nature. To determine if the discrepancies seen in the description of the data are limited to only the 1e1γ channel and to further check our background

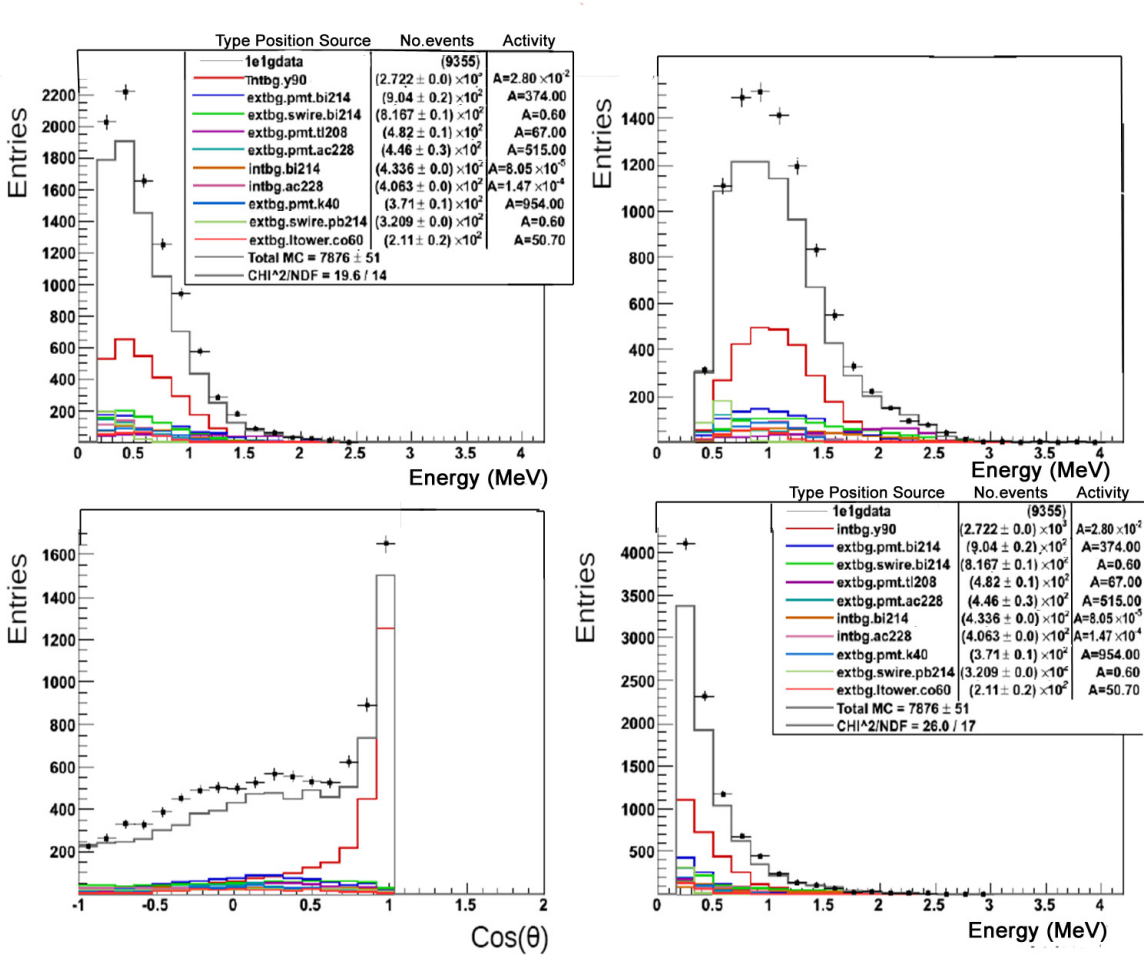

Figure 5.9: Example of 1e1γ distributions (top left: Single electron energy, top right: Sum of electron and gamma energy, bottom left: Cosine of angle between the electron and gamma and bottom right: Single gamma energy).

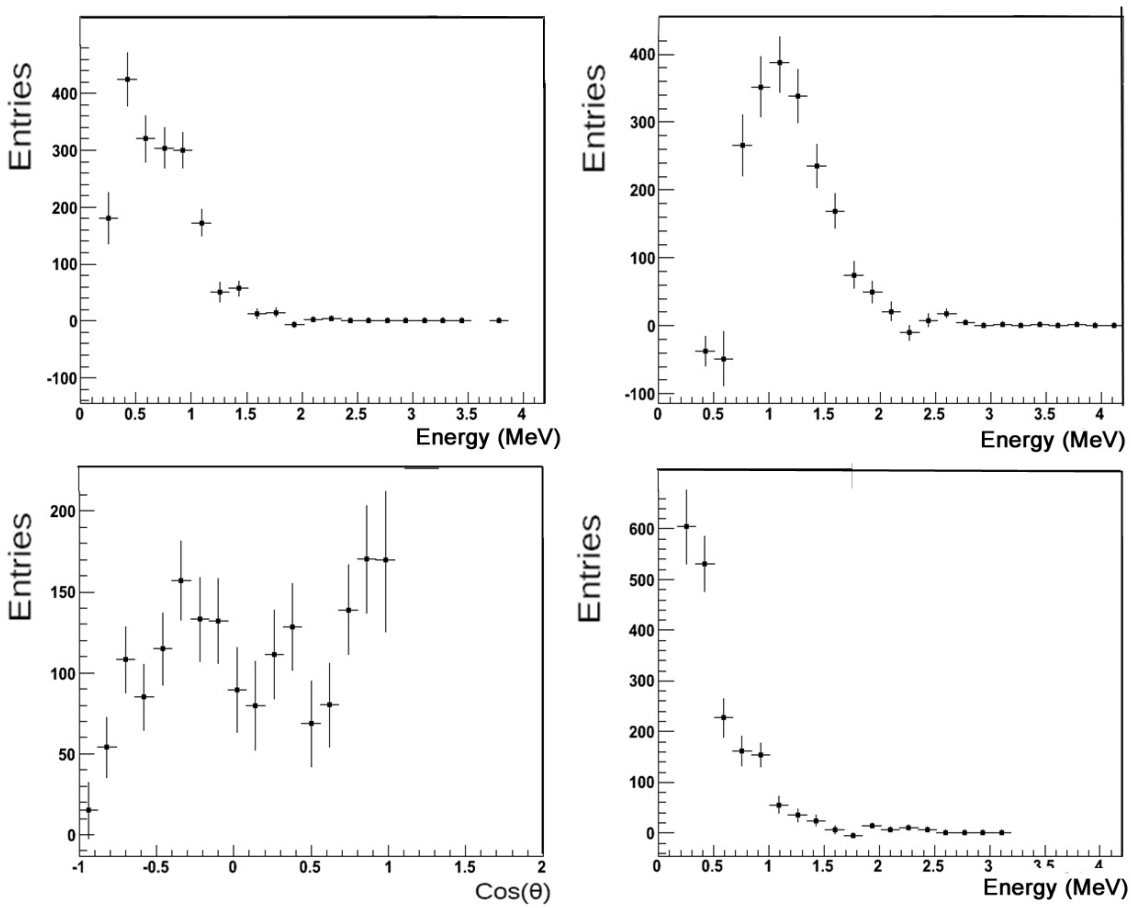

Figure 5.10: Example of 1e1γ residuals (top left: Single electron energy, top right: Sum of electron and gamma energy, bottom left: Cosine of angle between the electron and gamma and bottom right: Single gamma energy).

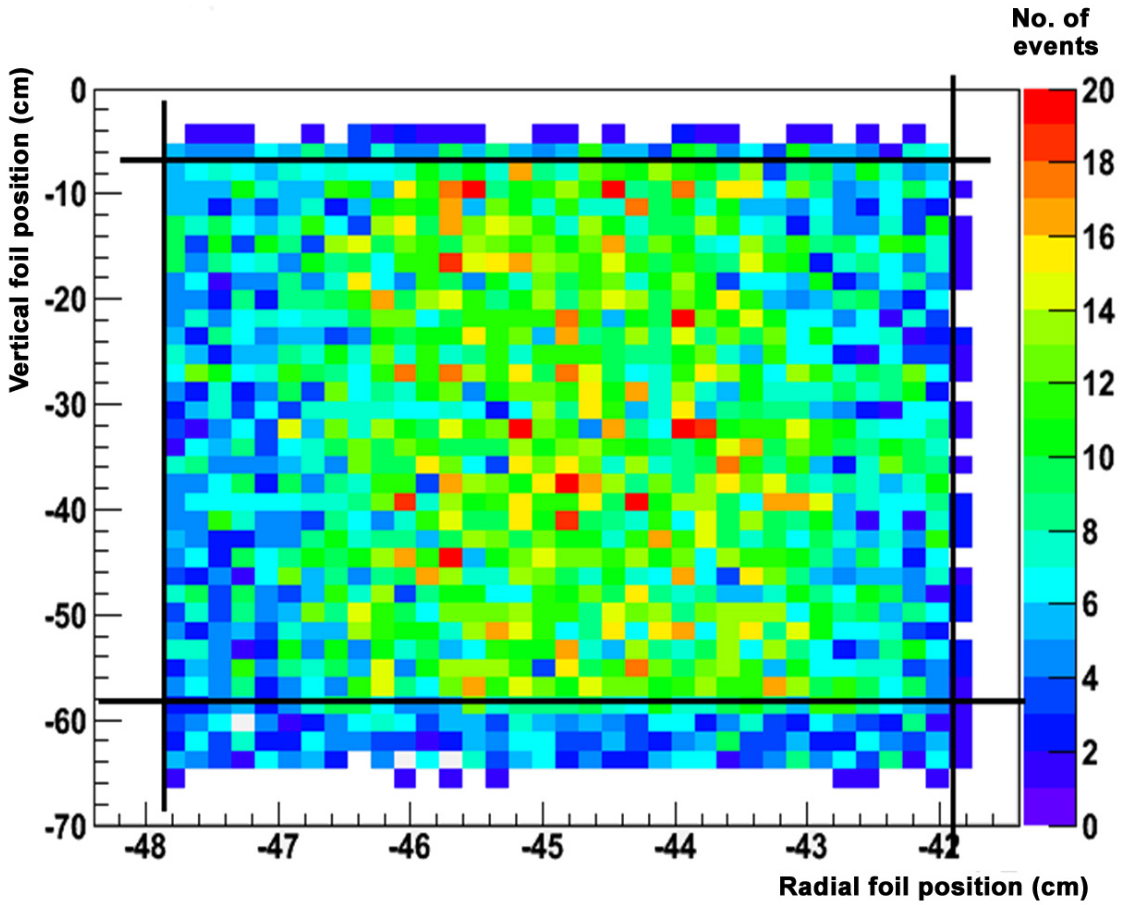

Figure 5.11: Spatial distribution of event vertices across the foil surface.

model for contributions such as ^{208}Tl, the 1e2γ channel was examined.

5.3.2.4 The 1e2γ Channel

As the 1e1γ channel has shown big deficits which could be caused by extra background contributions further channels were explored to see if they could either provide more information for background fitting or evidence of the type of emission from the unknown background. To that end the 1e2γ and 2e1γ channels were selected by the same processes of cuts as that of the above channels. For the 1e2γ plots were made of the summed energy for all three particles as well as the electrons and gamma particles separately and also the angle between the electron and one of the arbitrary gammas (Fig.5.12).

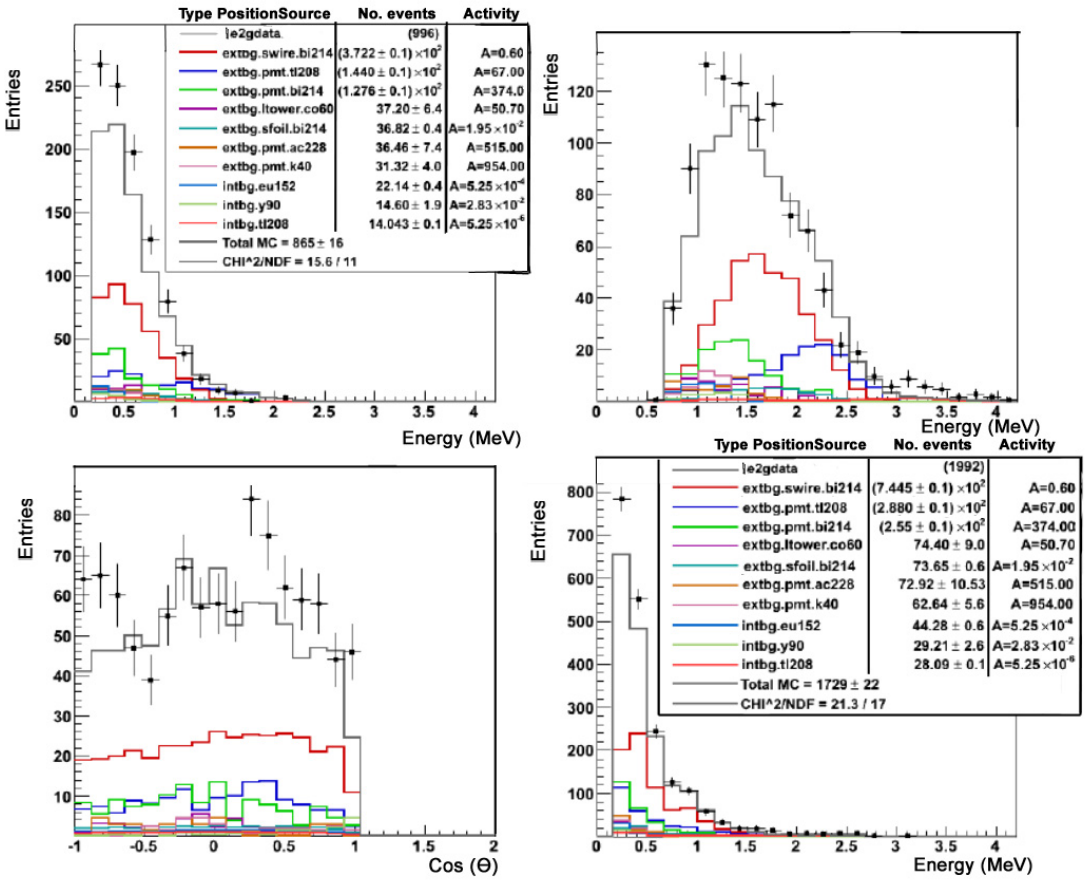

Figure 5.12: Example of the 1e2γ distribution (top left: Electron energy spectra, top right: Sum of the electron and gammas energy, bottom left: Cosine of angle between electrons and arbitrary gamma and bottom right: energy spectra of single gammas).

As can be seen from fig.5.12 ^{214}Bi on the surface of the wires is the biggest contribution with ^{208}Tl and ^{214}Bi from the PMT glass being the next most dominant components. It's also apparent that once again there is a deficit in the total MC for lower energies (below 1.5MeV) which is consistent with what has been seen in other channels. To this end and to help with further study the residuals have been plotted (Fig.5.13).

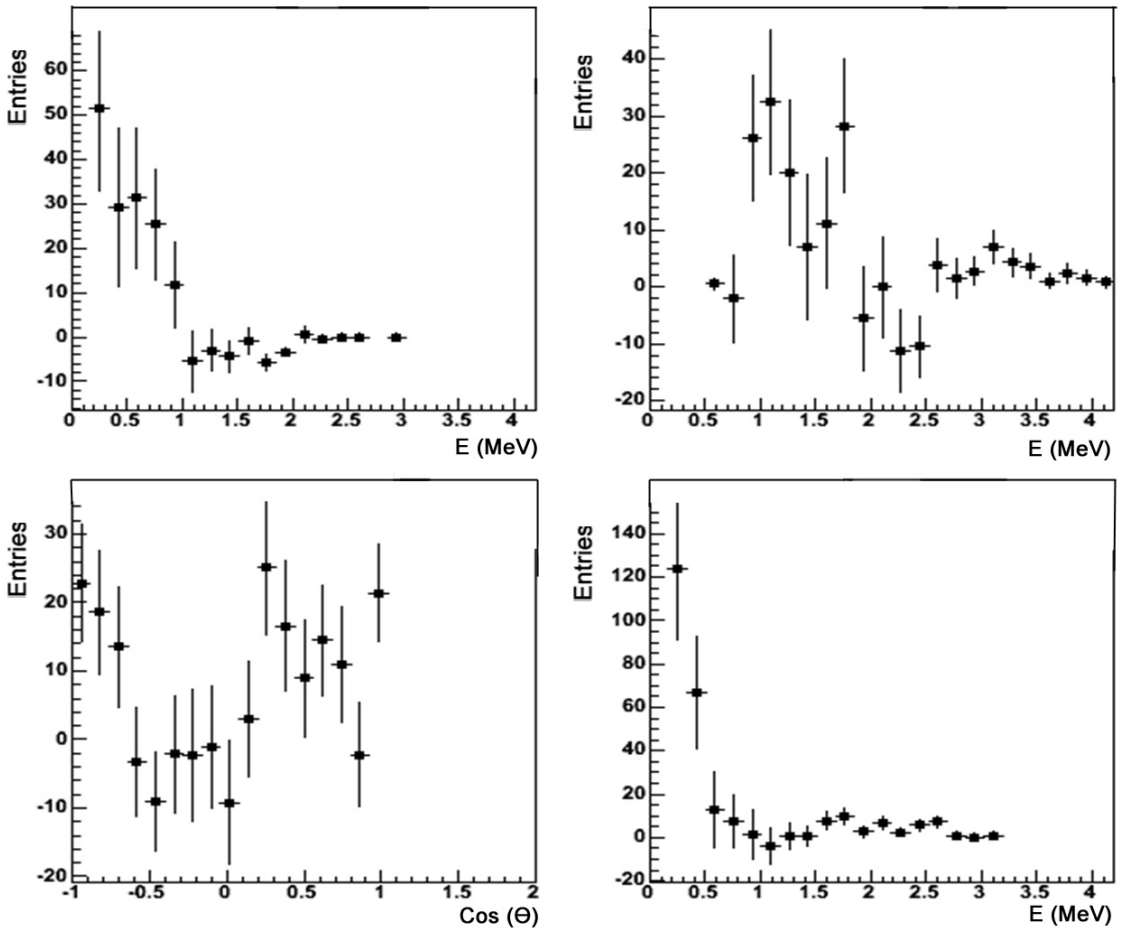

Figure 5.13: Example of the 1e2γ residuals (top left: Electron energy spectra, top right: Sum of the electron and gammas energy, bottom left: Cosine of angle between electrons and arbitrary gamma and bottom right: energy spectra of single gammas).

The 2e1γ channel was also examined however very low numbers of events in this channel made its contribution to understanding the source of the deficit negligible. However as two channels now have a similar issue, further study by examining all channels was undertaken. (See sec.5.5). However before undertaking this it was important to examine the 2e channel to see if there were any effects within our signal channel.

5.4 The 2e Signal Channel

The 2e channel is the channel in which our double beta decay signal will be apparent and ultimately used to perform measurements of its half-life. However before undertaking these measurements investigation of whether the known issues of the other channels cross into the 2e channel is important. To perform such an analysis first we must perform 2e selection cuts on the data.

Two electron events were selected by applying the basic electron cuts as outlined in sec.5.2.2. These cuts where applied to each electron and other cuts were applied allowing only a total of 2 scintillator hits for the event, where each hit must be associated to a track. These tracks had to have reconstructed event vertices on the CaF_2 disks to ensure each electron was from ^{48}Ca. Each of these electrons is required to have energy above that of 200keV (our low energy background) and also be isolated, such that no scintillator blocks adjacent to any triggered by the electrons have hits. Also cuts for delayed alpha particles were applied and TOF probability cuts on the internal probability (Pint) of $0.01 \leq \text{Pint} \leq 1.0$ and the external probability (Pext) of $0.0 \leq \text{Pext} \leq 0.04$ were used to suppress background events which mimic the signal. As two tracks are apparent in 2 electron events the event vertex was described by the average position of the two separate reconstructed event vertices on the foil and it was this position that was used to determine if the event came from the CaF_2 region of the foil. Cuts were also applied to the data to limit the separation of these reconstructed event vertices to ensure that the two tracks were from the same event but within resolution errors. The limits for these positional differences were ΔXY $\leq$2 cm, ΔZ $\leq$7cm.

Using these cuts as outlined above on data and MC and applying the activities of both the NEMO3 measured backgrounds (my internal background measurements and the NEMO3 measured external background model) and the contaminations from the HPGe measurements, distributions of the sum of the electron energies, the cosine of the angle between them at emission and the minimum and maximum individual electron energies of each event were plotted (Fig.5.14). The ^{48}Ca $\beta\beta2\nu$ signal was fitted to the distribution of the electron's summed energy above 1.5 MeV. This was done as in this region the shape of the total MC gives a reasonable description of the data distribution for the 2e channel and also the 1e1γ and 1e2γ channels .

The two electron distributions in Fig.5.14 are dominated by the ^{90}Y internal background component and the ^{48}Ca ($\beta\beta2\nu$) signal. There is however disparity between the expected total MC levels and the data. This lack of events in MC appears to be focused at lower energies below 1.5MeV for the sum spectra (as seen in the 1e1γ and 1e2γ channels) and to large angels $\cos(\theta) \leq 0$. However

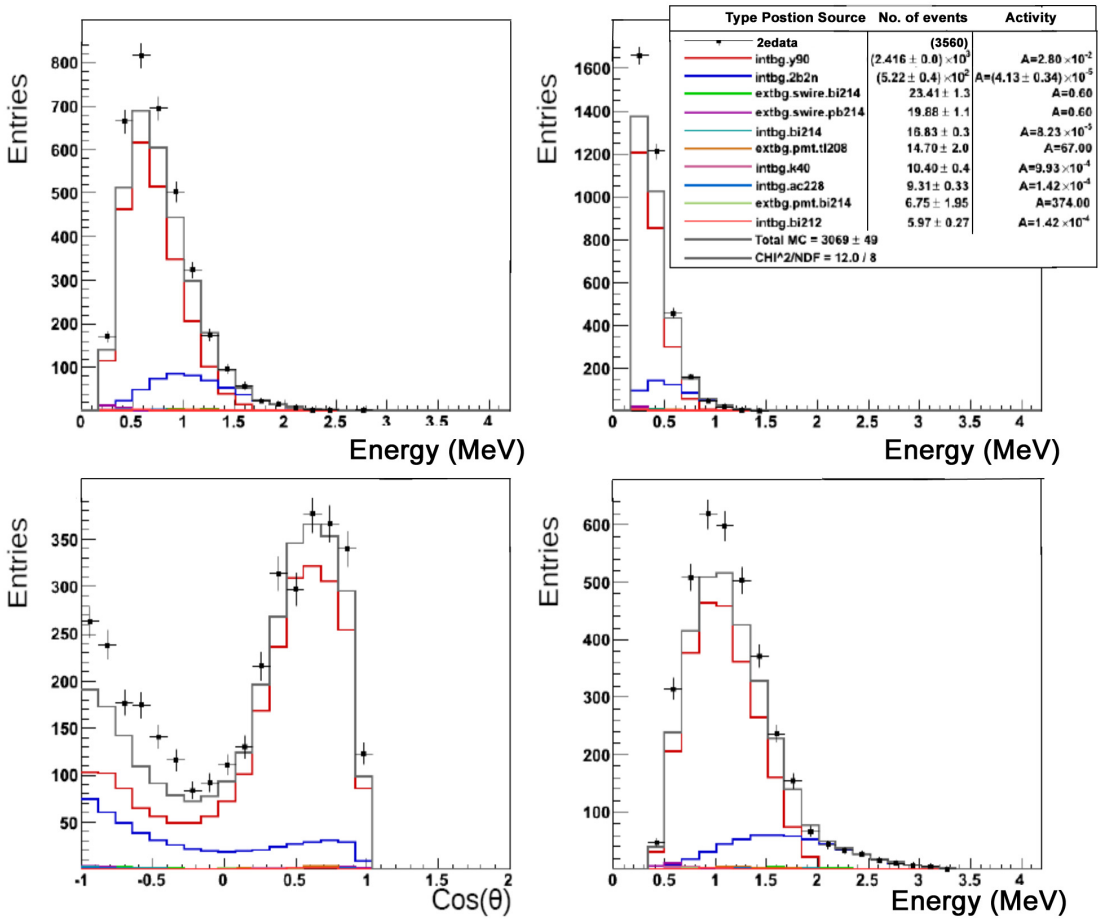

Figure 5.14: Example of 2e distributions (top left: maximum electron energy, top right: minimum electron energy, bottom left: Cosine of angle between electrons and bottom right: Sum of electron energies).

the major background ^{90}Y is focused on small angles $\cos(\theta) \geq 0$ due to Moller scattering being a low momentum transfer interaction. As with previous channels the residuals were plotted (fig.5.15) to help searches for additional background causes and the distribution of event vertices on the source foil surface to examine possible hotspots (fig.5.16). When searching for the hotspots as the deficit was concentrated in the $\cos(\theta) \leq 0$, events from this region only were plotted to see if extra events seen in data were concentrated in particular regions.

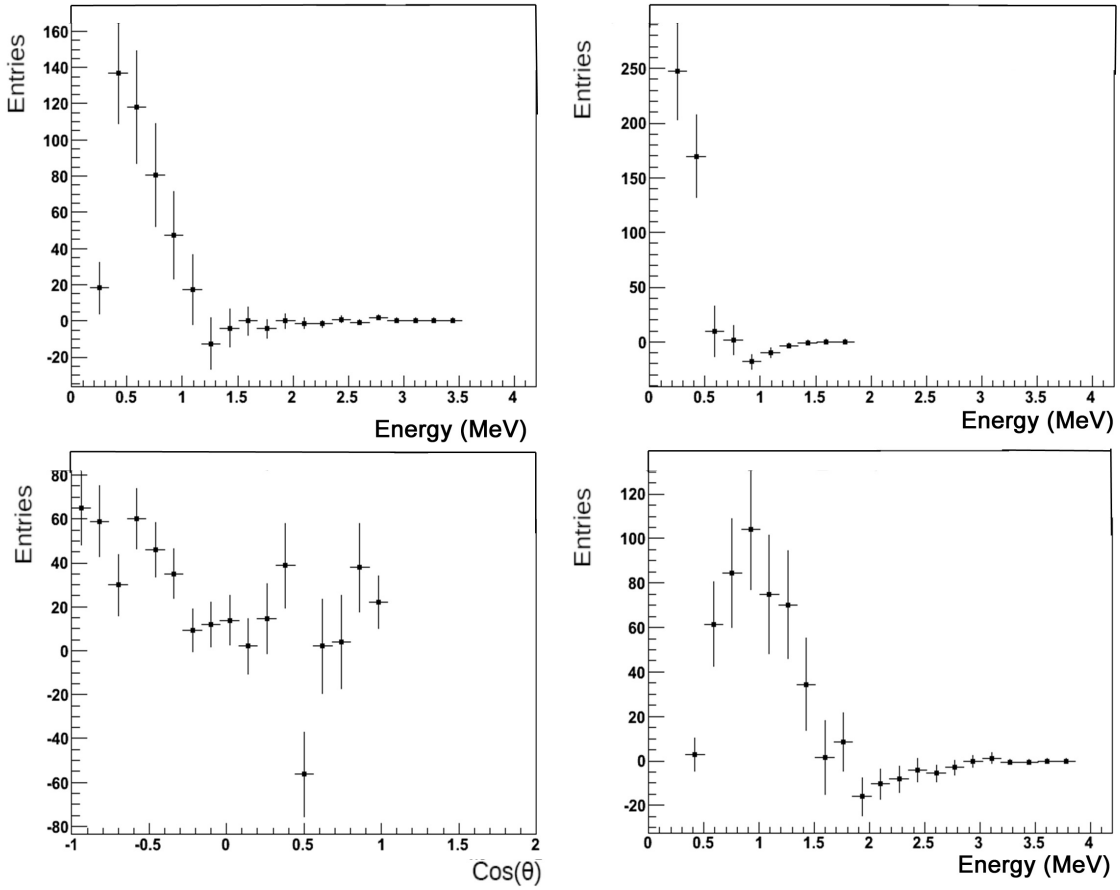

Figure 5.15: Example 2e residuals (top left: maximum electron energy, top right: minimum electron energy, bottom left: Cosine of angle between electrons and bottom right: Sum of electron energies).

The statistics for the two electron foil vertex distribution in the large angle region ($\cos(\theta) \leq 0$) are very low, but no apparent hotspots can be seen. This confirms the same problems seen in other channels so additional studies were undertaken to try and determine its nature.

5.5 Investigation of Deficit

Many channels have seen a deficit in low energies and for 2 electron events they were predominantly in large angles. Possible reasons for this deficit are an unknown or underestimated background of either internal or external nature (note that the ^{48}Ca source in the detector was not the source that was initially tested in the HPGe detector), or some form of detector effect in the region that

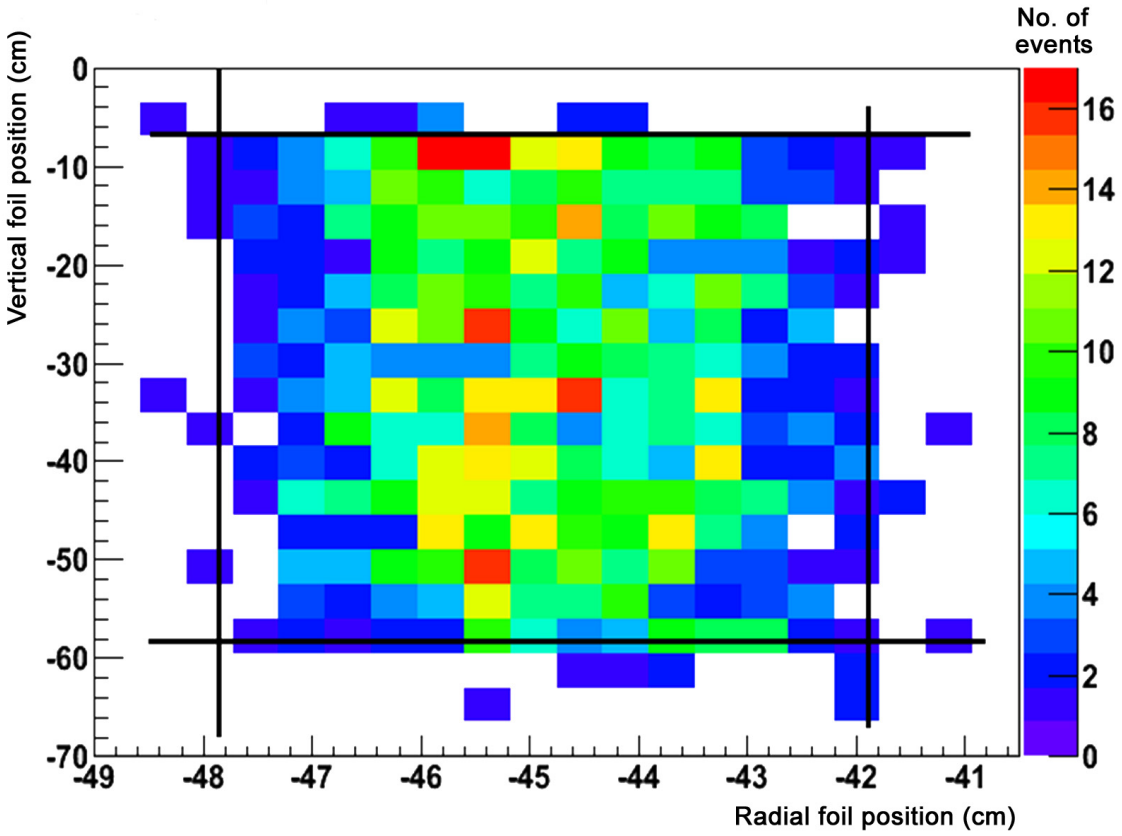

Figure 5.16: Distribution of reconstructed 2e event vertices over the surface of the foil for large angles ($\cos(\theta) \leq 0$).

affects ^{48}Ca but not the nearby ^{96}Zr or ^{150}Nd foils [56, 61]. As adjoining sources had no unknown background components that made detector effects less likely so initially backgrounds were focused on.

5.5.1 Multichannel Background Search

A multichannel search was conducted of various possible backgrounds, in which a single current or a new possible backgrounds were floated in a single channel fit (fitting was always carried out on the energy sum spectra), to find if the addition or enhancement of specific backgrounds would fit the deficit, whilst the other backgrounds were kept at their constant original levels. The results of one channel fit for the activity of the single floated background were then applied as a fixed background to other channels to see if a consistent background description could be formed across all channels. As the effect was only apparent in the ^{48}Ca analysis and not other sources in the region, added to the fact that external backgrounds provide a small contribution owing to the small source mass, it was thought that the source was probably an internal or foil surface contamination, so background searches started with internal backgrounds whilst other contaminants were fixed to their previously determined levels (see Table.5.5). The isotopes considered were selected either due to a previous history of contamination with these isotopes by the source manufacturer, or because they were able to reproduce the topology of the deficit seen for large angles for the 2e channel and 1e1g channel (eg. 1e1g source where the gamma is emitted at an uncorrelated angle or where the gamma could produce a conversion electron or Compton scatter).

Source \ Channel	1e1γ	1e2γ	2e
Standard background model χ^2	26.0/17	21.3/17	12/8
^{152}Eu Activity (Bq/kg)	0.214	0.208	6.286
χ^2	281.8/22	30.6/22	27.4/18
^{40}K Activity (Bq/kg)	3.383	55.429	2.2
χ^2	209.9/22	53/22	33/18
^{212}Bi Activity (Bq/kg)	0.247	0.535	0.537
χ^2	54.3/22	24.3/22	9.8/18
^{60}Co Activity (Bq/kg)	0.282	0.086	10.286
χ^2	66.8/22	31.5/22	14.8/18

Table 5.5: Example of some internal contamination fits for multiple channels, listing the activity of the source and the associated χ^2.

From the studies it was found that any increase in ^{90}Y (the dominant background) in any channel would negatively affect the 1e spectra pushing the total MC contribution way over the observed data level and associated error. Also as ^{90}Y contributes mainly to small angles in the 2e distribution it would not account for the deficit. However one background was found (^{212}Bi) that, as seen in table.5.5, was the only source tried whose contributions in all channels which were fitted independently were of a consistent order of magnitude and with correct distributions to fit the residuals of each spectrum (eg. Fig.5.17).

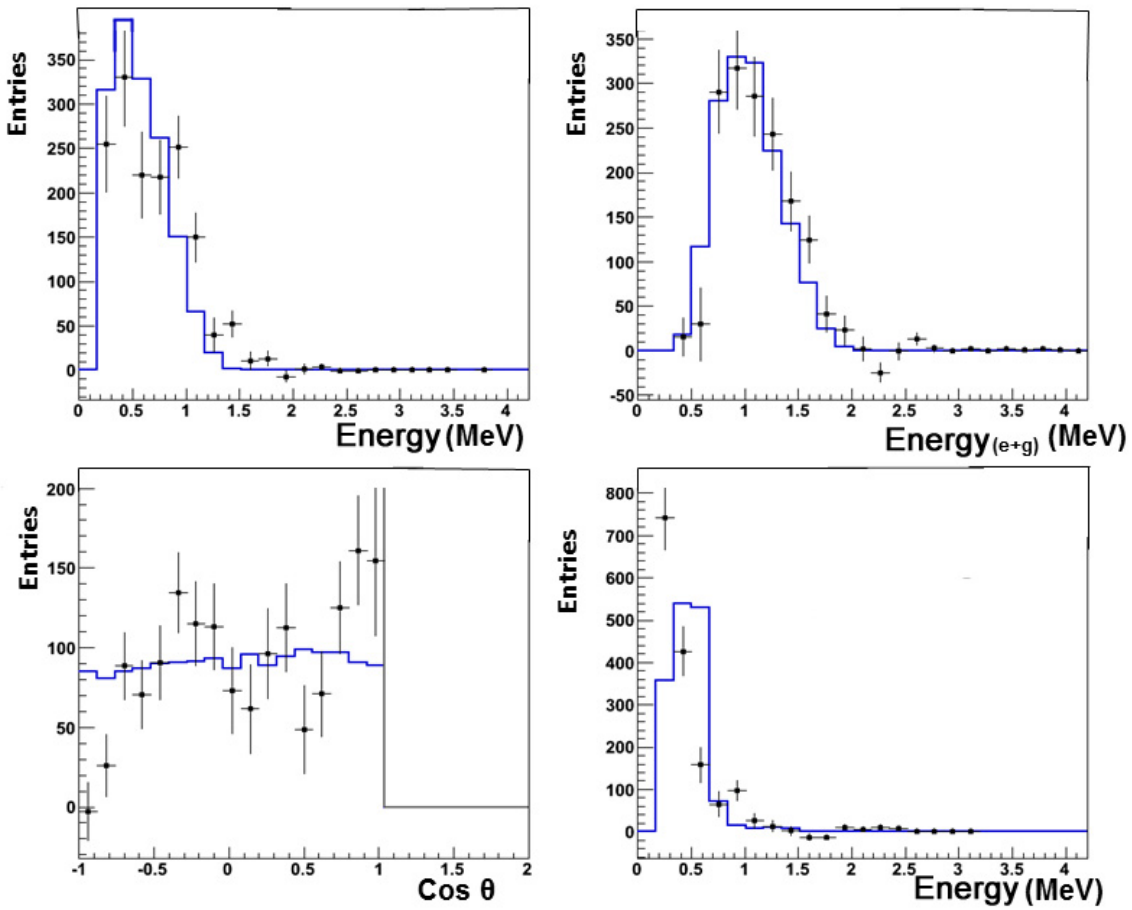

Figure 5.17: 1e1γ residuals fitted with internal ^{212}Bi contamination.

At this point in the investigation the detector had begun to be dismantled and a priority of the collaboration was to re-measure the CaF_2 disks in a HPGe detector as the sample used in the disks was never measured (see table.5.4). These measurements of the internal backgrounds did not show the significant level of ^{212}Bi needed to fit this deficit.

Therefore it was decided to look at external sources of the ^{212}Bi. Two possibilities, for its external origin include natural radioactivity from thorium in the detector which by its decay chain would produce ^{212}Bi (fig.5.18). If this was the case the ^{212}Bi would be in equilibrium with the other atoms in the chain like ^{228}Ac and ^{208}Tl. Another possibility is local leak of ^{220}Rn. We are already aware that radon leaked into the detector in Phase 1 of the detector and that barriers were erected to reduce it, but if there was a local leak in the barrier and ^{220}Rn came in it could settle on the wires and surface of the foil in that region. ^{220}Rn is a much shorter lived isotope than ^{222}Rn having a half-life of just 55 seconds. This would mean that a local contamination could occur that would not affect the detector as a whole or neighbouring sources. However as with thorium in the bulk ^{208}Tl would still be in equilibrium with it.

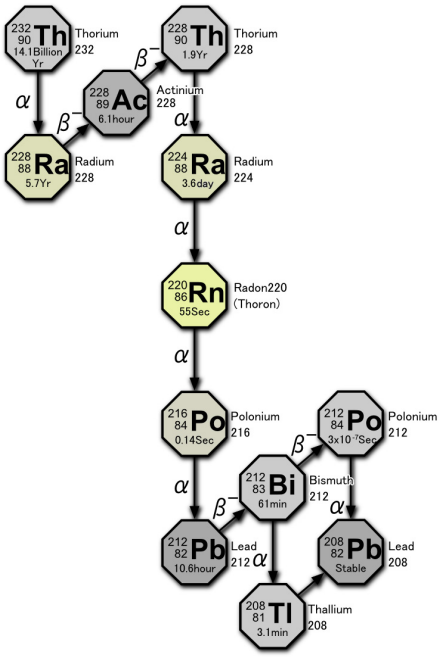

Figure 5.18: Thorium decay chain. [158]

To this end we tried fitting local ^{212}Bi on the surface of the wires both with and without ^{228}Ac for each channel to the particle sum energy spectra. The results of these fits are shown below in table.5.6.

However with very low statistics for the ^{212}Bi MC on the surface of the wires the fits are inconclusive and have large χ^2. The ^{212}Bi on the surface of the foil has a much greater number of events and so better statistics, however any addition of ^{212}Bi to account for the deficits in the 1e1γ, 1e2γ and 2e channels negatively affects the 1e channel which can only be solved by reducing the ^{90}Y

Channel	^{212}Bi Activity (Bq)		
	Fitted ^{212}Bi (swires)	Fitted ^{212}Bi (sfoil)	fitted ^{212}Bi & ^{228}Ac (swires)
1e1γ	0.257 ± 0.015	0.0108 ± 0.001	0.0440 ± 0.0002
1e2γ	0.48 ± 0.14	-	0.06 ± 0.012
2e	0.16 ± 0.04	0.0887 ± 0.0136	0.079 ± 0.017

Table 5.6: ^{212}Bi activities from fits to ^{48}Ca channels.

component as can be seen in fig.5.19, which will in turn cause more problems in the other channels. So it appears that ^{212}Bi is not the answer.

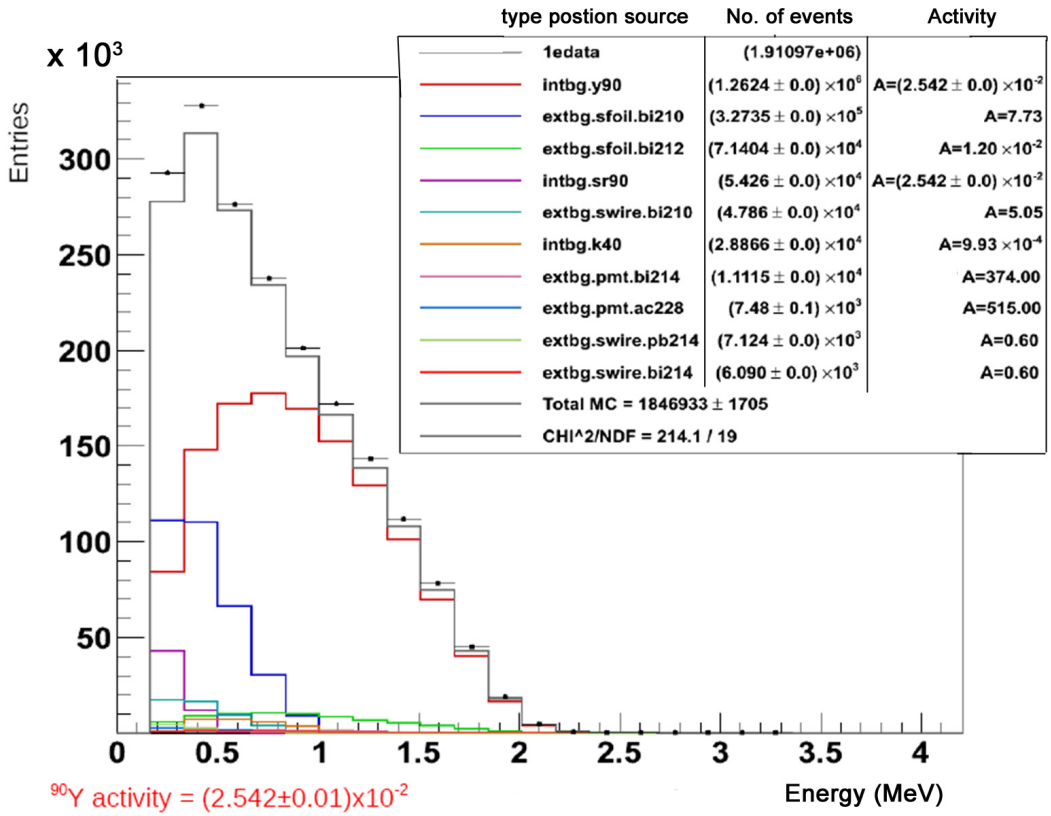

Figure 5.19: Example 1e spectrum with ^{212}Bi (sfoil) the ^{90}Y component (red) has been reduced to account for the addition of the ^{212}Bi component (light green).

5.5.2 Detector Effects

Since the ^{48}Ca source is located in the same sector and even strip as other sources, any detector effects in either the Geiger cells or PMTs would impact all the sources in this region. Therefore it is very unlikely that instrumentation error of this kind is responsible. However an abnormality in the source geometry description for ^{48}Ca specifically might cause individual errors for this one source and not affect others. To find such an effect we can begin by examining if problems arise and their extent, when examining the energy distributions of events that take place which produce particles on one particular side of the foil. If a defect is seen on one particular side over another then it will

be apparent by this method.

This study was done for the 1e, 2e and 1e1γ channels by cutting and separating events that happen on the inside calorimeter wall closer to the centre of the toroid or the outside. For the channels where two particles are produced (2e and 1e1γ) three distributions were made, where both particles go to the inside, both go to the outside and one each side (see fig.5.20).

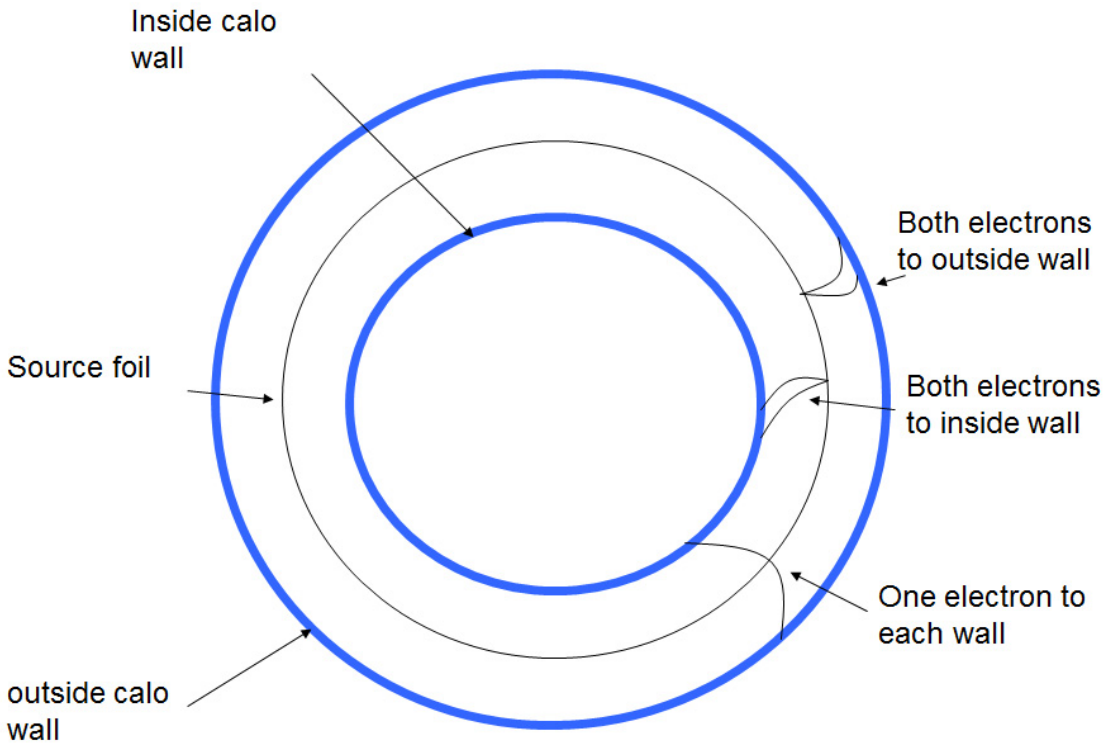

Figure 5.20: Schematic of the 3 types of 2 electron events for inside and outside wall interactions.

For the 1e distributions (Fig.5.21) the plots were fitted for ^{90}Y and ^{210}Bi independently and the external and internal backgrounds were set at their previous levels. The events to the inside wall give a better fit to the higher energy but at lower energies there is a slight disparity. With the outside wall events, the lower energy is fitted better but at the expense of some of the distribution around 1-1.5 MeV. Overall there is not much difference in the χ^2 with the inside wall distribution performing slightly better.

For the 2e channel (fig.5.22 , fig.5.23 and fig.5.24) once again the background levels fitted in the previous analysis where all data was combined were used. Fig.5.22 and Fig.5.23 show that for both electrons emitted on the same side of the detector there is a good agreement between MC and data. However, the distributions from electrons hitting opposite walls (fig.5.24) shows a greater disparity than the combined analysis. It's clear as with the combined analysis, that the deficit is predominantly present at large angles. This is why it probably correlates that the biggest deficit is seen in the distribution where one electron goes to either wall, where it is now very apparent.

For the 1e1γ channel (fig.5.25, fig.5.26 and fig.5.27) the deficit was more evenly spread throughout

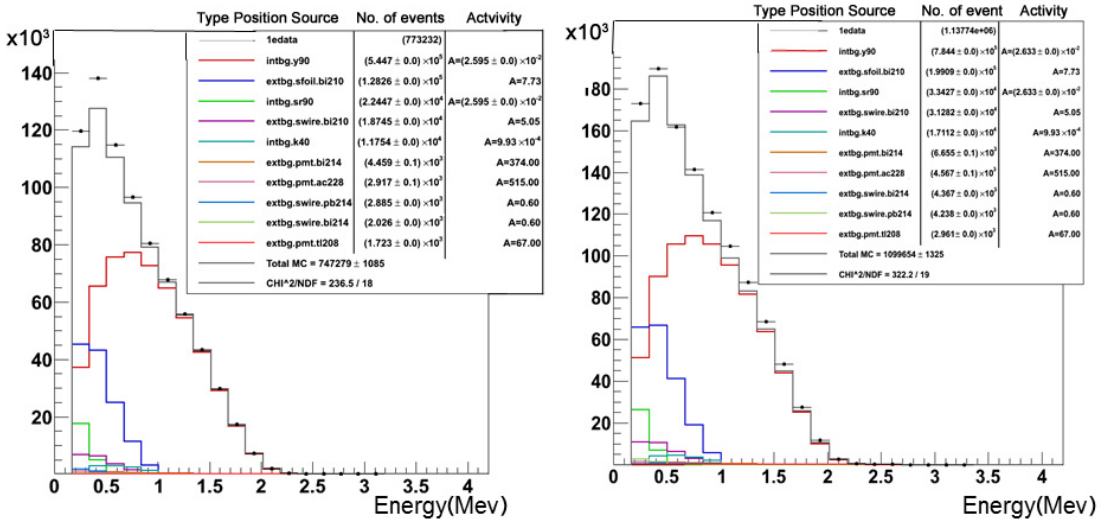

Figure 5.21: Energy distributions for the 1 electron events on either side of the foil (left:inside calorimiter wall, right:outside calorimiter wall).

the angular distribution. The events impacting the outside wall are a better fit to the data, whereas both the inside wall and both wall events have a much larger deficit for the low energy region.

From these studies we can see that in the 1e1g channel all 3 directions appear to have deficits in the MC for the lower energy region. However it would also appear that events impacting the inside wall have a greater disparity than those hitting the outside wall. This directionality of deficit, along with the absence of an extra background component that would fit it, points towards a potential detector effect. Such an effect could occur from a problem with the source geometry or orientation description. These findings were subsequently confirmed in sec.5.9

It was also decided to see if over the data taking period there were any times at which a fault in the detector might have caused unusually high event rates in events hitting in any one direction (inside or outside). However plots of the event direction against time showed no evidence of temporal effects in the acquisition period.

As no consistent approach has managed to either determine or help remove this deficit in our MC model, it was decided that to limit its effect that a cut of 1.5 MeV would be applied where the backgrounds appear reasonably understood in all channels.

5.6 $\beta\beta2\nu$ Decay Analysis and Results

The final selection criteria for 2e events used to measure the $\beta\beta2\nu$ decay half-life of ^{48}Ca are as above for the 2e channel analysis (Sec.5.4), plus the addition of an energy cut in the summed electron energy of E>1.5MeV. This new cut is to remove the region below 1.5MeV for which our background model shows discrepancies from the data in both the 2e and the 1e1γ channels. A second cut is also

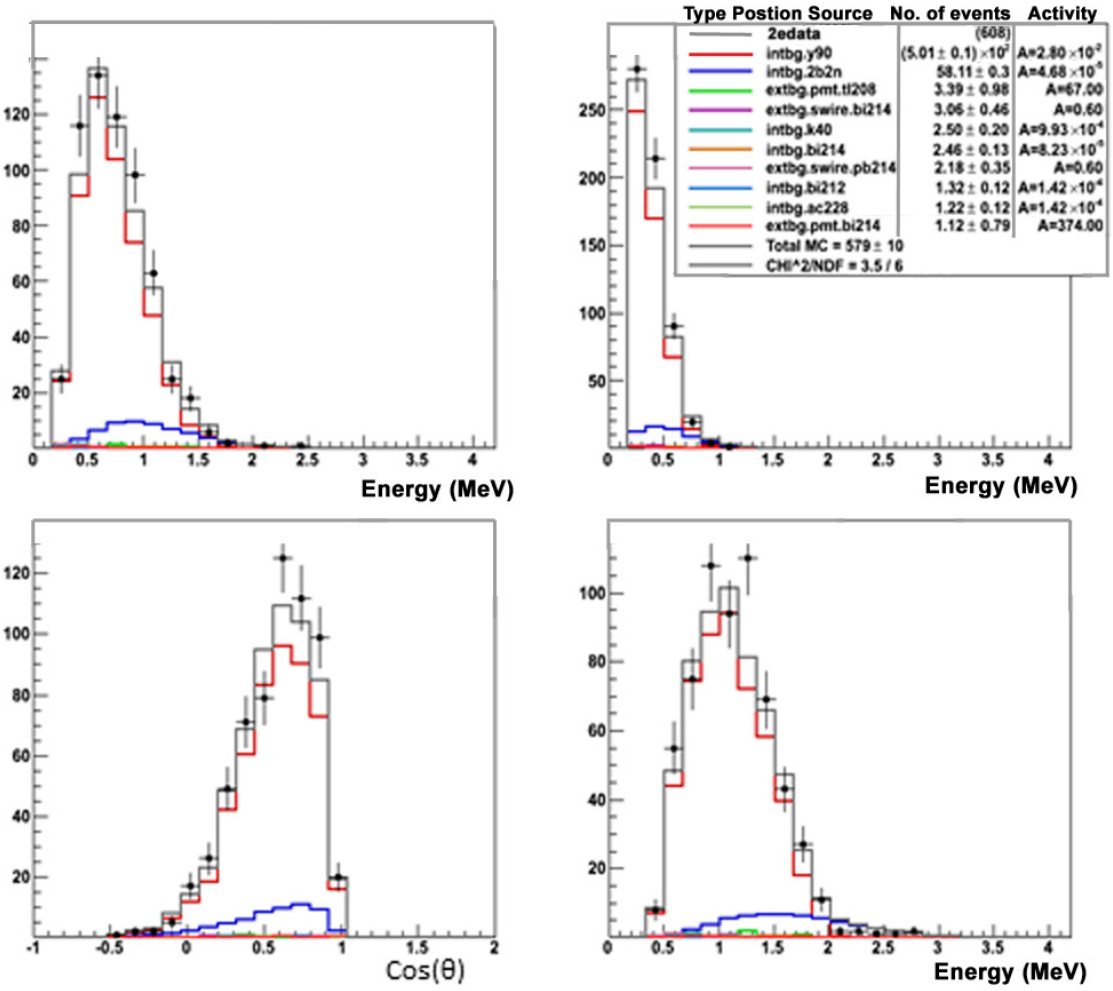

Figure 5.22: Energy and angular distributions for the 2e events where both electrons go to the calorimiter wall on the inner side of foil.

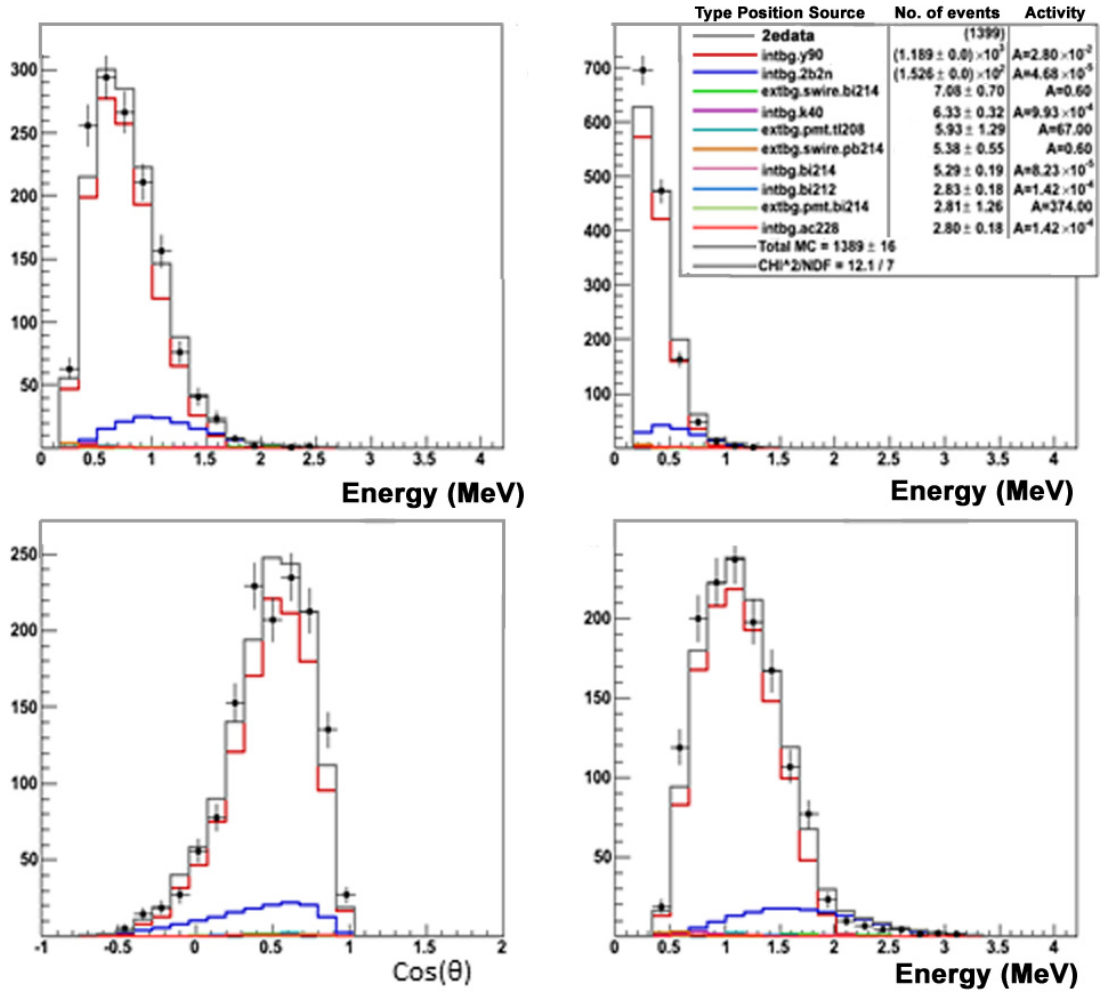

Figure 5.23: Energy and angular distributions for the 2e events where both electrons go to the calorimiter wall on the outer side of foil.

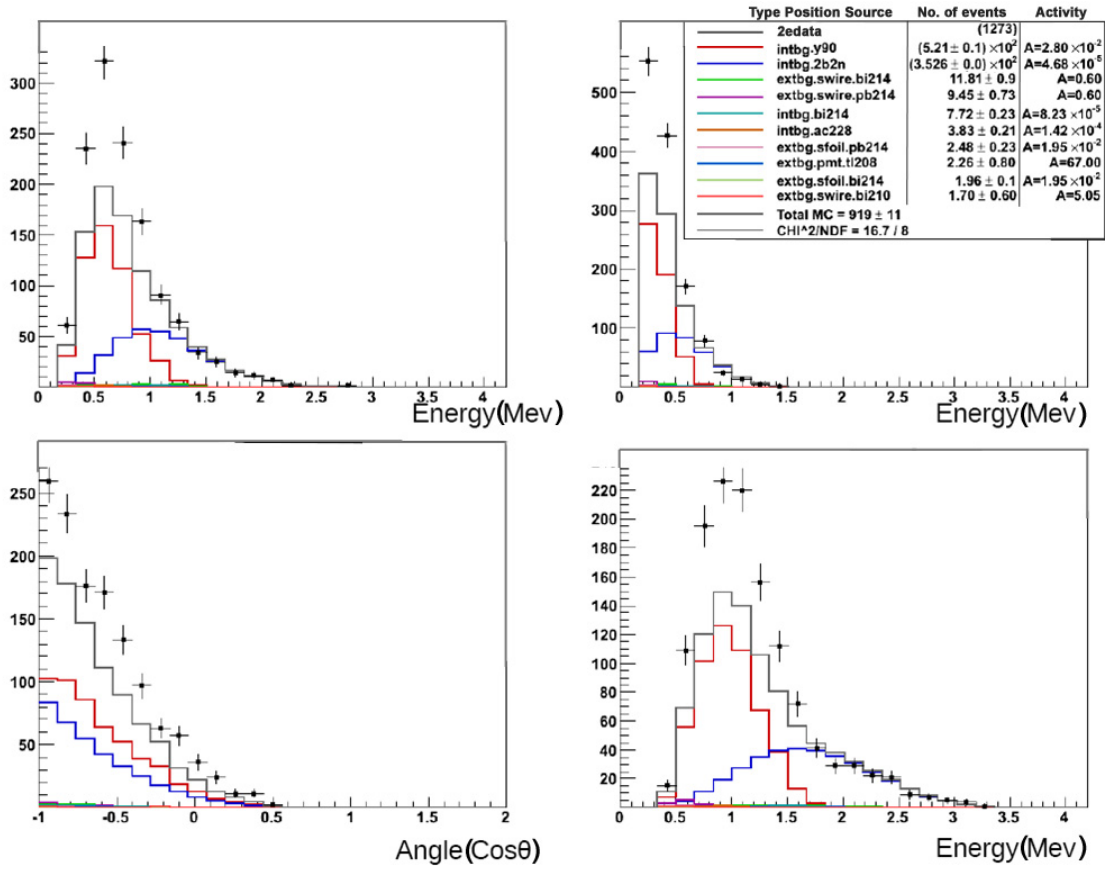

Figure 5.24: Energy and angular distributions for the 2e events where one electron goes to either side of the foil.

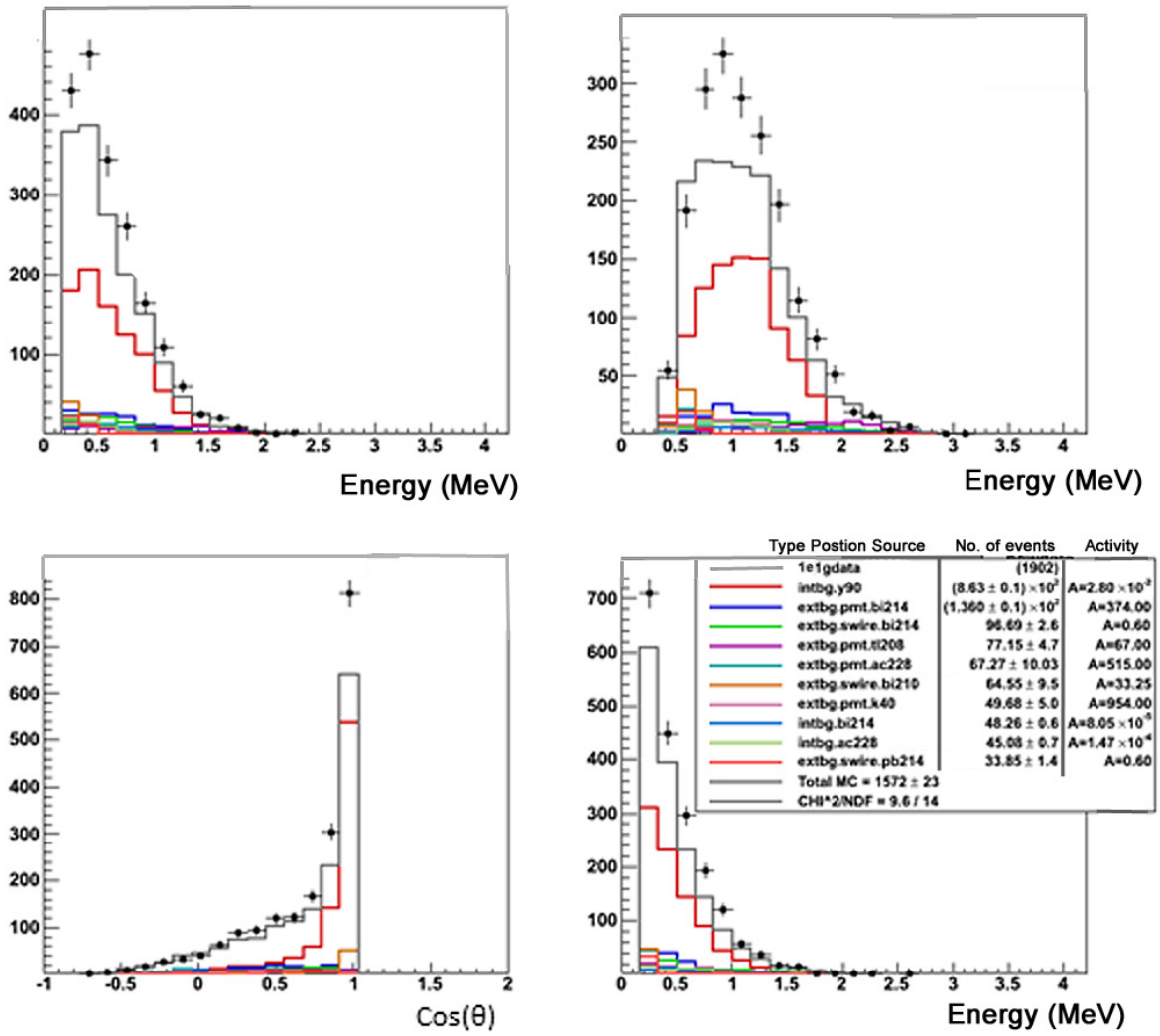

Figure 5.25: Energy and angular distributions for the 1e1γ events where both particles go to the calorimiter wall on the inner side of foil.

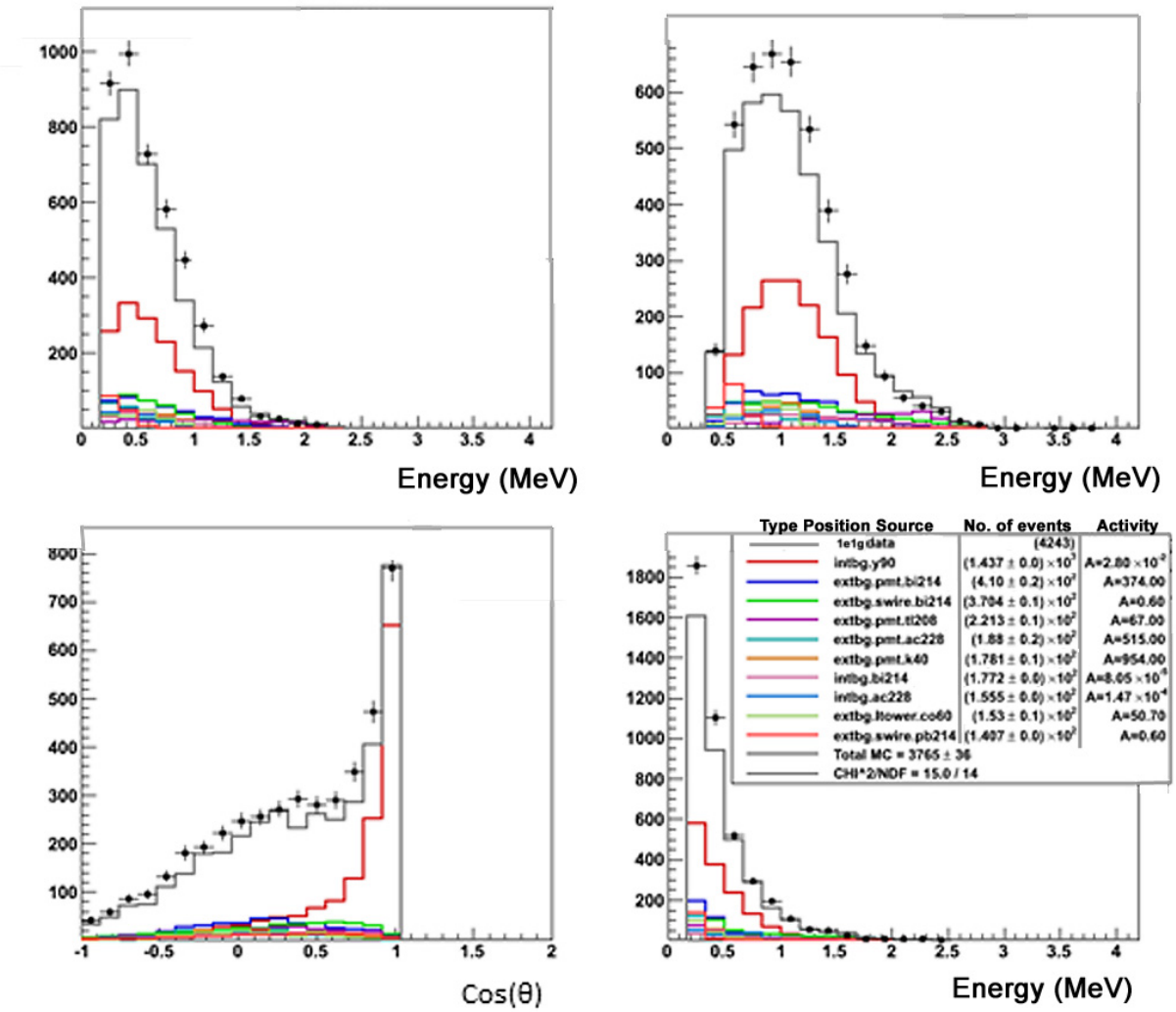

Figure 5.26: Energy and angular distributions for the 1e1γ events where both particles go to the calorimiter wall on the outer side of foil.

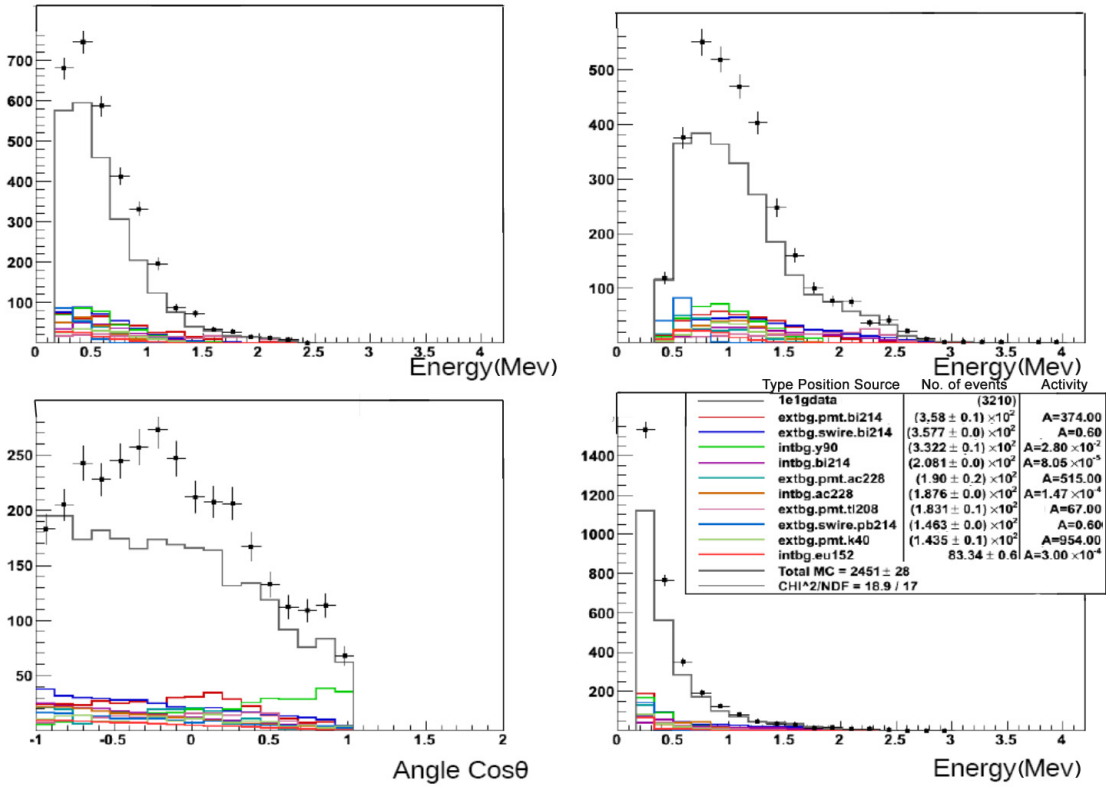

Figure 5.27: Energy and angular distributions for the 1e1γ events where one particle goes to either side of the ^{48}Ca foil.

made in the angular distribution such that only events where the cosine of angle between the two electrons is less that 0 ($\cos(\theta) < 0$) are kept (Fig.5.28). This cut was made to increase the signal to background ratio of the analysed region from 0.19 to 8.6 by removing a large proportion of the dominant backgrounds ^{90}Y, which is most prevalent in small angles ($\cos(\theta) > 0$).

Fig.5.28 shows the use of a maximised binned likelihood fit to establish the number of $\beta\beta2\nu$ signal events within the sample region (see sec.5.2.4) N_{dec} = to 189±11.

When measuring the half-life of the $\beta\beta2\nu$ decay process of ^{48}Ca we make use of eqn.5.22. For this equation the value of the enriched ^{48}Ca mass (m_i) is 6.99g, the mass number (A_r) is 48 and the detection time (t) is 4.25 years (see sec.5.2.7). The efficiency (ϵ) is found using MC generation and is the percentage of generated $\beta\beta2\nu$ events that passed the cuts, in this case it is 0.03. Using this information and the number of $\beta\beta2\nu$ decays (N_{dec} = 189±11) from the $\beta\beta2\nu$ signal fits of the 2 electron spectra we can determine a value for the half-life of the process (Eqn.5.35).

$$T_{1/2} = \epsilon \frac{m_i N_A}{A_r N_{dec}} ln(2) t = 0.03 \frac{6.99 \times 6.023 \times 10^{23}}{48 \times 189} ln(2) \times 4.25 = 4.11^{+0.23}_{-0.20}(stat.) \times 10^{19} years \quad (5.35)$$

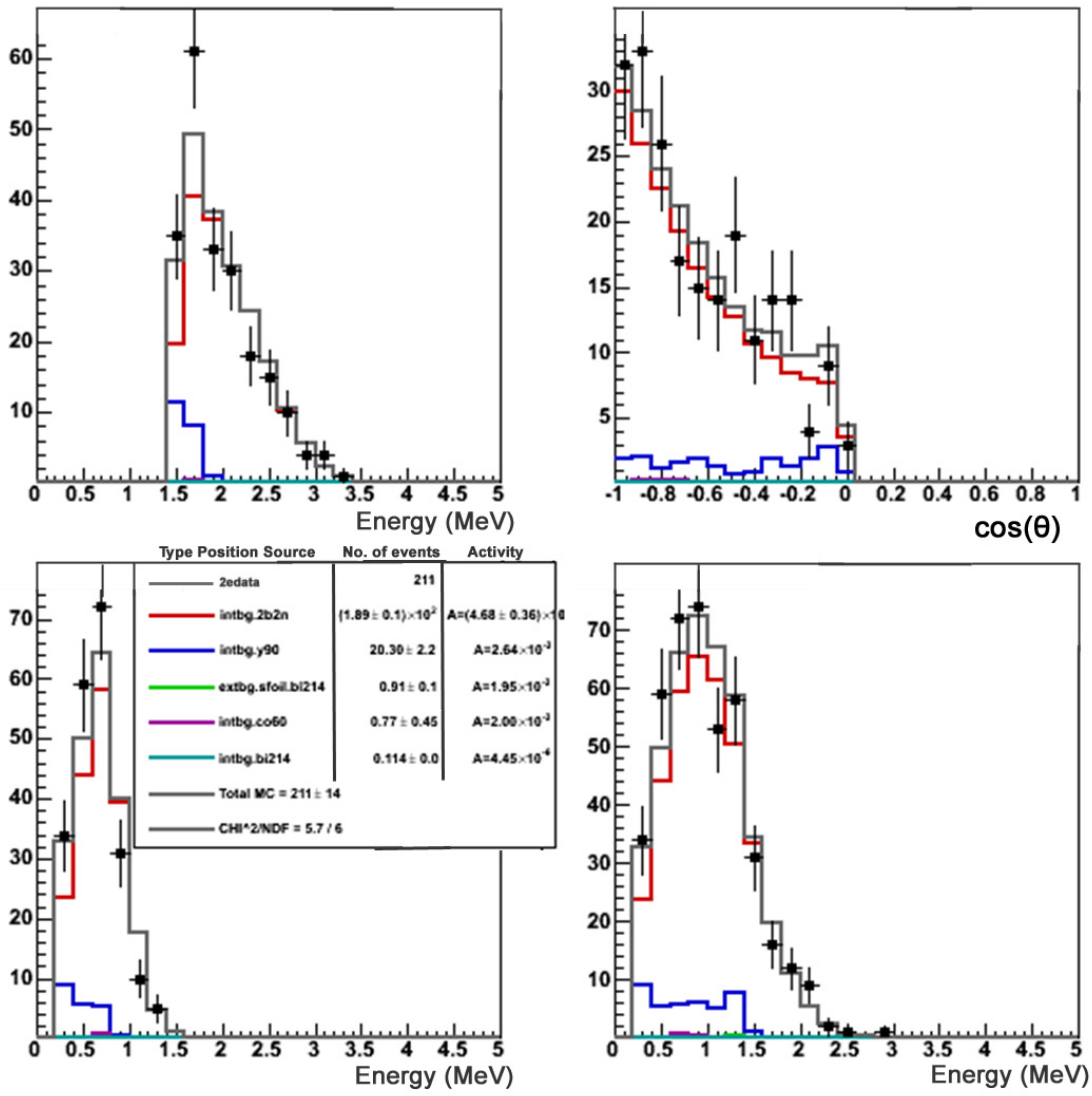

Figure 5.28: 2e distributions of events with applied energy cut (E_{sum} >1.5MeV) and angle cut ($\cos(\theta) < 0$) (red component is the ^{48}Ca $\beta\beta2\nu$ signal and the blue component is the ^{90}Y background).

5.7 Systematic Errors

The systematic errors on the final half-life result for $\beta\beta2\nu$ decay of ^{48}Ca come from a cumulative effect of a number of uncertainties in the detector and processes listed below.

- The enrichment processes of ^{48}Ca have an associated uncertainty on the quoted enrichment percentage of 73.2% which translates to an error on the half-life of of 2.2% [147].
- There is an inherent error in the GEANT simulations when producing MC, and errors from the reconstructing of tracks that both affect the MC efficiency calculations when simulating ^{48}Ca events. This efficiency error has been measured by simulations of the calibration sources and measurements of their activity. These errors have been found to contribute an uncertainty of 5% [159].
- When calibrating the energy scale of the detector there is an associated uncertainty of 1%. This translates to a 1% systematic error on the half-life that must be included. This value comes from estimation of variations in the energy scale data by fluctuating the gains of the PMTs [159].
- There is an uncertainty from the determination of the ^{90}Y activity measured from the 1 electron channel. This uncertainty on the major background is based on the calibration ^{90}Sr sources placed in the detector via the calibration tubes. Measurements were made of the ^{90}Sr sources' half-lives using a HPGe detector before placing them in the detector and that measurement has a 12.5% error that will give 12.5% uncertainty on the ^{90}Y activity. This can be propagated to give an error of 1.7% on the $\beta\beta2\nu$ half-life [159].
- The position of the CaF_2 disks within the detector has an associated uncertainty that affects the half-life. Distributions of the 1e channel were compared with MC for the azimuthal position (X) and the height (Z) and discrepancies were seen between the data and MC. These discrepancies could be due to either incorrect source geometry or uncertainties in the descriptions of the calibration tube geometry on which the coordinates are based. The effect of this uncertainty on the half-life was simulated and estimated to be 2.5% for the X vertex variations and 0.5% for the Z vertex (see fig.5.29) [156, 159].

The summation of the effect of these systematic errors gives a total of 6.34% which can be applied to the calculated half-lives of ^{48}Ca.

Therefore the ^{48}Ca $\beta\beta2\nu$ decay half-life measured in sec.5.6 will become $T_{1/2} = 4.11^{+0.23}_{-0.20}(stat.) \pm 0.26(syst.) \times 10^{19}$ years.

5.8 $\beta\beta0\nu$ Analysis and Results

As no data events can be seen in the 2 electron energy sum spectrum above 3.5 MeV and no events are expected from the simulated background (see fig.5.30) we can set a limit on the half-life of ^{48}Ca

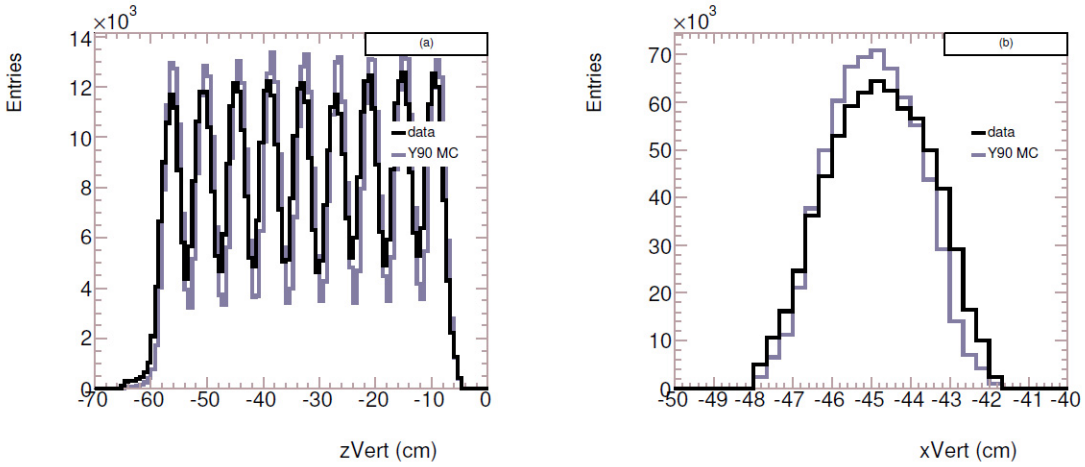

Figure 5.29: Spatial distribution of 1e events in the azimuthal position (X) and the height (Z). [156]

$\beta\beta0\nu$ decay using the formula in eqn.5.22 and the method described in sec.5.2.6 to find the number of expected events. This method was employed in two algorithms called the Helene method and MClimit. The Helene method uses a window method where the window must first be optimised and then the confidence limits of the encompassing bins are combined, whilst MClimit takes the spectrum as a whole and performs the confidence limits binwise for the whole spectrum.

Firstly using the Helene method the energy window for which the algorithm should be run over was calculated by progressively moving the upper and lower limits and calculating the S/B to optimise it. This was found to be the window from 3.40MeV to 4.8MeV. The Helene method was then executed on this window and as no events are observed in this window and 0 background expected the number of excluded events from $\beta\beta0\nu$ at 90%CL is 2.3 (N_{dec}). Substituting this into eqn.5.22 along with the efficiency of $\beta\beta0\nu$ events (ϵ) for this window, which was 0.146 calculated by MC, and all the other associated variables, the limit on the ^{48}Ca $\beta\beta0\nu$ decay half-life was found to be $T_{1/2} > 1.64 \times 10^{22}$ years at 90% CL.

The MC Tlimit approach uses the whole spectrum taking into account the shape and gives an efficiency $\epsilon = 0.189$ and the number of excluded events at 90% CL N_{dec} <2.77. Using these in eqn.5.22 we obtain a ^{48}Ca $\beta\beta0\nu$ decay half-life of $T_{1/2} > 1.76 \times 10^{22}$ years at 90% CL.

5.9 Concluding Remarks

The measured ^{48}Ca $\beta\beta2\nu$ decay half-life value of $T_{1/2} = 4.11^{+0.23}_{-0.20}(stat.) \pm 0.26(syst.) \times 10^{19}$ years is the world's most accurate result to date. It is a big improvement on previous experimental results from both the TGV and Hoover Dam experiments which measured $(4.2^{+3.3}_{-1.3}) \times 10^{19}$ and $(4.3^{+2.6}_{-1.1} \pm 1.4) \times 10^{19}$ years respectively. It also supercedes that of $T_{1/2} = 4.44^{+0.49}_{-0.40}(stat.) \pm 0.29(syst.)$ years measured previously also by the NEMO3 detector using only 2.58 years of initial data [156].

Using my measured half-life, the value of the matrix element $M_{2\nu}$ can also be determined by

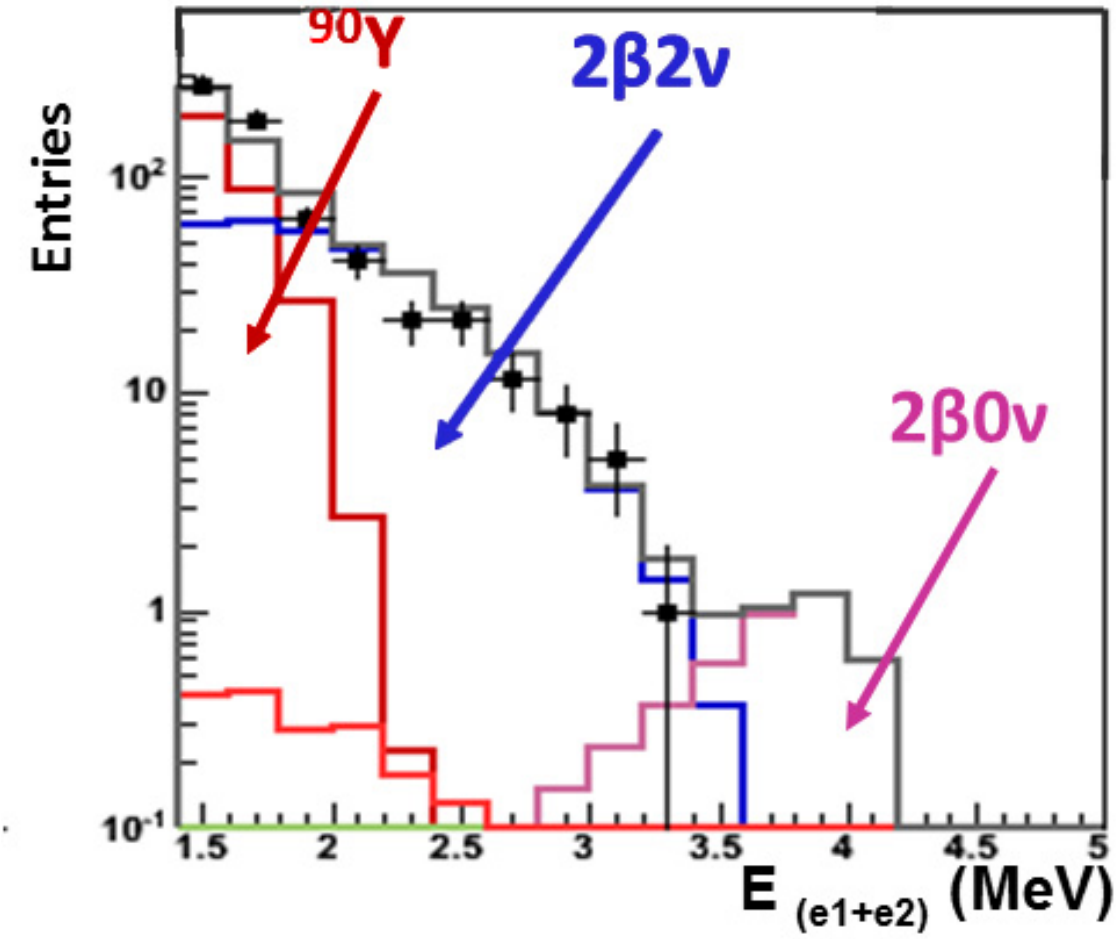

Figure 5.30: Example of tail of the 2e summed energy distribution (where no events can be seen above 3.5MeV and an example of the ^{48}Ca $\beta\beta0\nu$ decay contribution set at its upper limit has been added.

using eqn.2.10 and phase space factor G = 4.0 $\times 10^{-17}$. This gives a value for the matrix element of $M_{2\nu} = 0.0247 \pm 0.0015$ which is a very useful and important measurement for nuclear model theory. The precision of this measurement can help descriminate between different theories. The two most recent $M_{2\nu}$ calculations for ^{48}Ca $\beta\beta2\nu$ decay use different implementations of the shell model and obtain values that range from 0.026 - 0.028 in units of electron masses [160, 161]. As mentioned previously ^{48}Ca with its doubly magic nature is uniquely placed to provide a test bench and verification for shell model calculations which are seen to be some of the most reliable.

The limit obtained for ^{48}Ca $\beta\beta0\nu$ decay half-life was $T_{1/2} > 1.8\times10^{22}$ years at 90% CL. Using this value and eqn.2.13 and the theoretical nuclear matrix element $M_{0\nu} = 0.72$ we can determine a limit for the effective mass of the neutrino to be $\langle m_\nu \rangle < 19.8$ eV. This result is comparable to the current best measurement of the process by ELEGANT VI which obtained a result of $T_{1/2} > 5.8\times10^{22}$ years at 90% CL [127]. It is worth noting that with less than 7g of ^{48}Ca source, 3 orders of magnitude less than the ^{100}Mo used (6kg), which yielded a limit of $\langle m_\nu \rangle < 0.3 - 0.9$ eV, we obtain a limit of only just over one order of magnitude worse. This demonstrates the importance of ^{48}Ca as a promising double beta decay candidate.

At the time of writing this thesis the dismantlement of the detector had started. During this process problems with the source positioning and geometry were discovered confirming the hints found in the analysis. The problems included an incorrectly recorded size of the ^{48}Ca source disks, rotation of the source plane within the detector and others (see sec.10.2). The effect of these problems will all require further determination and study (See sec.10.2), but incorrect disk sizes would mean the density of the sources would be altered from the expected value simulated. This would change the internal energy losses and rotation of the source foil would mean a larger average path length through the gas volume creating larger energy losses associated from traversing it. Both of these effects could account for excesses seen in the low energy region. If these errors can account for the discrepancies between our model and data then future analyses will have greater statistics and more accurate background model to improve on the presented results.

Chapter 6

SuperNEMO

6.1 Case for SuperNEMO

SuperNEMO is the next detector by the NEMO collaboration. It has been under research and development since 2006 and is the successor to NEMO3. NEMO3 was very successful in measuring both the $\beta\beta2\nu$ decay half-lives of many double beta decay isotopes and in setting new and world beating limits on $\beta\beta0\nu$ decay. However it did not observe within its effective mass sensitivity range of $\langle m_\nu \rangle$ <0.3 - 0.9 eV any evidence for $\beta\beta0\nu$ decay in any of these isotopes including ^{100}Mo. Although a significant part of the previous KKDH (Klapdor) claim has been excluded the limit obtained by NEMO3 cannot exclude all the allowed parameter space (see Fig.2.7).

SuperNEMO will increase the half-life sensitivity from the NEMO3 level by two orders of magnitude to $> 1 \times 10^{26}$ years. This corresponds to an effective neutrino mass sensitivity of $\langle m_\nu \rangle$ <0.04 -0.1 eV, which as seen in Fig.2.7 would allow SuperNEMO to cover this region as well as probe the mass region of the inverted hierarchy. The ability to probe this region for the first time is a good justification for SuperNEMO. However it also has the added advantage of topological event reconstruction by use of tracking, which is offered uniquely by SuperNEMO [162]. This additional information could be invaluable in distinguishing and probing the mechanisms for observed events if seen. Additionally SuperNEMO, as with its predecessor NEMO3, has the facility to remove and replace its source, which allows it to make measurements of multiple double beta sources and adapt to future claims and new source availability. These advantages make the production of SuperNEMO vital to furthering the field.

6.2 SuperNEMO Detector Description

The SuperNEMO detector uses broadly similar technology, detection and tracking methods to that of the very successful NEMO3. This includes a source foil with double beta decay isotope contained within a Geiger wire tracking volume and surrounded on all sides by a matrix of scintillating

calorimeter modules (see Fig.6.1). However with years of research and development most areas have been improved and with a new modular structure and planar geometry a greater sensitivity will be achievable. A description of the detector can be seen below.

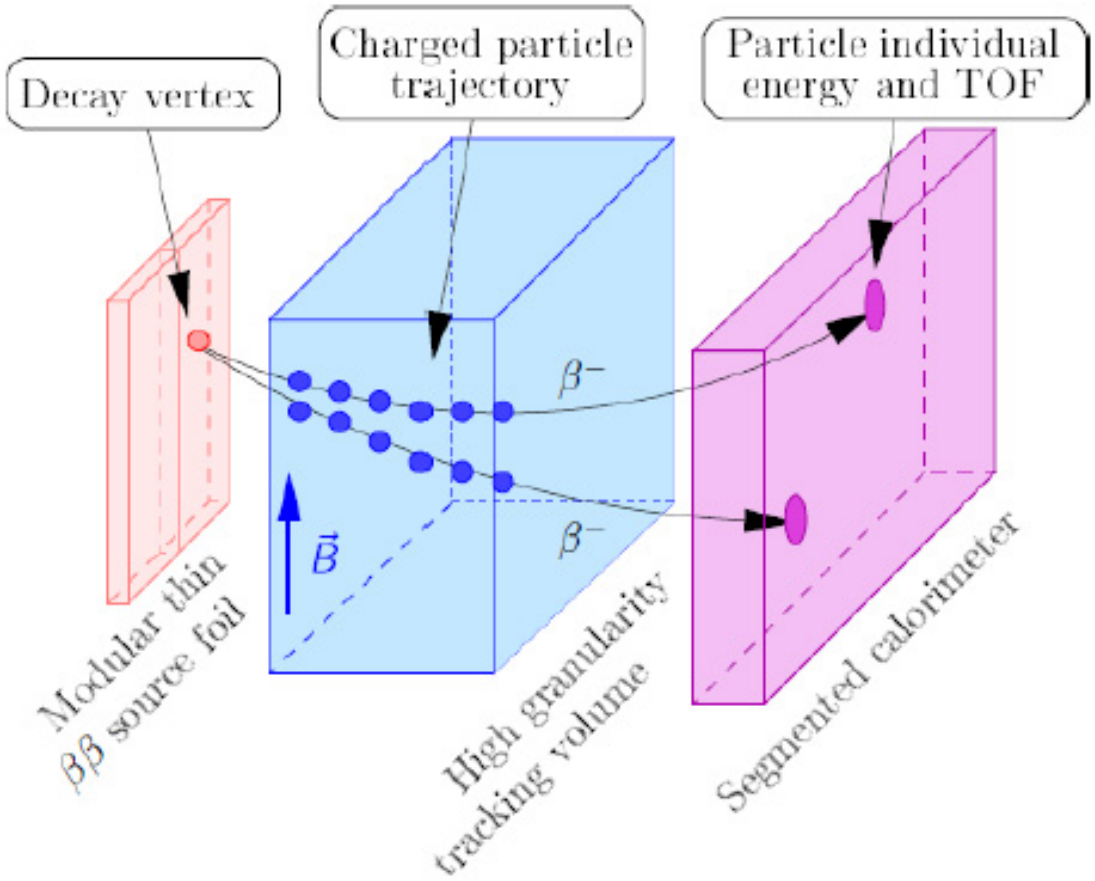

Figure 6.1: Simple schematic of SuperNEMO detector. [163]

6.2.1 SuperNEMO Detector Design

SuperNEMO will contain 100 kg of double beta decay source, an increase of 1 order of magnitude over NEMO3. This source will be ^{82}Se or possibly ^{150}Nd or ^{48}Ca depending on availability and price. The sources will once again be made into foils however research is on-going to try and move away from Mylar as the choice of backing film due to it producing additional unwanted contamination. However for the time being Mylar backing films ($\approx$40mg/cm^2) as with NEMO3, will be used in the demonstrator and suspended vertically inside it.

To accommodate the amount of source without making the foils thicker the detector will be made larger and separated into 20 identical modules (5kg of source in each). Each independent module will act as a fully operational detector able to start data taking as soon as they are built.

The modules will now take on a planar geometry measuring 4m high, 6m long and 2m wide with straight foils surrounded by Geiger tracking volumes and 6 calorimeter block walls forming an

enclosed cuboidal structure. The modules will have independent magnetic fields and be surrounded by shielding for background suppression (see Fig.6.2).

They will consist of 2000 44mm wide Geiger drift cells arranged into 9 rows with no gaps either side of the foil and 520 square scintillator blocks coupled to 8" PMTs arranged into surrounding walls. As can be seen in Fig.6.2 the six encompassing polyvinyl-toluene (PVT) scintillation block walls are grouped into three types, the large 4 x 6 m walls are known as the main walls, which have scintillating blocks of 250 x 250 mm that are directly coupled to the 8" PMT's. The side walls, which measure 4 x 2m, contain 4 columns of smaller 210w x 200.5h mm blocks which attach to the PMT's via light guides. Finally 2 more walls exist above and below the Geiger cell mounts which are much larger and of lower resolution and are not involved in electron energy measurements, but are there to act as a veto for gammas which pass through them.

An advantage of a modular design is that the modules can be housed in the same or different locations depending on space and resources and a faster commissioning time, allowing for data to be taken sooner. The first of the modules will be used as a demonstrator to prove the concept and to take ground breaking new measurements at the same time. This demonstrator is currently under construction and is expected to be placed in the same Modane underground laboratory where NEMO3 was. It is slightly smaller in height than the proposed other 19 modules due to space restrictions in the laboratory (see Sec.6.3). The others will be placed in the extension to the LSM tunnel which will provide space for the detector in the future. Also other locations in underground laboratories exist. Using proven and similar technology to that of NEMO3 has allowed for large confidence in the design and models. Plus this added experience and knowledge gained from NEMO3 has meant that research could be focused and more targeted on tackling the important advancements needed to reach the energy resolution of 7% FWHM at 1MeV, automated tracking detector production and suppression of backgrounds (see Sec.6.2.3).

6.2.2 Alternative Detector Designs

The detector went through many design changes and decisions during its R&D phase, including examining the possibilities for liquid or hexagonal plastic calorimeter blocks with varying shapes and sizes to increase energy efficiency.

However the most substantial alternative design was a multi module design idea to sandwich the modules together and make the intermediate calorimeter walls out of thin bars so that particles could propagate more than one module. This has the advantage of providing greater gamma detection efficiency as gamma particles can propagate through many calorimeters and a larger thickness of detection material. This would also be much more compact, cheaper and cleaner, due to fewer PMTs present.

The bar design would comprise seven modules (2.8m (height) x 6.65m (length) x 6.65m (width)) placed back to back, each housing source foils of 15kg vertically suspended as with other designs. This would give 105kg of source foil in total needed for an increase in 1 order of magnitude over

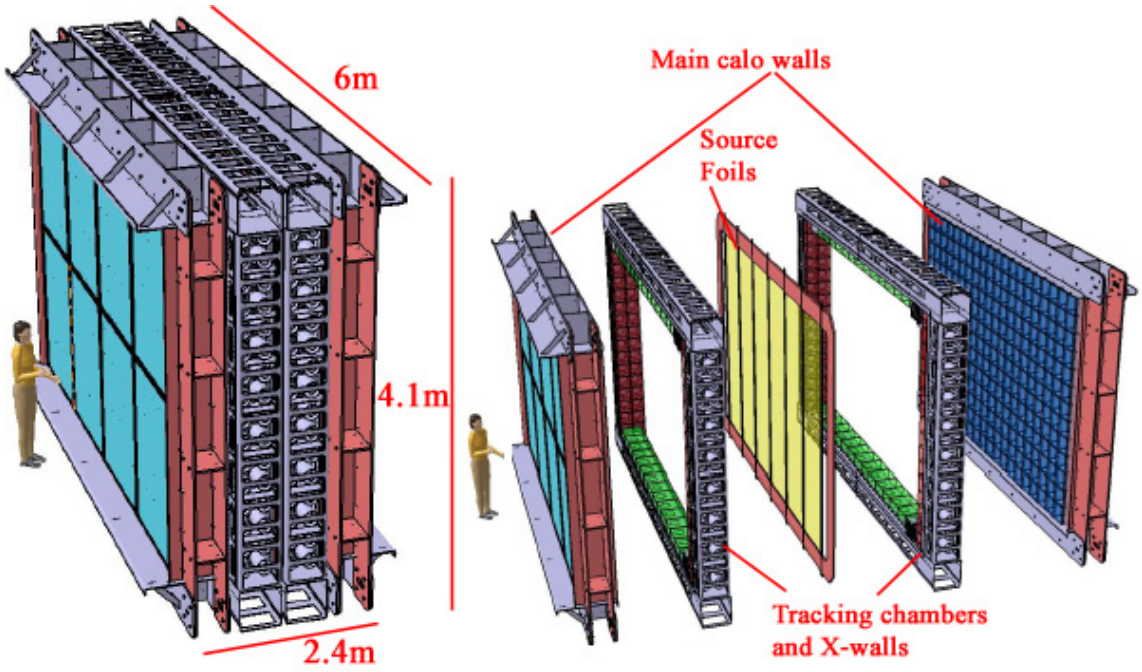

Figure 6.2: Diagram of a single SuperNEMO module. [164]

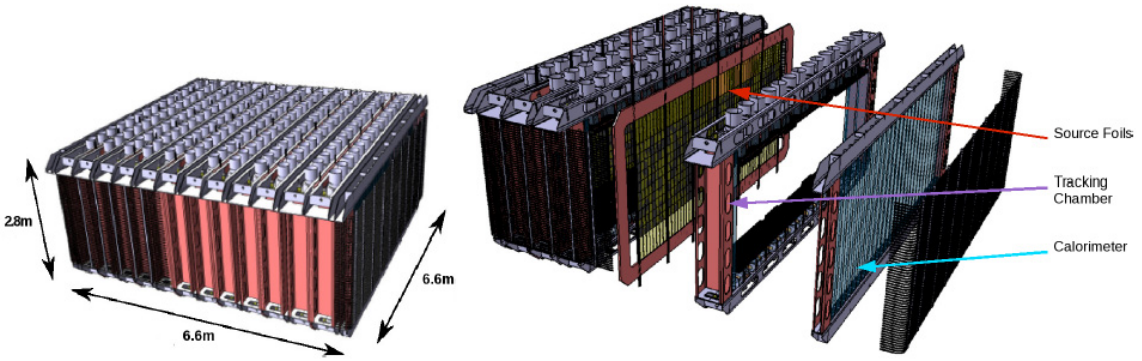

Figure 6.3: SuperNEMO bar design showing complete sandwiched module construction and exploded view.

NEMO3. Either side of the source foils would be layers of Geiger cells and then surrounding these would be a wall of scintillating bars 2m long, 10cm wide and 3cm thick separating the Geiger cells of one module from the next. This would create a sandwich effect reducing the number of calorimeter layers and allowing particles to pass from one module to another. The bars themselves would be PVT and instrumented at either end by 3" PMTs and tapered at the ends to couple to the flat front face of the PMT. Using this system the energy measurements would be provided by combined measurements by both PMTs and the vertical location of ionisation determined by the timing response. The advantages of this design over the previous are that as mentioned gammas will have an increased tagging efficiency as they would propagate through many layers. This tagging efficiency increase will help in background elimination as these events can be classified at a higher efficiency. Importantly also the number of PMTs is greatly reduced and due to 3" and not 8" PMTs being used the amount of glass in the detector (which is known to be a major source of background) is reduced significantly. Also from a cost perspective, the reduction of the size and quantity of PMTs to about 5,000 - 7,000 in total would be far cheaper. Other advantages of this design are less well quantified but increasing efficiency in background tagging could reduce the requirements in time of flight measurement and reducing the gaps between source foil and calorimeters has been shown to increase efficiency, as well as acheiving better spacial resolution on calorimeter hits (2 - 3cm).

There are of course disadvantages to using this form of detector, most noticeably the no longer independent nature of the modules means that you lose the flexibility of where each module is located (requires one central space) and the ability to construct and start data taking from each module separately. This affects the ability to build a demonstrator for this technology, as it would be considerably larger and not able to be housed in NEMO3's current location. These factors make it a much greater risk for an unproven technology. Also calorimeter bars are a not as well understood technology in the context of our experimental use, such as timing due to the internal scattering and attenuation of light during multi coincidence events. Because of this lots of research and development would be needed to understand them at the level which has been obtained for the block technology by the past experiment NEMO3. Issues such as uniformity and ageing also play bigger roles and resolution is 9% FWHM at 1MeV which is less than the blocks and efficiency must be considered and explored.

Some of these issues were explored during the research and development phase of SuperNEMO. These included simulations of gamma tagging efficiency increase which I undertook, as well as laboratory tests of achievable uniformity and energy resolutions and simulations of sensitivities with this method for required performances (see Sec.6.4).

However, the bar design technology is largely unproven and new and its extrapolation from simulation and NEMO3 performance is much harder. So a collection of these issues saw the SuperNEMO collaboration in February 2009 make the decision to put aside the bar design and focus efforts on the block design after examining the advantages and disadvantages of both.

6.2.3 SuperNEMO Research and Development

SuperNEMO's R&D lasted three years and focused on improving techniques and technology in five core areas, source foil production, tracker development, calorimeter development, ultra-low background materials production and measurement and software development

Source foil production R&D was focused on reducing, determining and characterising the source foil's contaminations before they entered the detector. Backgrounds were reduced using normal source production and enrichment techniques, such as chemical and distillation purification. However enrichment opportunities for sources such as ^{48}Ca using new techniques may still come to fruition. As mentioned previously research is still on-going to find alternatives to move away from Mylar foils to reduce contamination within the source foils and a large amount of effort was devoted to developing a dedicated detector known as BiPo, to measure and characterise ^{214}Bi, ^{208}Tl levels of specific foils before introduction in the commissioning stage of the detector.

The tracker development focused on two areas. One major area was to reduce contamination and improve operation and failure rate of the cells over NEMO3 levels. To do this it was decided that a robot would be used to construct and wire all the cells so its control systems and design and operation were a major focus. The second area of research was in optimisation of the cells looking at plasma propagation, efficiency, ageing, cross talk, materials and the dimensions of the new 44mm and longer cell. Prototypes were built including a 90 cell version which was tested with cosmic rays, that showed good plasma propagation and operation over the new dimensions with resolutions of ΔXY = 0.7mm and ΔZ = 1.3cm.

Calorimeter development for SuperNEMO, as seen in Sec.6.2.2, focused not only on improving the energy resolution of the experiment by researching materials and PMT configurations, which saw the move to PVT from polystyrene and directly coupling the scintillation blocks to the PMT fascia to achieve 7% FWHM energy resolution at 1MeV, but also looking at radically changing the design of the calorimeter and its technology to achieve the highest sensitivity. Another area of calorimeter research looked at the calibration methods used in NEMO3 hoping to solve issues that arose from previous methods and redesign delivery systems (See Sec.8).

Reducing the backgrounds of the experiment is paramount when looking for long lifetime processes. To that end where possible low background components are used throughout the detector. These include the use of uncoloured delrin connectors instead of metal, low contamination Mylar and PMTs with low Bi and Tl levels. To this end the collaboration has worked with Hamamatsu to develop radio-pure barium salt free glass. Whilst this is not available currently it is hoped to be tested soon. All other materials went through strict selection processes in which all component materials have been tested in germanium detectors to ensure they meet the necessary background levels during selection. Research was also undertaken to reduce the amount of radioactive contamination permeating into the detector. This has led to the use of new sealing techniques to limit radon diffusion into the detector and the development of new radon detectors to monitor this process.

The SuperNEMO software also underwent a lot of development in which we have seen 3 separate iterations as it has been refined and improved to deliver capable, reliable and expandable software for the collaboration. Apart from the event generator and use of GEANT, it has been built from the ground up in C++ for the specific needs of SuperNEMO (see Sec.7).

6.2.4 SuperNEMO and NEMO3 Detector Technical Differences

Below is a list of the major differences of SuperNEMO from its predecessor NEMO3

Feature	NEMO3	SuperNEMO
Detector Geometry	Single toroidal detector	20 independent planar modules
Isotope	Several (7kg of ^{100}Mo)	^{82}Se (or possibly ^{150}Nd or ^{48}Ca)
Source	10kg	100kg
Calorimeter	Polystyrene with light guide	Polyvinyl-toluene with no light guide
Energy resolution at 1MeV	14 - 17%	7 - 8%
Geiger cells	30mm diameter with spacing	44mm diameter no spacing
Wiring process	By hand	Using robot
^{208}Tl in source foil	100 μBq/kg	< 2 μBq/kg
^{214}Bi in source foil	< 300 μBq/kg	< 10 μBq/kg
Rn	5 mBq/m^3	0.15mBq/m^3
$\beta\beta0\nu$ Detection Efficiency	18%	30%
Exposure	30 kg years	500 kg years
$T_{1/2}^{\beta\beta0\nu}$ Sensitivity	1×10^{24} years	1×10^{26} years
Effective Majorana Mass $\langle m_{\nu_e} \rangle$	0.3 - 1.0eV	40 - 100meV

Table 6.1: Comparison between major design and performance parameters of NEMO3 and SuperNEMO.

6.3 SuperNEMO Demonstrator

As mentioned previously the first module of SuperNEMO is currently under construction and will act as the demonstrator. This module will be housed in the same underground laboratory in which NEMO3 was placed and will be slightly shorter in height compared to the subsequent modules owning to the size of the laboratory in which it will be placed. The demonstrator has 3 key roles to play in the SuperNEMO project, the first of which is that it can demonstrate that the performance parameters listed in table.6.1 can be reached using the technology developed and that the target backgrounds needed for the project to reach the required half-life sensitivities can be achieved. It also will crucially be the first test bed for some of our new systems and technologies to work together, this will provide invaluable experience, methods and alterations that can used forward in the construction of the other modules. Thirdly the demonstrator individually will be able to achieve new ground breaking physics of its own, extending the sensitivity achieved by NEMO3 to now fully encompass the parameter space of the claimed observation by Klapdor as well as contributing to the total sensitivity of SuperNEMO once fully constructed.

6.4 SuperNEMO Sensitivity

The sensitivity of SuperNEMO has been studied and simulated extensively using the SuperNEMO software packages and the knowledge and experience gained from NEMO3. The full simulation takes into account all known detector effects including thicknesses of the source foils, efficiencies in the tracker and calorimeters, the effects of backgrounds on the sensitivities, the magnetic field, the energy, space and time resolutions and exposure time. The desired half-life sensitivity for the detector is 10^{26} years which would give a mass sensitivity of between (40-100 meV). The energy resolution of the calorimeter has a profound effect on the reachable sensitivity as can be seen from Fig.6.4.

Fig.6.4 shows the reachable half-life sensitivity for 500kg years for both the bar and basic block designs versus calorimeter energy resolution. Calorimeter development for SuperNEMO has shown than a resolution of 7% FWHM at 1MeV is possible with our current technology and we are limited to no less than 5% resolution due to the smearing of emanating electrons that interact with the foil. With 7% resolution and the SuperNEMO expected backgrounds we would expect to reach a half-life sensitivity of $\approx 10^{26}$ at 500kg years (5 years with 100kg source). If we plot the sensitivity versus exposure at 7% calorimeter resolution (Fig.6.5) we can see that the 10^{26} sensitivity can be reached and surpassed for the basic block design by increasing the exposure time by a year or 2 to 600 or 700 kg years.

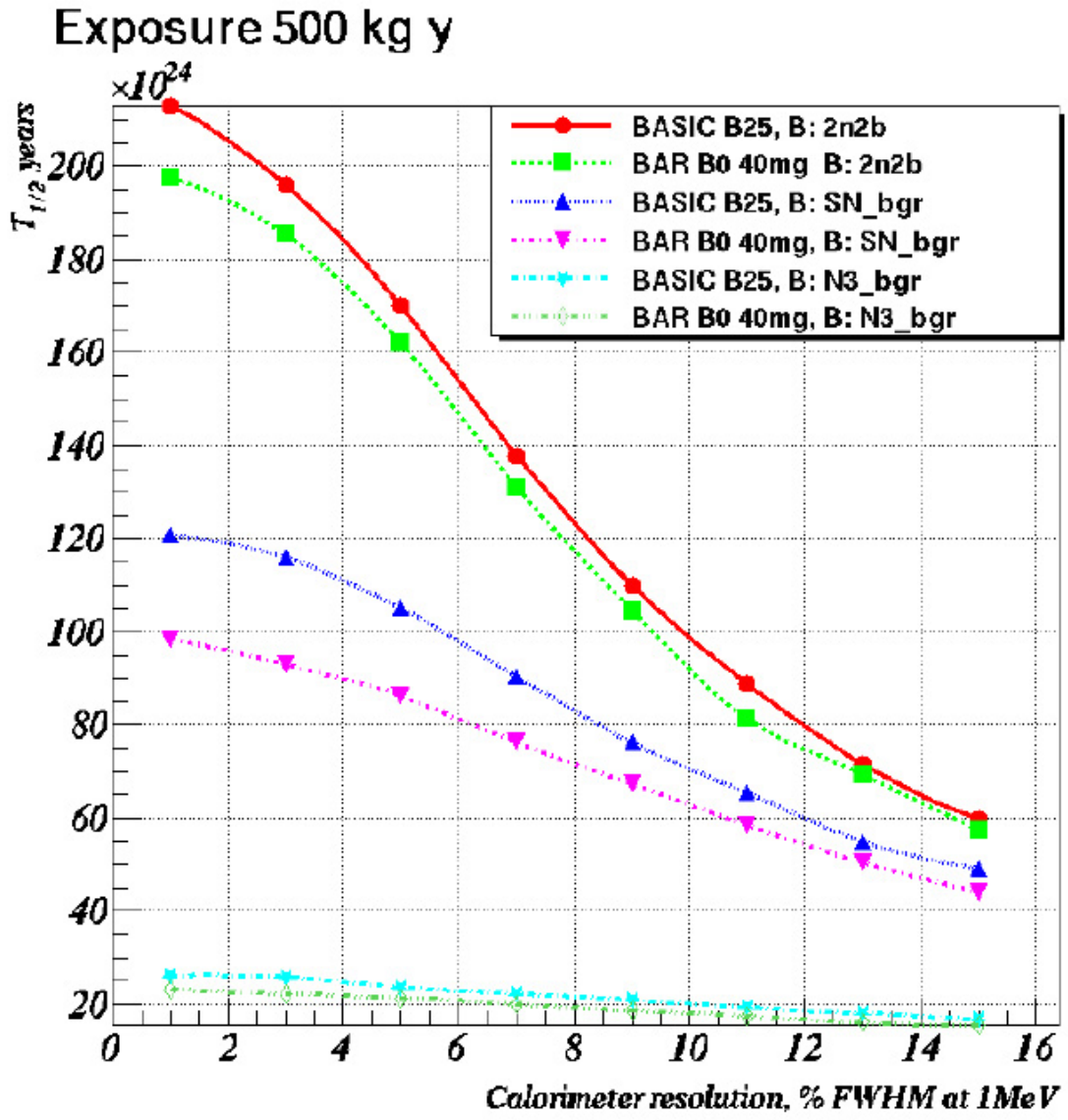

Figure 6.4: SuperNEMO two neutrino double beta decay half-life sensitivity for the basic block and bar design versus calorimeter energy resolution FWHM at 1MeV. Sensitivity data shown comes from effect of 3 different backgrounds (no background (2n2b) , NEMO3 background levels (N3_bgr) and SuperNEMO background level (SN_bgr)) for each of the detector designs. [165]

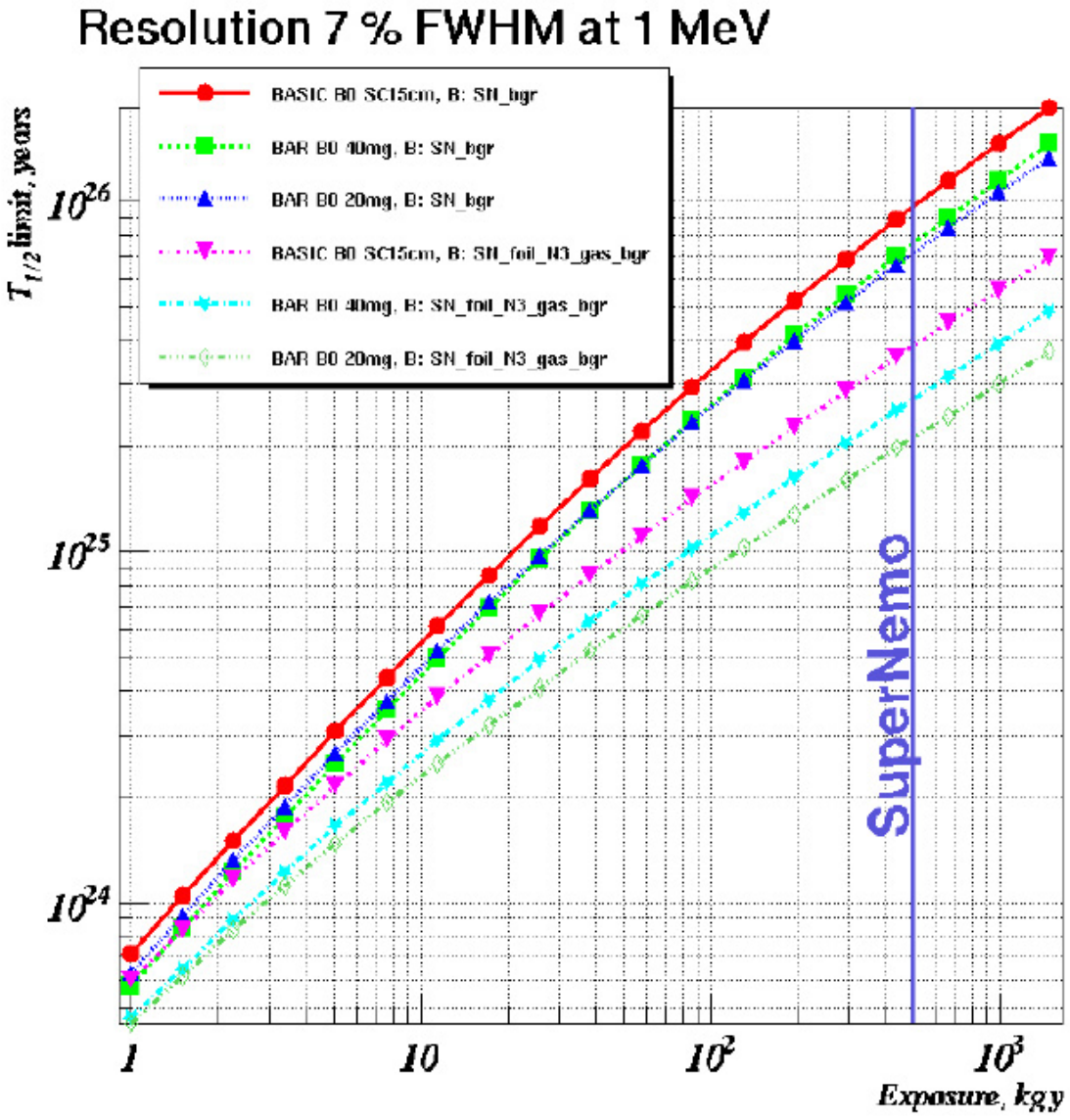

Figure 6.5: SuperNEMO two neutrino double beta decay half-life sensitivity verses the exposure in kg years for the bar and basic block design with varying foil thicknesses for the bar design and 2 different background models (SuperNEMO background levels (SN_bgr) and SuperNEMO foil backgrounds with NEMO3 gass backgrounds (SN_foil_N3_gas_bgr)). [165]

Chapter 7

SuperNEMO Software

7.1 SuperNEMO Software Description

The SuperNEMO software was designed and constructed to simulate the complicated particle interactions inside the SuperNEMO detector, to recreate the detector's physical response and data read out and to reconstruct and analyse both the simulated MC (Monte Carlo) and real detector data. It has undergone many revisions and changes from its initial inception and recently it has been decided that the first version of the software known as SNSW (SuperNemo SoftWare) would be superseded by a more flexible and versatile software which is split into two efforts focusing on generation and simulation structure, and analysis. I took part in the some of these designs and concepts as shown later on in this chapter by my framework design development and I also participated in design meetings and discussions. However the new software is still in its validation stage. Therefore SNSW was used for the design, sensitivity and physics studies presented here and it is this software which is presented below.

The SNSW software consists of a collection of executable packages that are run sequentially by a bash script called SNSW.sh (SNSW). The bash script can be used to control which packages are executed, at what step in the chain the sequence is started and ended, and is responsible for delivering the correct parameter files and data files to each application when executed and cleaning up and structuring outputs as the sequence progresses. Figure 7.1 shows the entire software structure and the individual executables in the chain are shown as pink squares. A description of the software's operation and each of the individual executables can be found in Sec.7.1.1. The software also includes 2 other purpose built bash scripts called PACKMAN and SNGRID which are responsible for the checkout and compilation of the software and its dependencies and the preparation and execution of the SNSW on the Grid. As well as the purpose built software listed, many of the applications and processes require proprietary libraries, such as CLHEP, GEANT and ROOT for standard physics quantities and containers, particle interaction simulation and data processing.

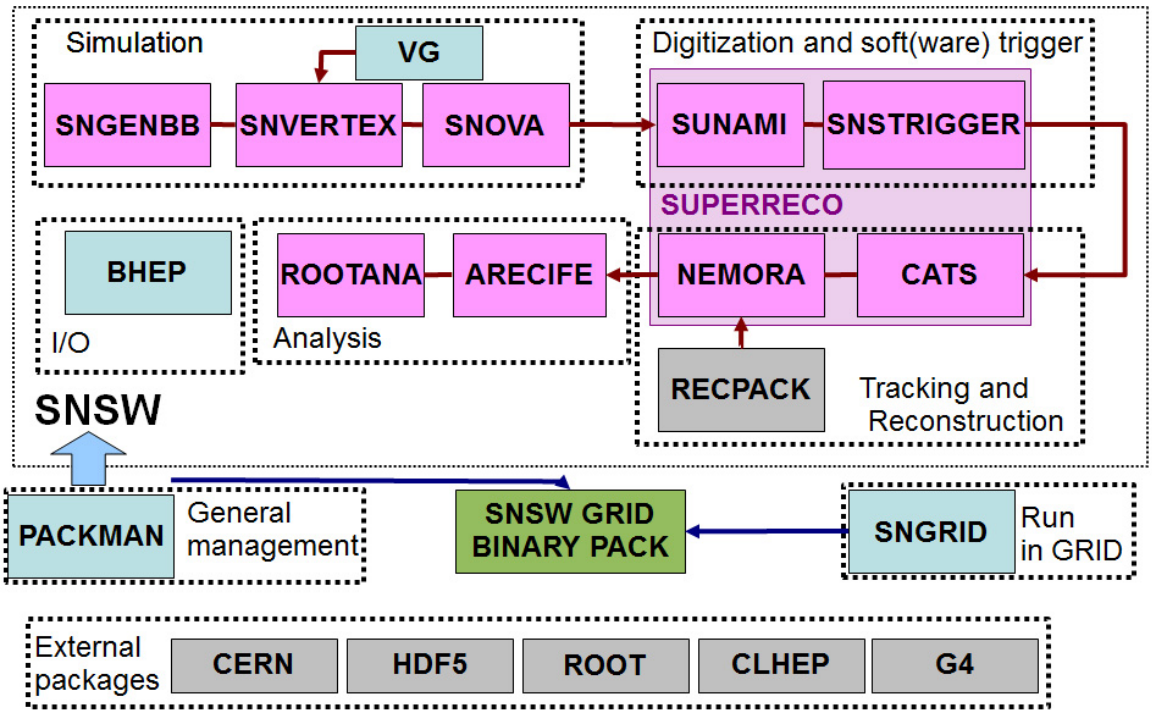

Figure 7.1: SNSW code diagram.

7.1.1 SuperNEMO Software Operation and Executables

The main software chain when run in its entirety can be subdivided into 4 steps, simulation, digitisation, tracking and reconstruction and analysis. These steps can be seen highlighted in Fig.7.1 and are described with their constituent executable packages below.

7.1.1.1 Simulation

The simulation step of SNSW is responsible for producing simulated events within the SuperNEMO detector. This is achieved by three executables SNGBB, SNVERTEX and SNOVA which are executed in that order.

SNGBB is a Python wrapper for Fortran code known as GENBB [151]. GENBB is an event generator for double beta sources and backgrounds. It contains the decay schemes for all the relevant isotopes needed, their daughters, energies, angular distributions and associated branching ratios. This application is therefore able to reproduce the decays of any isotopes needed for MC studies of double beta decay isotopes and background sources and is used under the name DECAY4 widely by low energy and dark matter experiments. The SNGBB package translates the output of GENBB into the data format BHEP used by all the packages in SNSW. BHEP is a C++ library for ascii based particle data storage.

SNVERTEX is a C++ written executable that is then responsible for reading the output of SNGBB and placing the generated events within the SuperNEMO geometry. It does this by assigning the event's physical locations in the detector depending on the configuration passed to it from its

configuration file. It can place the events within the source foil, on its surface, in the calorimeter blocks, on the calorimeter block's surface, outside the detector, in its support structures and other planes and specific locations specified by the user. It is responsible for determining the distribution of the events within the locations as well. The results of its operations are written out in BHEP format.

SNOVA is the GEANT simulation package written in C++. It uses GEANT-4 [166] and it is responsible for propagating each daughter particle from the initial decay through the detector and working out the subsequent decays, interactions and ionisations that occur from these interactions with the various materials in the detector's geometry. Once this is done all particle information is stored in a BHEP formatted file.

At the end of the simulation phase a file containing a list of all the events produced is created. Each event contains the initial decay information, all subsequent particle's interactions, locations, momenta and energy depositions.

7.1.1.2 Digitisation and Software Trigger

The digitisation step of SNSW is responsible for simulating the detector response to the particles and energy deposited, turning the exact true information into a smeared or digitized representation that the electronics would capture. This is achieved with a single package written in C++ known as SUNAMI, it uses a control file to determine how the smearing is done on different parameters.

There is another package known as SNTRIGGER which is executed in this step. This is a software based trigger package that simply slims the data by applying very loose cuts to reduce processing in following steps. It can be set to only include events when certain numbers of calorimetry or Geiger cells are triggered.

At the end of this step the data produced and saved should resemble the output of the actual detector, such that the two are ubiquitous.

7.1.1.3 Tracking and Reconstruction

The next step in the software chain is tracking and reconstruction, this is also the stage in which simulated MC data merges with real detector output as the succeeding steps would be run on both identically once the detector has started. This step uses two purpose built C++ packages CATS and NEMORA.

CATS is responsible for the association of Geiger hits within the detector. It takes the Geiger hits for an event and attempts to join them using pattern recognition into segments of 3 consecutive hits with possible paths of a particle connecting them.

NEMORA is used next which takes the track segments found by CATS and tries to join and fit them into complete helical tracks by minimising the chi-squared. The tracks are then associated with calorimeter hits if possible and extrapolated to the foil when close to it and necessary to reconstruct a decay location.

The end product of this step is a data file with complete collections of calo and Geiger hits as well as collections of associated hits, tracks and reconstructed vertices.

It should be noted that as can be seen from Fig.7.1 four of the packages SUNAMI, SNSTRIGGER, CATS and NEMORA which comprise the digitisation, software trigger, tracking and reconstruction were grouped and run with the help of another script called SUPPERRECO which aids their smooth execution and handling of relevant outputs and parameters.

7.1.1.4 Analysis

The last stage of the software is analysis, this originally comprised of two packages ARECIFE and Rootana. However these two were later redesigned by myself and will be presented in Sec.7.2.1.

ARECIFE was originally designed as a very simple inflexible package that combined both fixed analysis and plots of 2 electron events and later a simplified system for conversion between BHEP (the SuperNEMO SNSW data format) and ana10 ntuples the format used by Rootana. This conversion was problematic as the product did not contain all the information about events, there were large omissions in true information and tracking and reconstruction.

Rootana is the NEMO3 analysis package based on root ntuples. It comprised a wide range of tools hard coded into it for determining physical quantities and statistical analysis of NEMO3 data, but was not specifically designed for SuperNEMO or SuperNEMO data. So some algorithms needed tweaking and variables' roles and nomenclature needed optimising. It also had the disadvantage of being very dense and hardcoded to do certain things which didn't give people the confidence and flexibility needed to do analysis.

7.2 SuperNEMO Software Development

A large proportion of my work was in developing, designing, maintaining, repairing and validating software. As part of the remit I developed several software products for the SuperNEMO and NEMO3 projects which are described below

7.2.1 SuperNEMO Analysis Software

As mentioned in Sec.7.1.1 the analysis software for the SuperNEMO SNSW chain was not fully developed or reliable. It left users with 4 possibilities to produce their analysis, each of which had issues.

1. Creating user's own analysis code from SUPPERRECO BHEP ASCII file. This is hard to understand due to its structure and organisation, as well as requiring BHEP code to interpret, which itself has memory issues.

2. Rewriting ARECIFE to produce output analysis. This was used by developers but is overly

convoluted, not user friendly and rigidly restrictive of the types of events that could be processed (Double beta only and hard coded with hundreds of if statements).

3. Use the Rootana intended H10 ntuple to create own analysis code. This was never designed for SuperNEMO data, and as such does not capture all the data outputted by the simulation (eg. until recently truth data). The structure and variable names are meant for Rootana internal use and are not intuitive.

4. Use Rootana itself. This has the added advantages of statistical tools, but is working therefore with restricted data. It is also very convoluted and complicated, it's not user-friendly and important processes are hidden from the user.

So it was clear another more practical solution was needed so I developed a new analysis package to answer all of these problems. This was written in C++ and was used instead of ARECIFE and Rootana in the final analysis step. The analysis code was built to allow as much user choice and flexibility as possible whilst having the power and simplicity to be adapted for any task. Some of the key features are described below.

- Gave users access to the full BHEP data in a simple and easily understandable way
- Gave the ability to produce a clear and exhaustive ntuple format for use in a separate analysis script due to inclusion of a format converter.
- Gave the users a simple but powerful framework to develop custom analysis within the analysis package allowing them to produce user event selection, cuts and plots within the code
- Gave the fully ported and deconvoluted statistical tools available in Rootana for use with the SuperNEMO detector within the package
- Gave powerful new tools for event tracking, producing analysis of stepwise cuts, debugging and diagnostics via automated debug services.

This software was important as it made available the ability to produce an analysis of any aspect of the data or event topology with speed and simplicity. This can be seen subsequently in Sec.8 where it was used to produce the calibration analysis as well as forming a basis and inspiration for me when re-writing the NEMO3 analysis software.

7.2.2 SuperNEMO Event Display

As part of the research and development of SuperNEMO the design of the detector was not initially established. One proposed design was to use plastic bar calorimeters rather than blocks (which was later superseded). However as part of my work for the collaboration I did both design studies for this design looking at the efficiency of gamma propagation through such a device as well as designing software. One piece of software I designed was an event display for the bar geometry.

Before its creation the only available display of events was at the simulation level of SNOVA (the simulation application based on GEANT). This was not adequate as it was difficult to use, could only be implemented at the generation level, had fixed perspectives, could not filter particles or events, could only display true information and therefore could not be used as a tool to look at the detailed event information on a post processing basis.

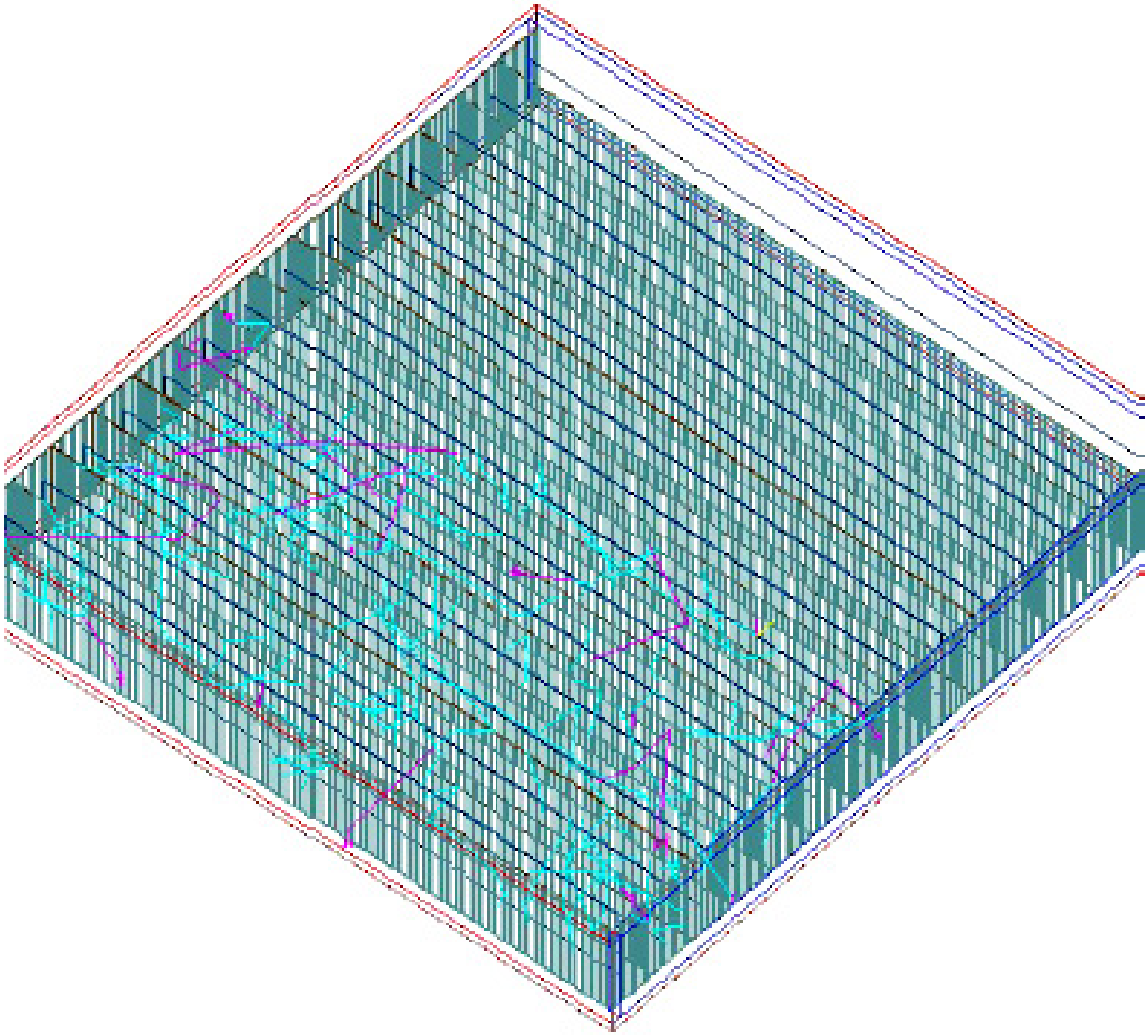

Figure 7.2: Example of old GEANT based event display.

To this end I wrote a new event display in C++ utilising OPENGL. The software could read the outputted data format from my new analysis package 7.2.1, meaning that on a post processing basis selected events could be viewed and analysed.

The key features of the application are listed below

- Full 3d module 1:1 mapping with GEANT, dynamic geometry from SNOVA geometry definitions

- Colour coded energy deposits
- 3D camera, so any imaginable viewing perspective. as well as flat projection
- 4 levels of detail with fixed frame rate draw mode available
- Can view on event by event basis

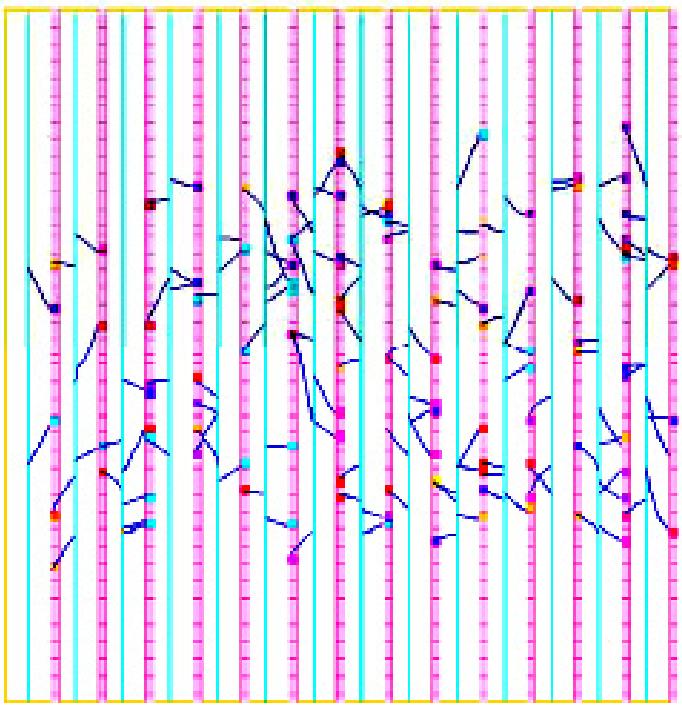

Figure 7.3: Example of new event display top down projection where red lines are source foils, green blocks are vertical bars and the electron tracks are shown in blue.

7.2.3 SuperNEMO Automated Nightly Build and Validation

Another piece of software I developed for the collaboration was a nightly build and testing application. Due to the frequency and development of the code such an application was essential and missing from the collaboration's efforts. To that end I wrote a collection of BASH and C++ scripts and applications that would check out the latest head of the code from our repository, build it logging any errors or failures at any stage and which applications were responsible and the associated error messages. Then it would run any pre-programmed tests desired on the installation of the code, such as unit tests, distributions from an example analysis and Valgrind memory leak tests. The results of comparisons of these tests with the output of the build code were also logged. The logs and plots

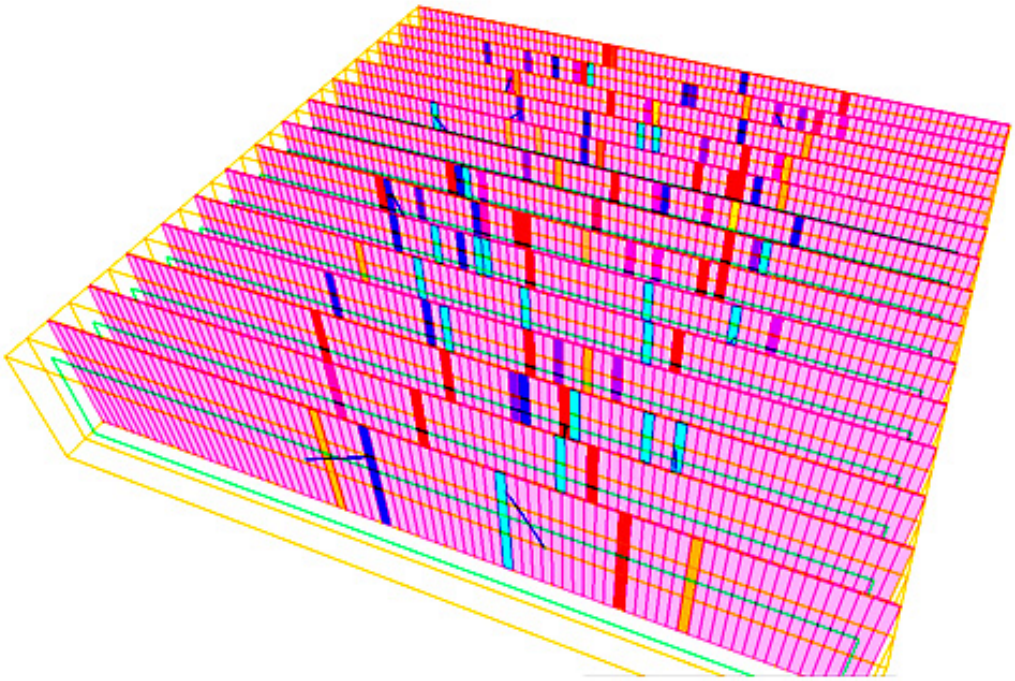

Figure 7.4: Example of side 3D view of event display showing colour coded energy deposits with particle impacts on bars.

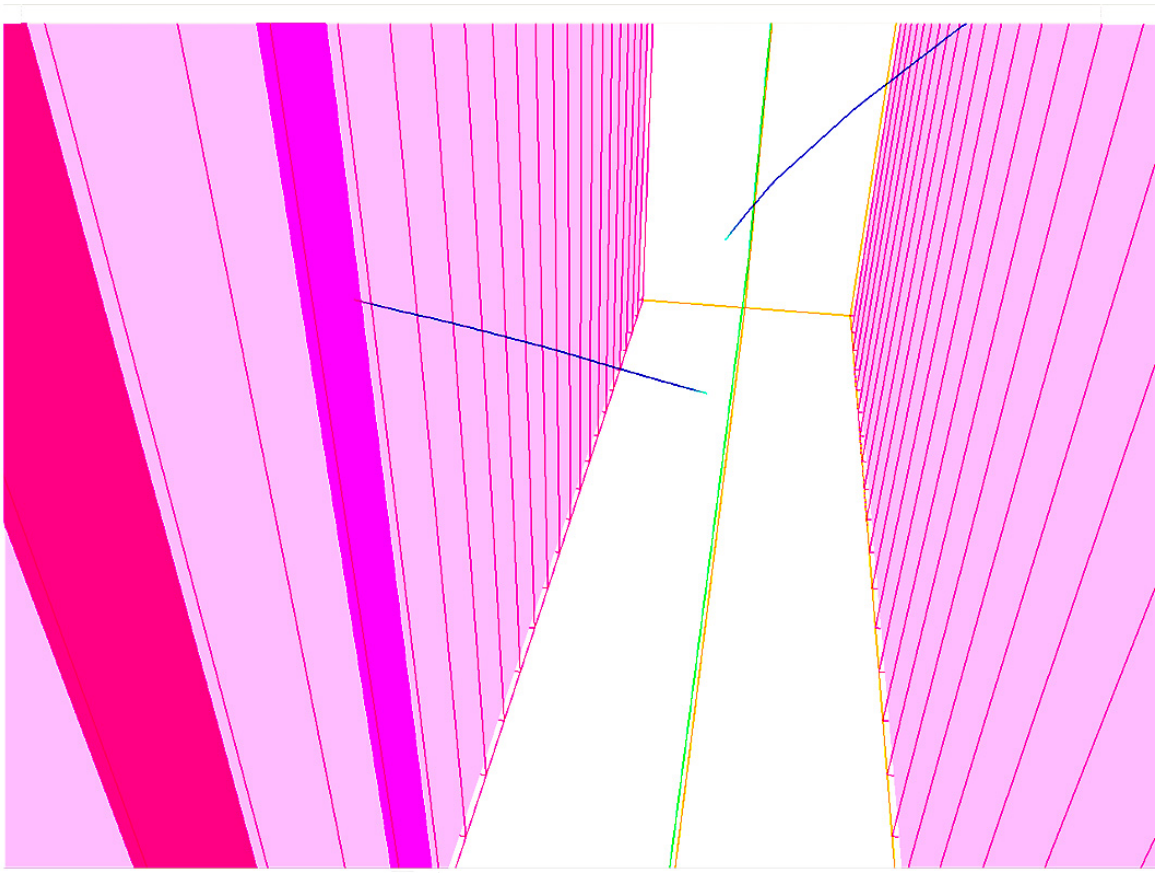

Figure 7.5: Example of close up 3D view of 2 single electrons emanating from green bounded source foil propagating through yellow tracking volume and impacting on scintillator bars.

were then updated and posted on a webpage automatically which could track the progress and errors and email the status to me so action could be taken and people could be informed.

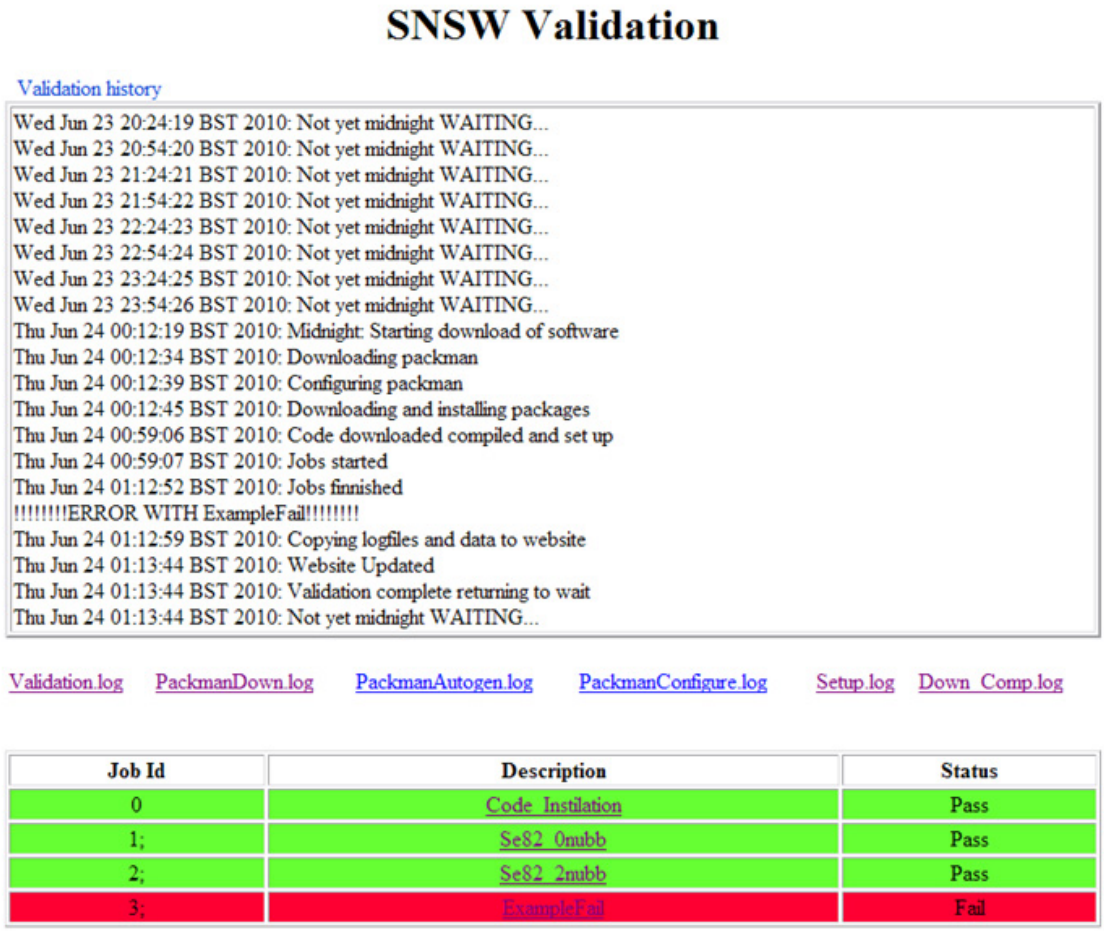

SNSW Validation

Validation history

Wed Jun 23 20:24:19 BST 2010: Not yet midnight WAITING...
Wed Jun 23 20:54:20 BST 2010: Not yet midnight WAITING...
Wed Jun 23 21:24:21 BST 2010: Not yet midnight WAITING...
Wed Jun 23 21:54:22 BST 2010: Not yet midnight WAITING...
Wed Jun 23 22:24:23 BST 2010: Not yet midnight WAITING...
Wed Jun 23 22:54:24 BST 2010: Not yet midnight WAITING...
Wed Jun 23 23:24:25 BST 2010: Not yet midnight WAITING...
Wed Jun 23 23:54:26 BST 2010: Not yet midnight WAITING...
Thu Jun 24 00:12:19 BST 2010: Midnight: Starting download of software
Thu Jun 24 00:12:34 BST 2010: Downloading packman
Thu Jun 24 00:12:39 BST 2010: Configuring packman
Thu Jun 24 00:12:45 BST 2010: Downloading and installing packages
Thu Jun 24 00:59:06 BST 2010: Code downloaded compiled and set up
Thu Jun 24 00:59:07 BST 2010: Jobs started
Thu Jun 24 01:12:52 BST 2010: Jobs finnished
!!!!!!!!ERROR WITH ExampleFail!!!!!!!!
Thu Jun 24 01:12:59 BST 2010: Copying logfiles and data to website
Thu Jun 24 01:13:44 BST 2010: Website Updated
Thu Jun 24 01:13:44 BST 2010: Validation complete returning to wait
Thu Jun 24 01:13:44 BST 2010: Not yet midnight WAITING...

Validation.log PackmanDown.log PackmanAutogen.log PackmanConfigure.log Setup.log Down_Comp.log

Job Id	Description	Status
0	Code_Instilation	Pass
1;	Se82_0nubb	Pass
2;	Se82_2nubb	Pass
3;	ExampleFail	Fail

Figure 7.6: Example of automated web status page.

7.2.4 SuperNEMO Framework Design

Another contribution I have made to the SuperNEMO software effort is to redesign the framework from a bash based script running individual executables to an integrated C++ pipeline framework with a transient data class. This step was needed due to the fact that the major bottleneck in the code's operation was the frequent need for input-output to a storage drive by each component along the chain as this is how data was transferred between then using BHEP data format. It was also needed as the BHEP format itself was counter intuitive, subject to erroneous variables and data duplication. The transient data class model meant that data was stored in memory between the steps of the operation drastically improving performance. To this end I designed and coded a new integrated C++ framework with simple factories and templates to make it modular and expandable. I also began conversion of the existing individual code executables to libraries that could be linked

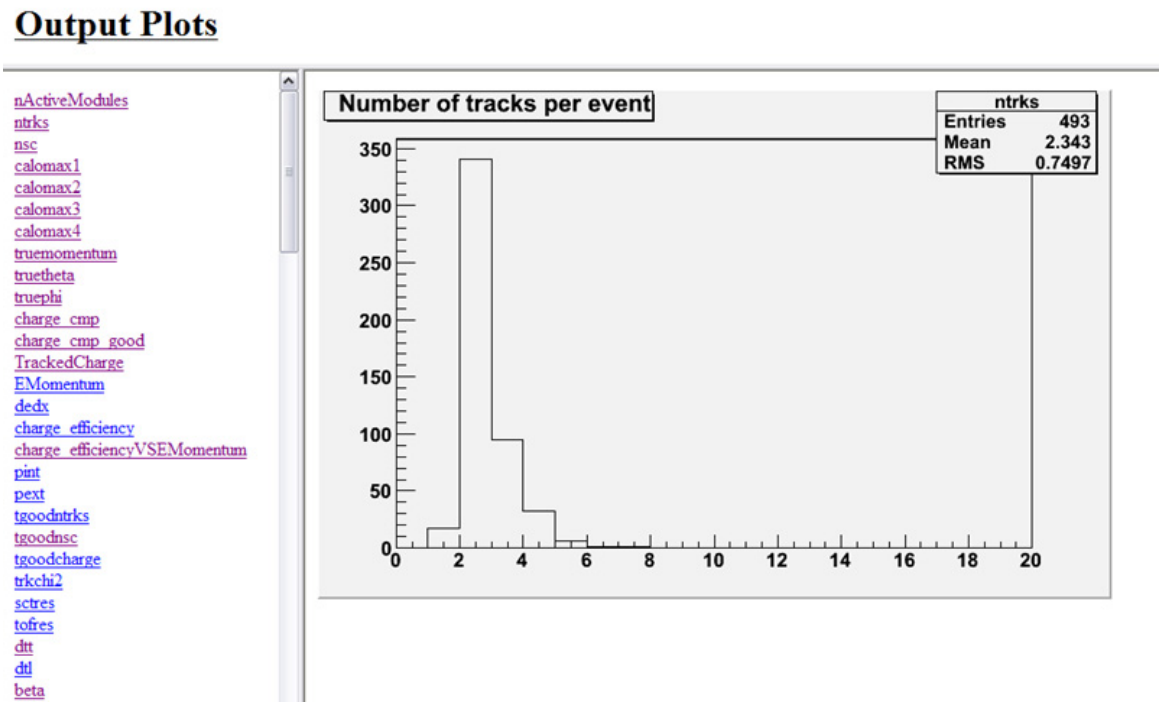

Figure 7.7: Example of automated plot generation from test run.

into the framework. This model was eventually adopted and adapted by the collaboration to produce the current new incarnation of the SuperNEMO software that is currently still under production.

Chapter 8

SuperNEMO Calibration

One of the many software studies that I took part in was the task of determining the positions and strengths of the calibration sources needed in SuperNEMO using the SNSW simulation software and my new analysis framework. This work would then be used to inform the design of the detector. Calibration is important for a long term experiment with multiple arrays of detectors in order to maintain its ability to accurately determine both the absolute energy and time of events when detected and to compensate and adjust for experimental drift and degradation with time on both relative and absolute scales. The process of calibration is carried out by two distinct calibration systems.

8.1 Calibration Systems

8.1.1 Light Injection Calibration System

The first is used daily and utilises light emitting diodes (LEDs) with emissions in UV wavelengths, a system of filters narrows the emission spectra and reduces the intensity of the light which then passes through a light cone and down optical fibres to inject light into the plastic scintillation blocks of each optical module. The UV wavelength, intensity, pulse shape and duration are designed to excite the block to produce its own scintillation light mimicking an electron ionisation event. This system can be used to check both the linearity of energy response of each optical module by altering the intensity as well as to adjust for drifting of gains between runs and modules on a relative basis. This calibration system underwent many design and testing studies by others in the collaboration and was not the focus of my own work and so will not be covered in any more detail in this section.

8.1.2 Radioactive Source Calibration System

The second system is used much more infrequently on the time scale of a few months and is used to provide an absolute time and energy reference point to ensure that the absolute scale of both

is maintained during the experiment. This is done by the temporary introduction of radioactive sources into the detection volume alongside the source foil and is the focus of this work

^{207}Bi is introduced into the detector due to its ability to produce mono energetic conversion electrons in roughly 10% of decays (see Sec.8.1.3). These conversion elctrons come from de-excitations of excited ^{207}Pb nuclei produced by the ^{207}Bi decays (Fig.8.1). These electrons have energies of 976keV and 482keV and can therefore provide 2 absolute reference points of known energy in the region of double beta decay electron energies. These known peaks can be used to calibrate the absolute energy scale of the optical modules ensuring they are correct. Importantly the calibration sources are introduced near the source foils and not the calorimeter blocks in order for the tracking detector to be used to differentiate gamma and electron emissions and to reduce the number of calibration sources inside the detector as one source can illuminate multiple blocks. An added advantage of placing the calibration sources next to the foil is that the known activity sources can be used to check the detector efficiency calculations for event taking. ^{90}Sr can also be used for a further calibration point in the higher energy range by decay of its daughter nucleus ^{90}Y providing a beta decay spectrum ($Q_\beta = 2.28$MeV)

^{60}Co is used much more infrequently, usually only during major commissioning or hardware changes, for relative time calibrations between DAQ calorimeter channels due to its emission of 2 photons of 1.17MeV and 1.33 MeV at almost instantaneous separation in time (Fig.8.2). This would correct for things like different cable lengths to optical modules of the calorimeter as the event's detection could be used to correct for any relative time shift as detection should be coincident.

My work however focused on ^{207}Bi as this is used most frequently on a monthly basis and so ultimately would determine the configuration of sources within the detector.

8.1.3 ^{207}Bi

^{207}Bi is a synthetic radioisotope with a half-life of 31.55 years. Its decay modes are via electron capture and β^+ decay to ^{207}Pb with a Q-value of 2398.2 keV 21 (Fig.8.1). The major emissions of the decay are electrons (Table.8.1), gammas (Table.8.2) and accompanying X-rays from K and L shells transitions (Table.8.3).

Eb endpoint (keV)	Ib (%)	Decay mode
58.25	7.70 4	EC
764.83	92.26 23	EC

Table 8.1: Betas from ^{207}Bi. [167]

As mentioned previously ^{207}Bi also can undergo emission of conversion electrons which is a quantum effect in which the wave function of the inner orbitals (usually K shell but can be L and M, S orbitals) overlaps with the nucleus, allowing the nuclear decay energy to be passed directly onto the electrons, liberating them from the atom. This effect happens in $\approx 10\%$ of decays of ^{207}Bi as an alternative de-excitation of the excited ^{207}Pb daughter nucleus. This competes with the more

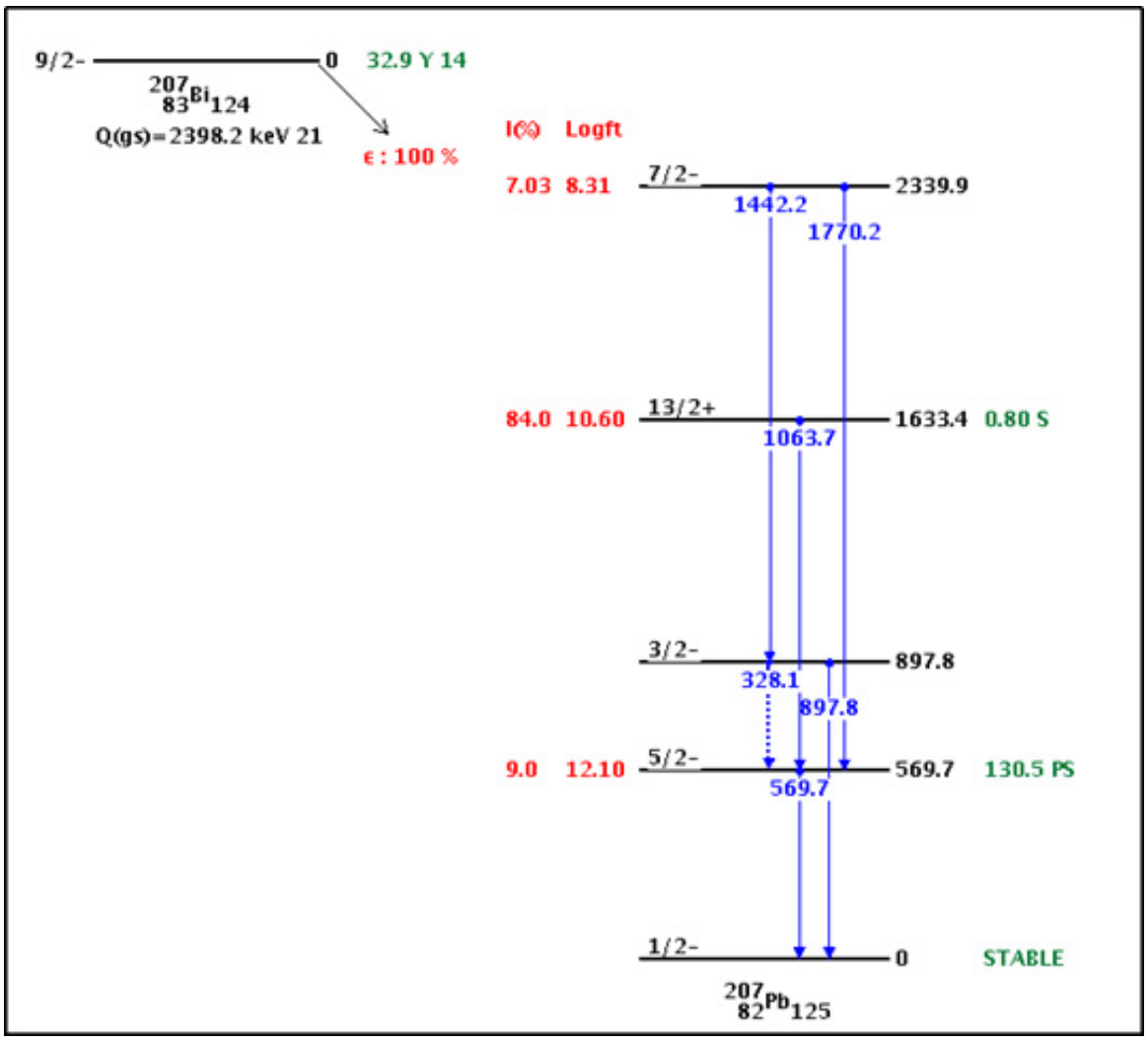

Figure 8.1: ^{207}Bi decay scheme.

Eγ (keV)	Iγ (%)	Decay mode
328.12 10	0.00067 8	ECβ^+
569.702 2 7	97.74 3	ECβ^+
897.80 5	0.121 8	ECβ^+
1063.662 4	74.5 2	ECβ^+
1442.20 9	0.130 3	ECβ^+
1770.237 10	6.87 4	ECβ^+

Table 8.2: Gammas from ^{207}Bi. [167]

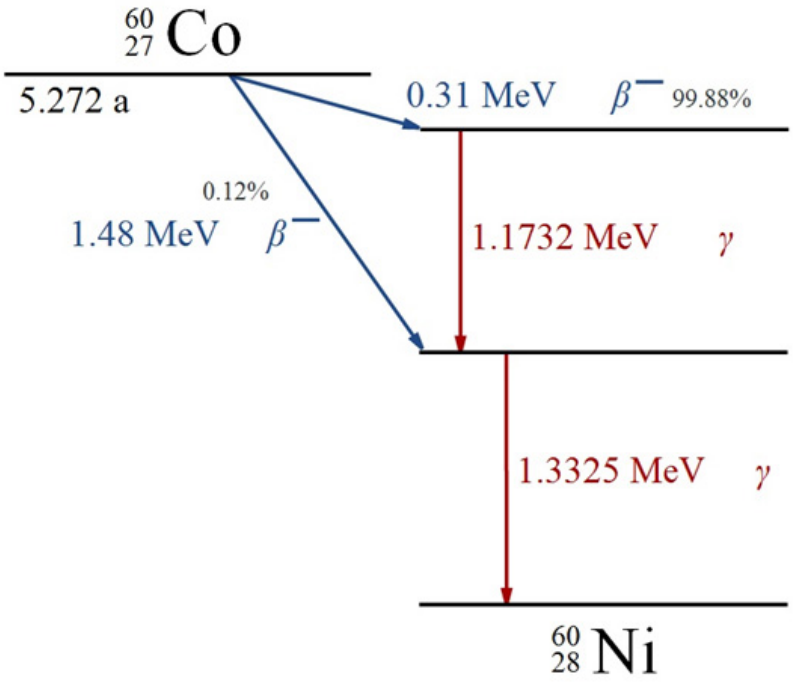

Figure 8.2: ^{60}Co decay scheme.

E (keV)	I (%)	Assignment
9.184	0.75 7	Pb L_l
10.450	1.50 7	Pb $L_{\alpha 2}$
10.551	13.3 6	Pb $L_{\alpha 1}$
11.349	0.182 10	Pb L_η
12.142	0.208 10	Pb $L_{\beta 6}$
12.307	0.91 14	Pb $L_{\beta 4}$
12.611	3.31 17	Pb $L_{\beta 2}$
12.614	7.9 5	Pb $L_{\beta 1}$
12.794	1.09 17	Pb $L_{\beta 3}$
13.015	0.428 20	Pb $L_{\beta 5}$
14.765	1.66 10	Pb $L_{\gamma 1}$
15.097	0.31 5	Pb L$-\gamma 2$
15.178	0.29 3	Pb $L_{\gamma 6}$
15.216	0.39 6	Pb $L_{\gamma 3}$
72.144	0.0326 11	Pb $K_{\alpha 3}$
72.805	21.3 6	Pb $K_{\alpha 2}$
74.969	35.8 10	Pb $K_{\alpha 1}$
84.450	4.26 11	Pb $K_{\beta 3}$
84.938	8.19 22	Pb $K_{\beta 1}$
85.470	0.238 10	Pb $K_{\beta 5}$
87.300	2.98 8	Pb $K_{\beta 2}$
87.580	0.67 3	Pb $K_{\beta 4}$

Table 8.3: X-rays from ^{207}Bi. [167]

frequent gamma de-excitation. The conversion electron is emitted with a fixed energy equivalent in energy to the excited state, unlike beta decay where a continuous spectrum of energy can be imparted due to the accompanying neutrino fraction.

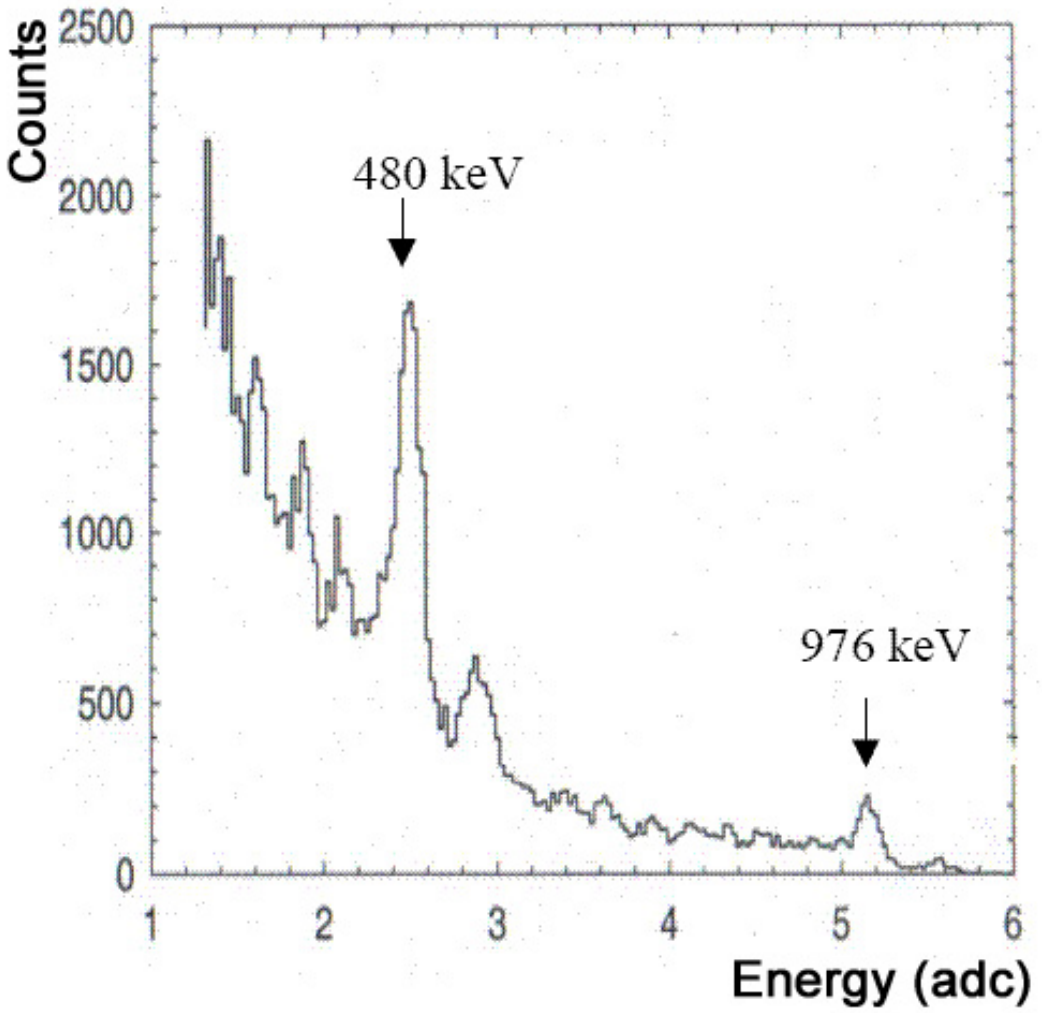

Figure 8.3: Example of energy spectrum from ^{207}Bi showing conversion electrons. [168]

Fig.8.3 shows conversion electrons from K and L shells of 2 different transitions. There will also be an M shell transition at lower frequency not visible in Fig.8.3, However with the energy resolution of our calorimeter (7% FWHM at 1MeV) the peaks from the K L M shells will not be resolved and so are combined into two peaks, one at 482keV and the other at 976keV which we fit with 3 Gaussians at the correct energy separations and relative amplitudes during fitting (see Fig.8.4).

After the emission of conversion electrons there will be a vacancy in the lower shells which will be filled by higher shell orbital electrons cascading down. These transitions will be accompanied by an emission of X-rays or Auger electrons which will be emitted isotropically and may end up in the

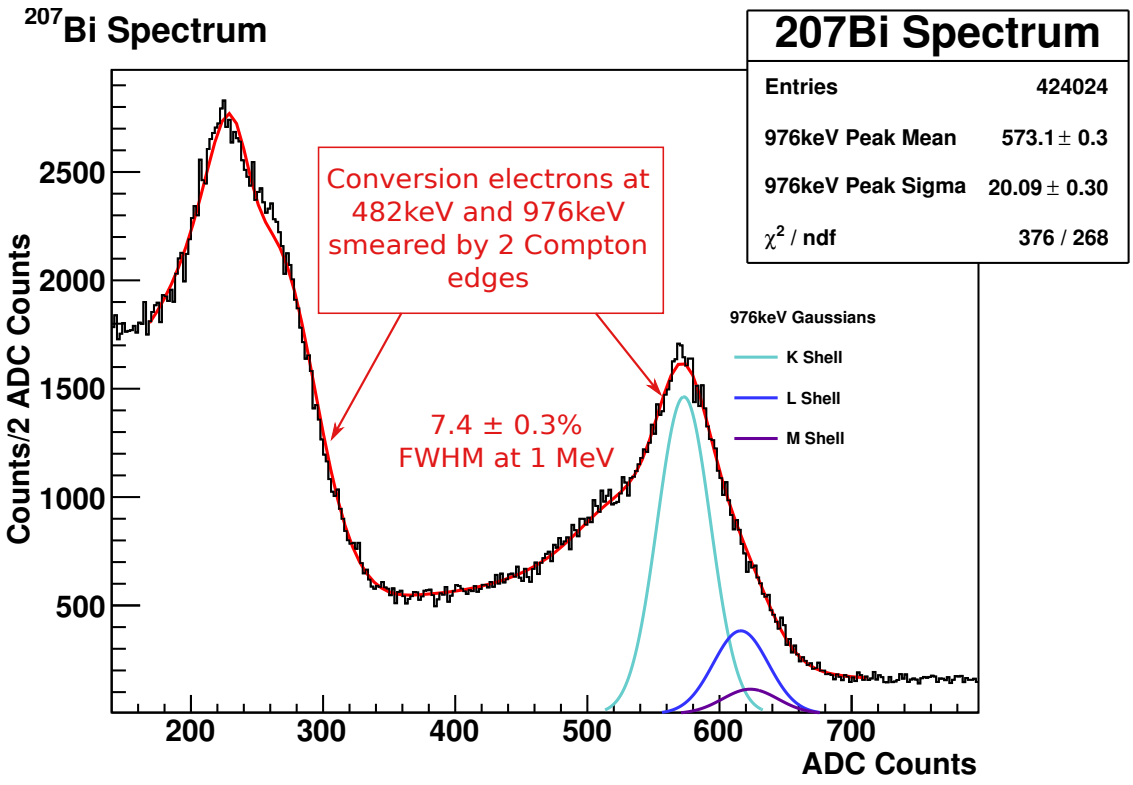

Figure 8.4: Example of energy spectrum from ^{207}Bi showing conversion electrons peaks with 7.4% energy resolution. [163]

detector.

8.2 Absolute Calibration Design

NEMO3 calibration was achieved via a similar process using 200Bq ^{207}Bi sources and reconstructing the energy peaks in the same way. However, the sources were lowered manually into the detector. This involved both removal of the shielding in the region and breaching the gas seal, which is an unfavoured method for introduction of the sources into the detector volume as it not only requires the process to be done manually but breaking the gas seals causes possible contamination of the clean inner detector.

In response to this, SuperNEMO is being designed such that the calibration sources can be introduced into the detector volume via an automated system and guided into position at the correct locations such that the sources can illuminate that calorimeter in their final position. The automated system would be entirely contained within the gas tight volume whilst being exterior to the detection volume such that no extraneous contamination would be brought in during the process.

Figure 8.5: NEMO3 manual source delivery system and holder.

8.2.1 Calibration Source Delivery Systems

Two competing systems currently exist to solve the automated delivery of the calibration sources to the correct positions in the detector whilst maintaining the gas tight seal. They are outlined below.

8.2.1.1 Vacuum Tube System

Vertical copper pipes are to be situated between sections of the source foil with kapton windows located at the calibration source positions on the foil plane and a vacuum system to deliver sources in source holders to the correct locations by suction down the tubes. This method is similar to that of NEMO3 using copper pipes to guide the sources to their correct positions but the vacuum system for delivery rather than a manual rod insertion is a new concept. A schematic of its intended construction can be found below (Fig.8.6)

The opening angles of the radiation from the calibration sources using this delivery system are restricted by the size of the tubes and windows cut in them (Fig.8.7). They are $\theta = 90^o$ and $\phi = 100^o$

The advantages of this design are that it is relatively simple and reliable. However the introduction of copper material into the detection volume provides extra contamination material and backgrounds. There might also be issues with the source holder alignment.

8.2.1.2 Tubeless Weighted Wire System

The tubeless design aims to reduce possible radioactive material inside the detection region by using guide wires and an automated winch to lower source holders on wires to the correct locations. The end of the wire has a small plumb weight that slots into a hole on the bottom of the detector.

The opening angle is no longer limited by the support tube structure in this method instead it is only limited by the angular acceptance of the source holder which is shown below (Fig.8.9).

This system has the advantage of less source material inside the detection volume, however without adequate support for plumb lines swinging could occur that would damage the foils and no guide means source alignment might be compromised. The system is more complicated to implement

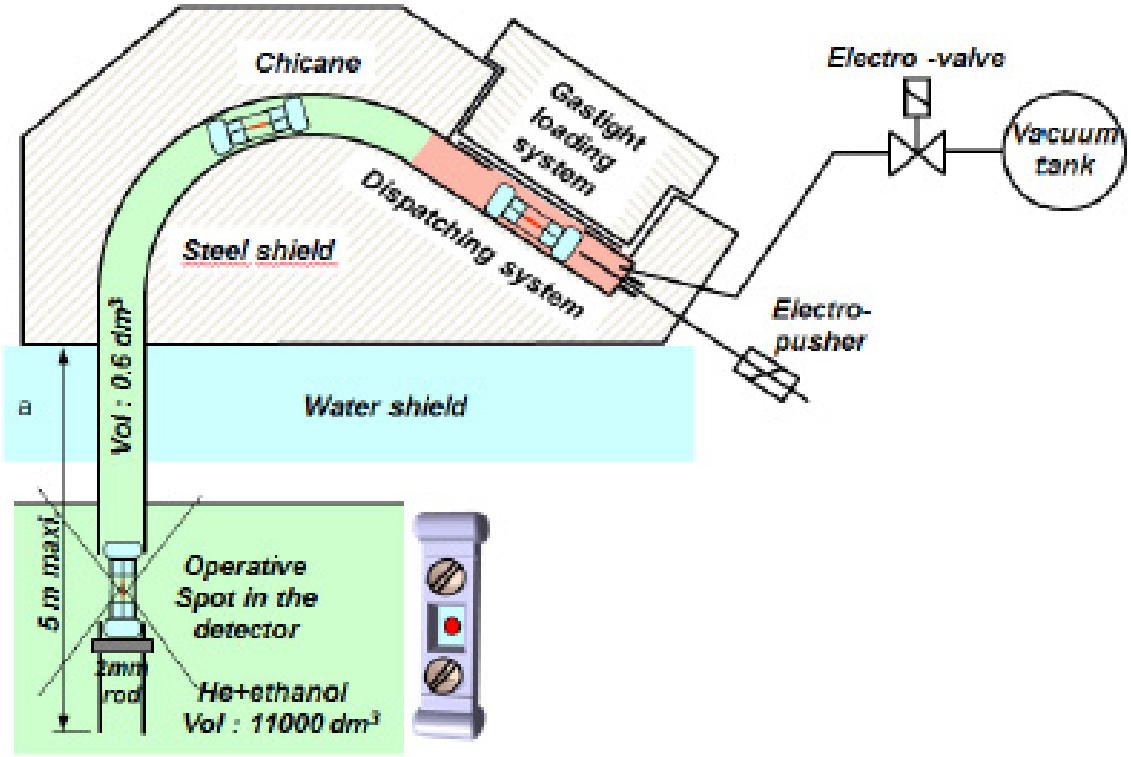

Figure 8.6: Schematic of copper tube vacuum delivery system.

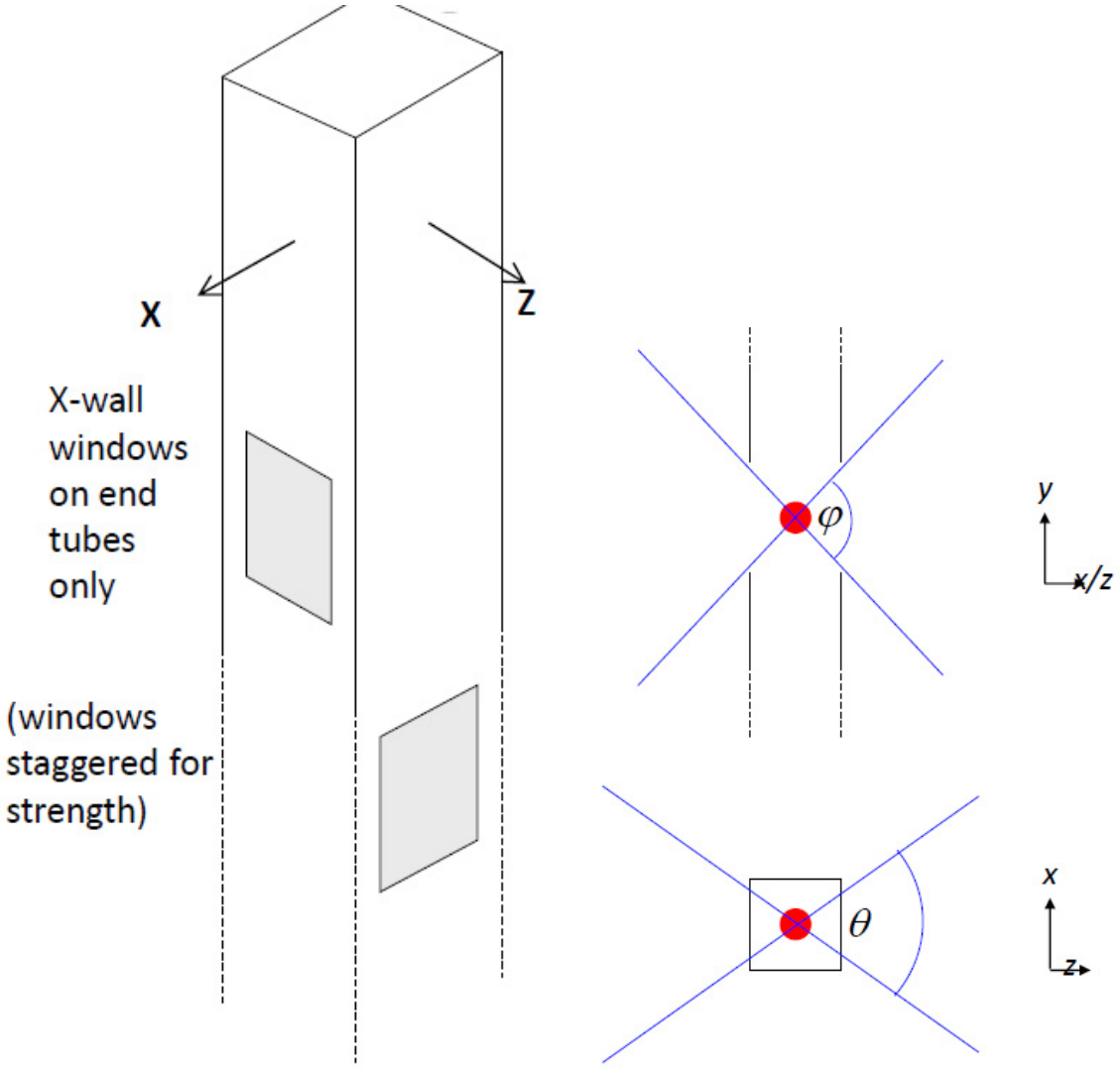

Figure 8.7: Schematic of opening angle acceptances for copper tube design.

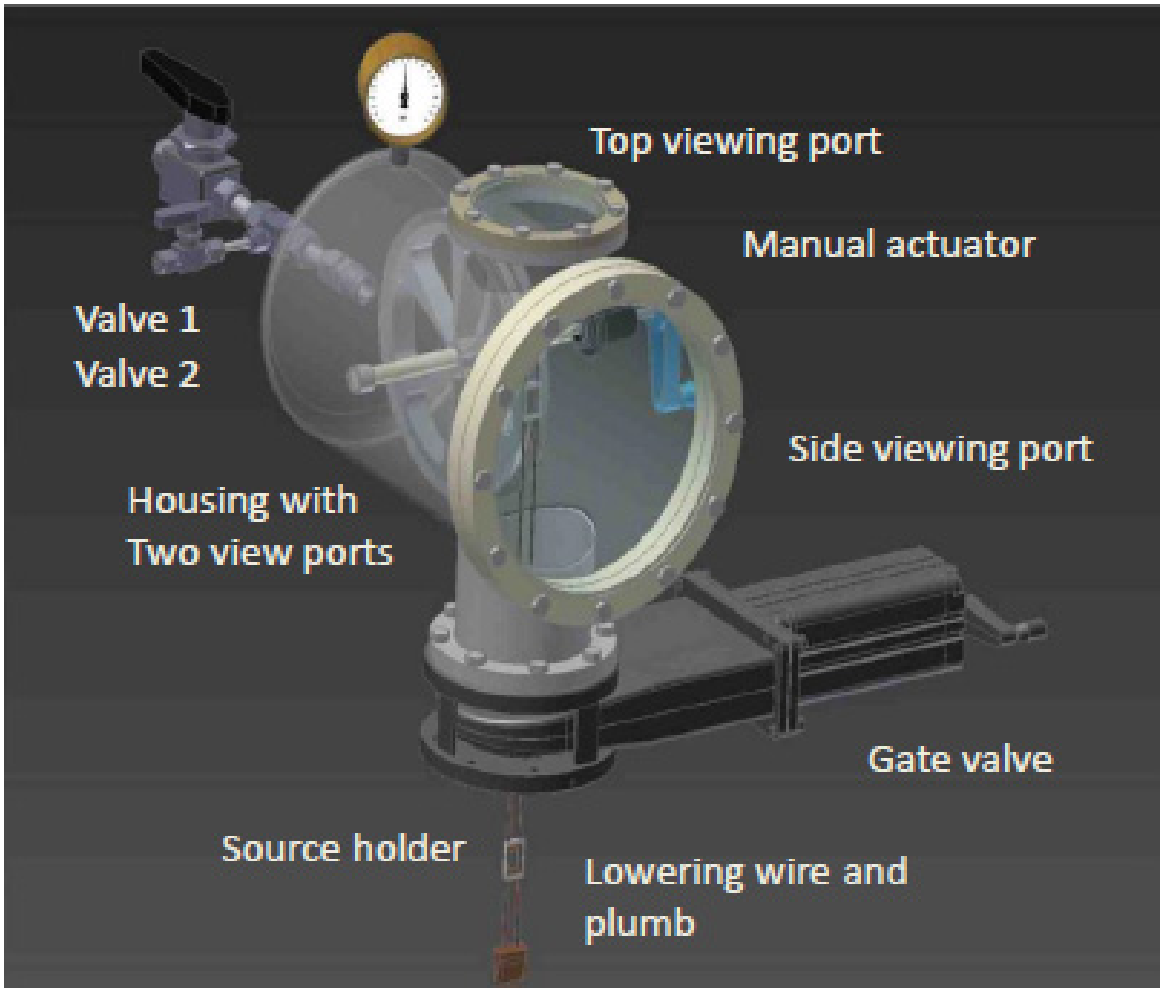

Figure 8.8: Schematic of tubeless wire delivery system.

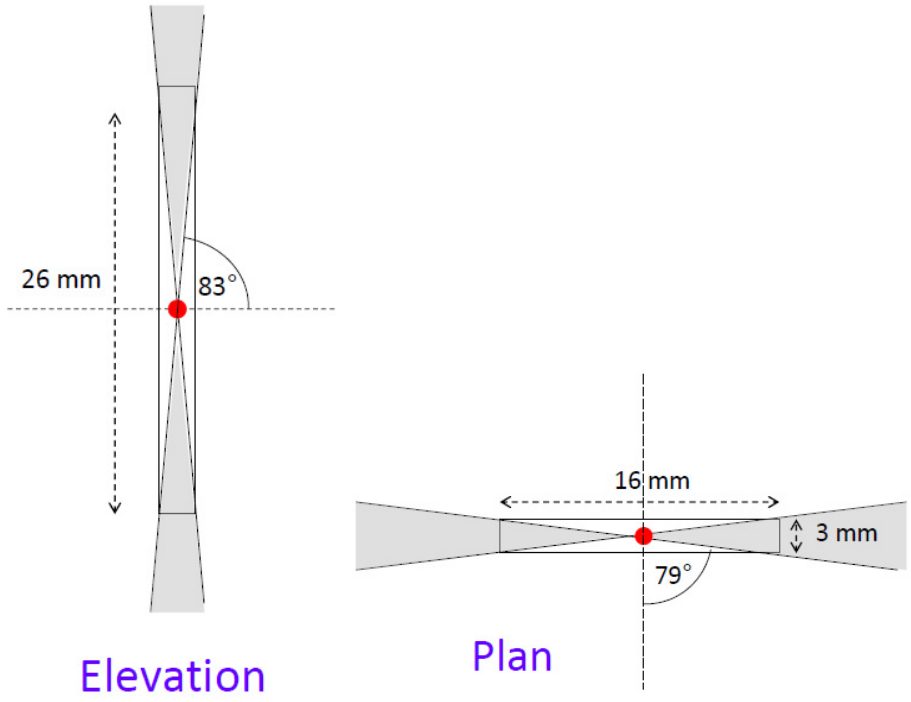

Figure 8.9: Schematic of tubeless source holder's opening angles.

as it has a mechanical winch inside the gas tight environment that cannot easily be serviced.

8.2.2 Calibration Source Distribution

However despite having two delivery systems the number and position of the source introduction lines (n_T), the number of sources per line (n_S) the separation of the sources in X and Y directions and the strength of the sources all need to be optimised (Fig.8.10) for whichever chosen system in order to meet certain constraints. This was the focus of my studies and simulation efforts and will be presented below in Sec.8.3

8.3 Simulation Studies

The design and distribution of sources and source lines inside the detector needed to be optimised and the calibration process simulated to ensure they met the design constraints presented by the experiment and physically possible within the detector geometry. Therefore it was important to understand what these constraints were and how they can influence the design. To this end the following simulations and studies were undertaken.

1. Determination of the maximum Geiger tracker cell hit rate so as to not overload it during calibration as it's needed to determine electrons from gamma emissions from the calibration sources' decays.

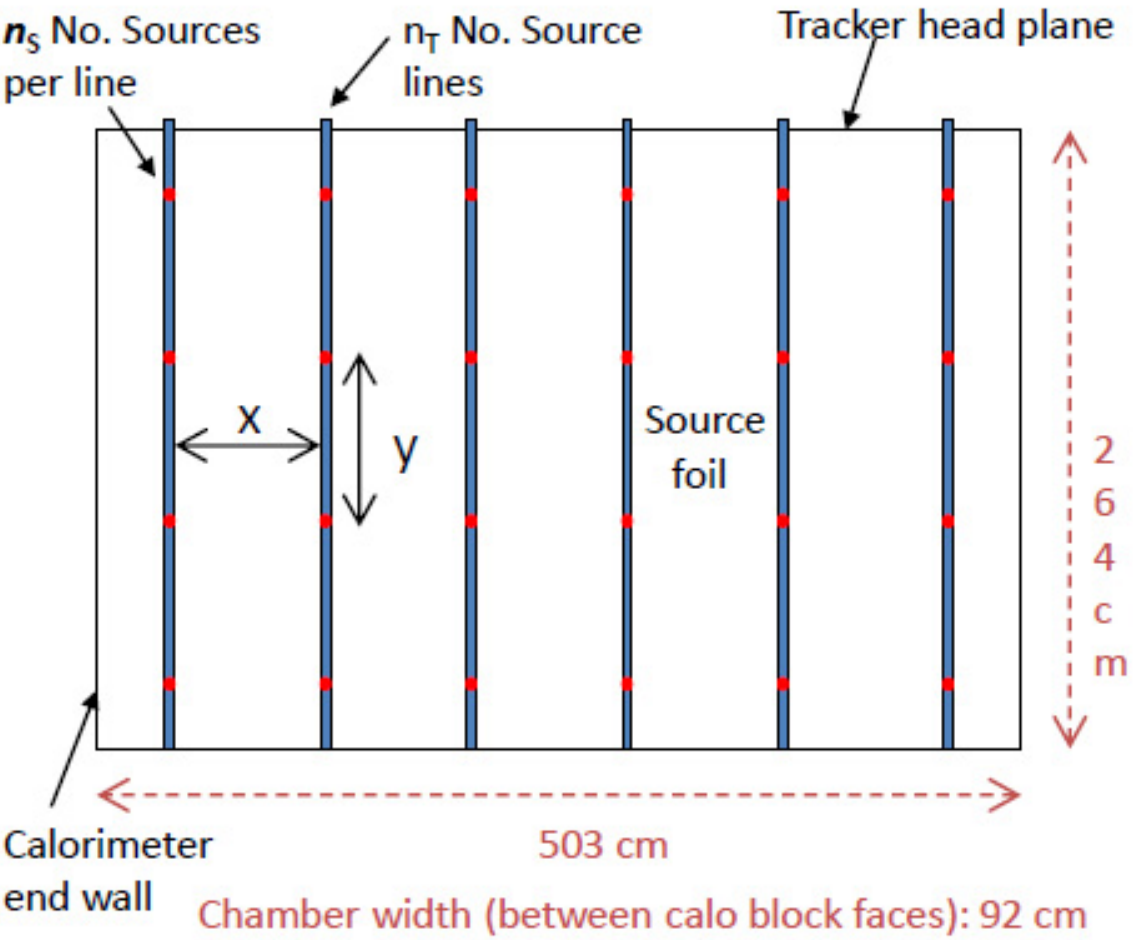

Figure 8.10: Schematic of source distribution compared to source foil position.

2. Optimisation of relative source Geiger cell alignment with respect to the tracking cells in order to minimise the tracker cell rates during calibration.

3. Number of electron events needed for 976keV peak reconstruction per optical module to achieve the required accuracy of 1%

4. Simulation and study of source placement designs within the detector

However before running simulations to determine these quantities we need to examine the geometry of the detector and the geometric constraints we do already know. A schematic diagram of the source's position and illumination can be seen below in Fig.8.11.

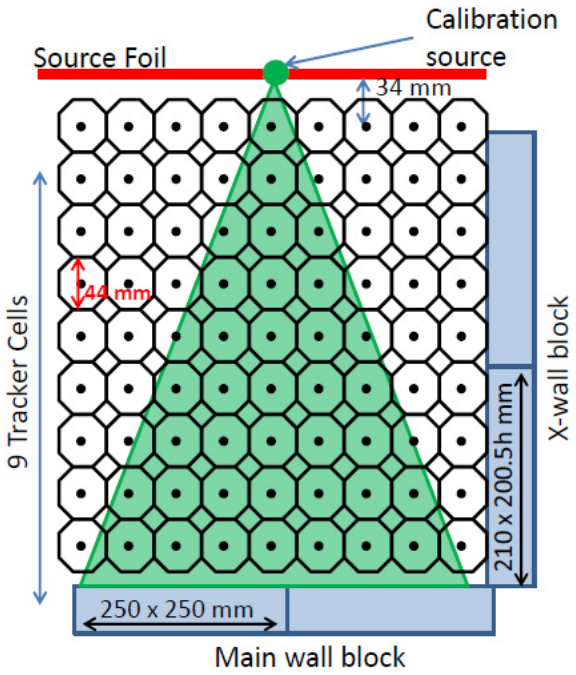

Figure 8.11: Schematic of source illumination.

- Maximum allowed gap between source foil and first tracker plane: **34 mm**
- Tracker cells (**44mm** dia) closely packed **in 9 rows** with **no intermediate gaps**
- Calorimeter blocks on main wall: square **250 X 250 mm**
- Calorimeter blocks on X-wall: rectangular **210w X 200.5h mm**
- Simulated events based on ^{207}Bi decay spectrum ($\approx$ 10% of decays include a conversion electron of 482 or 976 keV)
- Magnetic field turned on (**B = 2.5 mT**)

These were used to set up the simulation geometry for all of the aforementioned studies which will be discussed below.

8.3.1 Determination of the Maximum Geiger Hit Rate

When determining the maximum allowed tracker cell hit rate of the cells operating in the intrinsically slow Geiger regime we looked at 2 sources, theory and studies of the SuperNEMO Geiger cell performance and special NEMO3 data runs in which calibration sources were used.

The first comes from how the SuperNEMO Geiger cells operate and studies performed on the detector recovery between two consecutive events and how this affects the propagation of plasma. Generally, dead time of the cell should be 1ms (1kHz rate) which is the time needed after the electrons have finished drifting for the much heavier and slower ions to drift from the anode to the cathode. However feedback caused by drifting ions pulling electrons off the cathode starting more electrons to drift and cause cascades and more ions to drift back will increase this time. So this time will be made longer by electron and ion feedback and also cell cross talk. NEMO3 was run at 20Hz under which time the cells were found to be stable with no feedback.

Although SuperNEMO cells are structurally similar they are longer and wider, so were tested by looking at the propagation time and amplitude of the second of 2 events as the time difference between the events is increased.

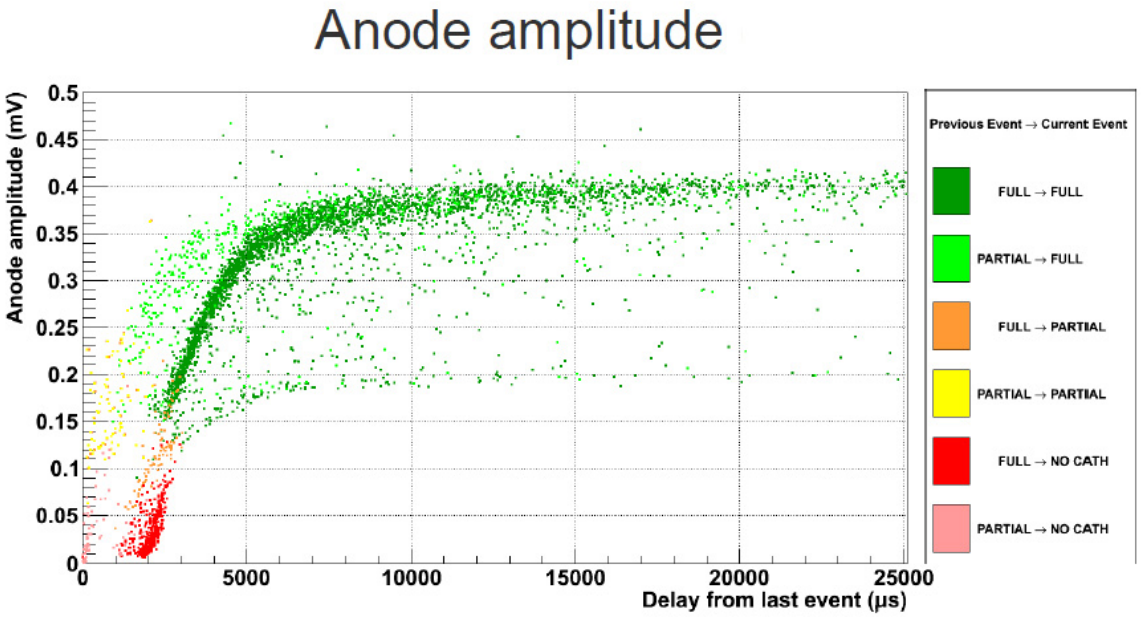

Figure 8.12: Distribution of second pulse amplitude with trigger time separation. [169]

Fig.8.12 shows that initially up to 7ms trigger separation, amplitudes alter greatly with separation, making them unreliable and that effect continues to about 10-15ms separation. The same effect is mirrored in the propagation time of the plasma as seen in Fig.8.13.

It can be seen clearly now that up to 3ms (shown in red), plasma is not propagating correctly and continues to be negatively affected till about 10-15ms where propagation time stabilises at about 45μs. This equates to a rate of between 100-66Hz so for safety and to ensure good operation 50Hz was chosen as the target maximum rate for any one cell during operation.

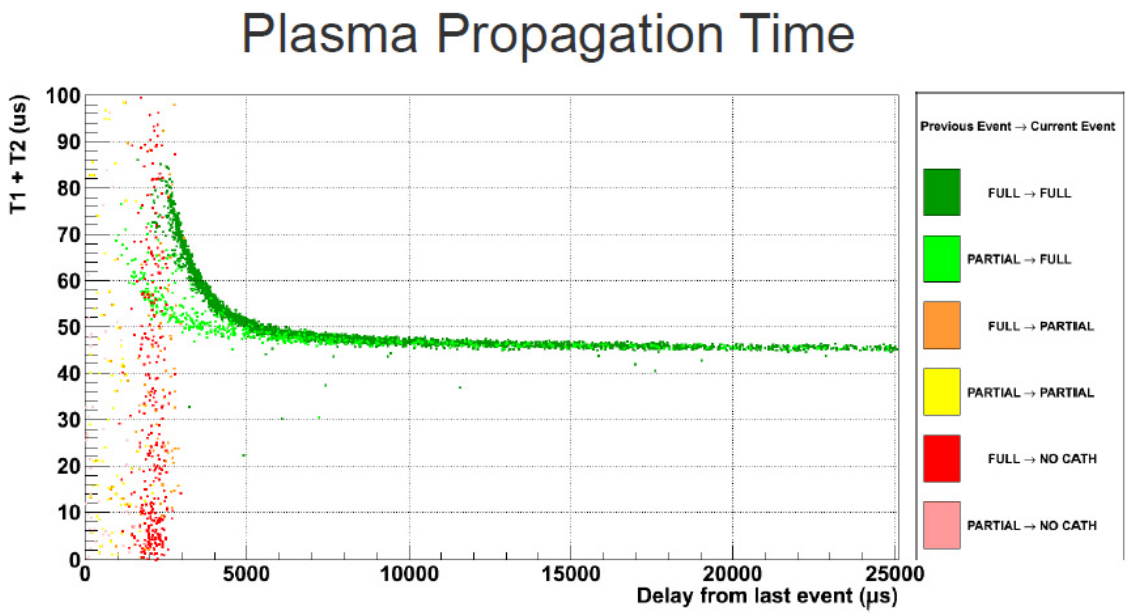

Figure 8.13: Distribution of second pulse plasma propagation times with trigger time separation. [169]

This is a safe maximum for a single cell but we must also look at the effect of adding many more cells and how this rate changes with effects such as cross talk between cells and feedback.

So we examined special runs from NEMO3 which had the calibration sources present as their trigger rate would be the highest experienced by the detector (Fig.8.14) and so give us information about the maximum rate for collections of cells. Also as well as using NEMO3 calibration data to determine the maximum allowed hit rate for the tracker cells, we can use it as validation of our simulations for SuperNEMO by altering the geometry to match that of NEMO3. This is even more relevant for the demonstrator as the plan is to use the same sources used in NEMO3.

A collection of plots made of the highest rate Geiger cells from various sectors of these special runs was generated to determine the maximum rate experienced by the cells during calibration.

The average Geiger cell rate during calibration from these plots was determined to be about 16Hz with a maximum of 20Hz and it was known from the technical design report of NEMO3 [147] that the maximum allowed rate for the DAQ was twice this, so 20Hz is what was decided upon as a safe maximum.

To validate our simulation software (Sec.7) we produced two simulations using comparable geometries to NEMO3 and then calculated the rates of the maximum Geiger cells triggered. The cells with the highest rates were then compared with the maximum rates determined from the NEMO3 calibration runs. These simulations used the known activity of the NEMO3 sources

The NEMO3 geometry has a 14mm distance from the closest cells' boundary which is the one that will be triggered most and is positioned with an 8mm offset to the anode wire. This gives it an illumination angle from the source of 62^o in the XY plane and 162^o in XZ (Fig.8.15)

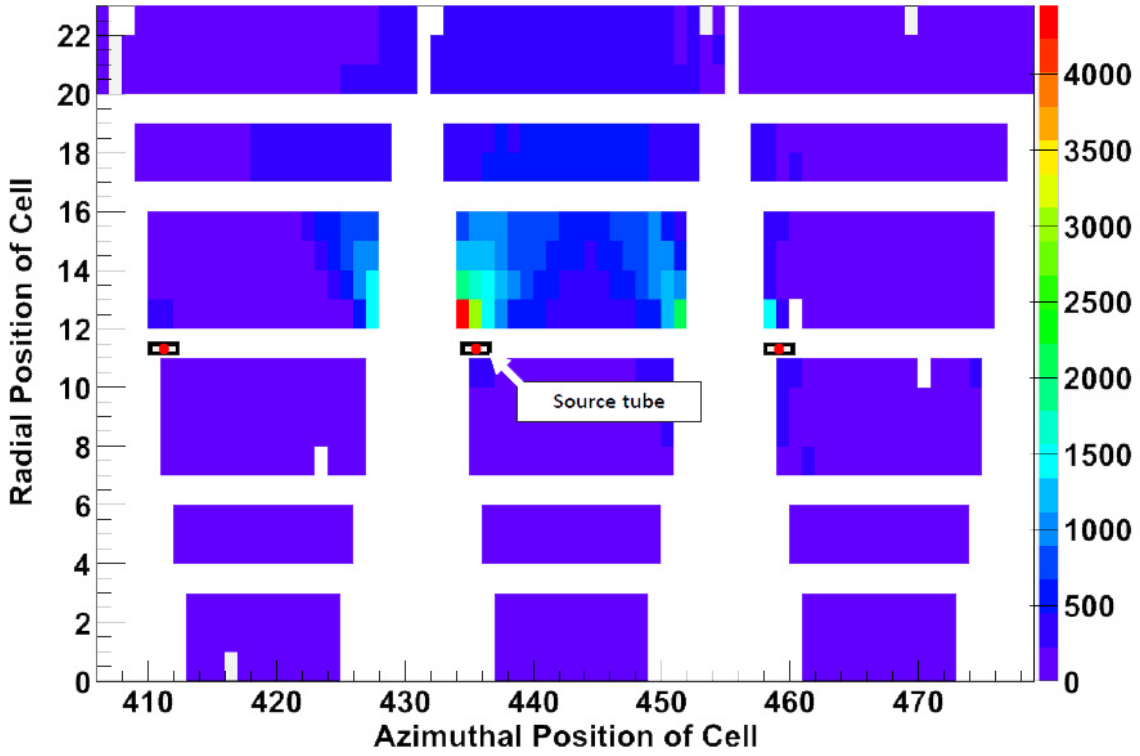

Figure 8.14: Example plot of special Geiger runs to test cell rate using NEMO3.

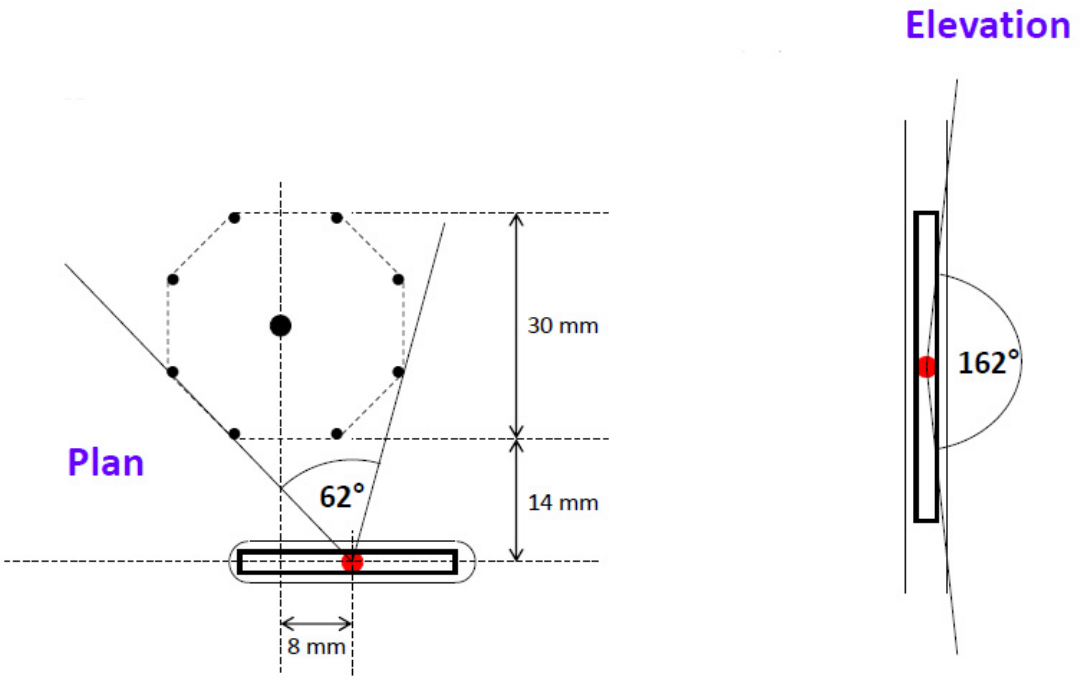

Figure 8.15: NEMO3 source cell alignment geometry schematic.

To reproduce this, one simulation was produced using the NEMO-3 cell size and source positions as simulation parameters and another using default SuperNEMO geometry with scaled-up NEMO-3 source positions. The results of these simulations saw maximum hit rates of 8.8 Hz and 8.6 Hz respectively, which is significantly lower than the average 16Hz seen from data.

The most likely reason for this difference is inaccuracy in the simulation of Auger electrons from ^{207}Pb atoms and their propagation in the detector. The detector effects of these keV-range electrons are notoriously difficult to simulate.

Calculation of the number of expected Auger electrons from this process would agree with the difference in levels seen and so in the end the empirical approach was used to finalise the maximum Geiger cell trigger rate to be 20 Hz. Additional studies would be desirable to confirm that missing events are indeed due to Auger electrons.

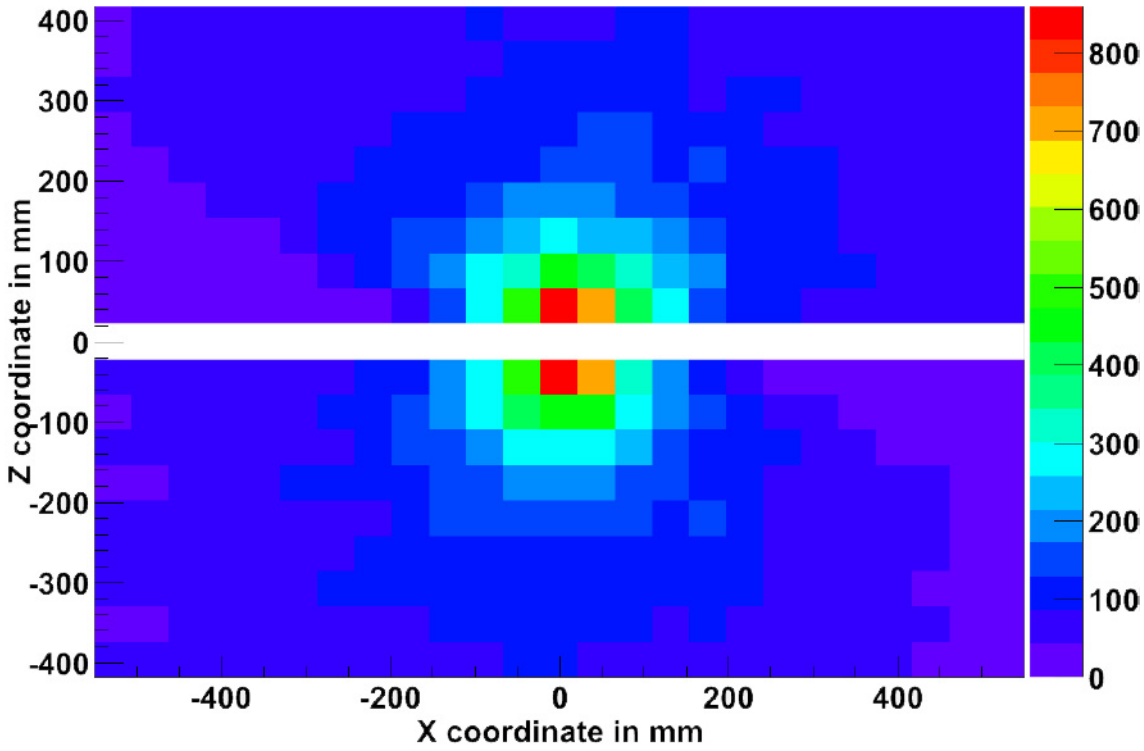

Figure 8.16: Simulation of Geiger triggering during calibration.

8.3.2 Optimisation of the Relative Source to Geiger Cell Alignment

As was seen in the previous section the position of the calibration source relative to the closest tracking cell will adjust the angular acceptance of emitted radiation into the cell region. Therefore the positioning of the calibration source relative to the tracking cells is important in order to meet and optimise the Geiger trigger rate (lower than a 20 Hz from Sec.8.3.1). To that end the position of

a ^{207}Bi source was altered in 2 directions X (alignment between the cell centre and boundary) and Z (the distance between the first cell and source). Z is limited by both the mechanical separation that needs to occur between the two elements and the need to minimise this distance to get more accurate vertex reconstruction (Fig.8.17).

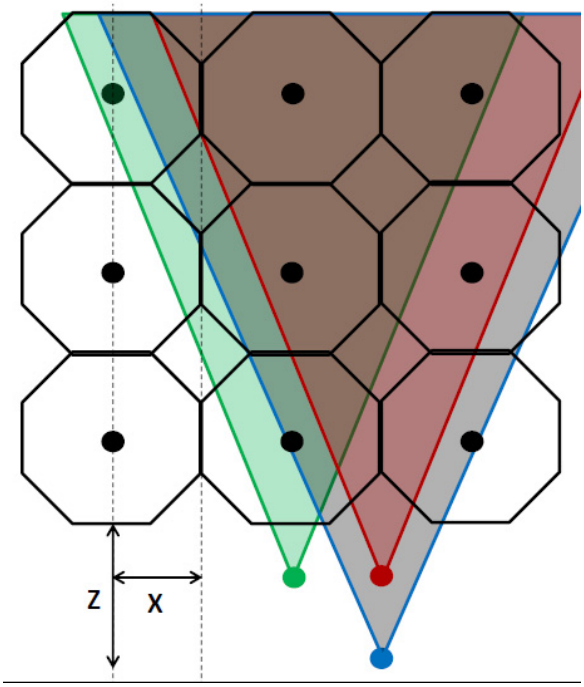

Figure 8.17: Schematic of source alignment with respect to Geiger cells.

Simulations were produced to experiment with the position of a calibration source with relation to the closest Geiger cell within the SuperNEMO geometry to minimise the closest cell's trigger rate whilst remaining within mechanically allowed limits. For each position a fixed number of ^{207}Bi events were simulated and then the number of times each Geiger cell was triggered near the source was recorded and plotted (Fig.8.18).

Through simulations it was found that increasing the source's distance from the closest cell boundary to its maximum value of 34mm would decrease the number of times the closest cells were triggered, as well as aligning the sources with the boundaries between 2 adjacent cells also gave the best reduction in maximum cell triggering (Fig.8.18). This equates to a reduction in the overall triggering rate of the process for any one cell.

Also the effect of an offset from this central inter cell boundary position on subtended angle was studied (Fig.8.19) to better understand this effect especially with respect to tolerances of alignment in construction.

The results of this study shown in Fig.8.20 demonstrate an effective subtended angle of the source from between 43^o and 50^o when moving from the cell boundary to in line with a cell which we can translate into an effective rate difference (Fig.8.21) of in the region of 17%. In terms of the tolerance for mechanical design and construction mm precision should be adequate as it can be seen a deviation

1)

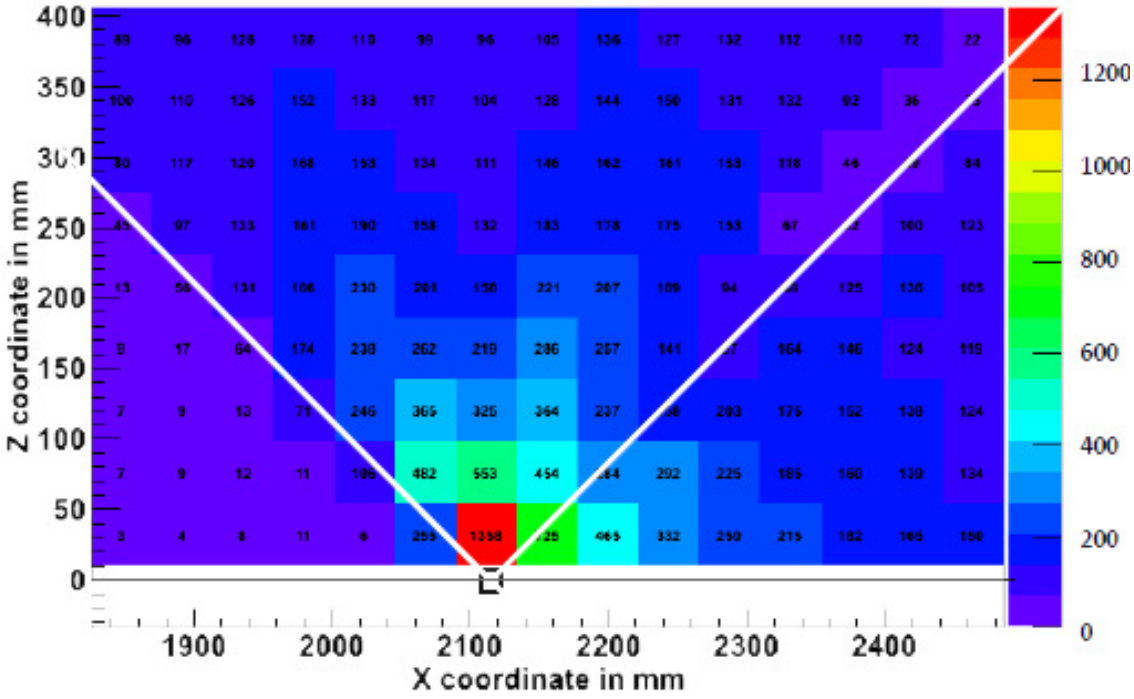
Z coordinate in mm
X coordinate in mm
0
50
100
150
200
250
300
350
400
1900
2000
2100
2200
2300
2400
200
400
600
800
1000
1200

2)

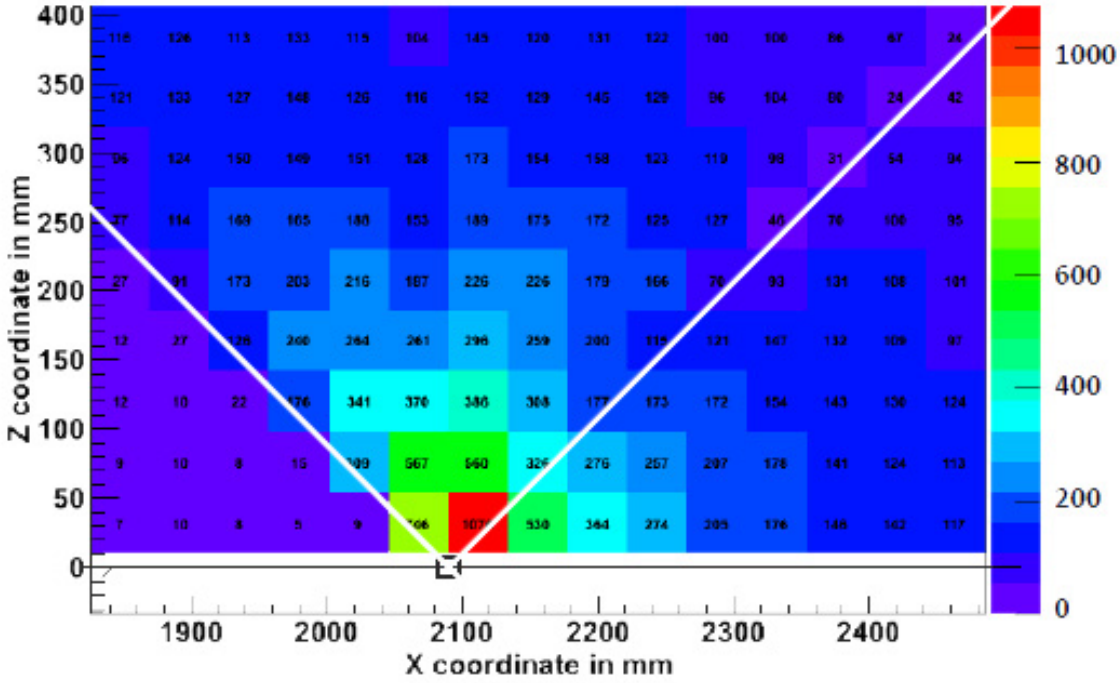
Z coordinate in mm
X coordinate in mm
0
50
100
150
200
250
300
350
400
1900
2000
2100
2200
2300
2400
200
400
600
800
1000

3)

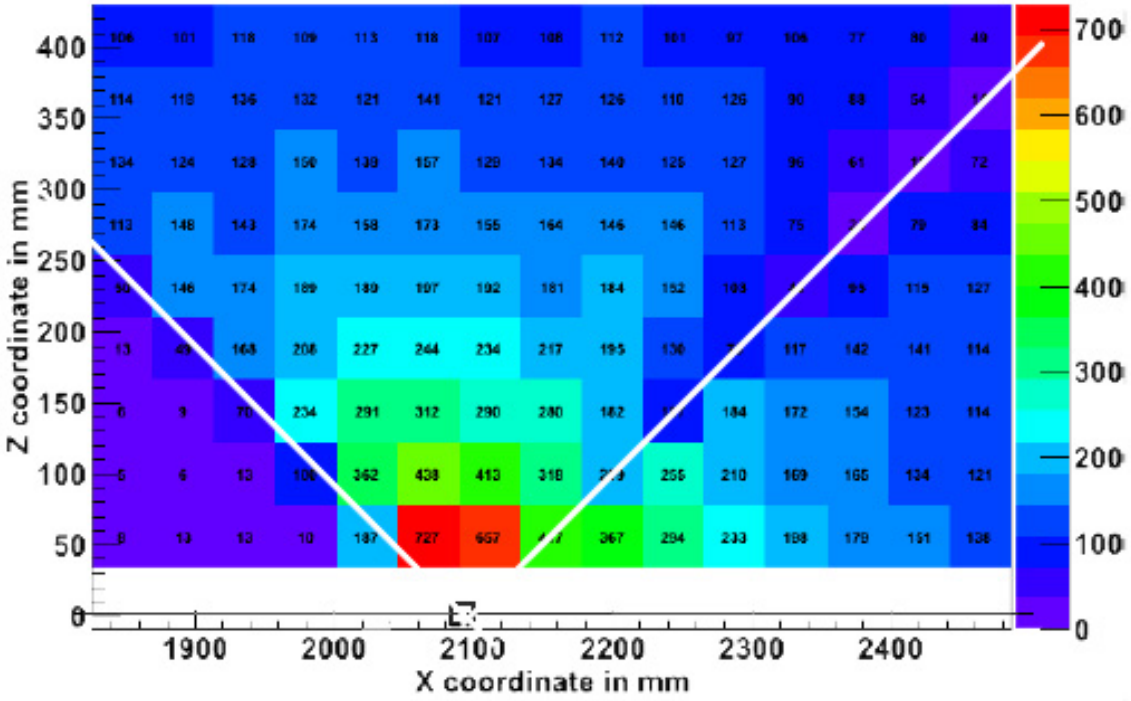

Figure 8.18: Example of cell trigger amounts for fixed number of events whilst the source position is varied in X and Y. 1) Source placed 10mm from the Geiger wires and aligned with the centre of the closest cell. 2) Source placed 10mm from the Geiger wires and aligned on the cell boundary of the closest two cells and 3) source placed 34mm from the Geiger wires and aligned on the cell boundary of the closest two cells.

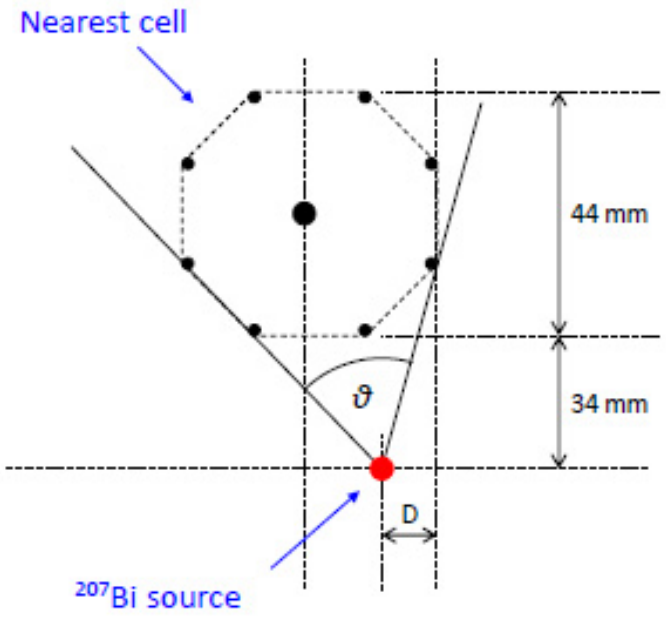

Figure 8.19: Schematic of angular acceptance of the closest cell where D is the distance from the cell boundary.

of 2mm from the boundary position has 2.5% effect on rate. However the exact allowed tolerance will be dependant of the chosen activity of the sources used.

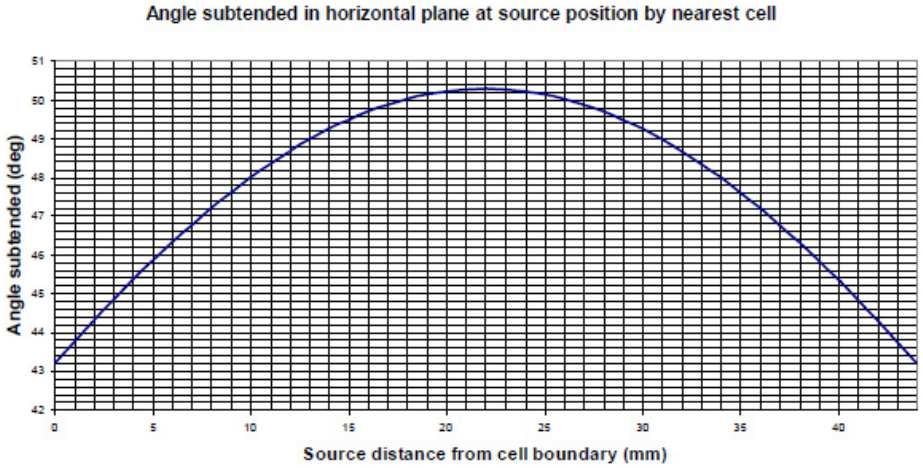

Figure 8.20: Effect of cell boundary source displacement on subtended angle.

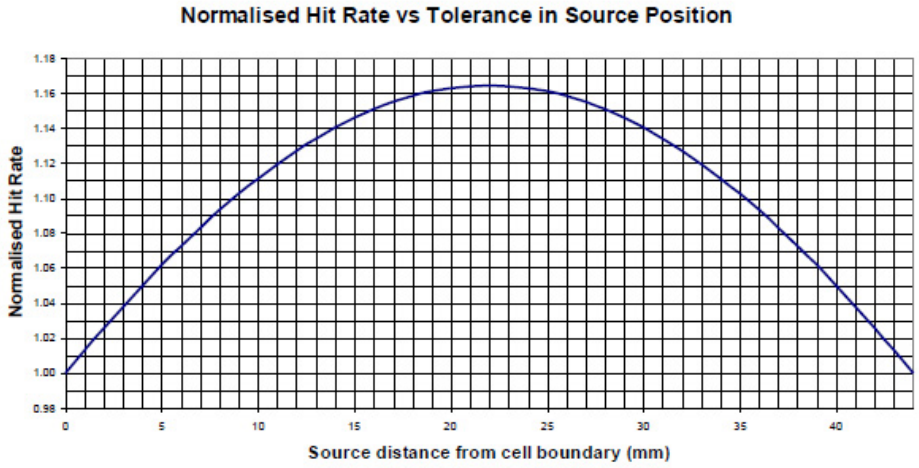

Figure 8.21: Effect of cell boundary source displacement on cell rates.

Now with a determination of the maximal allowed trigger rate and the effect of source position on the maximal trigger rate we can start to look at the required number of events, calibration time and activity of source required to produce the calibration procedure.

8.3.3 Number of Events Needed for Peak Reconstruction Calibration

In order to achieve absolute energy calibrations with the 976 keV peak of conversion electrons from ^{207}Bi, first electron events must be selected from calibration data (using the selection criteria for electrons seen in sec.5.2.2) whose energies are within the range of 0.7-1.2 MeV, then the peak in the electron energy distribution must be fitted to determine the peak position. The systematic error on the energy scale determination for NEMO3 was 1%. Assuming that the error on fitting the peak position should produce a negligible contribution to the total error of 1%, the fitting error was chosen

Source offset from cell boundary (mm)	Increase in hit rate over zero offset (%)
5	6
10	11
22	16.5

Table 8.4: Effect of boundary offset on trigger rate.

Transition	Relative Intensity (%)
976 keV K-shell	7.03
1048 keV L-shell	1.84
1060 keV M-shell	0.54

Table 8.5: Relative conversion electron intensities. [170]

not to exceed 0.2%. To determine this first NEMO3 calibration data was studied to examine the effect of the number of events on peak position error for a single calorimeter module. The peak being determined is a combination of three Gaussians representing the electron shells K, L and M (see sec.8.1.3). As the relative peak positions and intensities are well known (see table.8.5), we can express the L and M shell peaks in terms of the K peak by following the procedure below.

Each electron shell peak is described by a Gaussian distribution (G) defined by three parameters (I) the peak intensity, (μ) the mean energy and (σ) the standard deviation

$$IG(\mu,\sigma) = \frac{I}{\sigma\sqrt{2\pi}} e^{\left(\frac{-(x-\mu)^2}{2\sigma^2}\right)} \tag{8.1}$$

where x represents the QDC bin number. To relate the Gaussian distributions of the L and M shells to that of the K shell, we start by assuming the number of photo-electrons per unit deposited energy to be a linear relation. Therefore the following relation between shells can be made.

$$\frac{N_{pe}}{\mu} = \frac{N'_{pe}}{\mu'} \tag{8.2}$$

The number of photo-electrons (N_{pe}) for each peak can be approximated by using photon statistics (assuming N_{pe} >20), where fluctuations are Poission in nature with

$$\text{rms} = \sqrt{N_{pe}} \quad , \quad \text{mean} = k \times N_{pe} \quad , \quad \text{sigma} = k \times \text{rms} \tag{8.3}$$

where k is the conversion factor between charge and ADC. Thefore

$$N_{pe} \approx \left(\frac{\mu}{\sigma}\right)^2 \tag{8.4}$$

and substitution of this into eqn.8.2 gives the following relation.

$$\frac{\mu}{\sigma^2} = \frac{\mu'}{\sigma'^2} \tag{8.5}$$

As the mean energy of each peak is known relative to each other we can define μ' as

$$\mu' = \mu + E\alpha \tag{8.6}$$

where E is the real energy difference between the two peaks and α is a calibration constant to convert that to QDC bins (bins/energy).

Substitution of eqn.8.6 into eqn.8.5 and rearranging allows us to express σ' as

$$\sigma' = \sigma\sqrt{1 + \frac{E\alpha}{\mu}} \tag{8.7}$$

Using these relations and the known transition intensities from table.8.5 we can construct the following equation to fit to the triple Gaussian distribution.

$$I_K G(\mu_K, \sigma_K) + I_L G\left(\mu_K + E_{KL}\alpha, \sigma_K\sqrt{1 + \frac{E_{KL}\alpha}{\mu_K}}\right) + I_M G\left(\mu_K + E_{KM}\alpha, \sigma_K\sqrt{1 + \frac{E_{KM}\alpha}{\mu_K}}\right) \tag{8.8}$$

Where I_i are the transition intensities, E_{ij} the energy difference between the i and j peaks. This equation therefore only has 3 floated parameters to fit for, they are, the mean (μ_K), standard deviation (σ_K) and intensity (I_K) of the K shell and the calibration constant(α). This fit was performed for varying numbers of events to see how the peak position error was affected, the results can be seen in fig.8.22 and were scaled for SuperNEMO's energy resolution and plotted against the number of events before cuts .

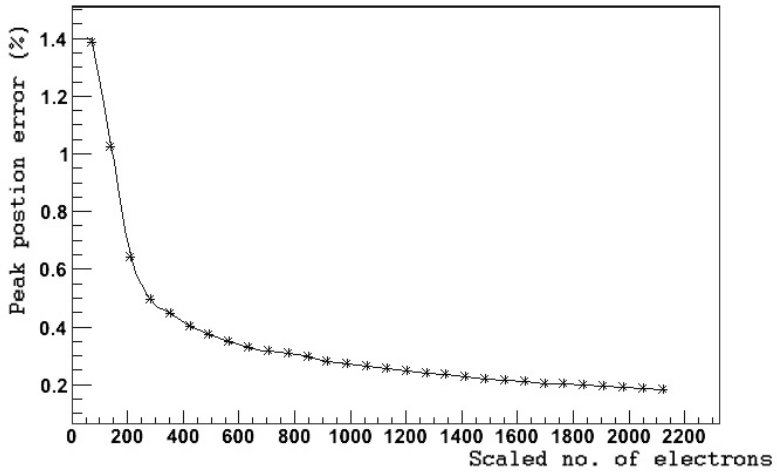

Figure 8.22: Effect of number of electrons on fitted peak position error for SuperNEMO.

As can be seen from fig.8.22 in order to reach the required 0.2% precision a minimum of 2000 electron events between 0.7 and 1.2MeV are required per optical module during an absolute calibration run. This corresponds to 47,000 events emitted by the source (before cuts) which determine the

required activity of the calibration sources.

8.4 Simulation and Study of Calibration Source Placement within the Detector

From the above studies we now know the constraint on maximum tracker rate for cells, we also know that sources should be positioned at cell boundaries at the maximum allowed perpendicular distance of 34mm from the first line of cells and that in order to achieve 1% calibration accuracy at least 2000 electron in the energy range of 0.7 - 1.2 MeV per calorimeter block are required. These constraints can be added to general constraints of timing and maximisation of foil area to produce the full list of operating constraints of our simulations when designing the source layout and their activities.

When designing the calibration source layout and strength (Fig.8.10) the following requirements summarised from the studies above had to be met.

1. No tracker cell should receive more than 20 (electron) hits per second.
2. All calo blocks in main and X-walls should receive sufficient (electron) hits in the calibration period to fit the 976 keV peak of ^{207}Bi to within 1%. with the fit contributing $< 0.2\%$. This translates into the minimum of 2000 events.
3. Space occupied by source lines in the foil plane should be minimised.
4. Spacing of source lines should allow foils to be made in standard widths
5. Time for calibration to be achieved should be minimised (max 21hrs allocated)

Using these constraints as criteria, the SuperNEMO geometry simulations were undertaken using the tubeless delivery design to determine the best configuration for calibration sources that matched these constraints for both systems. A nominal configuration of 5 vertical source lines with 4 evenly distributed sources in each was initially tested and then other possibilities explored.

The simulations were made with a fixed number of events and from each of these runs the quantities of the X and Y separations of the sources were recorded along with the number of source lines (N_L) and number of sources per line (N_S), as well as the number of events in the simulation (N_{events}), the determined values for T_{max} (the number of times the Geiger cell with the maximum number of discharges was triggered), C_{min} (the calorimeter block with the smallest number of recorded hits in the 0.7 - 1.2 MeV energy range). Using this data the time needed for calibration (T_C) and the desired source activity (A_S) (Fig.8.10) could be determined by using the following approach.

First the constraint on the tracker rate means that we cannot exceed 20Hz. Therefore the number of seconds the number of simulated events could minimally be produced over (T_{sim}) is given by eqn.8.9.

$$T_{sim} = T_{max}/20. \tag{8.9}$$

Within this time the minimum observed electrons by any calorimeter block is given by C_{min} and in order for this block to observe the 2000 events we need to calibrate it we need to do the following to find the calibration time (T_C).

$$T_C = \frac{2000 T_{sim}}{C_{min}} \tag{8.10}$$

Substituting eqn.8.9 into eqn.8.10 we obtain eqn.8.11 for the minimum time needed for calibration with a given source distribution.

$$T_C = \frac{100 T_{max}}{C_{min}} \tag{8.11}$$

Similarly the activity (A_S) of ^{207}Bi sources needed to achieve this calibration time can be calculated by finding the rate of a single source using the simulation time T_{sim}, the number of simulated events N_{events} and the number of sources in the distribution ($N_L \times N_S$).

$$A_S = \frac{N_{events}}{T_{sim} N_L N_S} \tag{8.12}$$

Substituting for the simulation time eqn.8.9 therefore gives eqn.8.13 for the ideal source activity (A_S).

$$A_S = \frac{N_{events} 20}{T_{max} N_L N_S} \tag{8.13}$$

The calibration time can then be calculated for the recycled NEMO3 200Bq sources used in the demonstrator and the expected highest Geiger tracker rate (T_{rate}) for these sources using Eqn.8.14

$$T_{rate} = \frac{4000}{A_S} \tag{8.14}$$

8.4.1 Calibration Distribution Simulation with Tubeless Weighted Line Delivery

As mentioned above, a distribution of 5 source lines and 4 sources per tube was simulated for 10^6 events first and then the number of tubes and sources per line altered to find the best configuration. This optimisation will alter slightly for the copper tube design owing to the weighted line systems taking up less space and therefore maximising the area of the source foil, and the slightly different angular distributions of the housings, but the distribution would be the same albeit with slight variation in X and Y. For the tubeless distribution simulations, plots were made of the main wall scintillator blocks (Fig.8.23) and the X wall blocks occupancy (Fig.8.25), as well as the number and distribution of Geiger cells triggered (Fig.8.26) and block energy distribution for the blocks in both

walls (Fig.8.24) can be seen below.

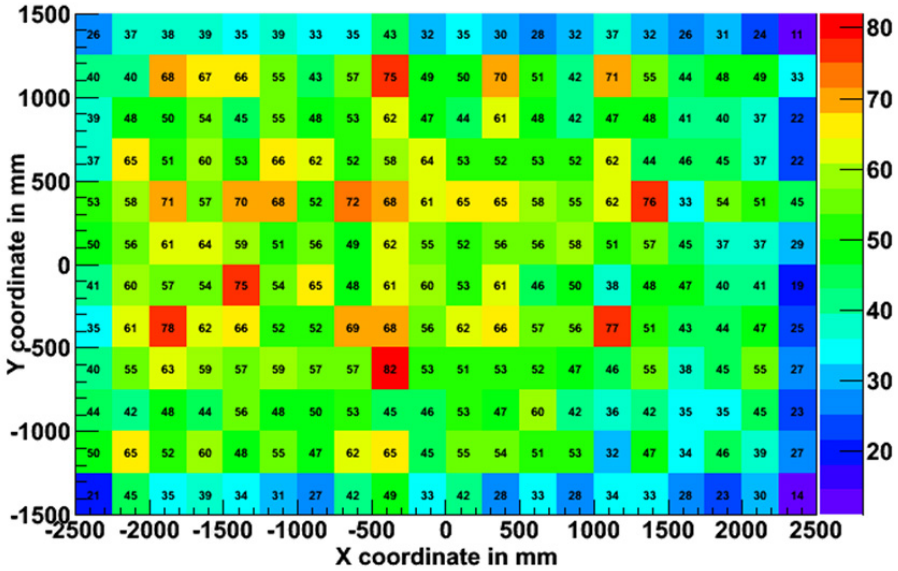

Figure 8.23: Main-wall scint block occupancies (0.7 < E < 1.2 MeV) for 6 x 4 grid (X = 836 mm) (no tubes).

The results of these simulations with the calibration time, optimum activity sources, the NEMO3 source calibration time and the configurations tested can be seen in Table.8.6.

Tubeless system									New sources		Existing sources	
(N_L)	(N_S)	X(mm)	Y(mm)	θ_H	θ_V	N_{events}	C_{min}	T_{max}	T_C(hrs)	A_S(Bq)	T_C(hrs)	T_{rate}(Hz)
5	4	1012	850	158^o	166^o	10^6	5	2200	12.2	455	27.8	8.8
6	4	748	850	158^o	166^o	10^6	5	1921	10.7	434	23.1	9.2
6	4	836	850	158^o	166^o	9.5×10^5	8	1771	6.1	447	13.7	8.9
6	4	924	850	158^o	166^o	10^6	8	1840	6.4	453	14.5	8.8
6	4	924	900	158^o	166^o	10^6	6	1897	8.8	439	19.3	9.1

Table 8.6: Calibration source distribution results showing minimum block occupancy (C_{min}) highest tracker cell firing (T_{max}) and the calibration time (T_C) and source activity (A_S).

Looking at the results in Table.8.6 we can see that a 6 x 4 grid arrangement with sources spaced 836 or 924 mm apart horizontally and 850 mm vertically could provide the necessary calibration of at least 2000 events above 0.7MeV per block within the required calibration time (<21 hours). The shorter this calibration time the better, and both can achieve calibration with the NEMO3 200Bq sources (used in the demonstrator) of about 14hours (same as NEMO3). They both also provide tracker rates well below that of 20Hz even when the 50% simulation underestimate is included, which is believed to be due to Auger electrons. If we do add 50% we can see that the maximum rate of the two configurations would be 17.8Hz, which can undergo a 12% increase in rate due to mis-alignment in construction before it reaches the maximum 20Hz, this correlates to a 10mm maximum mis-alignment in source position, so mm accuracy in construction should be adequate. These two configurations will also allow the source foils to be made in a standard width of 180 or 200 mm. The preferred option can be chosen according to mechanical criteria as demonstrated in Fig.8.27 and

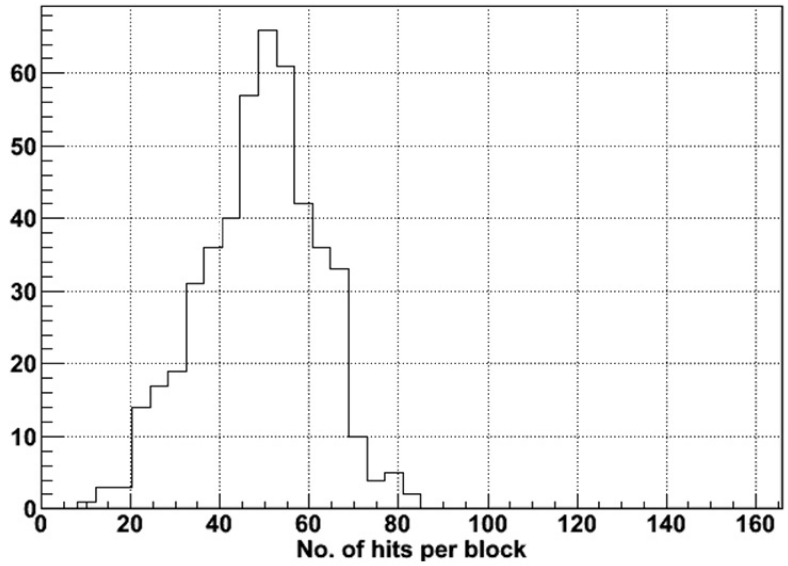

Figure 8.24: Main-wall scint block occupancies (0.7 < E < 1.2 MeV) for 6 x 4 grid (X = 836 mm) (no tubes).

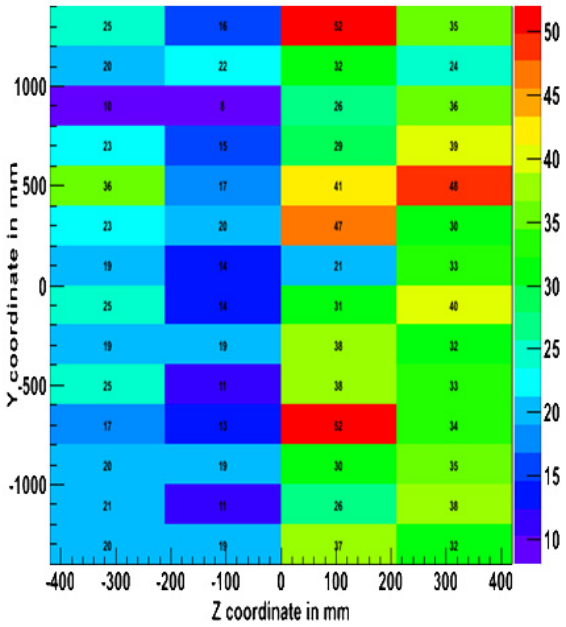

Figure 8.25: X-wall scint block occupancies (0.7 < E < 1.2 MeV) for 6 x 4 grid (X = 836 mm) (no tubes).

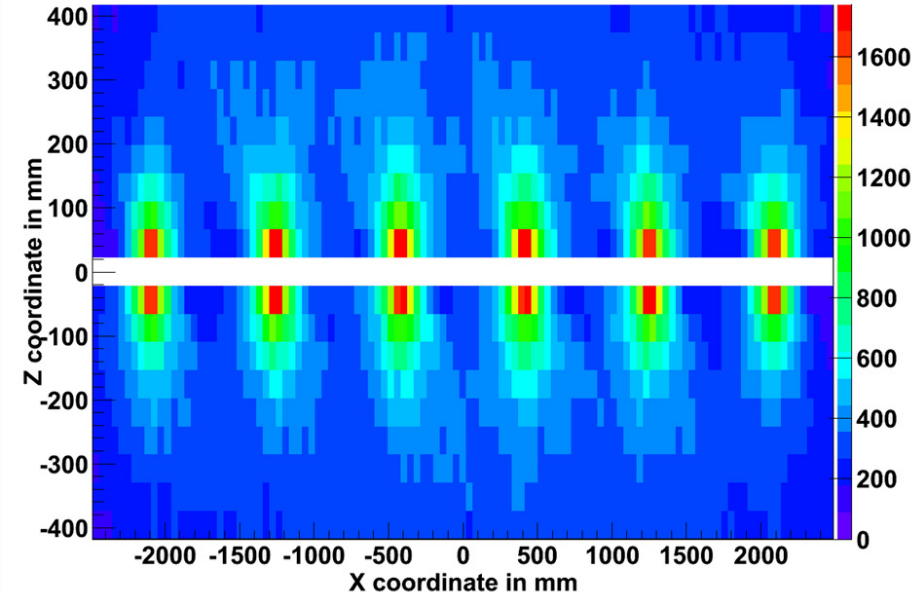

Figure 8.26: Simulation of tracking hits distribution.

Fig.8.28.

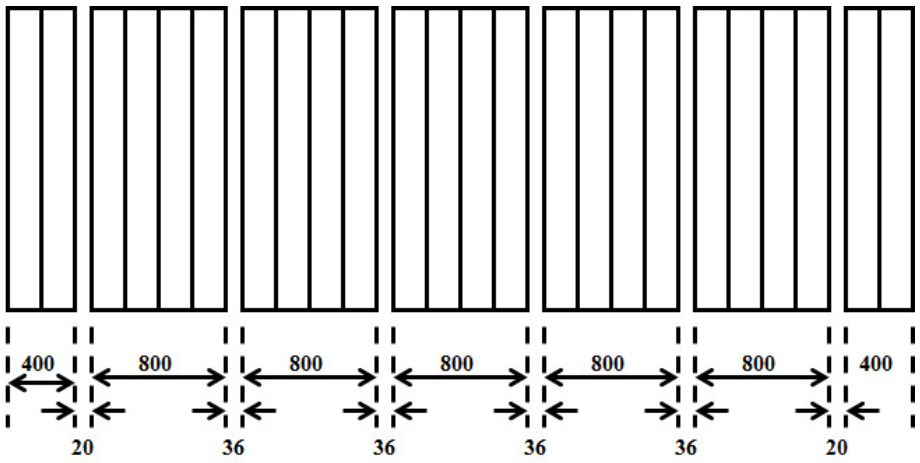

Figure 8.27: 6 x 4 grid: 836 mm horizontal source spacing and 200 mm foil strips (total width 4984 mm).

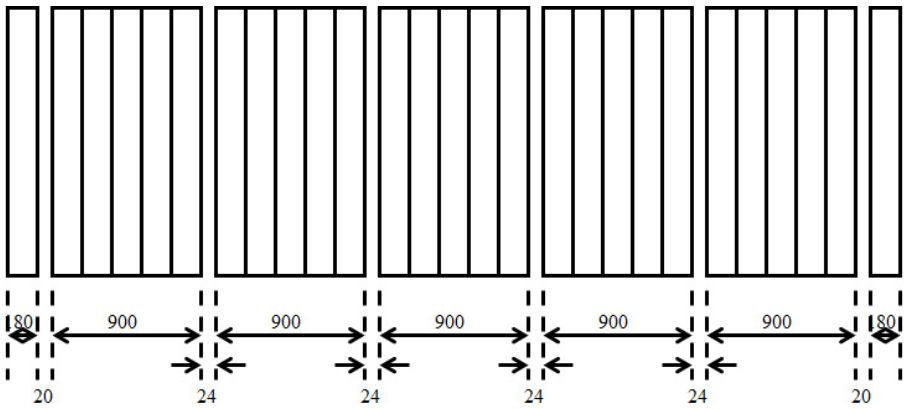

Figure 8.28: 6 x 4 grid: 924 mm horizontal source spacing and 180 mm foil strips (total width 4996 mm).

Chapter 9

Conclusion

NEMO3 is a toroidal detector that took data between February 2003 and January 2011. The detector was housed in the Laboratoire Souterrain de Modane in the Fejus mountain pass on the French Italian border. It was built to study and measure the process of double beta decay for several isotopes ($\beta\beta2\nu$) and to attempt to observe the theoretical process of neutrinoless double beta decay ($\beta\beta0\nu$). Neutrinoless double beta decay would be an important discovery as it is a lepton number violating process that is beyond the standard model. Its observation would help answer many fundamental questions with far reaching implications, as it would identify the neutrino as a Majorana particle and not a Dirac particle and allow for a direct measurement of the effective neutrino mass. Also, together with neutrino oscillation experiments, $\beta\beta0\nu$ measurements can probe the hierarchy of the neutrino masses and, although extremely challenging, can even explore CP-violation effects. The $\beta\beta2\nu$ decay is also very important as not only is it one of the longest life-time processes known, but it also can be used to help improve our understanding of nuclear models and calculation of matrix elements. The accurate measurement of this process also plays a key role in $\beta\beta0\nu$ decay as its the dominant irreducible background to the process.

The NEMO3 collaboration has published an array of results for $\beta\beta2\nu$ decay and $\beta\beta0\nu$ decay for each of the 7 double beta decay isotopes used in the experiment which is unprecedented and many have been world leading measurements including the ^{48}Ca measurements presented in this thesis. The strengths and distinguishing features of the NEMO3 experiment are that it records event topologies which help with particle identification, background suppression and mechanism determinations and that its detection apparatus and source are independent allowing for multiple isotope measurements. The detector itself is described in detail within the thesis covering all the components from tracking, calorimeters, source foils, magnetic field, calibration and shielding. Also outlined in the thesis is a full examination of the associated backgrounds to the experiment and the different event topologies for particles like electrons, gammas and alphas, as well as cuts used to select double beta events and for suppression of backgrounds from ^{48}Ca.

The isotope studied was 6.99g of ^{48}Ca and its double beta decay to ^{48}Ti over a period of 1555

days. The study observed internal contamination by ^{90}Sr and its daughter ^{90}Y which were the major backgrounds. The study was also made more challenging by the detector's resolution limitations at low energies and geometric problems with the source. However the final event selection was chosen with these considerations in mind.

The final result of the measurement of the half-life of ^{48}Ca $\beta\beta2\nu$ decay to the ground state is:

$$T_{1/2} = 4.11^{+0.23}_{-0.20}(stat.) \pm 0.26(syst.) \times 10^{19} \text{ years}$$

This is the world's most precise measurement of the half-life of this process. From this the corresponding NME was calculated as:

$$M_{2\nu} = 0.0247 \pm 0.0015$$

which due to Ca being uniquely double magic in nature with closed shells means it can constrain NME models and calculations, from which the NME for $\beta\beta0\nu$ decay can be extracted.

This result helps constrain nuclear models, in particular the nuclear shell model used for calculation of the ^{48}Ca NME. As ^{48}Ca is the only doubly magic nucleus among the double beta decay isotopes it provides an excellent test bench for theoretical calculations. The obtained result is close to the best available evaluations of 0.026-0.028. No excess of events were seen above that expected from $\beta\beta2\nu$ decay and backgrounds, so limits can be drawn for the $\beta\beta0\nu$ decay half-life of:

$$T_{1/2} > 1.8 \times 10^{22} \text{ years at 90\% CL.}$$

This corresponds to a limit on the effective mass of the neutrino of:

$$\langle m_\nu \rangle < 19.8 \text{ eV}$$

This result is comparable to the world's best measurement by ELEGANT VI $T_{1/2} > 5.8 \times 10^{22}$ years at 90% CL. [127]

Continuing with the efforts and technologies developed for NEMO3, SuperNEMO is set to become its successor project for the NEMO collaboration. The demonstrator for SuperNEMO is currently under construction and data taking is intended to begin in 2015. The full detector made out of 20 sub modules equal in size to the demonstrator is intended to hold ≈100 kg of ^{82}Se initially, with the ability to change the source at a later date. A half-life sensitivity of $\approx 10^{26}$ years for $\beta\beta0\nu$ decay will be achieved, which corresponds to an effective mass sensitivity of 40-100 meV. The R&D activities to improve on existing technologies in the areas of calorimety, tracking, calibration and software are summarised within this thesis, with its focus on software development and simulation studies of the calibration system. The calibration simulations presented obtained a spacial distribution for calibration sources of a 6x4 array, that could meet needs of having each optical module of the calorimeter calibrated to within 1% absolute energy scale. This calibration is carried out using ^{207}Bi as a source of conversion electrons and shows that with an activity of 200-153Bq all necessary calibrations could be achieved within 6.1-14.5 hours. The configuration presented will also allow for standardised widths of double beta decay source strips of either 180mm or 200mm to be used for construction, meeting all the requirements outlined for an absolute calibration system.

Chapter 10

Appendix

10.1 My Contributions to the NEMO Collaboration

- NEMO3 ^{48}Ca analysis studies
- Production of NEMO3 MC data
- Development of NEMO3 analysis software
- NEMO3 data taking and calibration shifts
- Sole Development of an independent SuperNEMO analysis software
- Sole Development of an independent SuperNEMO event display
- Sole Development of an independent SuperNEMO framework
- Sole Development of an automated nightly build and validation system
- Maintenance, development and design of SuperNEMO software (including generation, simulation, digitization and analysis)
- Testing and validation of SuperNEMO software physics
- SuperNEMO bar concept simulation studies
- SuperNEMO calibration simulation studies
- SuperNEMO commissioning hardware testing
- SuperNEMO calorimeter block studies

10.2 ^{48}Ca Source Issues

Work subsequent to my own analysis findings has shed light on a few problems with the experimental apparatus which will mean further analysis and alterations would be needed to be made to account for them. A description of each finding and their effect can be seen below

- It was discovered upon opening the detector, removing and unwrapping the Mylar from the CaF_2 disks for premeasuring in the HPGe detector that the size of the disks had been incorrectly recorded. In the technical design report produced at the detector construction it was recorded that the diameter of the disks was 40mm when in fact it was discovered that the disks were actually 46mm in diameter (see fig.10.1) [171] .

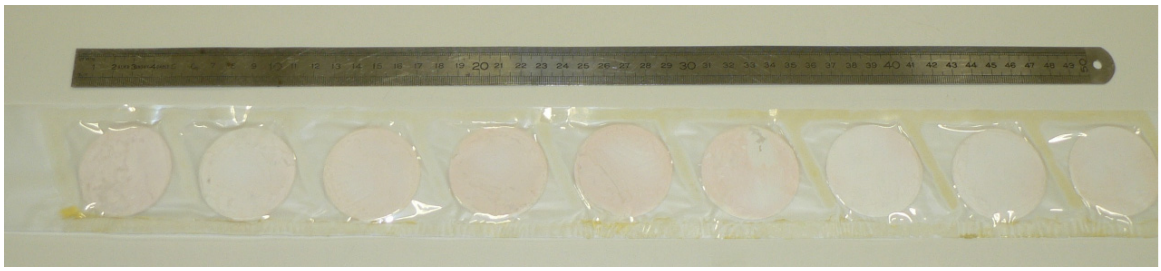

Figure 10.1: Photograph of the CaF_2 dicks after disassembly from Mylar foil. Picture shows correct geometric dimensions. [171]

- Due to the incorrect disk diameter we can no longer be confident of the planar density of the sources as the change in diameter would mean a change from 155 mg/cm^2 to 117 mg/cm^2 which would cause effects to both the energy and angular distributions [171] .

- It has also been suggested that a secondary 10μm thick Teflon coating may have been added to the disks, which if true would affect our simulations of the energy spectra due to interactions with this layer reducing the energy of higher energy events. This effect although thought to be marginal could in part account for the deficit of low energy events in MC.

- During the detector deconstruction some foil defects were discovered (see fig.10.2), these defects were in two forms. Firstly the end strips of each sector were only attached to the frame by a single central screw thread, unlike the other strips within a sector which have two. This means that these foils can rotate about a central axis greatly affecting the angle of emission from the face of the foil. It was decided on construction that to secure the end strips adhesive tape should be placed fixing them to the adjoining strip, but obviously from the illustration of fig.10.2 this has not been effective. This leaves three rather important questions, was that ^{48}Ca foil rotated? By how much? and was that rotation constant throughout data taking or has it altered with time?

  Analysis performed by Victor Tretyak has discovered that indeed the ^{48}Ca foil has been rotated by as much as 10.6^o, which increases the double beta decay efficiency by 8%. However no study

as yet has been done to evaluate the rotation angle with time [171].

Figure 10.2: Photograph taken during detector disassembly showing two foil defects. The first picture shows a rotated foil and the second a warped foil.

The second defect shown is the apparent bending or misshapen foil strip of a metallic foil which should not affect the composite foil of ^{48}Ca

All of these uncertainties can lead to a systematic effect on the half-life of 20-30%. Work is currently ongoing to try and address these issues, however initial results show that whilst some of these problems can reconcile deficits in the 2 electron spectrum, the 1e1γ channel remains problematic. These issues might be addressed by an extra background component or source of gammas (possibly the hot spot in the blank region) or calibration errors. However further study and a new effort to search for answers is needed.

Bibliography

[1] E. Fermi. "Versuch einer Theorie der β-Strahlen. I". *Zeitschr. f. Phys.*, 88:161–177, 1934.

[2] H. Bethe & R. Peierls. "The Neutrino ". *Nature*, 133:532, 1934.

[3] F. Reines & C. L. Cowan Jr. "Detection of the Free Neutrino". *Phys. Rev.*, 92:830–831, 1953.

[4] F. Rwines & C. Cowan. "The Neutrino". *Nature*, 178:446–449, 1956.

[5] F. Reines & C. Cowan . "Free Antineutrino Absorption Cross Section. I. Measurement of the Free Antineutrino Absorption Cross Section by Protons". *Phys. Rev.*, 113:273–279, 1959.

[6] M. Goldhaber, L. Grodzins, & A. W. Sunyar . "Helicity of Neutrinos". *Phys. Rev.*, 109:1015–1017, 1958.

[7] G. Danby *et al.* "Observation of High-Energy Neutrino Reactions and the Existence of Two Kinds of Neutrinos". *Phys. Rev. Lett.*, 9:36–44, 1962.

[8] B. Pontecorvo. *Sov. Phys. JETP*, 10:1236, 1960.

[9] B.T. Cleveland *et al.* "Measurement of the solar electron neutrino flux with the Homestake chlorine detector ". *Astrophys. J.*, 496:505–526, 1998.

[10] J. E. Augustin *et al.* . "Discovery of a Narrow Resonance in e+e- Annihilation". *Phys. Rev. Lett.*, 33:1406–1408, 1974.

[11] J. J. Aubert *et al.* "Experimental Observation of a Heavy Particle J". *Phys. Rev. Lett.*, 33:1404–1406, 1974.

[12] S. Herb *et al.* "Observation of a Dimuon Resonance at 9.5 GeV in 400-GeV Proton-Nucleus Collisions". *Phys. Rev. Lett.*, 39:252–255, 1977.

[13] Martin L. Perl. "Evidence for, and Properties of, the New Charged Heavy Lepton". *SLAC-PUB*, 77:23, 1923.

[14] UA1 Collaboration. "Experimental observation of isolated large transverse energy electrons with associated missing energy at $\sqrt{s} = 540$GeV". *Physics Letters B*, 122:103–116, 1983.

[15] K. Hirata *et al.* . "Observation of a neutrino burst from the supernova SN1987A". *Phys. Rev. Lett.*, 58:1490–1493, 1987.

[16] ALEPH Collaboration. "Determination of the Number of Light Neutrino Species". *Phys.Lett. B*, 231:519–529, 1989.

[17] Y. Fukuda *et al.* "Evidence for Oscillation of Atmospheric Neutrinos". *Phys. Rev. Lett.*, 81:1562–1567, 1998.

[18] DONUT Collaboration. "Observation of tau neutrino interactions". *Phys. Lett. B*, 504:218–224, 2001.

[19] Q. Ahmad *et al.* "Direct Evidence for Neutrino Flavor Transformation from Neutral-Current Interactions in the Sudbury Neutrino Observatory". *Phys. Rev. Lett.*, 89:011301, 2002.

[20] The Super-Kamiokande Collaboration. "Evidence for an Oscillatory Signature in Atmospheric Neutrino Oscillations". *Phys. Rev. Lett.*, 93:101801, 2004.

[21] M. Antonello *et al.* "Measurement of the neutrino velocity with the ICARUS detector at the CNGS beam". arXiv:1203.3433 [hep-ex], 2012.

[22] D. Verkindt. "Neutrino History". http://lappweb.in2p3.fr/neutrinos/anhistory.html, 1999.

[23] J. Learned, S. Pakvasa. "A Neutrino Timeline". http://www.phys.hawaii.edu/∼jgl/nu_timeline.html, 2005.

[24] D. Verkindt. "A short summary of the neutrino history". http://lappweb.in2p3.fr/neutrinos/, 1999.

[25] MINOS Collaboration. "Improved measurement of muon antineutrino disappearance in MINOS". *Phys.Rev.Lett.*, 108:191801, 2012.

[26] D. Karlen. "The Number Of Light Neutrino Types From Collider Experiments". *Rpp2011-rev-light-neutrino-types*, 2008.

[27] The ALEPH Collaboration. "Precision Electroweak Measurements on the Z Resonance". *Phys.Rept.*, 427:257–454, 2006.

[28] S. Goswami *et al.* "Global Analysis of Neutrino Oscillation". *Nucl. Phys. (Proc. Supp.)*, 143:121, 2005.

[29] K. Nakamuram, S.T. Petcov. "Neutrino Mass, Mixing, And Oscillations". *Rpp2012-rev-neutrino-mixing*, 2011.

[30] SNO Collaboration. "Low Energy Threshold Analysis of the Phase I and Phase II Data Sets of the Sudbury Neutrino Observatory". *Phys.Rev. C*, 81:055504, 2010.

[31] Super-Kamiokande Collaboration. "A Measurement of atmospheric neutrino oscillation parameters by SUPER-KAMIOKANDE I". *Phys.Rev. D*, 71:112005, 2005.

[32] MINOS Collaboration. "Measurement of Neutrino Oscillations with the MINOS Detectors in the NuMI Beam". *Phys.Rev.Lett.*, 101:131802, 2008.

[33] The Daya Bay Collaboration. "Observation of electron-antineutrino disappearance at Daya Bay". *Phys. Rev. Lett. 108, 171803*, 2012.

[34] D. Szam. "Proton proton cycle". http://en.wikipedia.org/wiki/File:Proton_proton_cycle.png, 2012.

[35] T. Thompson. "CNO Cycle". http://www.astronomy.ohio-state.edu/∼thompson/162/Lecture12.html, 2012.

[36] E.Kneringer, V.Grill. "Solar neutrino fluxes". http://physik.uibk.ac.at/05-06/physik4/proseminar/solar_neutrino_spectrum.gif, 2006.

[37] T. K. Gaisser. "Atmospheric Neutrinos". *AIP Conf.Proc.*, 944:140–142, 2007.

[38] The T2K Collaboration. "Neutrino Sources". http://t2k-experiment.org/neutrinos/sources-and-experiments/, 2011.

[39] P. Langacker, R. Rameika, H. Robertson conveners. "Report of the DPF Long Range Study". *Neutrino Mass Working Group*, 1995.

[40] B. Kayser, F. Gibrat-Debu and F. Perrier. "The Physics of Massive Neutrinos". *World Scientific, Singapore*, 1989.

[41] R. D. Klauber. "Pedagogic Aids to Quantum Field Theory : - The Seesaw Mechanism". http://www.quantumfieldtheory.info/TheSeesawMechanism.htm, 2012.

[42] Zykure. "KATRIN Spectrum". http://en.wikipedia.org/wiki/File:KATRIN_Spectrum.svg, 2012.

[43] R. Jimenez *et.al.* "Can we measure the neutrino mass hierarchy in the sky?". *JCAP*, 05:035, 2010.

[44] Ch. Kraus *et al.* "Final results from phase II of the Mainz neutrino mass search in Tritium beta decay". *Eur. Phys. J. C*, 40:447–468, 2005.

[45] E.W. Otten and C. Weinheimer. "Neutrino mass limit from tritium beta decay". *Rept. Prog. Phys.*, 71:086201, 2008.

[46] Y.G. Zdesenko, F.A. Danevich and V.I. Tretyak. "Has neutrinoless double beta decay of ^{76}Ge been really observed?". *Phys. Lett. B*, 546:206–215, 2002.

[47] U. Seljak *et al.* "Cosmological parameter analysis including SDSS Ly-alpha forest and galaxy bias: Constraints on the primordial spectrum of fluctuations, neutrino mass and dark energy". *Phys. Rev. D*, 71:103515, 2005.

[48] A.M. Malinovsky, A.A. Voevodkin, V.N. Lukash, E.V Mikheeva and A.A.Vikhlinin. "Cosmological constraints on the neutrino mass from CMB anisotropy and large-scale structure of the universe". *Astron. Lett.*, 34:445–450, 2008.

[49] N. Spooner. "Semi empirical mass curves". http://physics-database.group.shef.ac.uk/phy303/np-114.gif, 2012.

[50] Nemo Collaboration. "Physics goals - The Double Beta Decay". http://nemo.in2p3.fr/physics/dbd.php, 2012.

[51] K. Zuber. "Double Beta Decay". *Contemp. Phys.*, 45:491–502, 2004.

[52] R. Beuselinck, J.K. Sedgbeer, Y.A. Shitov. "SuperNEMO :- Double Beta Decay". http://www3.imperial.ac.uk/highenergyphysics/research/experiments/supernemo, 2012.

[53] V.B. Brudanin, N.I. Rukhadze, C. Briancon, V.G. Egorov, V.E. Kovalenko, A. Kovalik, A.V. Salamatin, I. Stekl, V.V. Tsupko-Sitnikov, T. Vylov. "Search for double beta decay of Ca-48 in the TGV experiment". *Phys.Lett. B*, 495:63–68, 2000.

[54] H.V. Klapdor-Kleingrothaus *et al.* "Latest Results from the Heidelberg-Moscow Double Beta Decay Experiment". *Eur.Phys.J.A*, 12:147–154, 2001.

[55] NEMO-3 Collaboration. "First results of the search of neutrinoless double beta decay with the NEMO 3 detector". *Phys.Rev.Lett.*, 95:182302, 2005.

[56] NEMO-3 Collaboration. "Measurement of the two neutrino double beta decay half-life of Zr-96 with the NEMO-3 detector". *Nucl.Phys. A*, 847:168–179, 2010.

[57] Fedor A. Danevich *et al.* "Search for 2 beta decay of cadmium and tungsten isotopes: Final results of the solotvina experiment.". *Phys.Rev. C*, 68:035501, 2003.

[58] A. S. Barabash. "Average and recommended half-life values for two neutrino double beta decay: upgrade"'. *Czech.J.Phys.*, 56:437–445, 206.

[59] C. Arnaboldi, C. Brofferio, C. Bucci, S. Capelli, O. Cremonesi, E. Fiorini, A. Giuliani, A. Nucciotti, M. Pedretti, C. Pobes *et al.* "A Calorimetric search on double beta decay of Te-130". *Phys.Lett. B*, 557:167–175, 2003.

[60] N. Ackerman *et al.* "Observation of two-neutrino double-beta decay in ^{136}Xe with EX0-200". *Phys. Rev. Lett.*, 107:212501, 2011.

[61] Nemo Collaboration. "Measurement of the Double Beta Decay Half-life of 150-Nd and Search for Neutrinoless Decay Modes with the NEMO-3 Detector". *Phys. Rev. C*, 80:03250, 2009.

[62] F. Simkovic. "Neutrinoless double-beta decay and related topic". *PEPAN - Joint Institute for Nuclear Research, Dubna,*, 42:98–612, 2011.

[63] S.M. Bilenky *et al.* "Neutrinoless double beta-decay and neutrino mass hierarchies". *Phys. Rev. D.*, 72:053015, 2005.

[64] S. Pascoli, S. T. Petcov. "Majorana neutrinos, neutrino mass spectrum, and the$| < m > |$ ∼10-3 eV frontier in neutrinoless double beta decay". *Phys. Rev. D.*, 77:113003, 2008.

[65] H.V. Klapdor-Kleingrothaus, I.V. Krivosheina *et al.* "Evidence for neutrinoless double beta decay". *Mod.Phys.Lett. A*, 16:2409–2420, 2001.

[66] J.C. Helo *et al.* "Neutrinoless double beta decay at the LHC". *arXiv:1303.0899 [hep-ph]*, 2013.

[67] F. F Deppisch *et al.* "Neutrinoless double-beta decay and physics beyond the standard model". *J. Phys. G: Nucl. Part. Phys.*, 39:124007, 2012.

[68] K. Zuber. "Neutrino physics". *Institute of Physics Publishing*, 2004.

[69] J. Schechter and J. Valle. "Neutrino decay and spontaneous violation of lepton". *Phys. Rev. D*, 25:774, 1982.

[70] R. Mohapatra and P. Pal. "Massive neutrinos in physics and astrophysics". *World Sci. Lect. Note Phys.*, 60:1, 2003.

[71] Z.G. Berezhiani, A.Yu. Smirnov and J.W.F. Valle. "Observable Majoron emission in neutrinoless double beta decay.". *Phys. Lett. B*, 291:99–105, 1992.

[72] R.N. Mohapatra, A. Perez-Lorenzana and C.A. Pires. "Neutrino mass, bulk Majoron and neutrinoless double beta decay". *Phys. Lett. B*, 491:143–147, 2000.

[73] P. Bamert, C.P. Burgess and R.N. Mohapatra. "Multi-Majoron modes for neutrinoless double beta decay". *Nucl. Phys. B*, 449:25–48, 1995.

[74] R.N. Mohapatra and E. Takasugi. "Neutrinoless double beta decay with double Majoron emission". *Phys. Lett. B*, 211:192–196, 1988.

[75] N. Fatemi-Ghomi. *"Measurement of the double beta decay half-life of ^{150}Nd and search for neutrinoless decay modes with NEMO-3 detector"*. PhD thesis, University of Manchester, UK, 2009.

[76] R. Mohapathra. "New contributions to neutrinoless double-beta decay in supersymmetric theories". *Phys. Rev. D.*, 34:3457–3461, 1986.

[77] J.D.Vergados. "Neutrinoless double beta-decay without Majorana neutrinos in supersymmetric theories". *Phys. Lett. B.*, 184:55–62, 1987.

[78] A. Faessler *et al.* "Pion dominance in R-parity violating supersymmetry induced neutrinoless double beta decay". *Phys. Rev. D.*, 77:113012, 2008.

[79] F. Simkovic, M. Krivoruchenko. "Mixing of neutral atoms and lepton number oscillations". *Part. Nucl., Lett*, 6:298–303, 2009.

[80] M. Duerr, M. Lindner, A. Merle. "The Quantitative Impact of the Schechter-Valle Theorem". *JHEP*, 06:091, 2011.

[81] M. Doi *et al.* "Double Beta Decay". *Prog. Theor. Phys.*, 69:602–635, 1983.

[82] S.M Bilenky, J. A. Grifols. "The possible test of the calculations of nuclear matrix elements of the $(\beta\beta)0\nu$-decay". *Phys. Lett. B.*, 550:154–159, 2002.

[83] F. Simkovic, A. Faessler. "Distinguishing the $0\nu\beta\beta$-decay mechanisms". *Prog. Part. Nucl. Phys.*, 48:201, 2002.

[84] F. Deppisch, H. Pas. "Pinning down the mechanism of neutrinoless double beta decay with measurements in different nuclei". *Phys. Rev. Lett.*, 98:232501, 2007.

[85] M. Hirsch *et al.* "Nuclear structure calculation of $\beta^+\beta^+$,β^+/EC and EC/EC decay matrix elements". *Z. Phys. A.*, 347:–160, 1994.

[86] V. Cirigliano *et al.* "Neutrinoless Double Beta Decay and Lepton Flavor Violation". *Phys. Rev. Lett.*, 93:231802, 2004.

[87] J. Schechter and J. W. F. Valle. "Neutrinoless double-β decay in SU(2)U(1) theories". *Phys. Rev. D*, 25:29512954, 1982.

[88] A. Poves. "Nuclear Structure Aspects Of The Neutrinoless Double Beta Decay". *Eur.Phys.J.*, A36:195–200, 2008.

[89] J. Li, G. Colo. "Self-Consistent Skyrme Quasi-particle Random Phase Approximation and the Giant Monopole Resonance in Sn isotopes". In *ECT Exotic modes of excitation conference*, 2007.

[90] N. Paar. "Relativistic Quasiparticle Random Phase Approximation". http://www.phy.pmf.unizg.hr/∼npaar/rrpa.html, 2003.

[91] P. K. Rath *et al.* "Uncertainties in nuclear transition matrix elements for neutrinoless $\beta\beta$ decay within the projected-Hartree-Fock-Bogoliubov model". *Phys. Rev. C*, 82:064310, 2010.

[92] J. Barea, F. Iachello. "Neutrinoless double-β decay in the microscopic interacting boson model". *Phys. Rev. C.*, 79:044301, 2009.

[93] T. R. Rodrigez, G. Martinez-Pinedo. "Energy density functional study of nuclear matrix elements for neutrinoless $\beta\beta$ decay". *Phys.Rev.Lett.*, 105:252503, 2010.

[94] A. Escuderos *et al.* "Contributions of different neutron pairs in different approaches for neutrinoless double-beta decay". *J. Phys. G*, 37:125108, 2010.

[95] A. Faessler *et al.* "Quasiparticle random phase approximation uncertainties and their correlations in the analysis of 0v$\beta\beta$ decay". *Phys. Rev. D*, 79:053001, 2009.

[96] E. Andreotti, C. Arnaboldi, F. T. Avignone III *et al.* "^{130}Te Neutrinoless Double-Beta Decay with CUORICINO". *arXiv:1012.3266v1*, 2010.

[97] C Arnaboldi *et al.* . "Physics potential and prospects for the CUORICINO and CUORE experiments". *Astropart. Phys.*, 20:91–110, 2003.

[98] M. Gnther *et al.* "Heidelberg-Moscow $\beta\beta$ experiment with ^{76}Ge: Full setup with five detectors". *Phys. Rev. D*, 55:54–67, 1997.

[99] C. E. Aalseth *et al.* "The Igex ^{76}Ge Neutrinoless Double-Beta Decay Experiment: Prospects for Next Generation Experiments". *Phys.Rev.D*, 65:092007, 2002.

[100] C. E. Aalseth *et al.* "The IGEX 76ge Neutrinoless Double-Beta Decay Experiment: Prospects for Next Generation Experiments". *Phys. Rev. D.*, 65:09, 2007.

[101] GERDA Collaboration. "A New ^{76}Ge Double Beta Decay Experiment at LNGS". *arXiv:hep-ex/0404039*, 2012.

[102] G. Zuzel *et al.* "The GERDA Experiment at Gran Sasso". *Acta Phys. Pol. B*, 41:1469, 2010.

[103] R. Saakyan. "Neutrino Physics without Neutrinos An experimental overview of Double Beta Decay". In *Conf. DBD , Chile*, 2012.

[104] D. G. Phillips *et.al.* "The Majorana experiment: an ultra-low background search for neutrinoless double-beta decay". *J. Phys.: Conf. Ser. 381 012044*, 2012.

[105] D. G. Phillips II *et al.* "The Majorana experiment: an ultra-low background search for neutrinoless double-beta decay". *J. Phys.: Conf. Ser.*, 381:012044, 2012.

[106] The COBRA collaboration. "First results on double beta decay modes of Cd, Te and Zn isotopes with the COBRA experiment". *Phys.Rev.C*, 76:025501, 2007.

[107] K Zuber *et al.* "COBRAdouble beta decay searches using CdTe detectors". *Phys. Lett. B*, 519:1–7, 2001.

[108] KamLAND-Zen Collaboration. "Measurement of the double-betadecay half-life of ^{136}Xe with the KamLAND-Zen experiment". *Phys.Rev.C*, 85:045504, 2012.

[109] SNO Collaboration. http://snoplus.phy.queensu.ca/, 2012.

[110] SNO+ collaboration. "Neutrinoless Double Beta Decay with SNO+". In *TAUP2011 Munich, Germany C11-09-0*, 2012.

[111] J-L. Vuilleumier. "The Gotthard and MUNU TPCs: From the past to the future?". *J. Phys.: Conf. Ser.*, 179:012013, 2009.

[112] EXO Collaboration. "The EXO-200 detector, part I: Detector design and construction". *JINST 7*, 7:P05010, 2012.

[113] M Auger *et al.* "The EXO-200 detector, part I: detector design and construction". *JINST*, 7:5010, 2012.

[114] M. Auger, D. J. Auty, P. S. Barbeau *et al.* "Search for Neutrinoless Double-Beta Decay in ^{136}Xe with EXO-200". *Phys. Rev. Lett.*, 109:032505, 2012.

[115] NEXT Collaboration. "NEXT-100 Technical Design Report (TDR). Executive Summary". *JINST 7 T06001*, 2012.

[116] V Alvarez *et al.* "NEXT-100 Technical Design Report (TDR). Executive summary". *JINST*, 7:6001, 2012.

[117] M.E. Wieser, J.R. De Laeter. "Evidence of the double β decay of zirconium-96 measured in 1.8109 year-old zircons". *Phys. Rev. C*, 64:024308, 2001.

[118] A. Kawashima, K. Takahashi, A. Masuda (TOKYC+). "Geochemical estimation of the half-life for the double beta decay of ^{96}Zr". *Phys. Rev. C*, 47:R2452R2456, 1993.

[119] H. Hidaka, C.V. Ly and K. Suzuki. "Geochemical evidence of the double β decay of ^{100}Mo". *Phys. Rev. C*, 70:025501, 2004.

[120] T. Kirsten, H. Richter, E. Jessberger (MPIH). "Rejection of Evidence for Nonzero Neutrino Rest Mass from Double Beta Decay". *Phys. Rev. Lett.*, 50:474–477, 1983.

[121] T. Bernatowicz *et al.* (WUSL TATA). "Neutrino mass limits from a precise determination of $\beta\beta$-decay rates of ^{128}Te and ^{130}Te". *Phys. Rev. Lett.*, 69:2341–2344, 1992.

[122] W.J. Lin et al. "Geochemically measured half-lives of ^{82}Se and ^{130}Te". *Nucl. Phys. A,*, 481:477–483, 1988.

[123] E. der Mateosian and M. Goldhaber. "Limits for Lepton-Conserving and Lepton-Nonconserving Double Beta Decay in ^{48}Ca". *Phys. Rev.*, 146:810–815, 1966.

[124] K. You *et al.* "A search for neutrinoless double β decay of ^{48}Ca". *Phys. Lett. B*, 265:53, 1991.

[125] A. Balysh *et al.* "Double beta decay of ^{48}Ca". *Phys. Rev. Lett.*, 77:5186–5189, 1996.

[126] I. Ogawa *et al.* . "Search for neutrino-less double beta decay of ^{48}Ca by CaF_2 scintillator". *Nucl. Phys. A*, 730:215–223, 2004.

[127] S. Umehara, T. Kishimoto. "Neutrino-less double-beta decay of ^{48}Ca studied by CaF_2(Eu) scintillators". *Phys.Rev. C*, 78:058501, 2008.

[128] CANDLES Collaboration. http://wwwkm.phys.sci.osaka-u.ac.jp/info/syoukai/CANDLES_project.htm, 2012.

[129] S. Umehara, T. Kishimoto *et al.* "CANDLES for double beta decay of ^{48}Ca". *J. Phys.: Conf. Ser.*, 39:356, 2006.

[130] A.S.Barabash et al. (NEMO-3 Collab.). "Investigation of double beta decay with the NEMO-3 detector". *PAN*, 74:312–317, 2011.

[131] V.B. Brudanin *et al.* (TGV Collab.). "Search for double beta decay of ^{48}Ca in the TGV experiment". *Phys. Lett. B*, 495:63–68, 2000.

[132] C. Doerr, H.V. Klapdor-Kleingrothaus. "New Monte-Carlo simulation of the HEIDELBERG-MOSCOW double beta decay experiment". *NIM A*, 513:596–621, 2003.

[133] H.V. Klapdor-Kleingrothaus, I.V. Krivosheina. "The evidence for the observation of 0nu$\beta\beta$ decay: The identification of 0nu$\beta\beta$ events from the full spectra". *Mod.Phys.Lett. A*, 21:1547–1566, 2006.

[134] S.R. Elliott *et al.* (UCI). "Double beta decay of ^{82}Se". *Phys. Rev. C*, 46:1535–1537, 1992.

[135] NEMO Collaboration. "Measurement of the background in the NEMO 3 double beta decay experiment". *Nucl.Instrum.Meth.A*, 606:449–465, 2009.

[136] M. Alston-Garnjost *et al.* (LBL MTHO+). "Experimental search for double-β decay of ^{100}Mo". *Phys. Rev. C*, 55:474–493, 1997.

[137] A. de Silva *et al.* (UCI). "Double β decays of ^{100}Mo and ^{150}Nd". *Phys. Rev. C*, 56:1451–2467, 1997.

[138] V.D. Ashitkov *et al.* "Double beta decay of ^{100}Mo". *JETP Lett.*, 74:529–531, 2001.

[139] W.J. Lin et al. "Double beta-decay of tellurium-128 and tellurium-130". *Nucl. Phys. A*, 481:484–493, 1988.

[140] R. Arnold *et al.* (NEMO-3 Collab.). "Measurement of the $\beta\beta$-decay Decay Half-Life of ^{130}Te with the NEMO-3 Detector". *Phys. Rev. Lett.*, 107:062504, 2011.

[141] N. Takaoka, Y. Motomura, K. Nagao (KYUSH OKAY). "Half-life of ^{130}Te double-β decay measured with geologically qualified samples". *Phys. Rev. C*, 53:15571561, 1996.

[142] C. Arnaboldi *et al.* "Results from a search for the 0v$\beta\beta$-decay of ^{130}Te". *Phys. Rev. C*, 78:035502, 2008.

[143] C. Arnaboldi *et al.* (CUORICINO Collab.). "New Limit on the Neutrinoless $\beta\beta$ Decay of ^{130}Te". *Phys. Rev. Lett.*, 95:142501, 2005.

[144] R. Bernabei *et al.* (DAMA Collab.). "Investigation of $\beta\beta$ decay modes in ^{134}Xe and ^{136}Xe". *Phys. Lett. B*, 546:23, 2002.

[145] A. L. Turkevich, T.E. Economou, G.A. Cowan (CHIC+). "Double-beta decay of ^{238}U". *Phys. Rev. Lett.*, 67:3211–3214, 1991.

[146] A.P. Meshik *et al.* "Weak decay of ^{130}Ba and ^{132}Ba:Geochemical measurements". *Phys. Rev. C*, 64:035205, 2001.

[147] NEMO Collaboration. "Technical performance of the NEMO 3 detector "Advantages and Limitations" ". Technical report, LAL 05-162, 2005.

[148] T. Conneely, T. Head. "Investigation of Geiger cell prototypes for the SuperNEMO detector". Master's thesis, Manchester University, 2008.

[149] Nemo Collaboration. "Influence of neutrons and γ-rays in the Frjus underground laboratory on the NEMO experiment". *Nucl. Instr. Meth.A*, 457:187–498, 2001.

[150] Klaus Eitel (for the Edelweiss collaboration). "Measurements of neutron fluxes in the LSM underground laboratory". *J. Phys. Conf.*, 375:012016, 2012.

[151] O.A.Ponkratenko, V.I.Tretyak, Yu.G.Zdesenko. "The event generator DECAY4 for simulation of double beta processes and decay of radioactive nuclei". *Phys.Atom.Nucl.*, 63:1282–1287, 2000.

[152] Thomas Junk. "Confidence level computation for combining searches with small statistics". *Nucl. Instr. Meth.A*, 434:135–443, 1999.

[153] Tom Junk. "Sensitivity, Exclusion and Discovery with Small Signals, Large Backgrounds, and Large Systematic Uncertainties". http://www-cdf.fnal.gov/ trj/mclimit/mclimit_csm.pdf.

[154] G. J. Feldman and R. D. Cousins. "Unified approach to the classical statistical analysis of small signals". *Phys. Rev. D*, 57:38733889, 1998.

[155] O. Helene. "Upper limit of peak area". *Nucl. Instrum. Meth.*, 212(1-3):319 322, 1983.

[156] S. King. *"Measurement of the Double Beta Decay Half-Life of ^{100}Mo to the 0+1 Excited State, and ^{48}Ca to the Ground State in the NEMO 3 Experiment"*. PhD thesis, University Colege London, 2008.

[157] A.S. Barabash, V.I. Umatov. "NEMO-3 source purity measurements with HPGe detector: ^{48}Ca and ^{100}Mo: Nemo conference". 2012.

[158] "Thorium decay chain". http://www.advancedlab.org/mediawiki/images/7/76/Thorium_Decay_Chain.PNG.

[159] R. Arnold *et al.* "Measurement of double beta decay of ^{100}Mo to excited states in the NEMO 3 experiment". *Nucl. Phys. A*, 781:209–226, 2007.

[160] E. Caurier *et al.* "$\beta\beta$ Decay and Nuclear Structure". *Int. J. Mod. Phys. E*, 16:552, 2007.

[161] M. Horoi *et al.* "Shell-model calculations of two-neutrino double-β decay rates of ^{48}Ca with the GXPF1A interaction". *Phys. Rev. C*, 75:034303, 2007.

[162] SuperNEMO Collaboration. "Probing new physics models of neutrinoless double beta decay with SuperNEMO". *Eur. Phys. J. C*, 70:927–943, 2010.

[163] NEMO Collaboration. "Development of a High Energy Resolution Calorimiter for the SuperNEMO Double Beta Decay Experiment". 2012.

[164] C.Bourgeois. "SuperNemo Calorimeter submodule Manchester". In *Conf.*, 2011.

[165] Yu. Shitov. "SuperNEMO sensitivity studies.". *NEMO3 Internal Note, NemoDocDB-doc-930-v2*, 2009.

[166] S. Agostinelli *et al.* "GEANT4 - a simulation toolkit". *Nucl. Instr. Meth.A*, 506:250–303, 2003.

[167] "Table of Radioactive Isotopes". http://ie.lbl.gov/toi/nuclide.asp?iZA=830207&sortG=D&sortA=E.

[168] A. Zimbal, L. Giacomelli, R. Nolte, H. Schuhmacher. "Characterization of monoenergetic neutron reference fields with a high resolution diamond detector". *Radiat.Meas.*, 45:1313–1317, 2010.

[169] E. Chauveau. "SuperNEMO Cell @ ManchesterEfficiency and Dead time". *Tracker phone meeting proceedings*, 2011.

[170] R.B. Firestone and V.S. Shirley. *"Table of Isotopes 8th Edition. "*. JohnWiley and Sons, 1999.

[171] V. Tretyak. "^{48}Ca and ^{90}Sr source". *Internal analysis meeting*, 2012.